

University of Southampton Research Repository ePrints Soton

Copyright © and Moral Rights for this thesis are retained by the author and/or other copyright owners. A copy can be downloaded for personal non-commercial research or study, without prior permission or charge. This thesis cannot be reproduced or quoted extensively from without first obtaining permission in writing from the copyright holder/s. The content must not be changed in any way or sold commercially in any format or medium without the formal permission of the copyright holders.

When referring to this work, full bibliographic details including the author, title, awarding institution and date of the thesis must be given e.g.

AUTHOR (year of submission) "Full thesis title", University of Southampton, name of the University School or Department, PhD Thesis, pagination

UNIVERSITY OF SOUTHAMPTON
FACULTY OF PHYSICAL AND APPLIED SCIENCES
Optoelectronics Research Centre



**Applications of Parametric Processes in Advanced Optical Communication
Networks**

by

Víctor J. F. Rancaño

Thesis for the degree of Doctor of Philosophy

March 2015

UNIVERSITY OF SOUTHAMPTON

ABSTRACT

FACULTY OF PHYSICAL AND APPLIED SCIENCES
Optoelectronics Research Centre

Doctor of Philosophy

APPLICATIONS OF PARAMETRIC PROCESSES IN ADVANCED OPTICAL
COMMUNICATION NETWORKS

by Víctor J. F. Rancaño

Fibre optic parametric amplifiers have been an important area of research during the last twenty years. However, several technological implications hinder their deployment in commercial communication systems.

The work reported in this thesis has studied these implications both theoretically and experimentally with the aim of understanding the limitations of parametric processes and demonstrating practical subsystems for use in modern communication networks.

The theoretical part of the project has analysed the various types of noise that are present in parametric amplifiers as well as their effects, both when an amplifier is considered on its own or as a part of a repeated transmission line. This task has been carried out on the basis of the statistical characterisation of the noise generated by parametric processes, providing an accurate description of the bit error rate induced by these nonlinear processes on modulated signals.

The experimental part of this work presents the demonstration of two wavelength conversion schemes showing their feasibility for turn-key operation. The respective designs address wavelength division multiplexing (WDM) and spatial division multiplexing (SDM) settings. The performance of these devices is demonstrated through field trials in point-to-point systems, optical switched networks and future SDM networks.

The demonstration of wavelength conversion in SDM networks was based on the multi-element fibre (MEF) technology. The features of this technology as an alternative implementation of SDM were experimentally demonstrated in transmission experiments. In addition, a critical comparison of the pros and cons of the actual implementations of SDM is provided.

A mi madre y a mi hermano

A man is as big as what he hopes and thinks

Kurt Vonnegut Jr.

Heart has its reasons of which reason knoweth not

Blaise Pascal

Contents

Declaration of Authorship	xiii
Acknowledgements	xv
Nomenclature	xvii
1 Introduction	1
2 Nonlinear Optics	9
2.1 Waveguide propagation	11
2.2 Nonlinear optics in optical fibres	13
2.3 Four-Wave Mixing	14
2.4 Conclusions	18
3 Noise in optical communication systems	21
3.1 Amplification	22
3.1.1 EDFA	23
3.1.2 Raman Amplification	24
3.1.3 Parametric Amplification	27
3.1.3.1 Amplitude Noise Sources	29
3.1.3.2 Phase Noise Sources	31
3.2 Propagation	35
3.2.1 Effects of Dispersion on Noise	35
3.2.2 Effects of Fibre Nonlinearity on Noise	36
3.3 Photodetection	40
3.4 Discussion	41
4 Noise Model of Optical Communications	43
4.1 Definitions and Assumptions	44
4.2 Single Stage Amplification	47
4.2.1 Noise Sources in Isolation	48
4.2.1.1 Additive Noise	49
4.2.1.2 Multiplicative Noise	50
4.2.1.3 Phase Noise	54
4.2.2 Combined Noise Sources	57
4.2.2.1 Additive + Multiplicative Noise	57
4.2.2.2 Additive + Phase Noise	59
4.2.2.3 Additive + Multiplicative + Phase Noise	61

4.2.3	Gaussian Approximations	62
4.3	Noise Accumulation and Propagation Effects	63
4.3.1	Additive Noise	64
4.3.2	Additive + Multiplicative Noise	66
4.3.3	Phase Noise	69
4.3.4	Additive + Multiplicative + Phase Noise	70
4.3.5	Interactions between Phase Noise and Dispersion	71
4.4	Effects on Channel Capacity	75
4.5	Analysis of Photodetection	77
4.5.1	Effects of Phase Noise on Photodetection	77
4.5.2	Efficiency of Phase Noise Detection	78
4.6	Discussion and Conclusions	81
5	Verification of Phase Noise Model	83
5.1	Experimental Setup	83
5.2	Preliminary Characterisations	86
5.3	Phase Noise in Differential Detection Schemes	88
5.4	Phase Noise in Coherent Detection Schemes	89
5.5	Conclusions	91
6	Wavelength Conversion Experiments	93
6.1	Basic Wavelength Converter Scheme	95
6.1.1	Performance Limiting Factors	99
6.2	Bidirectional Wavelength Converter	101
6.3	Automatic Pump Polarisation Alignment	104
6.4	Conclusions	107
7	Spatial Division Multiplexing Experiments	109
7.1	Aim of Spatial Division Multiplexing	109
7.2	Implementations of SDM	111
7.2.1	Multi-core Fibres	111
7.2.2	Multi-mode Fibres	112
7.2.3	Multi-element Fibres	113
7.3	Transmission Experiments	115
7.4	Conclusions	118
8	Network Experiments	119
8.1	Wavelength conversion in Point-to-Point Systems	120
8.1.1	Multi-Channel Operation: Scenario 1	121
8.1.2	Multi-Channel Operation: Scenario 2	122
8.2	Wavelength Conversion in Optical Switched Networks	123
8.3	Wavelength Conversion in SDM Networks	125
8.4	Conclusions	128
9	Conclusions	129
9.1	Modelling	129
9.2	Applications	131

Code of Phase Noise Simulations	133
Gaussian approximation of phase noise	139
PDFs after Photodetection	141
Bibliography	149

List of Figures

1.1	Global annual growth rate of IP traffic, from Ref. [28]	3
1.2	Data-revenue gap. The dilemma that threatens the economics of communication networks	4
2.1	Possible non-degenerate nonlinear interactions in a orthogonally-aligned dual-pump FWM process. PC: Phase Conjugation. UC: Up-Conversion. DC: Down-Conversion	15
2.2	Wavelength allocation of phase sensitive amplification schemes	17
3.1	Energy level transitions of an EDFA	23
3.2	Energy transitions of a Raman process	25
3.3	Energy transitions of a third-order parametric process	27
3.4	Perturbations induced by Kerr effect during propagation. Based on Ref. [128]	36
3.5	SPM efficiency for nonlinear coefficients depending on the dispersive properties of the optical fibre: (a) $D = -200 \text{ ps/nm} \cdot \text{km}$, (b) no dispersion and (c) $D = 200 \text{ ps/nm} \cdot \text{km}$	38
3.6	Optical noise sources in optical communication systems	41
4.1	Examples of QPSK (top row) and 16-QAM (bottom row) constellations degraded by additive (left column), multiplicative (middle column) and phase (right column) noise	48
4.2	Example of decision axes	49
4.3	BER comparison between additive noise and multiplicative for the case of PSK (left) and 16-QAM (right) modulation formats obtained through Monte-Carlo simulations	51
4.4	Procedure of projection of phase noise onto the real axis (top row) and their corresponding PDFs for different values of POSNR (bottom row) for (a) 8-PSK, (b) QPSK and (c) BPSK modulation formats	55
4.5	BER of BPSK, QPSK and 8-PSK (left) and 16-QAM (right) modulation formats degraded only by phase noise computed using the exact PDF	56
4.6	Monte-Carlo simulations of BER induced by additive, multiplicative and hybrid noise for M-PSK modulation formats (left) and for 16-QAM modulation format (right)	58
4.7	PDF of a Gaussian amplitude noise degraded by phase noise (AOSNR = 20 dB)	59
4.8	BER of a 16-QAM signal degraded by a mixture of additive and phase noise	60

4.9	BER for BPSK(a), QPSK(b) and 8-PSK(c) modulation formats degraded by additive and phase noise obtained from analytical expressions (solid) and simulation (dotted)	60
4.10	BER of a 16-QAM (left) and 64-QAM (right) signals degraded by a mixture of additive, multiplicative and phase noise	61
4.11	BER for BPSK(a), QPSK(b) and 8-PSK(c) modulation formats degraded by additive and phase noise obtained from a Gaussian approximation (solid) and simulation (dotted)	62
4.12	System model for a chain of EDFAs	64
4.13	System model for a multiplicative chain of EDFA/Raman amplifiers	67
4.14	System model for a hybrid chain of EDFA, Raman and OPA with nonlinear effects	70
4.15	Comparison of dispersion maps induced by uncompensated 2000 km optical EDFA-based and single-pump OPA-based systems using equally-spaced by 90 km amplification along the link for non-phase-conjugated systems (left) and phase-conjugated systems(right). Dashed green line represents the limit in chromatic dispersion compensation provided by current coherent receivers	73
4.16	Degradation of channel capacity as multiplicative amplitude noise increases (left) and phase noise increases (right)	76
4.17	Comparison between the degradation in BER induced by each detection scheme with respect to BER of the signal before the photodetection (labelled as optical) for additive noise (left) and phase noise (right)	78
4.18	BER induced by coherent detection compared to the BER of the signal before photodetection (labelled as optical) in a signal degraded by ASE and XPM (left column) and ASE and laser linewidth (right column) for different number of symbols used for carrier phase recovery (N_r)	80
5.1	Experimental setup comprising erbium doped fibre amplifiers (EDFA), a highly nonlinear fibre (HNLF) and an arrayed waveguide grating (AWG)	84
5.2	Constellation distortion induced by pump dithering	86
5.3	Comparison of the impact of XPM, PLT and PDT using unbalanced differential detection (left) and balanced differential detection (right)	87
5.4	Characterization of BER vs.frequency generated by pump dithering transfer (PDT) in BPSK signals detected by an unbalanced differential receiver (left). Same results and comparison with simulation if equation 5.2 is used to compute the POSNR(right)	88
5.5	BER curves for different values of pump dithering for unbalanced differential detection for a 40 Gbps BPSK signal (right).	89
5.6	Characterization of BER vs.frequency generated by PDT and PLT in BPSK signals detected by a coherent receiver (left). Same results if equations 5.3 and 5.1 are used to compute the POSNR(right). Solid lines represent the BER of the signal after differential detection, showing the larger degradation induced by the coherent receiver	90
5.7	Characterization of BER vs. POSNR generated by pump dithering transfer (PDT) and pump linewidth transfer (PLT) in BPSK signals at different repetition rates (left). Comparison of BER vs. POSNR generated by PDT in BPSK and QPSK signals at different repetition rates (right)	91

6.1	Wavelength converter set-up	95
6.2	An example of a multi-channel nonlinear interaction, as observed at the output of the HNLF	96
6.3	Characterization of the conversion efficiencies at the output of the HNLF for the three different types of idlers as a function of the wavelength of the signals	97
6.4	Wavelength converted signal output power as a function of the signal input power at the EDFA input for various input signal wavelengths. Only one signal is considered at a time	97
6.5	BER curves and constellation diagrams for the original (full circles) and wavelength converted (empty circles) 10 Gbd 16-QAM signal	98
6.6	OSNR penalty as a function of the power per pump wave (left) and conversion gain as a function of the power per pump wave (right)	100
6.7	Scheme for bidirectional implementation of a wavelength converter	102
6.8	Comparison of nonlinear interaction for both directions (left) and comparison between single- and multi-channel in one-direction operation (right)	102
6.9	BER degradation induced by the bidirectional WC on a 10 Gbd BPSK (left) and on a 10 Gbd 16-QAM (right)	103
6.10	Degenerate nonlinear pump interaction for a random (left) and optimum (right) alignment of the pumps	105
6.11	Modifications performed in the wavelength converter scheme to provide polarization stability. PD: photodiode	105
6.12	Experimental characterization of the pump alignment system: response time after switching on the automatic feedback (left) and BER curves in function of time in absence (right - black solid line) and presence (right - red dashed line) of the automatic feedback system	106
7.1	Fibre geometries of the current implementation of SDM	112
7.2	Different types of MEF implementations: passive MEF (left) and erbium doped MEF (right)	113
7.3	Fibre geometries of the current implementation of SDM	115
7.4	Gain and noise figure of the ME-EDFA	116
7.5	Spectrum of signals transmitted through the dark fibre link (left) and through the MEF (right) before and after being amplified by the ME-EDFA	116
7.6	BER degradation induced by the ME-EDFA	117
8.1	Experimental set-up of the transmission experiment. Rx: receiver. WSS: wavelength selective switch	120
8.2	Spectral allocation of the various signals at the output of the transmission link for Scenario 1. Frequency references are given in THz	121
8.3	OSNR values for a BER of 10^{-3} at different transmission points for scenario 1 (left) and eye diagrams for the OOK signal (top row - time scale: 20 ps/div) and constellation diagrams for BPSK (middle row) and QPSK (bottom row) signals at different transmission points for scenario 1 (right)	122
8.4	Spectral allocation of the various signals at the output of the transmission link for Scenario 2. Frequency references are given in THz	123

8.5	OSNR values for a BER of 10^{-3} at different transmission points for scenario 2 (left) and BER curves for QPSK1 back-to-back (B2B, open triangles), after the first transmission (600 km, solid circles), the wavelength conversion (600 km + WC, open circles) and the second loop transmission (600 km + WC + 600 km, solid triangles) (right)	123
8.6	Scenario for characterisation of the WC in optical switched networks. Constellation and eye diagrams corresponding to the transmitted and received signals of the signal path	124
8.7	BER values measured for OOK signals (left) and PSK signals (right) in the optical switched scenario	125
8.8	Contention problem arisen in hybrid SDM/SSMF systems	126
8.9	Scenario for characterisation of the WC in SDM networks	126
8.10	BER values measured for PDM-QPSK 40 Gbd signals (left) and constellation diagrams at transmission and reception for both modulation formats (right)	127
C.1	Block diagram of a direct detection scheme	141
C.2	Block diagram of a differential detection scheme	142
C.3	Evolution of probability density functions for differential detection when OSNR decreases (top row) and when POSNR decreases (bottom row). Analytical curves shown in red and histograms from Monte-Carlo simulation shown in blue	143
C.4	Block diagram of a balanced differential detection scheme	144
C.5	Evolution of probability density functions for balanced differential detection when OSNR decreases (top row) and when POSNR decreases (bottom row). Analytical curves shown in red and histograms from Monte-Carlo simulation shown in blue	145

List of Tables

4.1	NFs and gains for a chain of EDFA and Raman amplifiers	66
4.2	NFs and gains for a multiplicative chain of EDFA and Raman amplifiers	68
4.3	NFs and gains for a chain of EDFA, Raman and OPA with fibre nonlinearities	71

Declaration of Authorship

I, **Víctor J. F. Rancaño**, declare that the thesis entitled *Applications of Parametric Processes in Advanced Optical Communication Networks* and the work presented in the thesis are both my own, and have been generated by me as the result of my own original research. I confirm that:

- this work was done wholly or mainly while in candidature for a research degree at this University;
- where any part of this thesis has previously been submitted for a degree or any other qualification at this University or any other institution, this has been clearly stated;
- where I have consulted the published work of others, this is always clearly attributed;
- where I have quoted from the work of others, the source is always given. With the exception of such quotations, this thesis is entirely my own work;
- I have acknowledged all main sources of help;
- where the thesis is based on work done by myself jointly with others, I have made clear exactly what was done by others and what I have contributed myself;
- parts of this work have been published as: [1–14]

Signed:.....

Date:.....

Acknowledgements

As with any effort that spans for several years, the work collected in this document has been influenced by many persons to whom I owe the due acknowledgements.

First of all, I want to thank my family for the support provided during those periods of frustration (an essential part during the attainment of the doctoral degree) in which experiments do not work.

Similarly, I want to thank my supervisors Periklis Petropoulos and David Richardson for their guidance and patience through this process. Even though we do not share similar points of view about the practical applicability of research due to my background, this different perspective has resulted in a worthy openness.

In the same manner, I want to thank the people who spent many hours with me in the lab: Liam Jones, Mohammed Ettabib, Kyle Bottrill, Saurabh Jain and Francesca Parmigiani.

Last but not least, I want to thank my good friend Adam Breen for helping me to keep the remains of my sanity during those enjoyable afternoon trainings at Area 51.

Nomenclature

AOWC	All Optical Wavelength Converter
ASE	Amplified Spontaneous Emission
AWG	Arrayed Waveguide Grating
B2B	Back-to-Back
BER	Bit-Error Rate
BPSK	Binary Phase Shifting Keying
CGWN	Complex Gaussian White Noise
CW	Continuous Wave
DCM	Dispersion Compensation Module
EDFA	Erbium-Doped Fibre Amplifier
FOPA	Fibre-Optic Parametric Amplifier
GVD	Group Velocity Dispersion
HNLF	Highly Non-Linear Fibre
IFWM	Intra-channel Four-Wave Mixing
IXPM	Intra-channel Cross Phase Modulation
NF	Noise Figure
NRZ	Non Return-to-Zero
OOK	On-Off Keying
OPA	Optical Parametric Amplifier
OSNR	Optical Signal-to-Noise Ratio
PAS	Parametrically-Amplified System
PDF	Probability Density Function
PDH	Plesiochronous Digital Hierarchy
PDL	Polarisation Dependent Loss
PDT	Pump Dithering Transfer
PLT	Pump Linewidth Transfer
POSNR	Phase Optical Signal-to-Noise Ratio
PSA	Phase Sensitive Amplifier
PSD	Power Spectral Density
PSNR	Phase Signal-to-Noise Ratio
QAM	Quadrature Amplitude Modulation
QPSK	Quaternary Phase Shifting Keying

RIN	Relative Intensity Noise
RZ	Return-to-Zero
SBS	Stimulated Brillouin Scattering
SDH	Synchronous Digital Hierarchy
SDM	Spatial Division Multiplexing
SNR	Signal-to-Noise Ratio
SPM	Self Phase Modulation
SRS	Stimulated Raman Scattering
SSFM	Split-Step Fourier Method
SSMF	Standard Single Mode Fibre
SRS	Stimulated Raman Scattering
TOD	Third Order Dispersion
XPM	Cross Phase Modulation
WC	Wavelength Converter
WDM	Wavelength Division Multiplexing

Introduction

The most important lesson of history, it has been said, is that nobody learns history's lessons

Aldous Huxley

During last twenty years, the field of optical communications has lived under the sword of Damocles of an unseen ghost that, so far, has been reluctant to appear: the capacity crunch. This is an abstract concept that defines the hypothetical turning point in the ever decreasing cost of communications that would lead to a hampering in the development of the related technologies of information. Ironically, the rush to beat this unseen ghost led to the actual crash that this field suffered in the turn of the century: the burst of the dot-com bubble [15].

Since the mid eighties this perfect storm has threatened to outbreak several times, dying down every time through either the development or the enhancement of optical or electronic technologies, which allowed an increase in the existing capacities of optical transmission systems. Thus, capacity shortages seem to be a chronic disease of communication systems, making the analysis of its time evolution of interest in order to propose definitive solutions to this recurring problem whilst avoiding the consequences that the field of communication systems experienced during the last crash. These solutions are better understood in the light of the historical evolution of optical communications.

Evolution of Optical Communication Networks

Communications has been a field very prone to hype and exaggerated expectations even before the era of the optical fibre. Examples of this were the bubbles and overestimation in sales expectations of cable modems that took place in the 1960s [16] and of hybrid fibre-coax solutions in the early 1990s [17]. In both cases, a large traffic growth during several years led to overexpectations first and to large financial losses subsequently.

During the 1980s the first generation of commercial digital optical communication systems were deployed, the plesiochronous digital hierarchy (PDH) [18], providing digital

single-carrier modulation formats at speeds of Mbit/s. But it was at the beginning of the 1990s when the boom started. During this decade, the Erbium doped fibre amplifier (EDFA) started to be deployed in commercial systems and the second generation of optical communications systems was developed: the synchronous digital hierarchy (SDH) [19], providing single carrier digital communication systems synchronised by atomic clocks, increasing the achievable bit rates to 2.5 Gbit/s.

In 1993 one of the most important events for optical communications happened in the field of computer science: Mosaic [15], the first graphical browser was released. The internet became popular outside the scientific circles. This was not the only event that led to the spectacular growth of the internet during 1995 and 1996 ($\approx 900\%$ annual growth), but it was one of the most important. Since then, the traffic of communication systems has been dominated by data communications. It was in those days when the term capacity crunch was definitively bound to communications and the myth was spread across different sectors [20].

This overwhelming growth during these very years spawned the overestimation that the size of the internet doubled each four months [15]. This chimera, together with that of the pantagruelian voracity of bandwidth from users, resulted in the fast development of a third generation of optical systems: the wavelength division multiplexing (WDM) [21]. This generation was the first to provide multi-carrier transmission. The rush of those days to overcome the upcoming capacity crunch pushed a developed such that the 8 channels of 2.5 Gbit/s supported in 1995 to be expanded to 160 channels of 10 Gbit/s by 2000.

However, the astronomical growth rates observed during 1995 and 1996 decreased to a still appreciable level of 100% a year. The result of this mismatch between the achieved capacity and the actual traffic demands was the main reason of the burst of the dot-com bubble [15]. In fact, data show that 2001 was a watershed in the annual growth rate, which has been decreasing ever since (see Fig. 1.1); not even killer applications, such as video on demand (either free or subscription based), social networks or the emergence of powerful mobile devices like smartphones being capable of revitalizing it.

Since 2000 the main approach followed to achieve an increase in the capacity of optical communication systems has involved the adoption of higher order modulation formats with an increased spectral efficiency, chiefly by mimicking the evolution of wireless systems. The increase in the density of modulation formats and the spectrum allocation along with the use of techniques of coherent detection led to the development of the polarisation multiplexed coherent receiver in 2006 [22], and its subsequent standardisation by the Optical Internetworking Forum (OIF) [23, 24] as well as the standardisation of the flexible optical grid [25]. These developments sky-rocketed the interest in electronic processing of optical signals for transmission and nonlinear compensation, to the current level of development in which 16 quadrature amplitude modulation (QAM) and higher

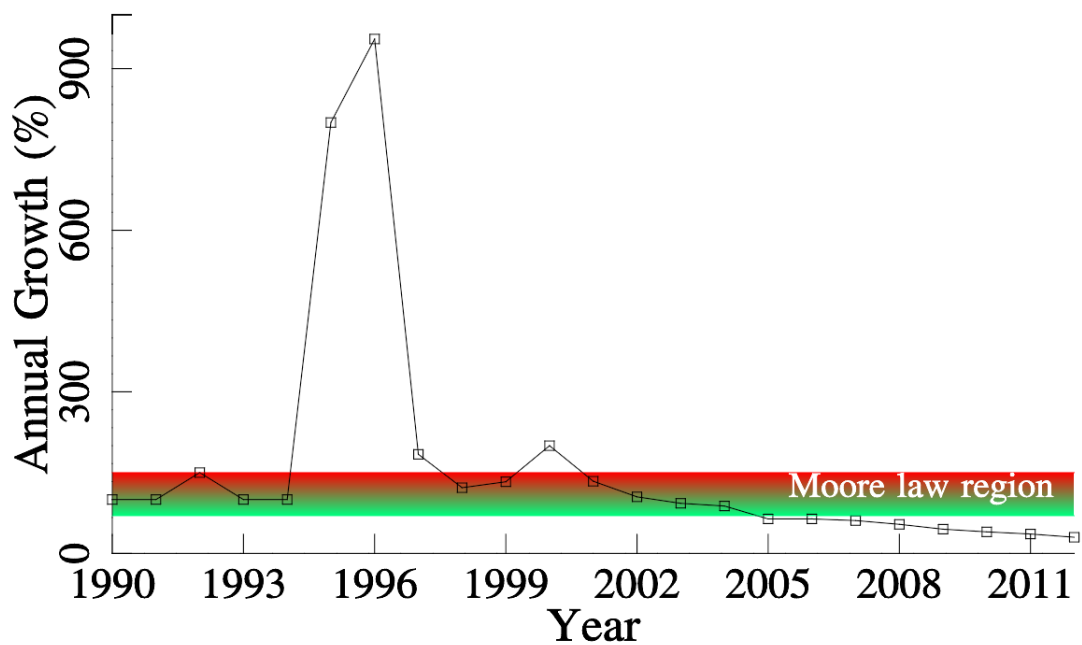


Figure 1.1: Global annual growth rate of IP traffic, from Ref. [28]

order modulation formats are considered with the aim of transmitting *superchannels* of terabits per second.

This shift from the optical to electronic processing has not come for free, since the power consumption of the digital signal processing (DSP) at gigabit per second rates is very demanding and escalates with the clock frequency. Therefore the application of wireless techniques is very challenging at optical bit rates. A side effect of this high power consumption of DSP has been the decrease in the ratio of power consumed by EDFAs compared to that of transponders in long haul communication systems from $\approx 25\%$ for an 80-wavelength system of 10 Gbit/s in 2000 to $\approx 3\%$ for 80-wavelength systems of 100 Gbit/s in 2012 [26].

Since 2000 one of the most popular creeds regarding the traffic growth has been the so-called *Moore's law* of optical communications [27], by which, Internet traffic annually grows in the range of 70-150%. Although data show that this law has not been in force since 2005 (see Fig. 1.1 for actual trends), its echoes still reverberate nowadays as happened between 1997 and 2000 with the myth of the Internet doubling each four months. Data from different sources [28–32] agree that the growth rate of Internet is decreasing each year, the current annual growth rate being in the region of $\approx 30\%$.

Effects of Traffic Growth in Telecommunication Markets

One of the platitudes very common is that users of communication networks are so bandwidth-greedy that the traffic demand grows *pari passu* with capacity growth, even though the demonstrated capacities are not really implementable in commercial systems. In this sense, a common misconception assume that the capacity achieved by hero experiments [33] is immediately filled with user traffic. The reality is that telecommunication markets behave like any other market, in the sense that once an increasing ratio of the population has gained access to communication networks for longer and longer periods of time everyday, the growth rate of this market decreases.

Even though the growth rates are decreasing each year, the increase in the total volume of the data traffic is significant and must be dealt with. As was already mentioned, the approach adopted in optical communications to overcome this growth has been the adoption of technological advances.

Technology advances provide the required cost reduction for communication companies to increase their revenues. However, the distinctive tight competition of this market enforces a price reduction that limits the maximum profit. In this situation, Internet service providers (ISPs) are in the middle of a hobbesian trap in which they must offer increasing capacity services at decreasing prices to retain their subscribers, which seriously diminishes the economic benefits achieved by technology advances. Such is the irony of this business, the only one that refuses to increase the price offered to customers for an increasingly scarcer resource: the bandwidth.

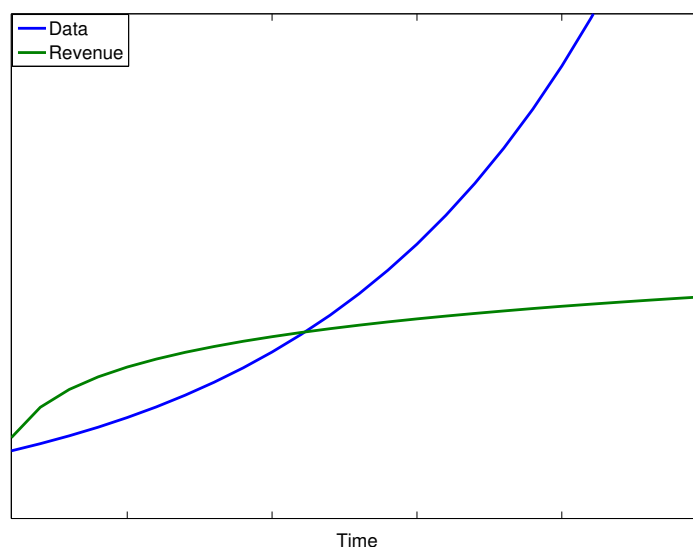


Figure 1.2: Data-revenue gap. The dilemma that threatens the economics of communication networks

So far, the only viable exit to this trap has been the adoption of the technological developments made in the field of communication systems. Since ISPs are not in favour of a price increase to their subscribers (which would expel them from the market), new solutions to this dilemma are needed in order to improve the long-term cost efficiency of the future communication systems.

However, in the last years this cost reduction is becoming more and more difficult as the airwave spectrum saturates and the capacity limits of optical fibres and of silica-based electronic circuits are in sight. These difficulties have generated the so-called *data-revenue gap* that expresses the divergence between the exponential-like growth of data offered to customers and the only logarithmic-like growth of revenue obtained from that traffic (see Fig. 1.2). In this quandary, the perfect storm alarm was triggered again.

Trends in Optical Communications

Since the last warning of capacity crunch was spoken [34], several approaches have been proposed to overcome it. These are chiefly revamped ideas adapted to the current state of development of the optical communications. Currently, the two most important approaches are: (1) the bandwidth expansion provided by the use of Thulium, Praseodymium, Bismuth and Ytterbium doped fibres [35] and (2) the use of multi-core [36], few mode [37] and multi-element fibres [38].

The main line of research has been dominated by spatial division multiplexing (SDM) and aims at reducing the costs and power consumption of components deployed in parallel in different WDM systems. In this way, a SDM transponder, a SDM amplifier or a SDM fibre would provide the same functionality as N parallel WDM ones but require lower cost and/or power consumption [39]. Therefore, this approach does not offer an increase in the effective capacity of current systems but an improvement in their economics.

An effective implementation of SDM would entail great benefits but, up to now, the main target of this line of research has been the merging of the cheapest and least power consuming elements of WDM systems: fibres and optical amplifiers. The evolution of the existing fibres and amplifiers into their SDM counterparts can provide cost saving by optimising their manufacturing process and by allowing an economy of components (ie. using a single pump diode for all the amplifiers) but their impact must be considered by analysing the communication systems as a whole. From this point of view, the saving coming from the integration of fibres and amplifiers is quite meagre.

The average unit cost of a 100 Gbit/s transponder is, at least, one order of magnitude higher than that of an amplifier. Taking into account that in a fully-loaded 2000 km point-to-point link the number of amplifiers is about 25 (one each 80 km) and the number

of transponders is 80, it can be estimated that the cost of the amplifiers sums up to $\sim 3\%$ of the total cost of the hardware. In addition, as was already mentioned, the power saving coming from these approaches can be at most a 3% per merged WDM system. Therefore the advantages of SDM are quite limited in optical communication systems, as conceived nowadays. The imminent implementation of flexigrid networks, with a denser packaging of signals, will further reduce the number of EDFAs compared to that of transponders in a optical system (EDFA-to-transponder ratio), decreasing even more these savings. The potential benefits of SDM based on fibre and EDFA integration in optical switched and short reach communication networks are even more limited, since these types of networks exhibit a smaller ratio of EDFA-to-transponder, which can make SDM not economically viable in these environments.

In this context, and in order to enhance the cost efficiency of SDM solutions, an increased EDFA-to-transponder ratio is necessary. This ratio can be improved in two main ways: a) increasing the reach of optical systems without increasing the complexity (and therefore the cost) of the transponders and b) replacing electrical regenerators/transponders at intermediate locations required for the optimisation of the optical spectrum. The former approach mainly applies to point-to-point networks whereas the latter one applies to optical switched networks.

Both approaches can be implemented by using all-optical signal processing techniques, that have the potential to compensate and regenerate optical signals without increasing the complexity of the transponders, and all-optical wavelength conversion techniques, that provide functionality for the resolution of contention problems in optical switched networks.

In both cases the result is the increase in the significance of the optical part of communication systems that can process several channels simultaneously, independently of modulation formats and bit rates. The increasing difficulty in the development of optical systems is calling for a comeback to the exploitation of an essential feature that the mimicking of wireless environment cannot exploit: optical fibres can be engineered whereas the airwave medium is "as is". The exploitation of this feature, heavily relying on an optical approach, can highly improve the effectiveness of SDM approaches.

Scope of this Work

In light of the current state of optical communication systems, an emphasis on their optical part is required to compensate for the growing imbalance between the relative importance of the electrical versus the optical parts of these networks. One of the methods that can be used for this compensation is the application of optical parametric amplification to substitute electrical with optical processing of signals.

All-optical signal processing offers the potential of implementing functionalities such as wavelength conversion [1], nonlinearity compensation [40] and optical regeneration [41]. Nevertheless, the core part of the work related to optical parametric amplification has been performed in laboratory experiments.

In this context, the objective of this thesis is the development, characterisation and field demonstration of all-optical signal processing devices capable of performing in real communication systems. The aim of this work is the demonstration of the required degree of reliability to replace electrical devices with optical ones performing similar tasks.

The work contained in this thesis comprises three contributions. The main contribution presented in this work consists of the development of an all-optical multichannel-modulation- and bit rate-independent polarisation insensitive wavelength converter and the demonstration of the feasibility of its operation in real systems under different network topologies. However, the implementation of nonlinear devices of this type requires background work to characterise the effects induced by them on amplified signals. This work is the second main contribution of this thesis and allows a better understanding of the cumulative effects induced by these types of nonlinear devices working together with the optical components currently present in communication systems.

The last chief contribution presented is the feasibility of implementation of these kind of devices in future SDM networks and the demonstration of the potential benefits that can be obtained from them and this is experimentally demonstrated on several network topologies.

The structure of the rest of the thesis is as follows: Chapter 2 presents the required theoretical basis of nonlinear optics, paying special attention to parametric amplification implemented in optical fibres. The noise features of this process are analysed in Chapter 3, where a comparison with the noise features of erbium doped fibre amplifiers and Raman amplifiers is presented.

Chapters 4 and 5 develop a comprehensive theory characterizing the degradation induced by parametric amplifiers on modulated signals and experimentally verifying its validity. On this basis more complex accomplishments can be developed in the future. The work presented in these chapters is planned to be published in upcoming publications.

Chapter 6 discusses the development of two novel all-optical wavelength converter (AOWC) schemes based on parametric processes, and the experiments performed on it back-to-back. The work collected in this chapter has already been published in Refs. [1, 2, 7].

Chapter 7 presents the viability a candidate to SDM that addresses most of the issues that previous SDM approaches suffer from and the possible benefits of its use. The work collected in this chapter has already been published in Refs. [3–6].

Finally, Chapter 8 shows the performance of the previously presented AOWC schemes in point-to-point, switched and SDM optical communication systems. The work collected in this chapter has already been published in Refs. [9, 13, 14].

Nonlinear Optics

It requires wisdom to understand wisdom: music is nothing if the audience is deaf

Walter Lippmann

Unlike linear communication channels, where the information capacity can be increased indefinitely by increasing the power of the transmitted signal according to the Shannon theorem $C = W \cdot \log_2(1 + SNR)$ [42], optical fibres are nonlinear communication channels. Nonlinearity prevents from increasing the amount of information transmitted through them to arbitrarily high values [43]. The constraints that fibre nonlinearity imposes on modulated signals are tightly bounded to the physical properties of nonlinear media. Therefore, if the aim is to maximize the transmission capacity of optical fibres, an understanding of these nonlinear phenomena is required. This chapter provides an outline of the nonlinear effects that distort modulated signals during their propagation along optical fibres. These effects can degrade the quality of the signal or, under certain conditions, improve it. A more detailed description of the physical effects of interest in this work will be provided in Chapter 3.

A dielectric medium, such as the optical fibre, is generally nonconducting and nonmagnetic and the electrons are regarded as being tightly bound to the nuclei. For such media the interaction between light and matter can be regarded as a dielectric subjected to an electric field. The applied field polarises the molecules in the medium, displacing them from their equilibrium positions and inducing a dipole moment. The bulk polarisation P resulting from this dipole moment induces a reduction in the electric field inside the material by a factor of $1 + \epsilon$ [44], where ϵ is the dielectric constant of the medium. This bulk polarisation can be expressed as:

$$\bar{P} = \chi^{(1)} \cdot \bar{E} \quad (2.1)$$

where the proportionality constant, called susceptibility, is related to the dielectric constant by the expression:

$$\epsilon = 1 + \chi^{(1)} \quad (2.2)$$

The dielectric constant ϵ is a complex magnitude whose real and imaginary parts respectively account for the absorption and refraction induced by the medium. These properties are also represented by the refractive index $n_0^2 = \epsilon$.

Similarly, the response to magnetic fields can be characterised by the magnetic permeability μ . However, at optical frequencies, the value of this magnitude in most of the materials is very close to one and its influence can be neglected. Silica optical fibres, being nonmagnetic materials, also exhibit this behaviour.

Thus, the absorption and refraction induced in a linear medium by an external electric field are aligned with the direction of polarisation of the incident wave and are independent of its power. However, when a medium is subjected to an intense electric field, such as that due to a laser pulse, the polarisation response is not adequately described by the previous equations. Assuming that the polarisation of the medium is still weak compared to the binding forces between the electrons and nuclei, the polarisation can be expressed as a power series of the applied electric field [45]

$$\vec{P} = \chi^{(1)} \cdot \vec{E}_i + \chi^{(2)} : \vec{E}_i \vec{E}_j + \chi^{(3)} \vdots \vec{E}_i \vec{E}_j \vec{E}_k \quad (2.3)$$

where the operations labelled as \cdot and \vdots represent the third-rank and fourth-rank tensorial products respectively. This type of product accounts not only for optical properties derived from the lattice geometry of the medium (represented by χ^2 and χ^3), but also for the interactions between the possible polarisations and/or frequencies of the waves taking part in the nonlinear interaction (represented by \vec{E}_x where $x = i, j, k$). Therefore, nonlinear interactions can induce coupling effects between different waves and polarisations.

This formalism leads to the corresponding definitions for the nonlinear dielectric constant, the nonlinear susceptibilities and the nonlinear refractive index [46, 47]

$$\begin{aligned} \epsilon &= 1 + \chi^{(1)} + \frac{1}{2}\chi^{(2)}|E| + \frac{3}{4}\chi^{(3)}|E|^2 \\ n &= n_0 + n_1|E| + n_2|E|^2 \end{aligned} \quad (2.4)$$

where $n_1 = \Re\{\chi^{(2)}\}$ and $n_2 = 3/8n_0\Re\{\chi^{(3)}\}$. These relations show that an applied external field modifies the optical properties of the material and that, for the case of a nonlinear medium characterized by χ^3 , this modification is intensity dependent.

However, the changes induced by the external field on the material affect at the same time the field itself. Thus, the propagation characteristics of light need to be described to fully understand the interaction of light with the medium. The transformation that optical signals undergo during their propagation along a medium is fully described by Maxwell's equations. Following from these equations, the propagation of light in an insulating and nonmagnetic medium can be described by [48]

$$\nabla \times \nabla \times \bar{E} = -\frac{1}{c^2} \frac{\partial^2 \bar{E}}{\partial t^2} - \mu_0 \frac{\partial^2 \bar{P}}{\partial t^2} \quad (2.5)$$

The presence of time derivatives on the right hand side of this equation requires to take into account the nature of the particles involved in the interaction. This is represented by time-dependent susceptibilities, thus the polarisation turns out to be the convolution between the susceptibilities and the corresponding electric fields. Most of linear and nonlinear interactions between light and matter are carried through by electrons or nuclei [49]. On one hand, electronic interactions are very fast, their lifetime being in the order of few femtoseconds, and their interactions can be considered as instantaneous. In this sense, if only electronic interactions are considered, the susceptibilities are assumed as Dirac delta functions in time and the convolution reduces to a product. On the other hand, interactions involving nuclei (such as Raman scattering [50]) are much slower than electronic ones, their lifetime being in the order of hundreds of femtoseconds. This feature does not allow such interactions to be treated as Dirac delta functions and more cumbersome analysis is required. In this work, only electronic interactions are assumed, considering all the optical nonlinearities as Dirac delta functions.

Not all nonlinear media exhibit the same type of nonlinearity. The microscopic symmetry of the molecules and their arrangement of the lattice play an important role in the macroscopic properties exhibited by materials [51]. Regarding the microscopic symmetry of the materials, crystals can be classified in two main categories: centrosymmetric and noncentrosymmetric. In general, noncentrosymmetric materials only exhibit second order nonlinear optical response ($n_1 \neq 0$) whereas centrosymmetric materials only exhibit third order nonlinear optical response ($n_2 \neq 0$). Since silica optical fibres are centrosymmetric systems, henceforth the discussion will be centered about third order nonlinearities.

2.1 Waveguide propagation

Equation (2.5) provides a general formalism for the third order nonlinear effects in media. However, the complexity of this equation restricts the number of situations in which it can be exactly solved. One of these cases is the propagation of Gaussian beams through a bulk material [52].

Nevertheless the inherent divergence of these beams prevents from its use in long distance systems. For these applications, where light needs to be confined so that the attainable power at the end of the system is maximised, waveguides were developed. An optical waveguide is a dielectric structure that confines and transmits energy at optical wavelengths [53].

Conversely to the case of uniform bulk materials, the cross-section of the waveguide is engineered to provide confinement and low-loss transmission. This feature imposes an additional complexity to equation (2.5) and as a result analytical solutions can only be obtained for a small set of waveguide geometries. In this work, only cylindrical geometries are discussed, since we are concerned with optical fibres only.

Applying equation (2.5) for the case of a cylindrical geometry, the equation that rules light propagation in an optical fibre is obtained:

$$\frac{\partial^2}{\partial \rho^2} \bar{E} + \frac{1}{\rho} \frac{\partial}{\partial \rho} \bar{E} + \frac{1}{\rho^2} \frac{\partial^2}{\partial \phi^2} \bar{E} + \frac{\partial^2}{\partial z^2} \bar{E} + n^2 k_o^2 \bar{E} = 0 \quad (2.6)$$

where ρ , ϕ and z are the cylindrical coordinates, n is the refractive index and k_o is the wavenumber.

At any frequency ω , optical fibres can support a finite number of guided modes whose spatial distributions $E(r, \omega)$ are solutions of the wave equation (2.6) [48]. In addition, any optical fibre can support a continuum of unguided radiation modes.

The solutions of the guided modes are ruled by an eigenvalue equation that sets the value of the propagation constant for each mode [54]. These solutions are usually expressed by β_{mn} , where both m and n take integer values. The corresponding modal field is well defined by the pair mn leading to four different types of modes: TM_{0n} , TE_{0n} , HE_{mn} and EH_{mn} . TM modes are solutions characterised by a null longitudinal magnetic field, whereas TE modes are characterised by a null longitudinal electric field. On their part, EH and HE are hybrid modes with longitudinal electric and magnetic fields.

The number of modes supported by a given fibre at a given wavelength depends on its design parameters, namely the core radius and the core-cladding refractive index difference. These parameters determine the cut-off frequency of each mode, below which the mode does not propagate. A single-mode fibre only supports the mode with the lowest cut-off frequency, the mode HE_{11} , also called the fundamental mode.

A standard single-mode fibre is not truly single mode because it supports two degenerate modes that are polarised in two orthogonal directions. In theory both modes do not couple but in real fibres small departures from cylindrical symmetry result in the coupling of the two polarisation states by breaking the mode degeneracy.

2.2 Nonlinear optics in optical fibres

The generic result of (2.6) can be applied to the special case in which an applied electric field with a slowly varying envelope propagates through a silica standard single-mode optical, yielding the nonlinear Schrödinger equation (NLSE) which rules the behaviour of a single-polarisation signal with a slowly varying envelope [48]

$$\frac{\partial A}{\partial z} + \frac{i\beta_2}{2} \frac{\partial^2}{\partial t^2} A + \frac{\alpha}{2} A = i\gamma (|A|^2 A) \quad (2.7)$$

where β_2 represents the dispersion of the waveguide, α the attenuation coefficient and γ the nonlinear coefficient that relates to nonlinear refractive index as $\gamma = \omega n_2 / c A_{eff}$. Since the nonlinear coefficient of the fibre is related to the nonlinear refractive index, the effects induced on the propagating electric field are also intensity dependent.

The right hand side of eq. (2.7) shows that as the power of the applied electric field increases, a phase shift proportional to the power of the wave is induced. This distortion, induced by the signal on itself is known as self phase modulation (SPM) and induces a signal distortion in the information carried that prevents from the increase of the amount of information carried by the fibre by arbitrarily increasing the signal power.

The second term on the left hand side of equation (2.8) represents the dispersive effects induced during propagation. Dispersion is related to the dependence of the refractive index on the frequency. It is a linear effect that causes a different propagation speed for each frequency component of the propagating signals and also distorts the information carried through the fibre. The frequency dependence of the group velocity gives rise to a group velocity dispersion (GVD) that broadens the pulses of modulated signals. Since the signal power is not changed because of dispersion, the peak power of the signal decreases as the signal propagates through the fibre, reducing the effect of nonlinearities on the signals.

Equation (2.7) models the propagation of a single wave propagating through an optical fibre. However, in multichannel operation, the nonlinear polarisation can induce the interaction between different waves giving rise to additional nonlinear effects. As was already mentioned, nonlinear polarisations induce the simultaneous interaction of several electric fields (see eq. (2.3)) without any *a priori* restriction in their frequency, polarisation or wavenumber. In this sense, the very values of the susceptibility tensor set the nature and importance of the nonlinear interactions for each particular crystal.

These additional nonlinear effects cannot be addressed with the equation (2.7) and needs to be extended in order to model multichannel propagation [48]. For the particular

case of optical fibres, that are amorphous isotropic materials, the propagation of two-polarised optical signals takes the form of the so-called Manakov system of equations [55, 56]

$$\frac{\partial}{\partial z} \begin{pmatrix} A_i^x \\ A_i^y \end{pmatrix} + \frac{i\beta_2}{2} \frac{\partial^2}{\partial^2 t} \begin{pmatrix} A_i^x \\ A_i^y \end{pmatrix} = i \left(\gamma_{SPM} \begin{vmatrix} A_i^x \\ A_i^y \end{vmatrix}^2 + \gamma_{XPM} \begin{vmatrix} A_j^x \\ A_j^y \end{vmatrix}^2 \right) \begin{pmatrix} A_i^x \\ A_i^y \end{pmatrix} \quad (2.8)$$

where the superscripts refer to the polarisation of the wave and the subscripts represent wave indices. The values of the nonlinear matrices γ_{SPM} and γ_{XPM} depend on the relative alignment of the polarisation of the signals and the birefringence and dispersion characteristics of the fibre [57]. The large variety of types of existing optical fibres [58] prevent from obtaining a well defined value for nonlinear coefficients in all the possible cases.

The values of the effective nonlinear coefficients have been calculated for several cases. In particular, the nonlinear interaction in fibres with high or constant birefringence, that maintain the polarisation of the signals relatively constant, leading to a more efficient nonlinear interaction, result in $\gamma_{SPM} = \begin{pmatrix} \gamma_0 & \gamma_0/3 \\ \gamma_0/3 & \gamma_0 \end{pmatrix}$ and $\gamma_{XPM} = \begin{pmatrix} 2\gamma_0 & \gamma_0/3 \\ \gamma_0/3 & 2\gamma_0 \end{pmatrix}$ where γ_0 is the nonlinear coefficient of the single wave NLSE. On the contrary, the nonlinear interaction in fibres with low or random birefringence, that produce an averaging of the nonlinear interaction, result in $\gamma_{SPM} = \gamma_{XPM} = \begin{pmatrix} 8/9\gamma_0 & 8/9\gamma_0 \\ 8/9\gamma_0 & 8/9\gamma_0 \end{pmatrix}$ [56, 57]. Furthermore, the dispersion induces a different propagation speed for each of the signal transmitted within the fibre. This feature results in an additional averaging of the nonlinear interactions induced between different waves in the presence of dispersion [59].

Not only do nonlinear effects cause interactions between existing waves but they can also generate new frequencies from the original ones. In general, third order nonlinear effects can induce third harmonic generation (THG) [45] and four-wave mixing (FWM) [48, 56] interactions. In this work, only FWM will be discussed.

2.3 Four-Wave Mixing

Four-wave mixing is a nonlinear process by which three waves of similar or different frequencies generate a fourth one, while energy and momentum is conserved. Accounting for this effect entails an extension of the previous Manakov equation with an additional term, leading to a system of coupled equations [56]

$$\begin{aligned} \frac{\partial}{\partial z} \begin{pmatrix} A_l^x \\ A_l^y \end{pmatrix} + \frac{i\beta_2}{2} \frac{\partial^2}{\partial t^2} \begin{pmatrix} A_l^x \\ A_l^y \end{pmatrix} = i \left(\gamma_{SPM} \begin{vmatrix} A_l^x \\ A_l^y \end{vmatrix}^2 + \gamma_{XPM} \sum_{j=m,n,o} \begin{vmatrix} A_j^x \\ A_j^y \end{vmatrix}^2 \right) \begin{pmatrix} A_l^x \\ A_l^y \end{pmatrix} \\ + i \sum_{m,n,o} \gamma_{FWM}^{mno} \begin{pmatrix} A_m^x \\ A_m^y \end{pmatrix} \begin{pmatrix} A_n^x \\ A_n^y \end{pmatrix} \begin{pmatrix} A_o^x \\ A_o^y \end{pmatrix}^* \end{aligned} \quad (2.9)$$

where l, m, n, o are the indices of the four waves involved in the nonlinear interaction. The last term on the right hand side of equation (2.9) represents the additional contribution coming from FWM. The summation comprises all the frequency components generated by the waves m, n, o at the frequency of the wave l . As before, γ_{FWM} depends on the relative alignment of the polarisation of the signals m, n, o and on the birefringence and dispersion characteristics of the fibre.

γ_{FWM} , usually called the efficiency of the FWM interaction, is defined as $\gamma_{FWM} = 2\gamma_0 \exp(-i\Delta kz) \cdot f_{1234}$, where f_{1234} is the overlap integral and Δk the *phase matching* [45, 48]. Phase matching describes the relative phase difference between the waves involved in a nonlinear interaction and is one of most important factors that define the very value of γ_{FWM} . A constant or quasi-constant phase relation between the waves yields the most efficient energy transfer between them, thereby increasing the efficiency of the FWM. In the most general case, phase matching is defined as [48]

$$\Delta k = k_m + k_n - k_l - k_o = (n_m\omega_m + n_n\omega_n - n_l\omega_l - n_o\omega_o) / c \quad (2.10)$$

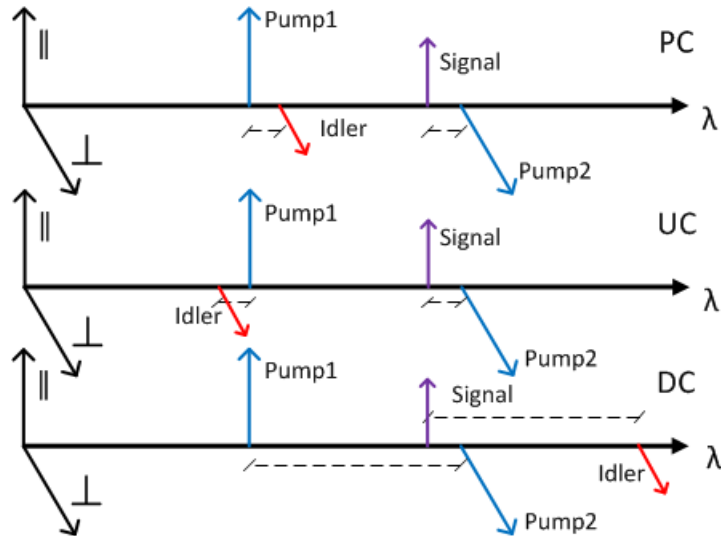


Figure 2.1: Possible non-degenerate nonlinear interactions in a orthogonally-aligned dual-pump FWM process. PC: Phase Conjugation. UC: Up-Conversion. DC: Down-Conversion

where k_i represents the propagation constant of each wave. In fibre optic parametric amplifiers (FOPAs), phase matching heavily depends on the dispersive features of the optical fibre, making the use of dispersion-tailored fibres necessary in order to achieve high FWM efficiencies.

The arbitrary labelling of the wave m, n, o implies that the wave indices can be swapped. Restricting to the non-degenerate case, the different frequencies generated by the permutations of the three waves m, n, o FWM are three and, therefore, a full model must include a six wave model [56]. The possible non-degenerate nonlinear interaction between the input signal and the pump waves are shown in Fig. 2.1. The idlers labelled as up-converted (UC) and down-converted (DC) are identical copies of the input signal whereas the idler labelled as phase conjugated (PC) undergoes an inversion of the imaginary part of the electric field. However, the value of the phase matching shown in eq. (2.10) differs for each idler, commonly leading to an optimisation of the phase matching for only one of them, reducing the complex six wave model to a four-wave one.

One of the potential benefits of FWM applied to optical communication systems is the possibility of implementing amplifiers based on it. In this sense, if two of the four photons of the nonlinear interaction come from continuous wave (CW) signals, then the generated signal will be either a copy or a conjugated copy of the original one. This situation leads to a simplification in the coupled equations (2.9). Then, for the case of phase conjugation (see Fig. 2.1) and single polarised waves, a simplified model for the wave interaction is obtained [56]

$$\begin{aligned} \frac{\partial}{\partial z} A_s + \frac{i\beta_2}{2} \frac{\partial^2}{\partial t^2} A_s &= i\gamma A_{p1} A_{p2} A_i^* \\ \frac{\partial}{\partial z} A_i + \frac{i\beta_2}{2} \frac{\partial^2}{\partial t^2} A_i &= i\gamma A_{p1} A_{p2} A_s^* \\ \Delta k_{NL} &= \Delta k - 2\gamma P_0 \end{aligned} \quad (2.11)$$

where A_s, A_i represent the slowly varying envelopes of the signal and idler respectively and A_{p1}, A_{p2} represent the amplitudes of the pump waves. These equations assume that the slowly varying envelope of both waves propagates at the same speed. If the frequency spacing between the waves is very large, this assumption cannot be done and an additional term must be included to account for the walk-off effect that this difference in speed induces.

The third equation represents the *nonlinear phase matching*, where P_0 is the power of each pump wave and γ the nonlinear coefficient of the fibre. This modification is required to account for the phase shift induced by self-phase modulation on the CW pumps during the propagation along the fibre. This phase shift modifies the phase of the pump waves and therefore impacts on the efficiency of the FWM process.

More complete analyses of FWM processes including the case of dual-polarised waves have already been published [60, 61]. These studies show that the flexibility in the wavelength and polarisation allocation of equation (2.9) makes the implementation of functionalities not achievable through linear optics possible. The two most important applications in optical communications of FWM are the implementation of wavelength converters (WCs) and of phase sensitive amplifiers (PSAs).

WCs are devices that provide a shifting of the carrier frequency of the signal while the information (carried by the slowly varying envelope) remains unchanged. In fibres, these devices can be implemented by single- or dual-pump FWM processes in highly nonlinear fibres (HNLFs). One of the main differences between the two implementations is the polarisation sensitivity that single-pump WC exhibits. As follows from eq. (2.9), FWM is a polarisation sensitive nonlinear process. In this sense, only the component of the signal parallel to the polarisation of the pump waves is amplified, leading to a uneven performance in the case of single-pump WCs. In order to avoid this undesirable effect, it is necessary to provide a mechanism for the simultaneous amplification of both components. This is only achievable in dual-pump schemes [62, 63]. Implementations of polarisation-insensitive fibre-based all-optical wavelength converters will be dealt with in depth in Chapter 6.

As has been shown, fibre-based FWM offer the possibility of implementing phase insensitive amplification (PIA), an example of which is the wavelength conversion. However, FWM can also provide phase sensitive amplification (PSA), in which a coherent interference between a signal and its phase conjugate can give rise to noise squeezing on one of the quadrature amplitudes of the signal at the expense of amplification on the

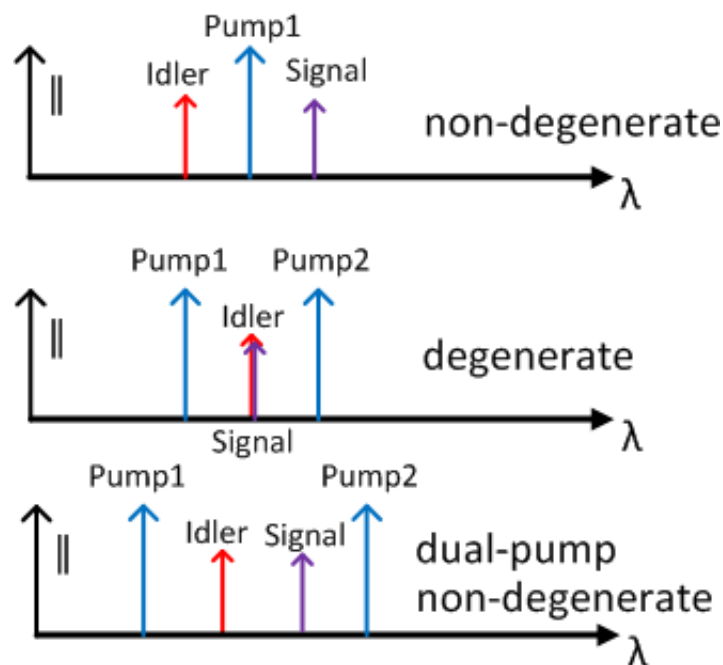


Figure 2.2: Wavelength allocation of phase sensitive amplification schemes

other [64, 65]. Unlike PIAs, where all the phases were amplified equal, PSA requires well-defined relations between the phases of the interacting waves. The experimentally demonstrated nonlinear interactions that can generate phase sensitive amplification in fibres are shown in Fig. 2.2 [66, 67].

By considering the pump waves as CW signals perfectly phase matched and co-polarised with the signal, the equation system (2.11) can be reduced to [68]

$$\begin{bmatrix} A_{1,out} \\ A_{2,out}^* \end{bmatrix} = \begin{bmatrix} \cosh(\gamma PL_{eff}) & i \sinh(\gamma PL_{eff}) \\ -i \sinh(\gamma PL_{eff}) & \cosh(\gamma PL_{eff}) \end{bmatrix} \begin{bmatrix} A_{1,in} \\ A_{2,in}^* \end{bmatrix} \quad (2.12)$$

where γ is the nonlinear coefficient of the fibre, P is the pump power and $L_{eff} = (1 - \exp(-\alpha L))/\alpha$ is the effective length of the fibre. By solving this system, and assuming that the power of signal and idler waves is identical, then the following expression for the signal gain is obtained

$$G_s = 1 + 2 \sinh^2(\gamma PL_{eff}) + 2 \sinh(\gamma PL_{eff}) \cosh(\gamma PL_{eff}) \sin(\theta) \quad (2.13)$$

The quantity θ is the relative phase among the waves involved in the phase sensitive process. In general $\theta = \phi_{p1} + \phi_{p2} - \phi_1 - \phi_2$. In case of PIA the value of θ is always zero because the relation $\phi_2 = \phi_{p1} + \phi_{p2} - \phi_1$ is enforced by the nonlinear process, resulting in a cancellation of the last term on the right hand side of the equation (2.13).

However, if the phase ϕ_2 is shifted by a constant value at the input of the optical fibre with respect to ϕ_1 , the term θ does not vanish anymore, leading to an additional gain of 6 dB for the case of $\theta = \pi/2$. Thus, phase sensitive amplification is heavily dependent on the relative phase of the waves involved in the nonlinear propagation.

PSAs exhibit features that can be used to implement functionalities not achievable through standard FWM processes. The additional gain obtained through the phase-sensitive interaction is exhibited only in one of the quadrature components at the expense of de-amplifying the other. In this sense, these de-amplification capabilities have been applied to phase regenerators [41, 69] and ultra low-noise amplification [70] in communication systems.

2.4 Conclusions

This chapter has described the physical properties of optical fibres with regard to their optical characteristics, showing that they are an amorphous weakly nonlinear transmission medium. These features, it has been shown, can be used to implement

both phase-insensitive and phase-sensitive amplifiers yielding new functionalities not attainable through linear processes.

Both PIAs and PSAs take advantage of the nonlinear optical properties of materials to generate new frequencies, providing wavelength conversion capabilities, or to transform the statistical features of the noise, providing optical regeneration. Additionally, both aim at reducing the limitations imposed on the optical communication systems by the physical nature of the materials employed.

However, an efficient development of these nonlinear devices requires an understanding of the transformation undergone not only by the signal but also by noise for them to be effective. The description of the noise transformation induced on a signal during its propagation along an optical fibre communication system is the subject of the following chapter.

Noise in optical communication systems

Know your enemy and know yourself and you can fight thousand battles without disaster

Sun Tzu

In the previous chapter, the signals have been considered as deterministic, thereby their value being accurately known at any time and location. However, real signals unavoidably suffer from random fluctuations and the previously presented theory of linear and nonlinear optics only applies to the mean values of these fluctuating signals.

Fluctuations arise from spontaneous changes in the state of a system at dynamic equilibrium with the environment. These fluctuations are characterized by the Stefan-Boltzmann law and exhibit a dependence with the fourth power of the temperature [71]. The equilibrium point of the system is modified by any interaction between system and environment. This alteration induces a change in both the dynamic equilibrium of the system and its fluctuating features.

The fluctuations around the equilibrium point of a system have been statistically characterised in terms of probability density functions and variances using statistical mechanics [72, 73]. This theory showed that the statistical properties of a material in thermodynamic equilibrium are dependent on the working point and are modified in the presence of an energy flux [74, 75]. This is the case of a dielectric medium subjected to an electric field.

A more specific case of this theory can be applied to linear and dissipative systems. A system can be defined as dissipative if it absorbs energy while it is exposed to a periodic perturbation in the time and can be defined as linear if the power dissipation is quadratic with the amplitude of the perturbation [76, 77]. An optical fibre can be considered as a linear and dissipative medium if a low intensity electric field propagates through it.

The equilibrium point of linear and dissipative materials is altered by the absorbed energy. This reversible and temporary alteration modifies the response of the material to an externally applied field which in turn modifies the effects that the material induces on

the applied field. Under these conditions, the induced deviations from the steady-state values depend linearly with the value of the external field so that if this vanishes the deviations decay and vanish as well [72, 73].

The characterization of the response of the material in time leads to the concept of impulse response. The impulse response is defined as the cross-correlation function between the fluctuations of the material and those of the external field. In case of linear systems, it can be calculated deterministically for small fluctuations [78].

In order to characterise the spectral response of the system, the Fourier transform of the impulse response is usually calculated. This Fourier transform is the linear susceptibility of the material shown in equation (2.1) [72, 78, 79]. Therefore, the linear susceptibility is the magnitude that characterises the behaviour of linear systems both in terms of mean values and fluctuations.

Unlike linear systems, the perturbations induced by nonlinear materials in response to intense external fields have, to the best of my knowledge, not been characterised even though the nonlinear susceptibilities have been defined. Nowadays, an analysis of the nonlinear perturbations can only be performed by the application of perturbation methods, that provide a linearisation of the nonlinear equations that govern the physical behaviour [80]. A detailed characterization of these nonlinear perturbations is out of the scope of this work but a phenomenological insight of the transformations that noise undergoes during propagation and nonlinear effects is necessary in order to understand how signals degrade during their transmission along optical communication systems.

The rest of this chapter is devoted to the description of the features of noise generated by the different noise sources in optical communication systems, the amplifiers, and of the transformation that this noise endures due to the physical properties of optical fibres during propagation.

3.1 Amplification

One of the key components of long haul communication systems are the amplifiers. They compensate for the attenuation that signals unavoidably undergo during their propagation through optical fibres. However, the additional power that these devices transfer to the signals comes at the expense of a degradation in the signal quality in the form of an additional noise.

Physical principles show that an ideal, noise-free amplifier actually violates Heisenberg's uncertainty principle [81], thereby any amplification process is noisy. The correlation features between the noise and the amplified signal depend on the underlying physical process that generates the former [82]. The most commonly used types of amplifiers

in optical communication systems generate noise that is not correlated with the signal, however the noise generated by parametric amplifiers, which rely on fibre nonlinearity for the amplification process, can be correlated with the amplified signal either in amplitude or in phase.

In this section, the physical noise sources of the different types of amplifiers available in optical fibre systems are discussed, paying special attention to the case of parametric amplifiers, that plays an important role in this work. In particular, the noise features of Erbium-doped fibre amplifiers (EDFAs), Raman amplifiers and parametric amplifiers are discussed.

3.1.1 EDFA

EDFAs are the most widely used type of amplifier in optical communication systems. They can simultaneously provide high gains and low noise figures in a lumped device comprising an Erbium-doped optical fibre of length ranging 8–12 metres [83].

The amplification capabilities of EDFAs around the central wavelength of 1550 nm are provided by the radiative transitions $4f \rightarrow 4f$ of the Erbium ions [84, 85]. Amplification is obtained by exciting the ions of Erbium to a higher energy level and inducing a stimulated emission from that level. An energy level diagram for the case of a C-band EDFA is shown in Fig. 3.1.

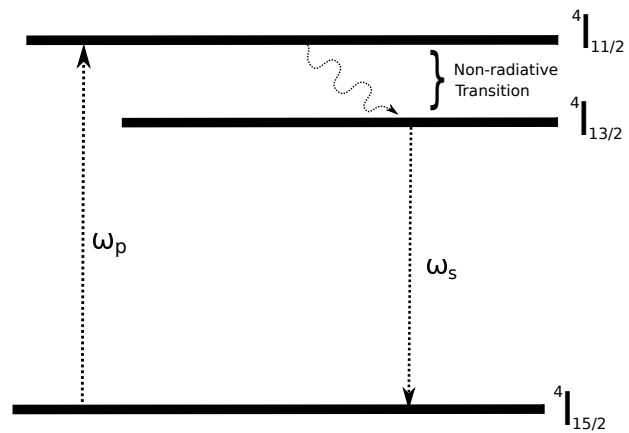


Figure 3.1: Energy level transitions of an EDFA

The transition to energy level $4I_{11/2}$ from the ground state is normally induced by using a pump wave at 980 nm although pumping at 1480 nm is also possible. From that state the ion decays non-radiatively to the metastable state $4I_{13/2}$, from which it will radiatively decay to the ground state either spontaneously or through stimulation from a photon with suitable energy. Stimulated transitions provide the amplification capabilities of the amplifier while spontaneous transitions are associated with the noise figure of the amplifier. Both gain and noise figure are related to a ratio that depends on the number of ions at the ground state N_1 and the number of ions at the metastable state N_2 . This ratio is called spontaneous emission factor n_{sp} , its definition being [86]

$$n_{sp}^{EDFA} = \frac{N_2}{N_2 - N_1} \quad (3.1)$$

Accurate calculations of N_1 and N_2 are complex because the transition ${}^4I_{13/2} \rightarrow {}^4I_{15/2}$ comprises a compound of 56 different sub-transitions, the probabilities of which must be averaged, leading to the concepts of emission and absorption cross-sections [86]. These cross-sections depend on the host glass, the dopant species and their relative concentrations. These magnitudes, closely related to the physical properties of the materials, ultimately define the value of the populations and, in turn, of the spontaneous emission factor and therefore the performance of the amplifier in terms of gain and noise figure.

The noise power of the EDFA is determined by its spontaneous emission factor, in such a manner that the power per-polarisation at the output of the amplifier coming from amplified spontaneous emission (ASE) is [83, 86]

$$P_{ASE}^{EDFA} = h\nu \cdot n_{sp}^{EDFA} \cdot B (G - 1) \quad (3.2)$$

where h is the Plank's constant, ν the centre frequency, B the optical bandwidth and G the gain of the amplifier.

The lifetime of the metastable state is very important in the characterization of the ASE noise. The lifetime of state ${}^4I_{13/2}$ is in the order of milliseconds. This is in contrast to the pulse width of optical communication signals which is several orders of magnitude shorter, typically in the range 25–100 ps. Under these conditions, the population of the metastable state can be considered as constant for the whole pulse duration of the modulated signals. The averaging of these slow fluctuations of the population leads to noise which is uncorrelated with the signal. This phase-independent noise, called *additive noise*, is mathematically modelled as a zero-mean Gaussian random variable whose variance is the noise power shown in equation (3.2).

3.1.2 Raman Amplification

The performance of EDFA-amplified optical systems deteriorates when long fibre spans are used. The lumped nature of the EDFA and the linear dependence of the output noise with the signal gain, as expressed in equation (3.2), limit the performance that these amplifiers can offer under such circumstances. The gains required in order to compensate for the losses of such spans generate a large amount of ASE noise during the amplification process that drastically constrains the reach of these systems.

It is under those conditions that Raman amplification excels. This type of amplifiers offers reduced noise figures and broadband amplification in long transmission spans. The distributed character of Raman amplifiers, providing amplification capabilities over several kilometres of fibre, prevents from such a large degradation suffered from lumped amplification processes, but the inherent practical difficulties associated with

their deployment in commercial networks made their adoption not as popular as that of EDFAs [50].

Conversely to EDFAs, amplification capabilities in these amplifiers are facilitated by stimulated Raman scattering (SRS). This nonlinear process turns optical fibres into broadband amplifiers. In any molecular medium, spontaneous Raman scattering can transfer a small fraction (typically $< 10^{-6}$) of power from one optical field to another one whose frequency is downshifted by an amount determined by the vibrational modes of the medium. In the case of silica optical fibres, the power transfer is most efficient when the difference in frequency between the two waves is approximately 13 THz [50].

SRS causes part of the power of an intense pump wave that is transmitted together with a signal to be transferred to the signal, amplifying it. The pump wave can propagate either in the same direction as the signal (co-propagating scheme) or in the opposite direction (counter-propagating scheme).

As in all processes, energy and momentum conservation conditions need to be satisfied during the Raman interaction. In fibres, the presence of optical phonons, the vibrational modes of the material, during the nonlinear interaction ensures phase matching independently of the dispersion characteristics of the fibre and the pumping scheme used (co- or counter-propagating) [87]. This results in an amplification process very different from that of the EDFA, the energy level diagram of which is shown in Fig. 3.2.

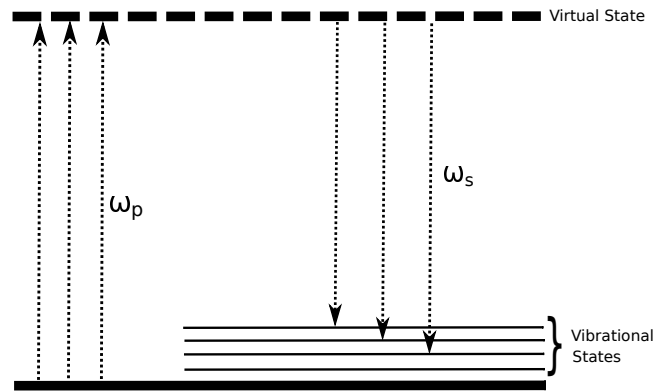


Figure 3.2: Energy transitions of a Raman process

As with EDFAs, stimulated emission is the main contribution to the gain of the amplifier, whereas spontaneous emission adds to the amplified signal and appears as noise because of the random phases associated with all the spontaneously generated photons. This allows a characterisation of the noise figure of these amplifiers in terms of a spontaneous emission factor given by [50]

$$n_{sp}^{Raman}(\nu) = \frac{1}{1 - \exp(-h\nu/k_B T)} \quad (3.3)$$

where k_B is the Boltzmann constant and T is the Kelvin temperature. n_{sp} allows the calculation of the total ASE noise power at the output of the amplifier. Since Raman amplification is a distributed process, the ASE noise power at the output of a Raman amplifier of length L takes the form [50]

$$P_{ASE}^{Raman} = 2h\nu \cdot n_{sp}^{Raman} \cdot B \cdot g_R \cdot G_L \int_0^L \frac{P_p(z)}{G(z)} dz \quad (3.4)$$

where g_R is the Raman gain coefficient, G_L is the effective gain accounting for the fibre length and its loss, that takes the value $G_L = \exp(g_R P_0 L_{eff} - \alpha L)$, P_p is the pump power, that takes the value $P_p(z) = P_0 \exp(-\alpha L)$ in a co-propagating scheme and $P_p(z) = P_0 \exp(-\alpha(L-z))$ in a counter-propagating one, P_0 is the transmitted pump power, α the attenuation coefficient of the fibre and L_{eff} the effective length of the amplifier.

Therefore, the ASE noise at the output depends both on the physical properties of the optical fibre (represented by g_R , α and n_{sp}) and the characteristics of the pump wave. This is a major difference with EDFAs, where the dependence between the pump power and the ASE power is of secondary importance.

The feature that determined the decorrelation of the ASE noise with respect to the population fluctuations of the EDFA both in amplitude and phase was the long lifetime of the metastable state. In contrast, the lifetime of the virtual states of the Raman interaction is in the order of hundreds of femtoseconds [48], ie. much faster than the pulse width of the modulated signals. Such lifetimes prevent pump waves from being considered constant as in the case of EDFAs, their fluctuations being unavoidably transferred to the amplified signals. This feature entails a transfer of the RIN of the pump wave to the amplified signal. In a co-propagating dispersionless configuration, the RIN transfer has been quantified as [88]

$$RIN_{out} = RIN_{in} + \langle (\Delta G)^2 \rangle = RIN_{in} + RIN_p \ln^2(G_A) \quad (3.5)$$

where $G_A = g_R P_p L_{eff}$ represents the Raman gain and RIN_{in} , RIN_{out} and RIN_p represent the RIN of the signal before and after the Raman and the RIN of the pump wave respectively. However, in the presence of dispersion or in counter-propagating schemes, the distributed character of Raman amplification induces a smoothing effect on the RIN transfer, resulting in a low-pass filtering of the transferred noise [88]

$$RIN_{out} = RIN_{in} + \langle (\Delta G)^2 \rangle = RIN_{in} + RIN_p \frac{\ln^2(G_A)}{L_{eff}} \frac{\alpha_p}{1 + \left(\frac{f}{f_c}\right)^2} \quad (3.6)$$

where α_p is the attenuation coefficient of the pump wave and f_c is the cut-off frequency of the noise transfer between pump and signal. The value of this frequency depends on the configuration, taking the value $f_c = \alpha_p / (2\pi D \Delta\lambda)$ for the dispersive co-propagating scheme and $f_c = \alpha_p V_g / 4\pi$ for the counter-propagating scheme; where D is the dispersion coefficient of the fibre, $\Delta\lambda$ the frequency spacing between waves and V_g the group

velocity. It is to be noted that the smoothing effect is more important in the counter-propagating case, being independent of the dispersive characteristics of the fibre.

As a result of this smoothing effect, any fluctuation of the pumps wave have negligible influence on the noise features of the amplifier. The smoothing causes a decorrelation of the phase of the generated noise photons with respect to that of the pump waves in such a manner that the pump fluctuations are incoherently transferred to the signal resulting, as with EDFAs, in a phase-independent distortion. In this manner, the noise generated by Raman amplifiers can be modelled as additive noise, the power of which is shown in equation (3.4).

3.1.3 Parametric Amplification

Although fibre optic parametric amplifiers (FOPAs) have been studied for more than two decades, no commercial implementation has been developed yet that meets the requirements of optical communication systems. Nevertheless, the functionalities that this type of amplifiers offer make them very interesting devices for future optical communication networks. For example, Chapters 6 and 8 of this work present implementations of FOPA prototypes with suitable performance for certain applications in optical communication systems, showing the potential of FOPA-based implementations in real networks.

The amplification capabilities that FOPAs exhibit are provided by the third-order nonlinearity of optical fibres that transfer energy from high power continuous wave (CW) signals to weaker modulated signals amplifying the latter ones in the process. The main physical difference between FOPAs, EDFAs and Raman amplifiers is that the amplification process of FOPAs do not involve any phonon interaction, resulting in more strict requirements for the enforcement of energy and moment conservation. In this sense, the amplification process is carried out through virtual levels of energy, as shown in Fig. 3.3, where only photons provide the amplification capability.

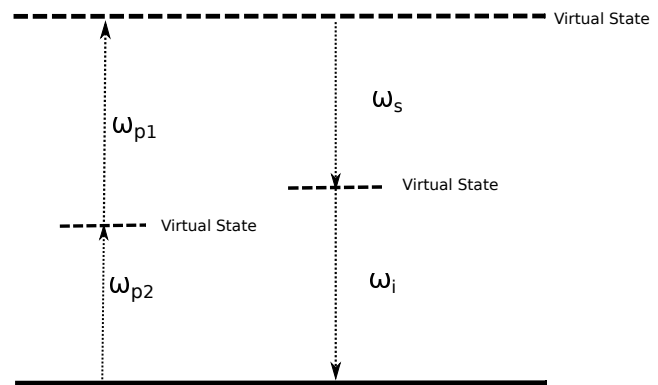


Figure 3.3: Energy transitions of a third-order parametric process

This feature imposes several limitations to FOPAs, since it entails constraints in terms of phase matching, wave polarisation and wavelength allocation, that are largely responsible for the distinctive characteristics of this kind of amplifiers in terms of noise.

Phase matching restrictions make the implementation of FOPAs more challenging than that of Raman amplifiers by requiring an almost constant phase relation between the waves involved in the parametric interaction. This feature prevents from counter-propagating schemes and dispersive fibres to be used, severely impacting on the properties of the amplifier in terms of noise figure. These forbidden smoothing mechanisms, that allow the decorrelation of pump wave fluctuations with respect to the amplified signals, together with the very fast ($\approx 1fs$ [89]) nonlinear electronic lifetime of the parametric interaction result in a coherent transfer of pump wave fluctuations to amplified signals.

Pump wave fluctuations are the main noise source in parametric amplifiers, however they are not the only one. The quantum limit of parametric amplification is achieved when no pump fluctuations are present [63], this would correspond to the case of ASE noise in EDFAs or Raman amplifiers. Under these conditions, only the amplified quantum noise (AQN) is present at the output of the FOPA. This represents the case of minimum distortion of the amplified signal, that is usually negligible with respect to the distortions induced by pump fluctuations.

Thus, accounting for both pump wave fluctuations and AQN, the amplified signal at the output of the FOPA A_{out} can be expressed as follows [90, 91]

$$A_{out} = e^{i\theta_n} A_{in} \times \sqrt{(G + \Delta G)} + n_{add} \quad (3.7)$$

where A_{in} represents the input signal, G the gain, ΔG the gain perturbations induced by the pump fluctuations, θ_n the phase perturbations induced by the pump fluctuations and n_{add} the additive noise generated during the amplification process. This equation accounts for both coherent (θ_n) and non-coherent (ΔG and n_{add}) noise superimposed to the signal.

However, the relationships between the physical processes that generate these fluctuations and the very fluctuations at the output of the FOPA are highly nonlinear, thereby not being possible to provide generic analytical equations for them, except for very specific configurations. Thus, only a qualitative insight about their respective effects on modulated signals is possible.

In the following sections, the physical processes induced by the pump fluctuations in fibre optic parametric amplifiers are described. In this sense, and for the sake of clarity, these processes have been classified according to the type of induced fluctuation: amplitude and phase fluctuations. Additionally a short subsection referring to AQN has been included for completeness.

3.1.3.1 Amplitude Noise Sources

The amplitude fluctuations of the waves involved in parametric interactions influence at the output of a FOPA in three different ways. First, the amplitude fluctuations of the signal already present at the input of the FOPA are amplified in a similar manner as in EDFAs and Raman amplifiers. Second, the gain of the FOPA, being heavily dependent on the pump power, fluctuates proportionally to these fluctuations. And third, the energy transfer from pump waves to signals already involves the transfer of part of the ASE noise that has been added to the pump waves prior to the parametric amplification process. In this manner, pump wave and signal wave fluctuations impact on the noise at the output of the FOPA in very different ways.

Signal wave fluctuations can be assumed to be chiefly AQN and ASE generated in previous amplification stages [90, 91]. Thus they are considered to be incoherent with the signal. They are unavoidably amplified by FOPA gain and can be characterized by a power spectral density (PSD).

On their part, pump amplitude fluctuations are mainly generated by residual ASE noise coming from pump wave amplification and by relative intensity noise (RIN) coming from the laser sources [90, 91]. These fluctuations, being independent on the phase of the amplified signal, do not induce any additional phase distortion in the amplified signal. However, they induce gain variations that are correlated with pump wave fluctuations, resulting in a transfer of the pump fluctuations to the amplified signal via gain modulation. Their characterization is far more complex than that of signal waves because they undergo nonlinear transformations. In this work only qualitative characterisation of these fluctuations is provided.

Amplified Quantum Noise

According to quantum theory, the vacuum is filled with low-energy electromagnetic waves of random amplitudes and phases, that propagate in all possible directions. Quantum vacuum is the lowest state of the empty space and its energy is called zero-point energy. Fluctuations of this energy are described by Heisenberg's uncertainty principle and create the so-called quantum noise. The power spectral density of this noise is flat up to the Planck frequency ($\nu_p \sim 10^{43}$ Hz) [92], therefore it can be considered flat at any frequency as far as communication systems are concerned. Thus, at the input of the amplifier the PSD of quantum noise can be written as

$$S = \frac{h\nu}{2} \quad (3.8)$$

This noise acts as an input signal at any frequency within the bandwidth of the amplifier and is unavoidably amplified, generating noise with power P_{AQN}^{FOPA} at the output of the FOFA [90, 91]

$$P_{AQN}^{FOPA} = \frac{h\nu}{2} (2G - 1) B \quad (3.9)$$

where h is the Planck constant, ν is the frequency of the signal, G is the gain of the FOFA and B is the bandwidth of the filter after the amplifier.

ASE Pump Noise

Pump waves used in FOPAs generally require prior amplification. This amplification increases the amplitude fluctuations of the pump waves in such a manner that the OSNR of the pump wave is directly related to the OSNR of the amplified signal [93]. Thus the pump OSNR is an important factor in the computation of the noise figure of FOPAs.

The ASE noise added during pump amplification is [94]

$$P_{ASE}^{FOPA} = h\nu (G_A - 1) n_{sp} B \quad (3.10)$$

where h is the Planck constant, ν is the frequency of the signal, G_A is the gain of the amplifier, n_{sp} is the spontaneous emission factor and B is the bandwidth of the filter after the amplifier.

Part of this noise power is transferred to the signal via the parametric interaction whereas the remaining power generates fluctuations in the power of the pump waves that induce random gain variations. The nonlinear equations that describe these two simultaneous processes (see eq. (2.11)) can be linearised with respect to the pump fluctuations, leading to the following gain equation for the case of a FOFA with two identical pump sources (that can easily be reduced to the case of a single pump FOFA) degraded by ASE noise and RIN [91]

$$P_{out}^{FOPA} = 2 \{ h\nu (G_A - 1) n_{sp} + RIN \times P_{0,av} \} B \left(\frac{\partial G}{\partial P_{0,av}} \right)^2 \quad (3.11)$$

The sum inside the braces on the right hand side of equation (3.11) represent the parametrically transferred noise. The first addend of this sum accounts for the transferred ASE noise of the pump waves whereas the second addend represents their RIN. Additionally, the term $\frac{\partial G}{\partial P}$ represents the gain variation due to pump power fluctuations. The exact value of this factor depends on the fibre or the FOFA characteristics. Expressions

of $\frac{\partial G}{\partial P}$ for the case of single-pump FOPAs can be found in Ref. [90] and for the case of dual-pump FOPAs in Ref. [91].

When signal and pumps travel at the same group velocity, as is the case in a FOPA, they remain synchronous throughout the whole fibre and no averaging of fluctuations takes place. On the contrary, when the group velocity mismatch is not negligible, the net gain at the end of the fibre will correspond to the averaged power of the two pumps. Noise transfer is considerably reduced under such conditions [59].

Relative Intensity Noise

RIN describes the inherent amplitude fluctuations of any laser source. As was discussed in the previous section, the effect of these fluctuations in FOPAs is the same as that of ASE pump noise, the main difference between them being that the fluctuations induced by this noise source are usually orders of magnitude smaller than those induced by ASE pump noise [95]. RIN is usually neglected in case of amplified pump waves but should be considered in the case of unamplified pump waves.

Raman Amplitude Noise

High pump powers can induce stimulated Raman scattering (SRS). In a standard optical fibre, Raman contributions amount for just 18% of the total nonlinear interaction, whereas nonlinear refraction is responsible for 82% [48].

The Raman gain spectrum in the presence of parametric processes has been studied in standard single mode fibres (SSMFs) [96–98], resulting in the development of a model for the Raman-induced noise figure of parametric amplifiers [89]. The Raman noise spectrum generated by FOPAs shows to be similar to that of classical Raman amplifiers.

However, the Raman gain decreases with phase matching in the presence of parametric processes [99] and theoretically equals zero in the case of perfect phase matching [100]. This feature makes the Raman amplitude noise of lesser importance in parametric amplifiers because phase matching is required to build efficient parametric amplifiers.

3.1.3.2 Phase Noise Sources

Apart from amplitude fluctuations, pump waves exhibit phase fluctuations that are transferred to the amplified signals via the nonlinear interaction or are generated during their propagation through the fibre via the Kerr effect. These fluctuations distort the information encoded in phase modulated signals, degrading their quality.

Parametric interactions, lacking a decorrelation mechanism, transfer phase fluctuations of the pump(s) to the amplified signal. The transferred phase fluctuations may originate from pump laser linewidth and/or pump dithering.

In addition, the effects of SPM on noisy signals and XPM originating from co-propagating modulated signals result in the transformation of amplitude fluctuations to phase fluctuations. The phase noise generated in this manner is called nonlinear phase noise [101] and degrades the quality of the modulated signals.

Pump Linewidth Transfer

Laser sources are only partially coherent, exhibiting random phase fluctuations that vary as a one-dimensional random walk [102, 103]. These fluctuations are defined as $\theta = \varphi(t+T) - \varphi(t)$, where φ is the instantaneous phase of the laser, and can be uniquely characterised by their linewidth [104].

The laser linewidth links the spectral width induced by the phase fluctuation with the variance of the fluctuation itself, leading to the relation [105]

$$\langle \theta_{linewidth}^2 \rangle = \pi \Delta\nu T \quad (3.12)$$

where $\Delta\nu$ is the linewidth, T is the sampling period and $\langle \theta_{linewidth}^2 \rangle$ represents the variance of the phase fluctuation.

As was already mentioned, during a parametric interaction the linewidth of the pumps is transferred to the amplified signal [106, 107]. However, equation (3.12) shows that the linewidth is related to the phase variance of the waves. This confers some distinctive features to the linewidth transfer.

As was mentioned in the previous chapter, phase matching enforces a relation between the phases (see equation (2.10))

$$\theta_i = \theta_{p1} + \theta_{p2} - \theta_s \quad (3.13)$$

where the subscripts $p1$, $p2$, s and i represent the first pump, second pump, signal and idler respectively. By applying a quadratic relation, such as the one shown in (3.12) to equation (3.13), a more general relation between the linewidths of the waves involved in a FWM process is obtained [107]

$$\langle \theta_i^2 \rangle = \langle \theta_{p1}^2 \rangle + \langle \theta_{p2}^2 \rangle + \langle \theta_s^2 \rangle - 2 \cdot Cov(\theta_s, \theta_{p1}) - 2 \cdot Cov(\theta_s, \theta_{p2}) + 2 \cdot Cov(\theta_{p1}, \theta_{p2}) \quad (3.14)$$

where Cov represents the covariance between the phase noise of the waves. The most common case assumes uncorrelated signal and pump waves, reducing the previous equation to

$$\langle \theta_i^2 \rangle = \langle \theta_{p1}^2 \rangle + \langle \theta_{p2}^2 \rangle + \langle \theta_s^2 \rangle + 2 \cdot Cov(\theta_{p1}, \theta_{p2}) \quad (3.15)$$

The correlation between the different pump waves depends on the very scheme used for the parametric interaction. In the case of degenerate FWM $Cov(\theta_{p1}, \theta_{p2}) = \langle \theta_{p1}^2 \rangle = \langle \theta_{p2}^2 \rangle$. However, in the case of non-degenerate FWM, the value of the covariance can be controlled by using injection locking [108] or pump correlation techniques [107]. In this work, dual-uncorrelated-pump schemes are assumed leading to $Cov(\theta_{p1}, \theta_{p2}) = 0$. Thus, the variance of the phase fluctuation of a parametrically amplified signal is then

$$\begin{aligned} \langle \theta_{single}^2 \rangle &= \pi (\Delta\nu_s + 4\Delta\nu_p) T \\ \langle \theta_{dual}^2 \rangle &= \pi (\Delta\nu_s + \Delta\nu_{p1} + \Delta\nu_{p2}) T \end{aligned} \quad (3.16)$$

where $\Delta\nu_s$ is the linewidth of the signal, $\Delta\nu_{p1}$, $\Delta\nu_{p2}$, $\Delta\nu_p$ and are the linewidths of the pump waves and, as before, T is the sampling period. $\langle \theta_{single}^2 \rangle$ and $\langle \theta_{dual}^2 \rangle$ respectively represent the variance of the idler for the case of single- and dual-pump FOPAs. This relation has been experimentally demonstrated for the case of single-pump FOPAs [109].

Equation (3.16) shows that the linewidth at the output of a degenerate FOPA grows as four times the linewidth of the pump waves whereas for the case of a non-degenerate FOPA with uncorrelated pumps, it grows as twice the linewidth of the pump waves.

Pump Dithering Transfer

Pump dithering refers to a low-frequency phase modulation of pump waves. This is a common technique used to overcome the Brillouin threshold in FOPA by broadening the spectral line of pump waves which in turn provides an increase in the pump power inside the fibre. Unlike the linewidth of the source, pump dithering is a deterministic perturbation whose phase variation between two consecutive times is

$$\Delta\theta_{dither} = \theta(t + T) - \theta(t) = 2\pi fT \quad (3.17)$$

where f is the dithering frequency and T is the sampling period. As with pump linewidth transfer (PLT), phase matching requirements are still enforced by the parametric interaction, which turns the phase matching expression of equation (2.10) into

$$\Delta\theta_i = \Delta\theta_{p1} + \Delta\theta_{p2} - \Delta\theta_s \quad (3.18)$$

Assuming that the input signal is not dithered, then the dithering of the amplified signal is

$$\Delta\theta_i = \Delta\theta_{p1} + \Delta\theta_{p2} = 2\pi(f_{p1} + f_{p2})T \quad (3.19)$$

In this manner and since the dithering is deterministic, the idler dithering grows as twice the dithering of the pump waves.

Nonlinear Phase Noise

The Kerr effect transforms amplitude fluctuations into phase fluctuations. This effect is usually called nonlinear phase noise (NPN) or the Gordon-Mollenauer effect [101, 110–119] after the scientists who first analysed it. NPN describes the phase noise induced by a propagating signal on itself due to the interaction between the Kerr nonlinearity of the optical fibre and the ASE noise that degrades the signal. Under these conditions, the approximate variance of generated phase noise can be expressed as [101]

$$\langle \theta_{NPN}^2 \rangle \cong \frac{2}{3} \frac{\gamma^2 P^2 L^2}{OSNR} \quad (3.20)$$

In parametric amplifiers, the NPN induced by the pumps on themselves is in turn transferred to the amplified signals via the nonlinear interaction. Since usually the power of the pump waves is several orders of magnitude higher than that of the amplified signals, these perturbations are much more important than the NPN generated by the amplified signals themselves.

In this manner, the only variable that allows a reduction in the influence of NPN in a FOPA is the reduction of the fluctuation of the pump waves, and consequently the increase in their OSNR. The significance of the OSNR of the pumps has been analysed in several papers [93, 120, 121] from different points of view. These studies show how the NPN of the pump waves impacts on the phase noise of the amplified signals, leading to the following approximate expression for the variance of the phase noise induced on a modulated signal by the pump-transferred NPN after a co-polarised dual-pump parametric interaction [120]

$$\langle \theta_{NPN-FOPA}^2 \rangle \cong 9 \frac{\gamma^2 L^2 P_p^2}{OSNR_p} \quad (3.21)$$

where γ is the nonlinear coefficient of the fibre, L the length of the fibre, P_p is the pump power ($P_1 = P_2 = P_p$) and the $OSNR_p$ is the OSNR of the pump wave. As was mentioned in the previous section, this OSNR mainly depends on the ASE noise generated during the pump wave amplification and on the RIN characteristics of the pump laser source.

3.2 Propagation

So far the noise generated during amplification has been discussed. Nevertheless, signal distortions are also introduced during propagation through the nonlinearity of the fibres. Wave propagation in optical fibres is a unitary process, ie. it neither generates nor dissipates energy, but induces a redistribution of the energy of the signals.

In the case of modulated signals, the energy redistribution induces mutual coupling between the in-phase and quadrature components of the signals. In particular, fibre dispersion induces a power exchange between the in-phase and the quadrature component whereas the Kerr effect induces a single-direction coupling from the in-phase component to the quadrature one [122].

These coupling effects distort the information encoded in the phase of modulated signals, thus making the discussion of the influence of fibre dispersion and nonlinearity on noisy signals interesting.

3.2.1 Effects of Dispersion on Noise

The two main effects of dispersion on modulated signals are pulse spreading and transformation from phase to amplitude noise. Pulse spreading reduces the peak power of optical pulses, thereby reducing the impact of fibre nonlinearity in highly dispersed pulse transmission systems. Since the development of electronic chromatic dispersion compensation techniques, dispersion unmanaged transmission systems have become the current *de facto* standard in optical communication.

On its part, the transformation from phase to amplitude noise, often called self-amplitude modulation [123] or phase modulation-to-amplitude modulation (PM-to-AM) conversion [118, 119, 124, 125], is generated by the dispersion of the various frequency components of a signal degraded by phase noise. These components arrive at the end of the fibre at slightly different times, causing amplitude modulation of the received signal. In addition to this effect, the group velocity dispersion (GVD) mixes the in-phase and quadrature components of the modulated signal. This, in turn, leads to a performance degradation in transmission systems.

During its propagation along the fibre, phase-modulated signals undergo a frequency-dependent phase shifting [116, 117]

$$\begin{aligned}\Delta\theta_I &= \frac{\beta_2}{2} (2\pi f_m)^2 \Delta z \\ \Delta\theta_Q &= -\frac{\beta_2}{2} (2\pi f_m)^2 \Delta z\end{aligned}\quad (3.22)$$

where β_2 is the group-velocity dispersion of the fibre and f_m is the frequency component of the signal. Equation (3.22) shows that this phase shift exhibits opposite signs for the in-phase and the quadrature components [117]. This effect induces a rotation of the circularly symmetric noise either clockwise or counter-clockwise depending on the sign of β_2 [116].

The effect of this rotation does not induce any measurable degradation on the quality of signals with circularly symmetric noise. However, combined with the effects of fibre nonlinearity, it can affect the performance of the signal.

Nevertheless, this penalty can be easily cancelled by means of chromatic dispersion compensation techniques, that ensure a synchronous reception of all the frequency components of the signal [126, 127].

3.2.2 Effects of Fibre Nonlinearity on Noise

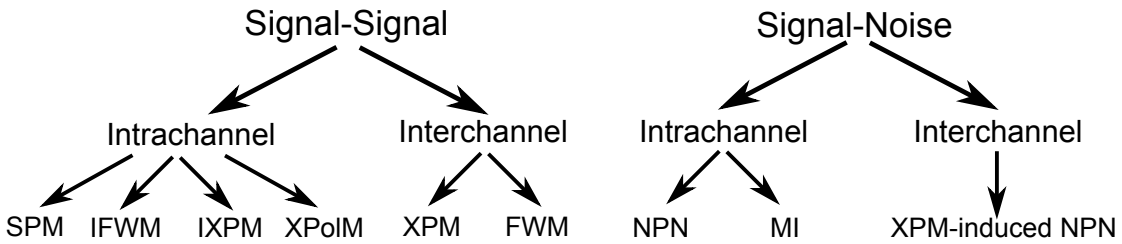


Figure 3.4: Perturbations induced by Kerr effect during propagation. Based on Ref. [128]

As was mentioned in the previous chapter, fibre nonlinearity can induce several interactions between propagating signals at different frequencies and/or polarisations. In the case of dispersive fibres, the list of perturbations induced by fibre nonlinearity must be enlarged because the nonlinear interactions between overlapping pulses at different time slots also induce signal distortions even after chromatic dispersion compensation has taken place. These distortions are collectively classified as intra-channel effects and are of critical importance at high bit-rate systems. In addition, interactions between signal and noise also degrade the signal quality and can also be classified as intra-channel or inter-channel perturbations.

The variety of nonlinear perturbations that signals propagating along an optical fibre can undergo requires a two-stage classification according to the nature of its interaction (signal-signal or signal-noise) and the frequency of the interacting signals (intra-channel or inter-channel). This classification, based on the one presented in Ref. [128], is shown in Fig. 3.4.

In single-wave systems, fibre nonlinearity generates self-phase modulation (SPM), modulation instability (MI) [48], nonlinear phase noise (NPN) [101], intra-channel four-wave mixing (IFWM) and intrachannel cross-phase modulation (IXPM) [129–139]. MI requires anomalous dispersion to appear and is only important in systems using dispersion compensation fibres, that are currently considered as legacy; therefore this perturbation is not discussed. The remaining perturbations are usually analysed in an integrated way [129, 130] and are collectively referred to as intra-channel effects. In the case of polarisation-multiplexed signals, an additional term due to cross-polarisation modulation (XPoIM) [140–142] must be included.

In multi-wave propagation systems fibre nonlinearity generates cross-phase modulation (XPM) [143–148], four-wave mixing (FWM) [149, 150] and XPM-induced NPN [151–153]. The rest of this section provides a brief explanation of each of these perturbations.

The noise variances induced by these various processes are largely dependent on the dispersive properties of the optical fibre and on the dispersion compensation mechanism. An example of this dependency arises in the analysis of the perturbation induced by FWM and XPM. For the case of dispersion managed systems, theoretical expressions for the noise variances induced by XPM and FWM have been derived, and show that the noise power induced by FWM has the characteristics of a zero-mean Gaussian additive noise, the power of which can be expressed as [154]

$$P_{FWM}^{managed} = \frac{12\gamma^2 P^3 L_{eff}}{\sqrt{\pi} B \cdot D \cdot \Delta\lambda} g\left(N, \frac{\Delta\lambda}{B}\right) \quad (3.23)$$

where g is a correlation function accounting for the possible modulation formats of the propagating waves the exact definition of which can be found in Ref. [154], P represents the average signal power, N the number of wavelengths co-propagating with the original signal, B the bandwidth of the signal, D the chromatic dispersion, $\Delta\lambda$ the spectral width of the signal and L_{eff} the effective length. The same publication also presented an expression for the variance of the XPM-induced phase noise, characterised as a zero-mean Gaussian phase noise

$$\langle \theta_{managed}^2 \rangle = 2 \cdot \ln(N/2) \frac{(\gamma P)^2}{B \cdot D \cdot \Delta\lambda} L_{eff} \quad (3.24)$$

where, as before, N represents the number of wavelengths co-propagating with the original signal, B the bandwidth of the signal, D the chromatic dispersion, $\Delta\lambda$ the spacing between signals and L_{eff} the effective length.

However, these expressions are completely different for the case of dispersion uncompensated systems. In this case the variance of XPM-induced phase noise generated by a co-propagating single channel results in [155–157]

$$\langle \theta_{unmanaged}^2 \rangle = (\langle |b_0|^4 \rangle - \langle |b_0|^2 \rangle^2) \frac{16\pi^2 c^2 \gamma^2 L}{|D\Delta\lambda|\lambda^4 T_S} \quad (3.25)$$

where T_S represents the pulse time, c the speed of light, λ the wavelength of the signal and b_0 are the amplitude coefficients of the modulation formats of the interfering signals. This expression can be generalized for a N-channel system assuming that the noise generated by each co-propagating channel is independent from each other [155].

Equations (3.24) and (3.25) show a clear dependence of the noise induced by the nonlinear effects on the dispersion properties of the fibre. SPM, being a self phase-matched nonlinear effect, could be considered as independent of dispersion but this is not the case. Conversely to the case of FOPAs, where the dispersion of the fibres is very small to improve the phase matching, the propagation over standard fibres is dispersive and affects the features of the amplitude-to-phase noise conversion. Several publications have analysed the impact of dispersion on the generation of NPN, showing that the phase noise variance depends on both the sign [114, 122] and the magnitude of the dispersion parameter [111, 112].

An example of the influence of the dispersion on the generation of NPN induced by SPM is shown in Fig. 3.5. This figure shows the evolution of the ASE of a 10 dBm signal for different effective lengths after a single-channel propagation along an standard optical fibre ($\gamma = 1 \text{ (W} \cdot \text{km)}^{-1}$). The initial circular ASE noise turns into a crescent shaped noise as the signal propagates along the fibre. However, this process varies for

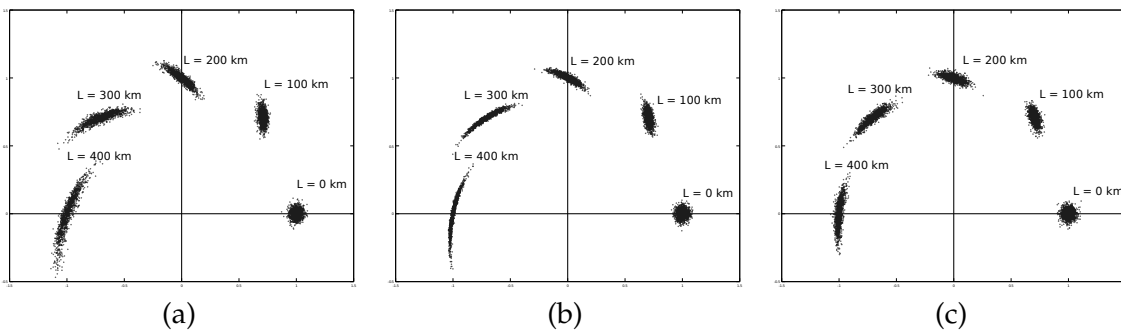


Figure 3.5: SPM efficiency for nonlinear coefficients depending on the dispersive properties of the optical fibre: (a) $D = -200 \text{ ps/nm} \cdot \text{km}$, (b) no dispersion and (c) $D = 200 \text{ ps/nm} \cdot \text{km}$

different values of the chromatic dispersion. NPN is generated more efficiently when the dispersion is low [112] (see Fig. 3.5b). Otherwise the process is not so efficient and a smaller amplitude-to-phase noise conversion is induced (see Fig. 3.5a and Fig. 3.5c). There exist two physical processes that explain this dependence: (1) the decrease in the peak power induced by the pulse spreading and (2) the different coupling between the in-phase and quadrature components depending on the sign of the dispersion. The latter effect induces an enhancement of the ASE noise in one of the quadrature components with respect to the other.

A theoretical expression for the phase variance induced by NPN in dispersion managed optical communication systems after F amplification stages was obtained in Ref. [112] as

$$\langle \theta_{NPN-disp}^2 \rangle \cong 2\gamma^2 n_{ASE} P_0 T_0 \frac{L_{eff}^2}{T_{eff}^2} [I_2 + K^2 I_4 + 2K I_3] \quad (3.26)$$

where γ is the nonlinear coefficient of the fibre, P_0 the average pulse power, T_0 the pulse width at $1/e$, $T_{eff} = \sqrt{\pi} T_0$, L_{eff} the effective length, $I_j = \sum_{n=1}^F n_{ASE}^j$, n_{ASE} the power spectral density of the ASE generated by each amplifier and K a parameter the expression of which can be found in Ref. [112]. It is to be noted that in the case of no dispersion, K vanishes and equation (3.26) reduces to (3.20).

Thus, the influence of NPN is deeply intertwined with the dispersive characteristics of the fibre. This feature, together with its nonlinear dependence, complicates the characterisation of this perturbation in the most general case. But the principal difficulty of this derivation is the non-stationary character of the NPN that, being correlated with the information signal, changes its statistical properties over time [111]. NPN is the only one of the discussed types of noise that exhibits a non-stationary behaviour, requiring a different mathematical treatment.

In addition to NPN, and for the case of polarisation multiplexed signals, the randomly varying birefringence that standard optical fibres exhibit induces an interference between the two polarisation components of the signals, that has been called cross-polarisation modulation (XPolM) [140]. This perturbation is highly dependent on the modulation format and can be successfully suppressed by using polarisation alternating modulation formats [141] or by means of precoders [142]. The modulation dependence exhibited by this nonlinear effect prevents from a unique statistical treatment. In this manner, the XPolM is not considered further in this work.

The last nonlinear propagation-induced perturbation is generated by the sequential transmission of pulses through an optical fibre, that generates impairments collectively referred to as intrachannel effects. During their propagation, the pulses are rapidly dispersed after being launched into the fibre, spreading in time over hundreds or even

thousands of symbols. Then, with proper dispersion compensation the original signal is recovered with minor impairments [130, 131].

The importance of these impairments increases with the total number of symbols that the original pulse has spread into. In this manner, uncompensated transmission links and high symbol-rate signals are more affected by intrachannel nonlinear effects. In particular two main perturbations are generated: intrachannel cross-phase modulation (IXPM), that results in a broadened pulse after the chromatic dispersion compensation [129, 137, 139], and intrachannel four-wave mixing (IFWM), that generates temporal side bands or ghost pulses [133, 134].

IXPM has been shown to induce a timing jitter that affects the synchronisation of communication systems [138] and, as such, it cannot be characterized as noise affecting the detection of the signal, therefore not being considered in the rest of this work. On its part, in OOK systems IFWM has been shown to generate ghost pulses that deteriorate the bit-error rate [134, 135] whereas in phase-modulated signals IFWM induces a non-Gaussian phase noise (although Gaussian approximations can be obtained)[136]. The main inconvenience in the statistical analysis of IFWM is the correlation induced by this nonlinear effect between the phase noise of consecutive symbols [132].

The relative importance of the discussed propagation-induced phase perturbations (NPN, XPM and IFWM) in dispersive environments has already been analysed [148]. This study has shown that NPN and XPM decrease with dispersion whereas, in fact, IFWM increases. This feature leads, for the case of standard single mode fibres, to a situation in which the most important phase noise generated during propagation is the NPN, followed by IFWM and XPM respectively.

3.3 Photodetection

So far optical signals have been discussed, however they must be eventually converted into electrical signals by means of photodetectors to recover the information they carry. Photodetection, being a square-law process, transforms the statistical features of the optical signal and noise [158]. In addition, photodetection generates electrical noise sources that degrade the quality of the signal further [94].

The electrical noise sources generated during photodetection are mainly two: thermal noise and shot noise. Thermal noise arises from the unavoidable vibrations that electrons undergo during their transmission as electric currents [159]. On its part, shot noise arises from the quantum nature of the photons that spontaneously fluctuate according to a Poisson distribution [160]; this fluctuation induces additive noise over time. In the absence of optical ASE noise, these are the limiting factors that set the performance of the system. In particular, for the case of an on-off keyed (OOK) signal, the low energy

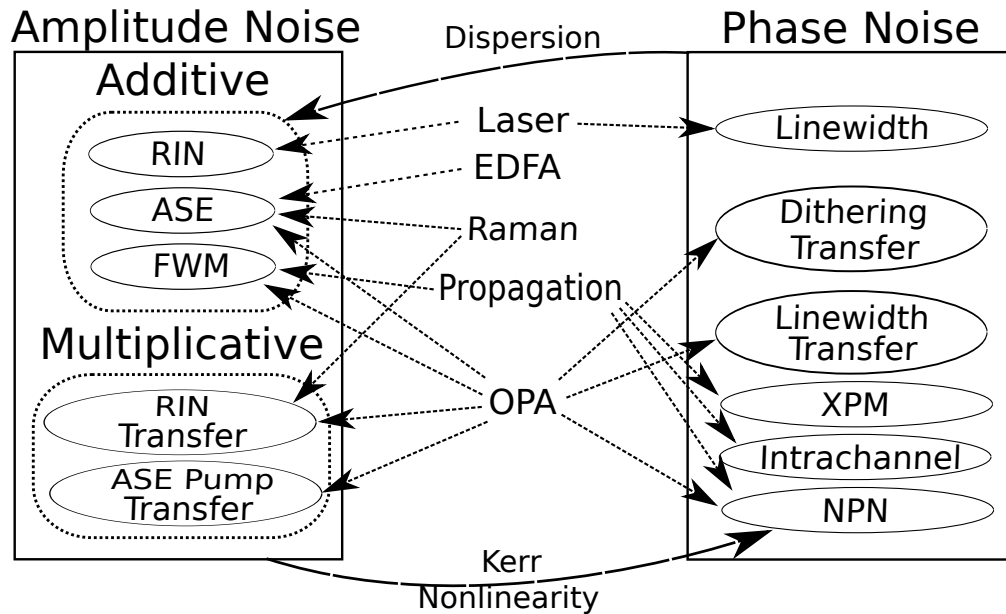


Figure 3.6: Optical noise sources in optical communication systems

level is degraded by thermal noise whereas the high energy level is degraded by shot noise [94].

In the presence of optical ASE, the optical noise is typically the limiting factor in the system performance, whereas the electrical noise sources are negligible with respect to the degradation induced by ASE noise [161]. In this case, the nonlinear response of the photodetection process creates a beating between the signal and the noise component altering the statistical features of the latter, leading to two different beatings: spontaneous-spontaneous beat noise, that exhibits a central chi-square probability density function (PDF), and signal-spontaneous beat noise, that exhibits a noncentral chi-square PDF. In this case the low energy level is degraded by the spontaneous-spontaneous beat noise whereas the high energy level is degraded by the signal-spontaneous beat noise.

3.4 Discussion

Throughout this chapter, a large number of different perturbations present in optical communication systems have been discussed. Each type of perturbation is generated by a different physical process and they mutually interact by modifying their features and inducing effects on modulated signals. The complexities of these large number of intertwined physical processes make the analysis of their impact cumbersome.

In the light of this complexity, a simplified model is desirable to provide an abstraction from the underlying physical processes with the aim of coping with such a variability of noise sources in an integrated way. The approach explained in this work proposes achieving such abstraction by paying attention to the statistical features of the different

noise sources with respect to the correlations exhibited with the amplified signals. In doing so, three distinct generic noise sources can be identified: amplitude additive noise, that is uncorrelated from the amplified signals both in phase and amplitude, amplitude multiplicative noise, that is correlated with the amplified signal in amplitude but not in phase, and phase noise, that is correlated with the amplified signal in phase but not in amplitude. Fig. 3.6 shows the classification of the discussed noise sources into this model. This classification will be used in Chapter 4 to compute the degradation in the bit error rate induced by each of these generic types of noise.

This classification shows that for the case of current optical communication systems, where only EDFA and Raman amplifiers are used, amplitude additive noise is the dominant noise source to be considered in order to characterise the degradation induced on modulated signals. However, when OPAs are considered as signal amplifiers, all three noise sources must be included to fully account for all the possible effects.

It is to be noted that among all of the possible noise sources considered in Fig. 3.6, NPN and intrachannel effects play a special role, because they are the only non-stationary or time-correlated noise sources, requiring special mathematical treatment. In this manner, neither NPN nor intrachannel effects are considered in the rest of this work, leaving this study as a future extension of the analysis presented in the following chapter.

Noise Model of Optical Communications

If I can make a mechanical model I can understand it. As long as I cannot make a mechanical model all the way through, I cannot understand it

Lord Kelvin

The previous chapter dealt with the physical noise sources present in optical communication systems and highlighted the complexities in the description of the underlying physical processes that generate the different types of noise. This led to a general classification of noise sources into three broad categories: additive noise, multiplicative noise and phase noise.

This simplification allows an analytical treatment of the effects that noise induces on optical communication systems. Current WDM networks are modelled as systems degraded solely by the additive noise generated by EDFAs or Raman amplifiers where phase noise is modelled as an OSNR degradation [162]. This model can be extended by including the two additional types of noise. The inclusion of multiplicative amplitude noise makes it possible to calculate more accurately the degradation induced by Raman amplifiers, whereas the inclusion of phase noise allows for the analytical computation of the degradation of the BER induced by propagation effects. By considering both types of noise simultaneously, the degradation induced by OPAs can be accurately computed.

The impact of these two additional types of noise on quadrature-amplitude modulated (QAM) signals has not been analysed in the literature, thereby this study being of interest. This chapter is devoted to this task. The analysis presented in the following pages studies the effects of different types of noise on communication signals modulated by different modulation formats.

This chapter is structured as follows: section 4.1 presents the assumptions and variables on which this study is based. This section connects the previous chapter, where the noise sources were statistically described, to the theory of communication based on stochastic processes and hypothesis testing. Section 4.2 develops a comprehensive analytical study of the BER degradation induced by these two unaddressed types of noise both in isolation and combination, making possible the single-stage modelling of

all the previously considered types of amplifiers under an unified formalism. Section 4.3 studies the accumulation of these types of noise in a chain of amplifiers, proposing extensions to the Friis equation to account for their distinctive features. Once this study is presented, a communication channel accounting for these features is proposed. Then, in Section 4.4 the effects of including these two additional types of noise in the capacity of such a communication channel are analysed. Subsequently, Section 4.5 studies the impact of photodetection schemes on the performance of modulated signals, showing that photodetection degrades the quality of phase modulated signals in the presence of phase noise. Finally, section 4.6 provides a summary of all the information provided by this chapter.

4.1 Definitions and Assumptions

The formalism presented in this chapter models the simultaneous impact of three different noise sources on quadrature-amplitude modulated signals. The first step in this modelling process is a proper characterisation of these types of noise, their relative importance and their relations. In this sense, the three types of noise are considered to be Gaussian white noise, uncorrelated from one another. These assumptions exclude from this analysis some of the noise sources that fall into the category of phase noise. More specifically, nonlinear phase noise, cross-polarisation modulation and intrachannel effects do not meet these statistical requirements and are neglected in this model.

In the standard theory of communication, the impact of additive noise is characterised by a single magnitude, the optical signal-to-noise ratio (OSNR)¹, that determines how large the noise power is with respect to the signal power. The approach described in this chapter proposes the definition of two additional OSNRs, each corresponding to a different type of noise. These definitions allow the use of the signal power as a common reference for the comparison of the relative importance of the three types of noise, making possible the individual characterisation of the phenomena induced by each type. Furthermore, it will be shown that these definitions allow a natural extension of the expressions for the computation of the bit error rate (BER) induced by them.

Thus, a proper definition of the *new* OSNRs is the key to this formalism because it must suitably describe the distinctive features that multiplicative and phase noise sources exhibit. In the most general case, in which a signal with power P_0 degraded by additive noise with power N_0 is amplified by an amplifier that generates the three types of noise, the result of the amplification process is

¹It is to be noted that since only optical amplifiers are analysed, OSNR and not SNR is considered in this section. This highlights the fact that no electrical noise sources are considered at this stage. SNR will be included in Section 4.5 where photodetection is discussed.

$$P_0 + N_0 \rightarrow G \cdot P_0 + G \cdot N_0 + N_A + \Delta G \cdot P_0 + N_P \quad (4.1)$$

where N_A accounts for the additive noise power added by the amplifier, G for the gain of the amplifier, ΔG for the gain fluctuations, N_P for the phase noise power and where the second order noise components have been neglected. This expression shows the different noise powers generated at the output of this hypothetical amplifier. The first term on the right hand side of equation (4.1) shows the amplified signal, the common reference. The second term represents the unavoidable amplification of noise already present at the input.

The third term represents the power of the generated additive noise, the values of which for EDFAs and Raman amplifiers are shown in equations (3.2) and (3.4) respectively. The OSNR bound to the additive noise retains the original definition of the standard theory of communication. In the following pages, this OSNR is referred to as additive OSNR (AOSNR) and its definition is

$$AOSNR = \frac{P_0}{N_0 + N_A/G} \quad (4.2)$$

The fourth term of equation (4.1) represents the multiplicative noise modelled as a gain fluctuation. For the case of Raman amplifiers, gain fluctuations model the RIN transfer, as shown in equations (3.5) and (3.6) whereas, for the case of OPAs, they model ASE pump and RIN transfers. This allows a definition of a multiplicative OSNR (MOSNR) that accounts for gain fluctuations as

$$MOSNR = \frac{P_0}{\frac{\Delta G}{G} \cdot P_0} = \frac{1}{\Delta G/G} \quad (4.3)$$

where ΔG is the variance of a zero-mean Gaussian white random variable.

The fifth term of equation (4.1) represents the phase noise power generated by this generic amplifier. The description of phase noise in terms of power, that is the squared electric field stripped of any phase information, may sound an inconsistency so a small digression to address this issue is required at this point.

It is well known that the spectrum of a tone with constant frequency and phase is a Dirac delta. However, if the phase of such a tone is allowed to vary over time, then its spectrum changes according to the Wiener-Khintchine theorem. This theorem states that the spectrum of a stationary random process is the Fourier transform of its autocorrelation [163]. Therefore, the variations of phase over time can be characterised by an autocorrelation function that, in turn, defines the spectral shape of the signal. The phase variations of phase-modulated signals are well-defined transitions, conversely

the phase variations of phase noise are random transitions. In the case of phase noise, the Wiener-Khintchine theorem relates the variance of the phase noise with the phase noise power (an example of this is the laser linewidth, as discussed in the previous chapter, see eq. (3.12)). Both for well-defined and random phase variations the result is similar: a broadening of the spectrum of the original tone dependent on the rate and autocorrelation of the phase variations.

In this context, the addition of phase noise to phase modulated signals induces a perturbation on their well-defined phase variations, modifying their autocorrelations and, in turn, their spectra. This alteration of the signal spectrum is commonly referred to as spectral broadening. In the light of this feature, the definition of the optical signal-to-phase-noise ratio (POSNR in this work) represents the amount of spectral distortion that a signal underwent during its amplification.

Unfortunately, a general definition of POSNR in terms of spectral distortion is not practical because, since the autocorrelation of a signal is modulation dependent, the spectral distortion is modulation dependent as well. To bypass this drawback, the definition proposed in this work adopts the approach of defining the POSNR in the phasor domain. As it was mentioned, the Wiener-Khintchine theorem provides a relationship between spectral densities and phases and, therefore, between powers and variances of phase fluctuations. In this sense, a phase noise power can be defined in the phasor domain in terms of the variance of the phase-induced distortion.

Under this approach, the signal power is represented by the absolute square of the phasor of the symbol and the phase noise power by the variance of the phase perturbation. Since the phase perturbation is usually defined in terms of an angle, a transformation to arc length must be performed to obtain the phase noise power, leading to the following relation

$$N_P = \langle \phi^2 \rangle P_0 \quad (4.4)$$

where $\langle \phi^2 \rangle$ represents the variance of the phase noise and P_0 the signal power. This definition of phase noise power leads to the following expression for the POSNR

$$POSNR = \frac{P_0}{N_P} = \frac{P_0}{\langle \phi^2 \rangle P_0} = \frac{1}{\langle \phi^2 \rangle} \quad (4.5)$$

It is to be noted that this expression is similar to definitions of POSNR already proposed previously [164] and that this term is not affected by the gain of the amplifier. In this sense, the previously presented equations (3.16), (3.21), (3.24), (3.25) and (3.26), that characterize the variance of the phase noise induced by different nonlinear interactions, can be used for this purpose.

So far, three OSNRs, bound to three different types of noise, have been defined. It has been shown that, from the perspective of signal theory, these magnitudes represent different degradations that a modulated signal can undergo in an optical transmission system.

In section 4.2.2, the simultaneous degradation of a signal induced by additive and multiplicative noise is analysed. In this context, a definition of a *combined* OSNR (COSNR) is required in order to provide a fair comparison between the performance exhibited by signals degraded by a mixture of additive and multiplicative noise. This parameter is defined as

$$COSNR = \frac{G \cdot P_0}{\Delta G \cdot P_0 + N_0 \cdot G + N_A} = \frac{MOSNR \cdot AOSNR}{MOSNR + AOSNR} \quad (4.6)$$

It is to be noted that, under this definition, if $AOSNR \rightarrow \infty$ (only multiplicative noise is present), then $COSNR \rightarrow MOSNR$ and conversely if $MOSNR \rightarrow \infty$ (only additive noise is present), then $COSNR \rightarrow AOSNR$. It is also important to note that these definitions of AOSNR, MOSNR and COSNR assume a noise power calculated in a reference bandwidth corresponding to the bit rate and, therefore, are independent of the bit-rate of the signals under consideration.

Once the three fundamental OSNRs necessary for this formalism and the auxiliary definition of the COSNR have been presented, then a procedure for the computation of the BERs of modulated signals degraded by these three types of noise can be developed. This is described in the following section.

4.2 Single Stage Amplification

In the last section, three different OSNRs were defined to individually model the degradation induced by the three types of noise considered. This section provides quantitative expressions for the BER degradation induced by them, showing that, under this formalism, the BER is a function of these previously introduced OSNRs and this function is a natural extension of the standard theory of communication.

In order to compute the BER induced by these types of noise, the distributions of their probability density functions (PDFs) in the phasor domain is used [165]. The PDFs set the distinctive features of the degradation induced by each type of noise on modulated signals. Examples of these distributions for different constellations degraded by additive, multiplicative and phase noise are shown in Fig. 4.1.

The most noteworthy feature of these constellations is that the PDF of the multiplicative amplitude noise shows properties very similar to those of additive noise and, in fact,

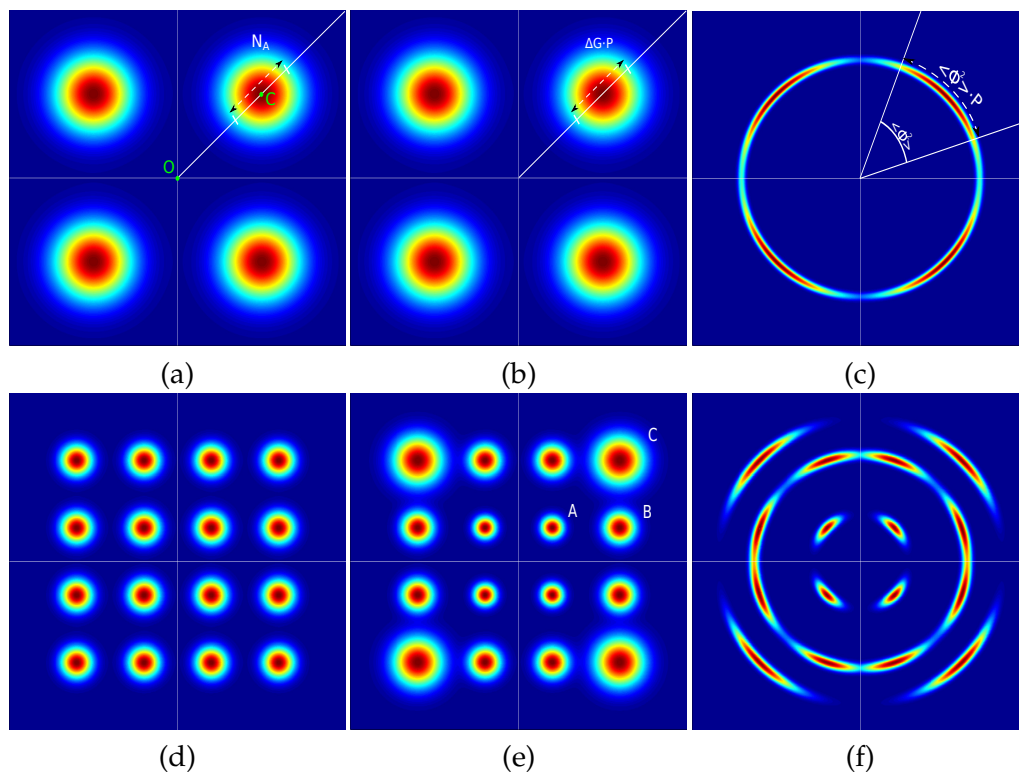


Figure 4.1: Examples of QPSK (top row) and 16-QAM (bottom row) constellations degraded by additive (left column), multiplicative (middle column) and phase (right column) noise

the two PDFs are identical for the case of M-PSK modulation formats. That is not the case of phase noise, whose PDF is very different. Despite these differences, the general procedure for the computation of the BER can still be applied to this PDF providing very accurate results.

The rest of this section develops a comprehensive analysis of the quantification of the BER induced by these PDFs. For the sake of clarity, the explanations are divided in two subsections, firstly dealing with the noise sources in isolation and subsequently dealing with them in a combined way.

4.2.1 Noise Sources in Isolation

The procedure of quantification of the BER induced by additive noise on modulated signals is well known [165, 166]. This particular case exhibits a symmetry in the phasor plane around the origin O and around the centre of the symbol C (see Fig. 4.1a) that makes the simplification of the problem to a single integration possible. On its part, the two new types of noise considered do not exhibit both symmetries simultaneously, thereby all the simplifications performed for the case of additive noise are not possible.

Multiplicative noise exhibits a symmetry in terms of the PDF of the symbols (around C) but only partial symmetry in terms of the whole constellation (see Fig. 4.1e), whereas phase noise does not exhibit symmetry in terms of PDF but only in terms of rotation of the constellation (around O).

For this reason, this section firstly explains the generic procedure for the calculation of the BER induced by additive noise, paying special attention to the simplifications that its symmetry allows for. Subsequently the simplifications that are not allowed for the case of the other two types of noise due to their symmetry characteristics over the phasorial plane are analysed.

4.2.1.1 Additive Noise

The discrimination process between noisy samples of symbols aims to minimise the probability of error during the decision process [165, 166]. This is performed by choosing appropriate Voronoi regions [167] for each of the symbols of the constellation depending on their PDFs, so that the location of the samples on the phasor plane determines the recovered symbol. There exist two main criteria for choosing these regions: Neyman-Pearson tests, if the probabilities of each symbol are not known *a priori*, and the maximum *a posteriori* (MAP) test if they are. For simplicity, the probabilities of all symbols of the constellations are assumed to be known and to be similar to each other.

In the most general case, once the PDFs of the symbols are known, their corresponding Voronoi regions can be defined so that the integration of these PDFs out of these regions determines the probability of error of that symbol. This integration is defined in the complex plane, namely, a two-dimensional space.

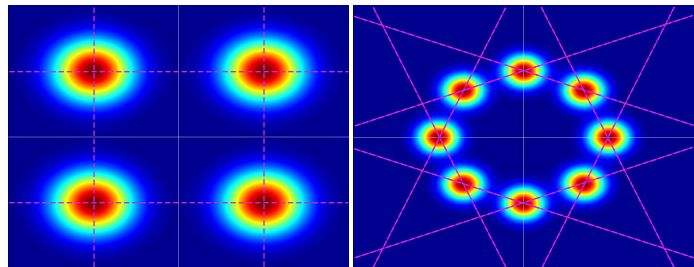


Figure 4.2: Example of decision axes

However, the decision problem can be reduced to a one-dimensional problem if a suitable axis is chosen [166] reducing the two-dimensional integration to a one-dimensional one. This axis is referred to as *decision axis* and its use largely simplifies the calculations of the probabilities of error. This simplification entails the definition of a decision axis for each pair of symbols so that only the projections of the PDFs of the symbols on these axes are relevant for the decision process whereas the orthogonal components of noise are irrelevant. This is called the theorem of *irrelevance* [166].

A common assumption is to take into account only the effect of the closest symbols for the calculation the probability of error, neglecting the effect of the rest of the symbols

[166]. Under all these assumptions, the decision axes used for QPSK and 8-phase shift keying (PSK) modulation formats are displayed in Fig. 4.2.

This generic procedure can be applied to the case of additive noise. Additive noise exhibits a circularly Gaussian distribution on the phasor plane [166] (see Fig. 4.1a and 4.1d). Thus its projection is completely independent of the orientation of the decision axis (see e.g. Fig. 4.2) and always results in a Gaussian distribution. This symmetry property of the PDF of additive noise, together with the symmetry that constellations exhibit simplifies the computation of the probability of error.

Thus the problem of the calculation of the probability of error reduces to the one-dimensional integration of the projected PDFs on the decision axis outside its corresponding Voronoi region, the solution of which results in the well known expressions for the probability of error of signals degraded by additive noise

$$\mathcal{P}_{BPSK}^{add} = \frac{1}{2} \operatorname{erfc} \left(\sqrt{AOSNR} \right) \quad (4.7)$$

$$\mathcal{P}_{QPSK}^{add} = \frac{1}{2} \operatorname{erfc} \left(\sqrt{\frac{AOSNR}{2}} \right) \quad (4.8)$$

These equations show that for any value of the AOSNR, the probability of error of a QPSK signal is higher than that of a BPSK one. This is consequence of the smaller distance between the symbols of a QPSK constellation.

It should be noted that the procedure previously detailed provides the probability of an errored symbol. However, we are interested in the calculation of the probability of an errored bit. Therefore, both in this analysis and the simulations presented in this chapter, Gray coding is assumed, providing similar probabilities of errored symbols and bits.

4.2.1.2 Multiplicative Noise

The case of multiplicative noise resembles that of additive noise. The PDFs of the symbols are still circular Gaussian random variables, therefore their projection is Gaussian and independent of the decision axes. However, the variance is not constant anymore, being dependent on the symbol power. Figs. 4.1b and 4.1e respectively show examples of QPSK and 16-QAM constellations degraded by multiplicative noise.

The most important feature of multiplicative noise is that, for the case of M-PSK modulation formats, its effects are exactly the same as those of additive noise. Thus the existence of a single power level in the constellation enforces the same noise variance for all the symbols of the constellation. In this manner, the well-known expressions for the

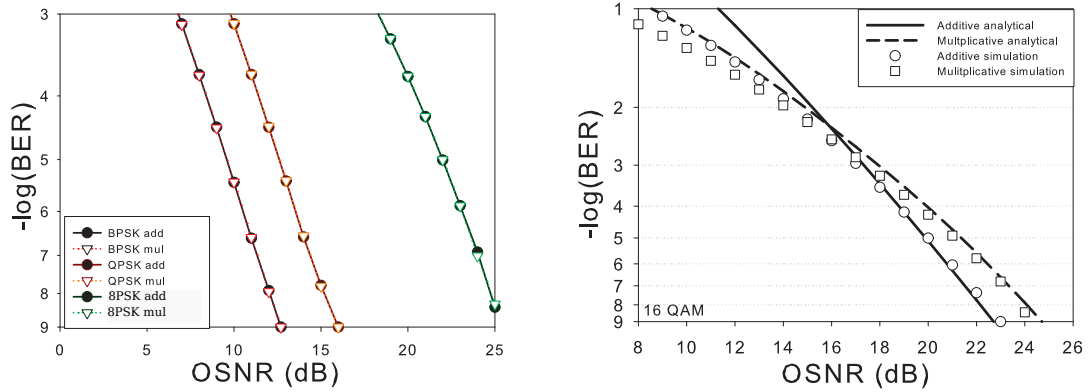


Figure 4.3: BER comparison between additive noise and multiplicative for the case of PSK (left) and 16-QAM (right) modulation formats obtained through Monte-Carlo simulations

calculation of BER of PSK modulation formats in the presence of additive noise are still valid for multiplicative noise replacing AOSNR for MOSNR. A comparison of the BERs induced on PSK modulation formats in the presence of additive and multiplicative noise obtained through Monte-Carlo simulations is displayed on the left of Fig. 4.3, showing no appreciable difference between both types of noise.

These Monte-Carlo simulations were performed by generating 10^9 random bits, subsequently used to generate symbols of different modulation formats. The symbols were degraded by different noise powers, demodulated and the bit error rate was obtained through error counting.

The case of multilevel amplitude modulations is different. Each power level exhibits a different noise variance (see Fig. 4.1e) and all the simplifications derived from the symmetry of the constellation cannot be performed. In this sense, the projections of the PDFs on the decision axes are Gaussian random variables whose variances are $\Delta G/G \cdot P_k$, where P_k represents the power of each symbol.

In this context, the computation of the probability of error cannot be reduced to a single integration anymore and the contribution of each symbol to the total probability of error must be weighted. This procedure is illustrated below for the case of the 16-QAM constellation shown in Fig. 4.1e.

The 16-QAM modulation format comprises three different amplitude levels (labelled as A, B and C in Fig. 4.1e) so that the variance induced by the multiplicative noise is different for each level. For this modulation format, there are 4 symbols of power A, 8 of power B and 4 more of power C. Assuming that the probability of all the symbols is equal and that the errors are evenly distributed among them, then the total probability of error can be calculated as:

$$\mathcal{P}_{16-QAM} = \frac{4}{16}\mathcal{P}_A + \frac{8}{16}\mathcal{P}_B + \frac{4}{16}\mathcal{P}_C = \frac{1}{4}\mathcal{P}_A + \frac{1}{2}\mathcal{P}_B + \frac{1}{4}\mathcal{P}_C \quad (4.9)$$

where $\mathcal{P}_A, \mathcal{P}_B, \mathcal{P}_C$ represent the probability of error of a symbol with power A, B and C respectively. These probabilities would be equal in the case of additive noise but, due to the different noise variances, this is not the case with multiplicative noise, so the probability for each symbol must be calculated independently. The probability \mathcal{P}_A can be calculated taking into account that a symbol with power level A has four closest neighbours, two of them with power level A and the other two with power level B (see Fig. 4.1e). In the same manner, \mathcal{P}_B and \mathcal{P}_C can be calculated by noticing that the symbols with power level B have three neighbours, each of them with different power levels, and the symbols with power level C have two neighbours with power level B. By assuming that the errors are only generated by the closest neighbours and that these errors are evenly distributed among them, then the probability of error can be expressed mathematically as

$$\begin{aligned} \mathcal{P}_A &= \frac{1}{2}\mathcal{P}_{AA} + \frac{1}{2}\mathcal{P}_{AB} \\ \mathcal{P}_B &= \frac{1}{3}\mathcal{P}_{AB} + \frac{1}{3}\mathcal{P}_{BB} + \frac{1}{3}\mathcal{P}_{BC} \\ \mathcal{P}_C &= \mathcal{P}_{BC} \end{aligned} \quad (4.10)$$

where \mathcal{P}_{XY} represents the probability that symbol of power level X is detected as a symbol of power level Y . Each addend of these equations represents the probability of error of the symbol with a closest neighbour of a different noise variance. Substituting (4.10) into (4.9) we obtain:

$$\mathcal{P}_{16-QAM} = \frac{1}{8}\mathcal{P}_{AA} + \frac{1}{6}\mathcal{P}_{BB} + \frac{7}{24}\mathcal{P}_{AB} + \frac{5}{12}\mathcal{P}_{BC} \quad (4.11)$$

Each probability \mathcal{P}_{XY} can be calculated using the theorem of irrelevance and projecting the PDF of each symbol on the decision axes. This results in the integration of two Gaussian random variables with different variances. By representing the distance between the symbols of the constellation by d , then, \mathcal{P}_{XY} can be calculated as

$$\mathcal{P}_{XY}(d, \sigma_1^2, \sigma_2^2) = \frac{1}{4} \left[\operatorname{erfc} \left(\frac{d}{2\sqrt{\sigma_1^2}} \right) + \operatorname{erfc} \left(\frac{d}{2\sqrt{\sigma_2^2}} \right) \right] \quad (4.12)$$

where σ_1^2 and σ_2^2 represent the variances of the multiplicative noise.

In the case of a 16-QAM modulation format with mean power P , the corresponding variances for symbols with power A, B and C are $\Delta G/G \cdot \frac{P}{5}$, $\Delta G/G \cdot P$ and $\Delta G/G \cdot$

$\frac{9 \cdot P}{5}$ respectively and the distance between the symbols takes the value $d = \sqrt{\frac{2 \cdot P}{5}}$. Substituting these values into (4.12) and subsequently into (4.11) we obtain:

$$\begin{aligned} \mathcal{P}_{AA} &= \frac{1}{2} \operatorname{erfc} \left(\sqrt{\frac{1}{2\Delta G/G}} \right) \\ \mathcal{P}_{BB} &= \frac{1}{2} \operatorname{erfc} \left(\sqrt{\frac{1}{10\Delta G/G}} \right) \end{aligned} \quad (4.13)$$

$$\begin{aligned} \mathcal{P}_{AB} &= \frac{1}{4} \left[\operatorname{erfc} \left(\sqrt{\frac{1}{2\Delta G/G}} \right) + \operatorname{erfc} \left(\sqrt{\frac{1}{10\Delta G/G}} \right) \right] \\ \mathcal{P}_{BC} &= \frac{1}{4} \left[\operatorname{erfc} \left(\sqrt{\frac{1}{10\Delta G/G}} \right) + \operatorname{erfc} \left(\sqrt{\frac{1}{18\Delta G/G}} \right) \right] \end{aligned}$$

whence

$$\mathcal{P}_{16-QAM} = \frac{13}{96} \operatorname{erfc} \left(\sqrt{\frac{MOSNR}{2}} \right) + \frac{25}{96} \operatorname{erfc} \left(\sqrt{\frac{MOSNR}{10}} \right) + \frac{10}{96} \operatorname{erfc} \left(\sqrt{\frac{MOSNR}{18}} \right) \quad (4.14)$$

where the relation (4.3) has been used. This equation resembles the standard expression for the probability of error of a 16-QAM degraded only by an additive noise

$$\mathcal{P}_{16-QAM}^{add} = \frac{1}{2} \operatorname{erfc} \left(\sqrt{\frac{AOSNR}{10}} \right) \quad (4.15)$$

but, in this case, there exists one term for each power level of the constellation. A comparison between the expressions (4.14) and (4.15) for the calculation of the BER induced by additive noise with respect to multiplicative noise in 16-QAM signals is shown on the right of Fig. 4.3. The solid lines in this figure represent the analytical equations (4.14) and (4.15) whereas the dots represent the result of the Monte-Carlo simulations. These graphs show a very good agreement between the analytical expressions and the simulations results, especially in environments with high OSNRs. In low OSNR scenarios, the assumption of errors distributed only among the closest neighbours is not valid anymore, leading to a decreased accuracy.

4.2.1.3 Phase Noise

The case of the phase noise presents more complications in terms of the symmetry of the PDFs than the case of multiplicative noise. The symmetry characteristics of the crescent-shaped PDFs (see Figs. 4.1c and 4.1f) induced by the phase noise are very different from those of circularly symmetric PDFs exhibited by additive and multiplicative noise. Then, the projection on the decision axis is very different from a Gaussian distribution. In fact, the projection is dependent on the orientation of the decision axis what induces a BER degradation that is modulation dependent. This section will show that for the case of multilevel amplitude modulation formats, even within the same constellation, the effect induced on each symbol can be different, leading to a weighting of the probability of error induced by each symbol of the constellation.

Figures 4.1c and 4.1f show that phase noise only affects symbols with the same power level, thus different power levels can be treated separately. In this way, the analysis of the effects of phase noise on modulated signals can be simplified by dividing a complex constellation in a set of disjunct M-PSK modulations and averaging out their probabilities of error. Thus, the calculation of the probability of error induced by phase noise firstly entails its calculation for PSK modulation formats and subsequently weighting it for the case of multilevel amplitude modulation formats.

The first step of this process is the calculation of the projection of the phase noise on the decision axis. As was previously mentioned, only Gaussian phase noise is to be analysed; its PDF can be expressed as

$$p_x(x) = \frac{1}{\sqrt{2\pi \langle \phi^2 \rangle}} \exp\left(-\frac{(\phi - \phi_0)^2}{2 \langle \phi^2 \rangle}\right) \quad \text{where} \quad \phi = \arctan\left(\frac{\text{Im}\{E\}}{\text{Re}\{E\}}\right) \quad (4.16)$$

where E represents the electric field and x its amplitude. Due to the nonlinearity of this equation, it is not possible to compute this projection for an arbitrary direction except when the axis is parallel to the real axis. In this case, this projection reduces to the calculation of the real part of a complex value.

The symmetry properties of the PSK modulation formats can be used to rotate the constellation around the origin in order to obtain one of the decision axes parallel to the real axis and subsequently compute the projection on it. Once this rotation is performed, this calculation reduces to a projection on the real axis (ie. equivalent to the calculation of the real part of a complex number). The graphical representation of this procedure is shown in the top row of Fig. 4.4 for different modulation formats, displaying underneath the corresponding projected PDFs for different variances of the phase noise.

Mathematically, this procedure comprises the choice of a proper value of the parameter ϕ_0 of equation (4.16), that represents the required rotation to get a decision axis parallel

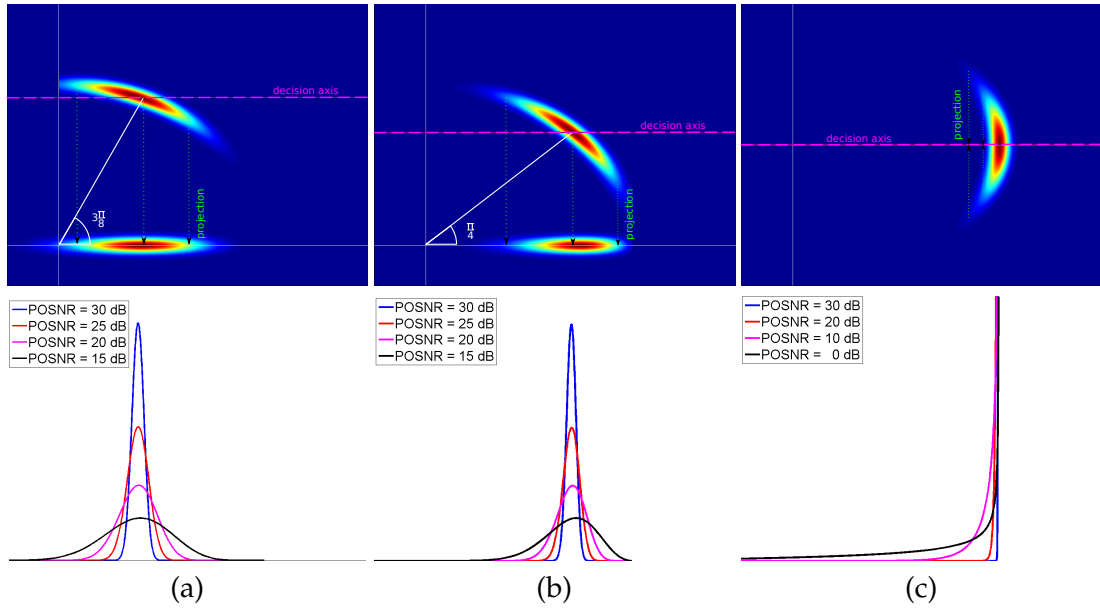


Figure 4.4: Procedure of projection of phase noise onto the real axis (top row) and their corresponding PDFs for different values of POSNR (bottom row) for (a) 8-PSK, (b) QPSK and (c) BPSK modulation formats

to the real one. In this manner, a BPSK modulation does not need to be rotated because the decision axis is already parallel to the real axis ($\phi_0 = 0$). That is not the case of QPSK and 8-PSK modulation formats, for which cases ϕ_0 takes the values $\pi/2$ and $3\pi/8$ respectively (see Fig. 4.4 for clarification).

Once the constellation rotation has been performed (that is, a proper value of ϕ_0 has been chosen), then the projection can be calculated through the standard rules of the PDFs [168]. In this particular case, the projection reduces to the calculation of the PDF of a function of a random variable. Standard rules of statistics state that if $y = f(x)$ and the PDF of x is $p_x(x)$, then the PDF of y is [168]

$$p_y(y) = \left| \frac{df^{-1}(y)}{dy} \right| f_x(f^{-1}(y)) \quad (4.17)$$

In this particular case $f(x) = \cos(x)$, which represents the projection of a complex number on the real axis. Applying this transformation to (4.16) the following PDF is obtained

$$p_y(y, \langle \phi^2 \rangle, \phi_0) = \frac{K}{\sqrt{2\pi \langle \phi^2 \rangle}} \exp\left(-\frac{(a \cos(y) - \phi_0)^2}{2 \langle \phi^2 \rangle}\right) \frac{1}{\sqrt{|1 - \text{sgn}(y) \cdot y^2|}} \quad (4.18)$$

where $\text{sgn}(y)$ represents the sign function and K is a normalisation constant. This PDF is characterized by two parameters: $\langle \phi^2 \rangle$, the variance of the Gaussian phase noise (that is related to the POSNR through equation (4.5)) and the rotation angle ϕ_0 . Then, for the

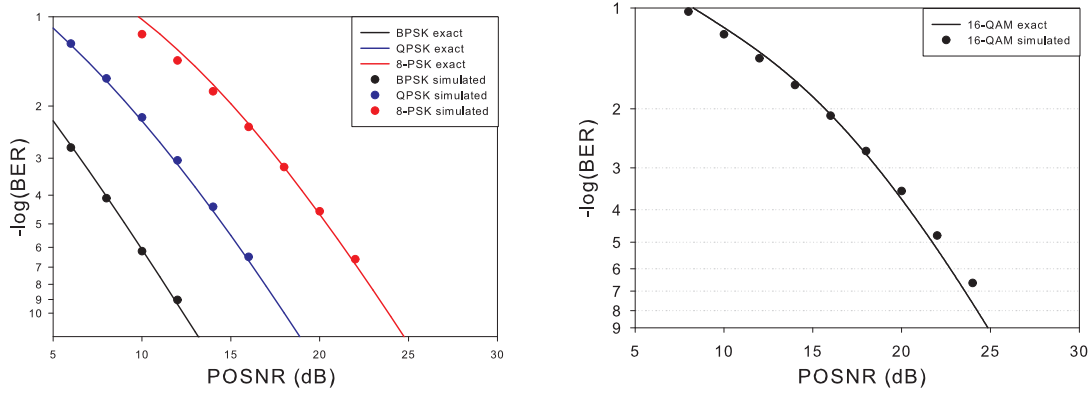


Figure 4.5: BER of BPSK, QPSK and 8-PSK (left) and 16-QAM (right) modulation formats degraded only by phase noise computed using the exact PDF

computation of the BER is necessary to know both the variance of the phase noise and the modulation format in question.

As with previous cases, once the projected PDFs have been calculated, the computation of the probability of error for the different modulation formats can be obtained by integrating the projected PDF shown in equation (4.18) outside the decision region. In this case this region is the interval $[-1, 0)$, i.e.

$$P_{err}(\langle \phi^2 \rangle, \phi_0) = \int_{-1}^0 p_y(y, \langle \phi^2 \rangle, \phi_0) dy \quad (4.19)$$

The results of these integrations for PSK modulation formats are shown in the left of Fig. 4.5. These graphs compare the results of the integration of the PDF² (solid lines) to those of a Monte-Carlo simulation (dots) performed assuming a zero-mean Gaussian random phase perturbation as the only source of noise.

On its part, the calculation of the BER for multilevel amplitude modulation formats requires an integration for each power level in the constellation. The case of the 16-QAM modulation format shown in Fig. 4.1f will be used to illustrate this procedure. Treating phase noise on rings of equal power does not always calculate nearest-neighbour errors, but simulations of Fig. 4.5 seem to justify this approximation. Based on this approach, a 16-QAM constellation consists of three different power levels that can be represented as two independent QPSK sub-constellations and one asymmetric 8-PSK sub-constellation. The cause of the asymmetry of the 8-PSK is the unequal spacing between its symbols (see Fig. 4.1f for clarification). Therefore, the total probability of error would be an average between the probabilities of error of eight QPSK symbols and eight asymmetric 8-PSK symbols, resulting in the following expression:

²The code used to generate these results has been included in Appendix A

$$\mathcal{P}_{16-QAM}(\sigma_\varphi^2) = \frac{8}{16}\mathcal{P}_{QPSK}(\sigma_\varphi^2) + \frac{8}{16}\mathcal{P}_{8-PSK^*}(\sigma_\varphi^2) \quad (4.20)$$

where the notation $8-PSK^*$ highlights the asymmetry of the 8-PSK sub-constellation. The calculation of the probability of error of the 8-PSK sub-constellation can be performed in the previously explained manner using a value $\varphi_0 = \frac{\pi}{2} - \text{atan}(1/3)$. The results of the complete numerical integrations are displayed in the right of Fig. 4.5, where the analytical result is compared to Monte-Carlo simulations, showing very good agreement between the two.

4.2.2 Combined Noise Sources

In the most general case optical communication systems do not generate only one type of noise. Thus it is necessary to quantify the effect of the three types of noise considered in combination. This analysis, relying on the procedure described in the previous section, is presented firstly by taking the noise sources in pairs to latterly analyse the simultaneous effect of the three noise sources in conjunction.

The problem of combined noise sources can be reduced to that of a signal degraded by a single noise source provided that an equivalent noise can be calculated. If the different noise sources are assumed to be uncorrelated, then an equivalent representation can be obtained. In the presence of several noise sources acting simultaneously, the projection of the PDFs of each noise source on the decision axis is individually calculated, obtaining a *projected* PDF for each of them [169]. The rules of statistics state that the PDF of the equivalent random variable is the convolution of the projected PDFs [168]. In this manner a single PDF equivalent to the mixture of the three types of noise is obtained and the probabilities of error can be calculated in the same way as explained in the previous section. It is to be noted that an implementation of this procedure has been included in Appendix A for the case of a mixture of additive and phase noise.

4.2.2.1 Additive + Multiplicative Noise

The case of a signal degraded by both additive and multiplicative noise models the degradation induced by Raman amplifiers where the two types of noise are simultaneously generated. Both types of noise exhibit a white circularly symmetric Gaussian PDF, only differing in the values of their variances (constant variance in case of additive noise and power dependent variance in the case of multiplicative noise). The previous section showed that the projection of circularly symmetric Gaussian noise on the decision axis always results in a Gaussian distribution. Therefore the PDF of the compound noise is the outcome of the convolution between two Gaussian PDFs, that is, a Gaussian PDF the variance of which is the sum of the two individual variances.

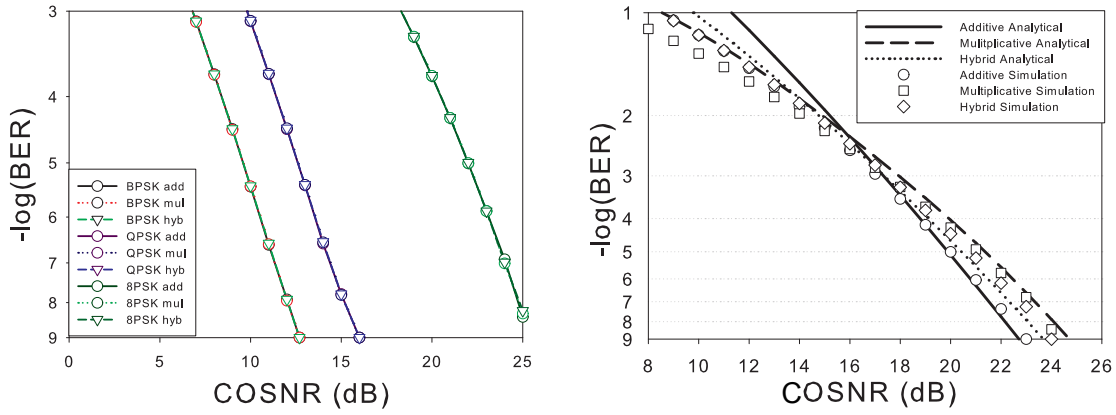


Figure 4.6: Monte-Carlo simulations of BER induced by additive, multiplicative and hybrid noise for M-PSK modulation formats (left) and for 16-QAM modulation format (right)

The effect of multiplicative noise on M-PSK modulation formats is exactly the same as that of additive noise. In this manner, the well-known expressions for the calculation of BER of PSK modulation formats in the presence of additive noise are still valid for a mixture of additive and multiplicative noise by replacing the OSNR with the combined OSNR defined in equation (4.6). This behaviour is shown in the left of Fig. 4.6 where the results of a Monte-Carlo simulation of BPSK, QPSK and 8-PSK signals degraded solely by additive noise, solely by multiplicative noise and by a mixture of 50% additive and 50% multiplicative noise (labelled as hybrid) are presented.

The BER induced on multilevel amplitude modulation formats by this mixture can be calculated analytically. In the case of 16-QAM modulation formats, the procedure explained in equations (4.9)-(4.14) can be extended to account for a Gaussian random variable whose variance comprising a constant component (additive noise) and a power dependent component (multiplicative noise). In doing so, the following general expression for the probability of error of a 16-QAM signal degraded by a mixture of additive and multiplicative noise can be obtained

$$\begin{aligned} \mathcal{P}_{16-QAM} = & \frac{13}{96} \operatorname{erfc} \left(\sqrt{\frac{AOSNR \cdot MOSNR}{2 \cdot AOSNR + 10 \cdot MOSNR}} \right) + \\ & + \frac{25}{96} \operatorname{erfc} \left(\sqrt{\frac{COSNR}{10}} \right) + \frac{10}{96} \operatorname{erfc} \left(\sqrt{\frac{AOSNR \cdot MOSNR}{18 \cdot AOSNR + 10 \cdot MOSNR}} \right) \end{aligned} \quad (4.21)$$

where the definitions (4.2), (4.3) and (4.6) accounting for the different OSNRs have been used. It is to be noted that this expression reduces to (4.15) in the case of only additive noise ($MOSNR \rightarrow \infty$) and to (4.14) in the case of only multiplicative noise ($AOSNR \rightarrow \infty$).

Fig. 4.6 right compares the expressions (4.14), (4.15) and (4.21), that respectively represent the analytical expressions (lines) for the BER of a 16-QAM signal degraded only by additive noise, only by multiplicative and by *hybrid* noise, and their corresponding Monte-Carlo simulations (dots). This graph shows that the effect of multiplicative noise on multilevel amplitude modulation formats is a change in the slope of the BER curve proportional to the ratio between the additive and the multiplicative noise. As with the multiplicative noise in isolation, the accuracy of the analytical expression is shown to increase with OSNR.

4.2.2.2 Additive + Phase Noise

The case of a signal simultaneously degraded by additive and phase noise can model PSK signals amplified by OPAs and/or signals propagating in EDFA-amplified WDM systems in the presence of XPM and FWM. The same procedure applied to a mixture of additive and multiplicative noise can be used to compute the effects of degradation induced by both additive and phase noise. In this case the PDF of the resulting random variable is obtained as the convolution of a Gaussian PDF and the distribution shown in equation (4.18). Conversely to the previous case, this convolution does not result in a Gaussian distribution. An example of the effects of this convolution on a symbol of a BPSK signal is shown in Fig. 4.7. This picture shows that the effect of phase noise is the generation of long tails in the PDF of the composite noise that induce an increase in the probability of error.

As before, this analysis can be divided for the case of M-PSK modulation formats and for multilevel amplitude modulation formats. The procedure is analogous to the previous case but in this case the calculations for multilevel constellations are very intricate. As described in the previous section, the PDF of the phase noise can be different for each amplitude level and, conversely to the amplitude noise, phase noise only affects in the azimuthal direction. These features lead to a large number of different cases to account for. Thus, in this section, and for the sake of clarity, only the analysis of M-PSK modulation formats will be discussed.

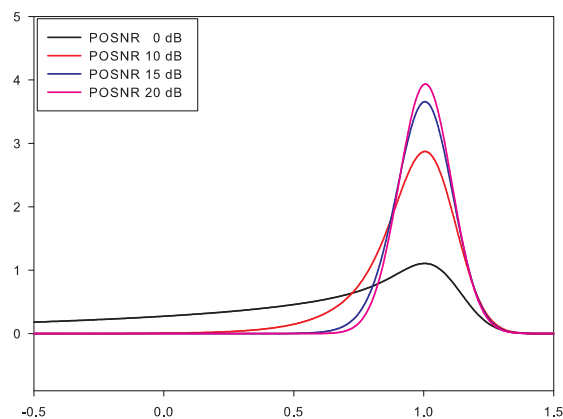


Figure 4.7: PDF of a Gaussian amplitude noise degraded by phase noise (AOSNR = 20 dB)

As with the mixture of additive and multiplicative noise, the probability of error induced by a mixture of additive and phase noise can be computed by integration of the resulting PDFs. The results of these integrations for BPSK, QPSK and 8-PSK modulation formats are shown in Fig. 4.9 showing an excellent agreement for BPSK and QPSK modulation formats between the theoretical model and the Monte-Carlo simulations.

The probability of error induced by a mixture of additive and phase noise on 16-QAM signals is shown in Fig. 4.8. In this case, only the results of the Monte-Carlo simulations are displayed.

These graphs show that the main effect that phase noise induces on a signal already degraded by additive noise is the generation of an error floor, the value of which depends on the POSNR, that is, on the variance of phase noise. Nevertheless, the error floor induced is different for each modulation format; high density modulation formats being more sensitive to phase noise.

A quantitative comparison between the effects of the same amount of phase noise on different modulation formats can be performed in the light of these results. This comparison leads to the conclusion that a minimum POSNR, as defined in equation (4.5), of 20 dB is necessary to avoid measurable degradation of BPSK signals, whereas this value increases to 25 and 30 dB for QPSK and 8-PSK modulation formats respectively.

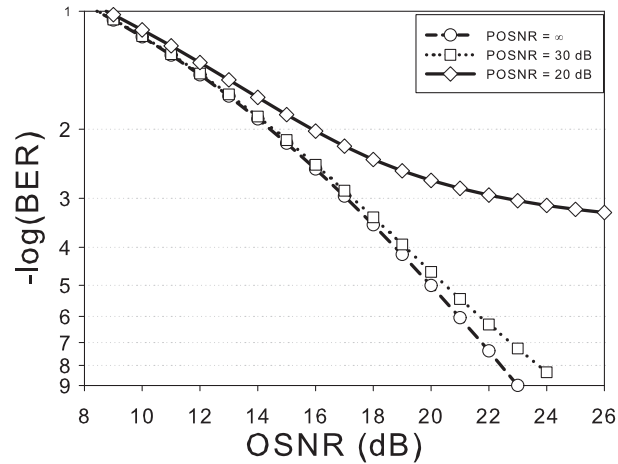


Figure 4.8: BER of a 16-QAM signal degraded by a mixture of additive and phase noise

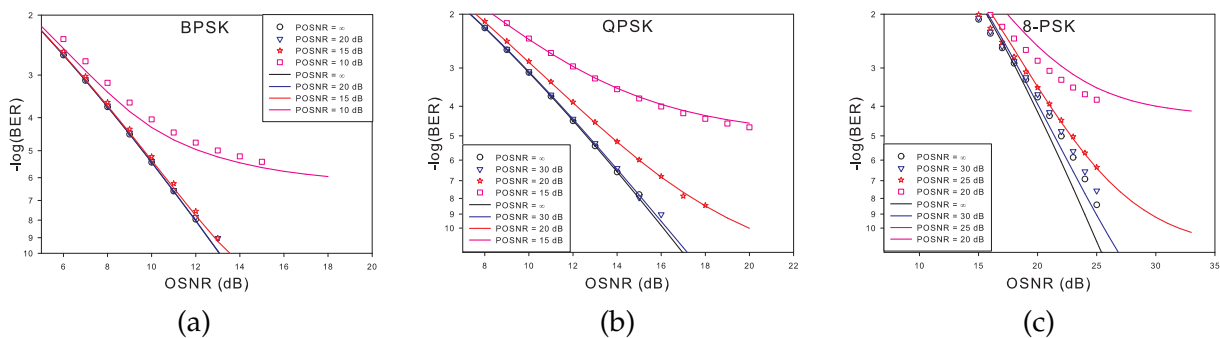


Figure 4.9: BER for BPSK(a), QPSK(b) and 8-PSK(c) modulation formats degraded by additive and phase noise obtained from analytical expressions (solid) and simulation (dotted)

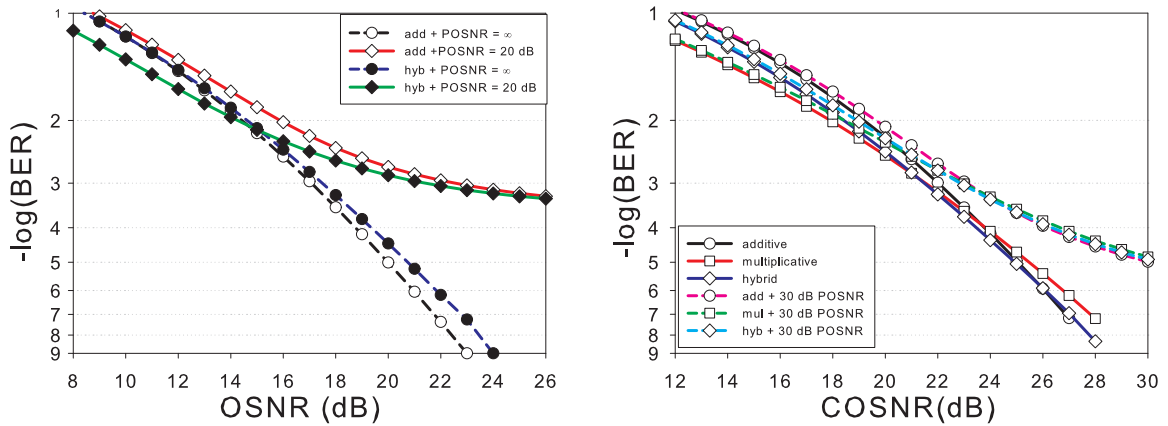


Figure 4.10: BER of a 16-QAM (left) and 64-QAM (right) signals degraded by a mixture of additive, multiplicative and phase noise

4.2.2.3 Additive + Multiplicative + Phase Noise

The case of a signal simultaneously degraded by the three types of noise models OPAs and hybrid EDFA/Raman systems enduring nonlinear effects. An extension of the previous analyses to account for the three types of noise is straight forward. In this case the noise model comprises three noise sources and the resulting PDF is the outcome of the convolution of the three projections of their PDFs, that is, two Gaussian random variables and the phase projected random variable, the PDF of which is shown in equation (4.18). The result of these calculations is very similar to that of the case of additive and phase noise only.

As with the mixture of additive and phase noise, the calculations for multilevel amplitude modulation formats become very complicated due to the large number of distinct cases to be accounted for. For the case of very high density modulation formats, this task can be performed more easily by simulation than through analytical modelling. In this work, only the full model for M-PSK formats is analytically calculated whereas the case of multilevel modulation formats is simulated.

The effects of the three types of noise on multilevel amplitude modulations induce a compound effect comprising the degradations induced by each individual type of noise. In this sense, the presence of multiplicative noise induces a change in the slope of the BER curve, requiring higher OSNRs in order to achieve the same BER whereas the presence of phase noise induces an error floor dependent on the POSNR value. These effects are clearly shown in Fig. 4.10 for the cases of 16-QAM (left) and 64-QAM (right) modulation formats, where these intertwined effects are presented.

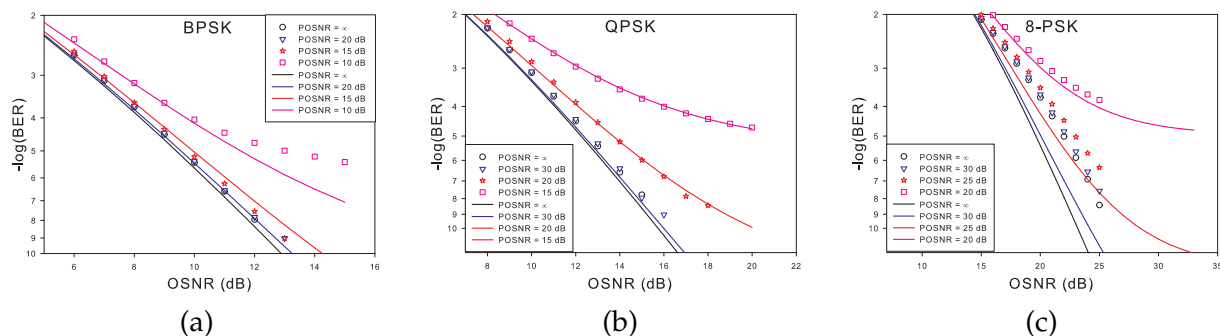


Figure 4.11: BER for BPSK(a), QPSK(b) and 8-PSK(c) modulation formats degraded by additive and phase noise obtained from a Gaussian approximation (solid) and simulation (dotted)

4.2.3 Gaussian Approximations

A common approach in communications is to approximate non-Gaussian PDFs that model the degradation induced by phase noise with Gaussian functions, and subsequently quantify this degradation as an OSNR penalty. The graphs on the bottom row of Fig. 4.4 show that as the density of the M-PSK constellation increases, the PDF of the projected noise resembles more and more a Gaussian distribution. However, this approach leads to an underestimation of the BER. The accuracy of these approximations is shown in Fig. 4.11. Comparing these results with those of Fig. 4.9, it is clear that the modelling of phase noise as an OSNR degradation only provides an accurate estimation of the BER for QPSK signals. The reason why the Gaussian approximation is only accurate for this modulation format is not completely understood but it is supposed to be related to the symmetry that this case exhibits with respect to both I and Q axes (see Fig. 4.4b for clarification).

A more detailed explanation about the Gaussian approximation of phase noise and analytical approximate equations has been included in Appendix B. However, as an alternative to the use of the Gaussian approximation, a similar approach to the erf function can be followed.

The calculation of the probability of error according to the standard theory of communication involves the non-analytical integration of a Gaussian distribution. This led to the tabulation and definition of the well-known error function. It has been shown that the extension of this standard model, allowing an accurate model of phase noise, requires the integration of a new PDF, shown in equation (4.18), that also suffers from not showing an analytical solution.

Then, by following the same procedure, an accurate computation of the probability of error induced by such a PDF would require two different tabulations: (1) for the case of phase noise only and (2) for the case of additive and phase noise.

For the first case, since the PDF of equation (4.18) depends on two parameters, that account for the variance of the phase noise and the modulation format, a tentative definition of a similar function would require one table per modulation format. On its part, for the second case of additive and phase noise, the PDF resulting from the convolution of a Gaussian PDF and the PDF shown in equation (4.18) depends on three parameters, the two previous ones and the AOSNR. This additional parameter increases the number of required tables of a tentative definition in order to accurately compute the probability of error. Such tabulations can be obtained from the example code included in Appendix A.

However, even though a tabulation of these hypothetical functions is the most accurate method for the computation of the BER, this task is out of the scope of this work.

4.3 Noise Accumulation and Propagation Effects

The previous section has analysed the effects induced by a single amplification stage that generates a mixture of additive, multiplicative and phase noise. However, one of the most important aspects of optical communications is the characterization of the accumulation of noise in a chain of optical amplifiers. This analysis allows the identification of key elements of the system, the enhancement of which maximizes the quality of the signal at the output of an optical fibre link. The aim of this study is to achieve the longest attainable reach without electrical regeneration, providing cost effective solutions for the implementation of optical communication systems.

Noise accumulation in chains of EDFA [94, 170, 171], Raman [50, 87, 88] and parametric amplifiers [172] has already been characterized extensively. However, these studies have only considered the accumulation of additive noise, neglecting both multiplicative and phase noise. This section analyses the accumulation of the three types of noise considered providing an understanding of how these types of noise accumulate relative to each other. This allows the characterisation of an optical link based on two parameters: the combined OSNR, as defined in equation (4.6), and the POSNR, as defined in equation (4.5).

Additionally, since phase noise not only degrades the BER of amplified signals but also distorts their spectrum, the combined effects of spectral broadening and fibre dispersion after a chain of amplification stages gives rise to some limiting perturbations that are necessary to model.

4.3.1 Additive Noise

The study of the accumulation of noise in a chain of amplifiers characterises the degradation that the OSNR suffers after each amplification stage. The mathematical measurement of this degradation yielded the concept of noise figure (NF), that accounts for the ratio between OSNR at the output and at the input of the amplifier [173]. Then, by knowing the AOSNR of a modulated signal at the input of an amplifier and its NF, the OSNR of the signal at the output, and therefore its BER, can be calculated.

This analysis was extended to obtain a NF equivalent to chain of amplifiers, leading to the well-known Friis formula [173], that characterizes the accumulation of electrical noise. With the advent of optical amplifiers this theory was adapted to the accumulation of noise in chains of EDFAs and Raman amplifiers [94, 170, 171].

This section is based on the concept of noise figure, that allows the mathematical calculation of the OSNR at the output of an optical communication systems. The system model assumed in the studies of EDFA and Raman amplifiers is shown in Fig. 4.12. In this model, a chain of N identical amplifiers and fibre spans is studied, assuming that the gain of the amplifiers exactly matches the losses of the fibres and that each amplifier in the chain generates an additive noise characterized by a noise figure.

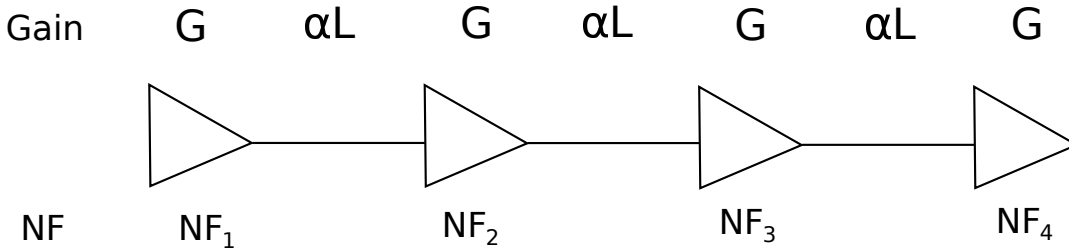


Figure 4.12: System model for a chain of EDFAs

For the specific case of a chain of EDFAs, the noise powers generated by all of the amplifiers are accumulated at the output of the chain, resulting in the following OSNR after N stages of amplification [170]:

$$AOSNR = \frac{P_0 \cdot G}{N \times P_{ASE}^{EDFA}} \quad (4.22)$$

where P_0 represents the average signal power at the input of the first amplifier and P_{ASE}^{EDFA} represents the ASE noise power generated by each EDFA (see equation (3.2)). Therefore, the noise power increases linearly with the number of stages of amplification.

Even though NF is a concept applicable only to lumped amplifiers and Raman amplification is a distributed nonlinear process that takes place along the propagation of the signals in the transmission fibre, it has also been modelled using an *effective* NF that

accounts for the added noise in a lumped element model (similar to an EDFA) leading to the following expression for for the AOSNR [88]

$$AOSNR = \frac{P_0 \cdot G}{N \times P_{ASE}^{Raman}} \quad (4.23)$$

where in this case P_{ASE}^{Raman} represents the ASE noise power generated by each Raman amplifier (see equation (3.4)).

Once the AOSNR at the output of a chain of optical amplifiers has been obtained, then the degradation imposed by each one within a chain is characterized by the noise figure of each amplifier. This characterisation can be performed either in terms of SNRs, that take the electrical noise into account [94], or in terms of OSNRs [171], that only account for the optical noise sources. Since the target of this section is the characterization of the optical effects only, the last approach is adopted, leading to the following definition of NF

$$NF_{opt} = \frac{OSNR_{input}}{OSNR_{output}} \quad (4.24)$$

Under this definition, and considering a quantum noise with power $h\nu B$ over a bandwidth of 1 Hz as the only noise source at the input, equations (3.2) and (3.4) can be used to yield the following noise figures for EDFA and Raman amplifiers

$$NF_{EDFA} = 1 + n_{sp}^{EDFA} \left(1 - \frac{1}{G}\right) \approx 1 + n_{sp} \quad (4.25)$$

$$NF_{EDFA} = 1 + n_{sp}^R \cdot g_R \int_0^L \frac{P_p(z)}{G(z)} dz \quad (4.26)$$

where n_{sp} represents the spontaneous emission factor of the amplifiers, g_R the Raman coefficient of the fibre and P_p the Raman pump power.

These noise figures are signal independent, which is the main feature of the NF of a linear amplifier [174]. Once the NF has been defined, an equivalent noise figure can be calculated for a chain of these amplifiers using the Friis formula:

$$NF_{sys} = 1 + \sum_{i=1}^N \frac{NF_i - 1}{\prod_{j=1}^{i-1} G_j} \quad (4.27)$$

In this manner, the computation of the AOSNR at the output of a chain of amplifiers can be obtained from the equivalent NF of the whole system of amplifiers.

When it comes to applying this formalism to the system shown in Fig. 4.12, it is important to define the noise figure of the optical fibre in a consistent manner. In this sense, if SNRs are used, the NF of the fibre must be $NF_{fibre} = L$, where L represents the attenuation of the fibre. This is due to the fact that in this case the shot noise is accounted for, which is equivalent to setting a photodetector at the output of each fibre span. This effect is clearly explained in [88]. On the other hand, if OSNRs are used, the NF of the fibre must be $NF = 1$ because photons belonging both to signal and noise are attenuated *ex aequo*, this leaving the OSNR unchanged after a propagation.

	Gain	NF
EDFA	G	$1 + n_{sp}(1 - 1/G)$
Raman	G	$1 + n_{sp}^R \cdot g_R \int_0^L \frac{P_p(z)}{G(z)} dz$
Fibre	$(\alpha L)^{-1}$	1

Table 4.1: NFs and gains for a chain of EDFA and Raman amplifiers

By applying the values shown in Table 4.1 into equation (4.27) the following expressions for the system noise figure are obtained

$$NF_{sys} = 1 + \sum_{i=1}^N (NF_{EDFA}^i - 1) = 1 + N \cdot n_{sp} \left(1 - \frac{1}{G}\right) \quad (4.28)$$

$$NF_{sys} = 1 + \sum_{i=1}^N (NF_{Raman}^i - 1) = 1 + N \cdot n_{sp}^R \cdot g_R \int_0^L \frac{P_p(z)}{G(z)} dz \quad (4.29)$$

These equations show that *the effect of EDFA and Raman amplifiers in a chain of optical amplifiers is independent of their position within it.*

4.3.2 Additive + Multiplicative Noise

An extension of the previous model accounting for multiplicative noise can be proposed that allows for a more accurate characterisation of Raman amplified systems. Such an extension makes it possible to account for the accumulation of the RIN noise generated by Raman amplifiers, and is therefore of interest.

At the output of an amplifier that generates a mixture of additive and multiplicative noise the power of the noise sources can be expressed as

$$N_{out} = N_0 \cdot G + P_0 \cdot \Delta G + N_A \quad (4.30)$$

where N_0 represents the input noise, P_0 the average signal power at the input, N_A the additive amplitude noise and ΔG the multiplicative noise generated by the Raman amplifier (see equations (3.5) and (3.6)) and where high order noise components have

been neglected. Thus, an extended noise figure (ENF) can be obtained from equation (4.24)

$$ENF = \frac{P_0}{N_0} \left(\frac{P_0}{N_0 \cdot G + P_0 \cdot \Delta G + N_A} \right)^{-1} = 1 + \frac{N_A}{N_0 G} + \frac{\Delta G}{G} \times OSNR_{in} \quad (4.31)$$

This expression has two factors, a signal independent one that represents the linear part [174] and a signal dependent one that represents the nonlinear contribution. In this work, the accumulation of these factors is modelled independently and they are respectively referred to as *linear term*(LT) and *nonlinear term*(NLT). The definition adopted for both terms is shown in the following equations

$$LT = \frac{N_A}{N_0 \cdot G} \quad NLT = \frac{\Delta G}{G} \quad (4.32)$$

Under these definitions, the linear term takes the value $LT = NF - 1$, where NF is the noise figure of a single amplifier. Then an EDFA is characterised by a $LT = NF - 1 = n_{sp}(1 - 1/G)$ and a $NLT = 0$ whereas a Raman amplifier is characterised as an amplifier with $LT = NF - 1 = N \cdot n_{sp}^R \cdot g_R \int_0^L \frac{P_p(z)}{G(z)} dz$ and $NLT = \Delta G/G$. The exact value of ΔG can be obtained from equations (3.5) and (3.6). Therefore, this formalism can model a system like the one shown in Fig. 4.13

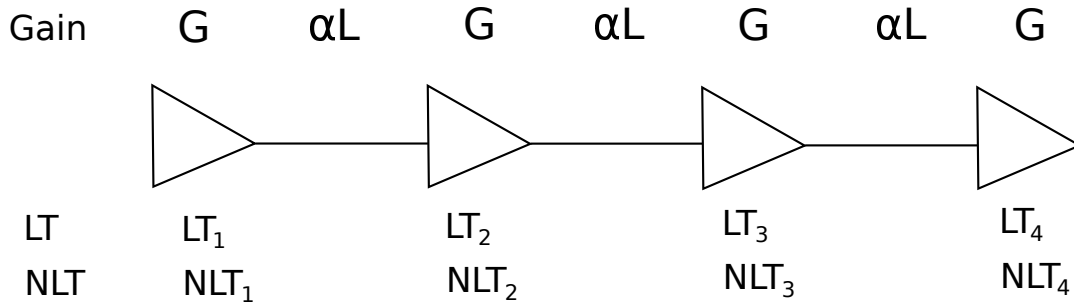


Figure 4.13: System model for a multiplicative chain of EDFA/Raman amplifiers

The presence of the NLT prevents from using the Friis formula for the calculation of the accumulation of noise in such a chain. The derivation of an extension of the Friis formula that accounts for the effect of the nonlinear term can be performed by induction based on equation (4.30). An example of the coefficients for the first stages of amplification are shown in following table

i	N_0	P_0	N_A
0	1	0	0
1	G_1	ΔG_1	N_{A1}
2	$G_1 G_2$	$G_2 \Delta G_1 + G_1 \Delta G_2$	$N_{A2} + G_2 N_{A1}$
3	$G_1 G_2 G_3$	$G_2 G_3 \Delta G_1 + G_1 G_3 \Delta G_2 + G_1 G_2 \Delta G_3$	$N_{A3} + G_3 N_{A2} + G_1 G_2 N_{A1}$

Proceeding recursively in this manner, the total noise power at the output a chain of nonlinear elements results in

$$N_N = N_0 \prod_{i=1}^{N-1} G_i + P_0 \sum_{i=1}^N \Delta G_i \prod_{j \neq i} G_j + \sum_{i=1}^N N_{Ai} \prod_{j=1}^{N-1} G_j \quad (4.33)$$

These terms can be easily paired with those of equations (4.30) and (4.32), resulting in the following expression for the ENF of the whole chain

$$ENF = 1 + \frac{P_0}{N_0} \sum_{i=1}^N NLT_i + \sum_{i=1}^N \frac{LT_i}{\prod_{j=1}^{i-1} G_j} \quad (4.34)$$

This equation shows that, in the most general case, the accumulation of additive amplitude noise is different than that of multiplicative noise. The importance of the additive noise in a chain of nonlinear elements decreases with the distance from the start of the chain, whereas the importance of the multiplicative noise is constant and independent of the position of the element within the chain.

This extension of the Friis formula allows for a characterization similar to that of linear amplifiers. By assuming a optical fibre whose noise figure is shown in Table 4.2, equation 4.34 leads to the extended noise figure that can be applied to hybrid optical fibre systems amplified using EDFAs and/or Raman amplifiers

	Gain	LT	NLT
EDFA	G	$n_{sp}(1 - 1/G)$	0
Raman	G	$n_{sp}^R \cdot g_R \int_0^L \frac{P_p(z)}{G(z)} dz$	$\Delta G/G$
Fibre	$(\alpha L)^{-1}$	0	0

Table 4.2: NFs and gains for a multiplicative chain of EDFA and Raman amplifiers

$$ENF_{sys} = 1 + \frac{P_0}{N_0} \sum_{i=1}^N NLT_i + \sum_{i=1}^N LT_i \quad (4.35)$$

This equation shows that, in optical fibre links, the accumulation of multiplicative noise is similar to that of additive noise, showing to be independent of the position within the chain of amplifiers.

Thus, the ENF allows for the computation of the COSNR at the output of a chain of EDFA/Raman amplifiers. The definition of the system ENF of the whole chain of amplifiers defined in equation (4.35) makes this characterisation possible and serves as a basis for a comparison between the performance of different optical systems.

4.3.3 Phase Noise

The accumulation of phase noise is mainly present in multi-span optical fibre system an/or systems with several parametric amplifiers. The accumulation of phase noise has been studied in the context of accumulation of nonlinear phase noise, XPM and intrachannel effects on optical communication systems [112, 154]. However, to the best of my knowledge, no model has been proposed to analyse it from system point of view.

As was mentioned before, phase noise models a different physical perturbation than amplitude noise. In this sense the accumulation of spectral distortion is considered not to be related to the accumulation of ASE noise. Thus, the model proposed in this work assumes a complete independence between both phenomena and no interaction between phase-related and amplitude-related perturbations is considered. In this manner, NPN and intrachannel and dispersion-induced effects are not accounted for.

Under these assumptions, a phase noise figure (PNF) can be defined to characterize the degradation in the POSNR induced by a communication system as

$$PNF_{opt} = \frac{POSNR_{in}}{POSNR_{out}} \quad (4.36)$$

where $POSNR_{in}$ represents the POSNR at the input of the system and $POSNR_{out}$ represents the POSNR at the output. This model assumes that phase noise, being independent of the signal power, is neither amplified nor attenuated. This assumption leads to a system PNF like

$$PNF_{sys} = 1 + \sum_{i=1}^N (PNF_i - 1) \quad (4.37)$$

This generic definition can be applied, amongst others, to characterise the effects of the accumulation of pump linewidth transfer (PLT) and cross-phase modulation (XPM).

As was described earlier chapter, the POSNR induced at output of an OPA by PLT is , $POSNR = 1/\langle\phi^2\rangle = 1/2k\pi\Delta\nu T$, where $\Delta\nu$ represents the linewidth and T the sampling period of the modulated signal; $k = 2$ for a single-pump OPA and $k = 1$ for a dual-pump OPA. In this sense, after a parametric interaction equation 4.36 becomes

$$PNF_{opt} = \frac{POSNR_{input}}{POSNR_{output}} = \frac{\frac{1}{\pi\Delta\nu_0 T}}{\frac{1}{\pi(\Delta\nu_0 + 2k\Delta\nu_p) T}} = 1 + \frac{2k\Delta\nu_p}{\Delta\nu_0} \quad (4.38)$$

where $\Delta\nu_0$ represents the linewidth of the signal at the input of the amplifier and $\Delta\nu_p$ represents the linewidth of pump lasers used during the parametric interaction.

By normalizing the input linewidth to 1 Hz (in the same manner as the NF of an EDFA is normalized to the same bandwidth [174]), a PNF for linewidth transfer can be defined as

$$PNF_{linewidth} = 1 + 2k\Delta\nu_p \quad (4.39)$$

This model can also be used to compute the phase noise accumulation induced by XPM effects after a propagation through a fibre. Equation 3.24 shows a generic expression for the variance of phase noise generated by XPM in a dispersion managed link. By applying it to the definition and normalising to a 1 Hz bandwidth, the PNF for a passive fibre undergoing XPM is

$$PNF_{XPM} = 1 + 2 \cdot \ln(N/2) \frac{(\gamma P)^2 L_{eff}}{D \cdot \Delta\lambda} \quad (4.40)$$

where N represents the number of wavelengths co-propagating with the original signal, γ the nonlinear coefficient of the fibre, P the average signal power, D the chromatic dispersion of the fibre, $\Delta\lambda$ the spectral width of the modulated signal and L_{eff} the effective length of the span of fibre.

4.3.4 Additive + Multiplicative + Phase Noise

Once the accumulation of multiplicative and phase noise has been modelled in isolation, a complete characterisation that combines all different types can be proposed. The most general case is shown in Fig. 4.14 and models the accumulation of the three noise sources generated by EDFA, Raman, OPAs and the fibre nonlinearity.

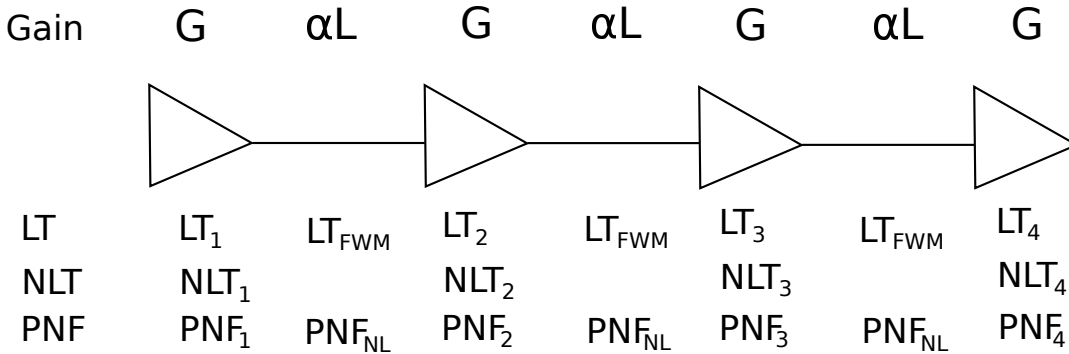


Figure 4.14: System model for a hybrid chain of EDFA, Raman and OPA with nonlinear effects

A system model that accounts for all these degradations require the calculation of both COSNR and POSNR at the output of the chain for a proper assessment of the BER. Based

	Gain	LT	NLT	PNF
OPA	G	LT_{OPA}	NLT_{OPA}	$1 + 2k\Delta\nu$
EDFA	G	$n_{sp}(1 - 1/G)$	0	1
Raman	G	$n_{sp}^R \cdot g_R \int_0^L \frac{P_p(z)}{G(z)} dz$	$\Delta G/G$	1
Fibre	$(\alpha L)^{-1}$	LT_{FWM}	0	$1 + N_{XPM}^\varphi$

Table 4.3: NFs and gains for a chain of EDFA, Raman and OPA with fibre nonlinearities

on the previous definition of the noise accumulation and applying the values of Table 4.3, in the most general cases, the system ENF and PNF result in

$$\begin{aligned}
 ENF_{sys} = 1 + OSNR_{in} & \left(\sum NLT_i^{OPA} + \sum \frac{\Delta G_i}{G} \right) + \\
 & + \sum LT_i^{OPA} + G \sum LT_i^{FWM} + \sum n_{sp}(1 - 1/G) + \sum n_{sp}^R \cdot g_R \int_0^L \frac{P_p(z)}{G(z)} dz
 \end{aligned} \quad (4.41)$$

$$PNF_{sys} = 1 + \sum 2k\Delta\nu_i + \sum N_{XPM}^\varphi \quad (4.42)$$

These equations show that, in an optical fibre link, both additive and multiplicative noise accumulate similarly and their effects are independent of the position that the amplifiers occupy within the chain. The same applies to the phase noise generated by PLT and XPM in the case of dispersion managed links, where the accumulation of phase noise is shown to be linear and independent of the position of the noise source within the chain.

4.3.5 Interactions between Phase Noise and Dispersion

As was shown previously, the accumulation of phase noise can be modelled by means of a phase noise figure. However, the accumulation of phase noise is not the only effect related to the spectral perturbation that signals undergo during their propagation along an optical fibre link. The dispersion of the fibre affects the performance of the signals and its impact is directly related to their spectral width.

This consideration is particularly relevant in OPA-based systems, where the spectrum of the amplified signal is broadened relative to the input. This broadening is given by the convolution between the input signal spectrum and that of the pump wave(s). If the pump wave(s) of an OPA are such that their spectrum is very narrow with respect to that of the signal, then the effects of spectral broadening will be small after a single parametric interaction. However, it is a common practice in fibre-based OPAs to dither the pump wave(s) to overcome the Brillouin threshold, thus broadening the spectrum

of the pump waves considerably. Several experiments have been performed using dithering with pump frequencies that are comparable to that of the signal [175, 176], thus severely distorting its spectrum after amplification.

In addition, several configurations of parametric interactions can be used to generate a conjugated version of the input signals. These are spectrally inverted and broadened copies of the input signals and can be used eg. for chromatic dispersion compensation. However, the effect induced by chromatic dispersion on a modulated signal after propagation depends on the spectral width of the signal itself. Since the conjugated signal obtained after the parametric interaction is spectrally broader than the input, chromatic dispersion affects it more. Several studies have been performed on the optimum placing of ideal optical phase conjugators to optimise the performance of optical communication systems [177, 178] but, to the best of my knowledge, the influence of the spectral broadening has not been considered yet in any of them. In this section an analysis of these effects is presented.

The widely adopted trend that has been followed since the development of polarization division multiplexing is the avoidance of optical chromatic dispersion compensation due to the undesired effects that dispersion compensating fibres induce on them [179, 180]. In this context, the chromatic dispersion is electrically compensated after the signal detection. Nowadays this technique of compensation can compensate distances in the order of ~ 10000 km. This is the scenario considered to model the effects of spectral broadening on modulated signals after the inclusion of OPAs.

This scenario consists of a set of identical amplifiers periodically spaced by a distance L along an uncompensated link with chromatic dispersion D . The spectral width of the signal at the input of the transmission system is noted as $\Delta\lambda_0$ and its value corresponds to a bandwidth of $\sim 1/T$ for NRZ signals and $\sim 1/2T$ for RZ signals. After each parametric interaction the spectrum of the signal is broadened by a fixed amount $r \cdot \Delta\lambda_0$, where r represents the *broadening factor*.

For EDFA and Raman amplifiers r takes a null value whereas for parametric interactions this value varies. Without any pump dithering, r takes the value $r = 2k \cdot \Delta\lambda_p / \Delta\lambda_0$ where $\Delta\lambda_p$ represents the pump linewidth and $k = 2$ for a single-pump OPA and $k = 1$ for a dual pump OPA (see equation (3.16)), whereas for parametric interactions with pump dithering r takes the value $r = 2 \cdot \Delta\lambda_D / \Delta\lambda_0$ where $\Delta\lambda_D$ represents the bandwidth of the dithering wave and $\Delta\lambda_D \gg \Delta\lambda_p$ is assumed. Under this formalism, the spectral width of the signal after N parametric interactions is $\Delta\lambda_0 (1 + N \cdot r)$. Therefore, for example, a value of $r = 2$ would represent a single-pump OPA in which the spectral width of the pump wave is half of that of the input signal, and a value $r = 1$ would represent a single-pump OPA in which the spectral width of the pump wave is a quarter of that of the input signal.

Three cases are considered for this scenario: (a) EDFA amplification which is used as a benchmark for the comparison, (b) non-phase-conjugated OPA and (c) phase-conjugated OPA. For each case the pulse spread and the dispersion maps at the output of the link are calculated.

For the case of EDFA (as well as Raman amplification), the chromatic dispersion accumulates linearly, leading to the following pulse spread after the propagation [181]

$$\Delta t_{out} = \sum_{i=1}^N DL\Delta\lambda = DL\Delta\lambda_0 N \quad (4.43)$$

and the transmission length for a given pulse spread ΔT_{max} can be expressed as

$$L_{EDFA} = L \times N = \frac{\Delta T_{max}}{D\Delta\lambda_0} \quad (4.44)$$

For the case of a non-phase-conjugated OPA, D remains constant but $\Delta\lambda$ increases after each interaction leading to an accumulation of chromatic dispersion that can be described as an arithmetical series, the ratio of which is the broadening factor

$$\Delta t_{out} = \sum_{i=1}^N DL\Delta\lambda_i = \sum_{i=1}^N DL\Delta\lambda_0 (1 + r(i-1)) = DL\Delta\lambda_0 N \left(1 + r \frac{N-1}{2}\right) \quad (4.45)$$

This is a quadratic equation that should be solved to obtain the dependence of the distance with the number of OPAs. However, if the aim is the comparison with the

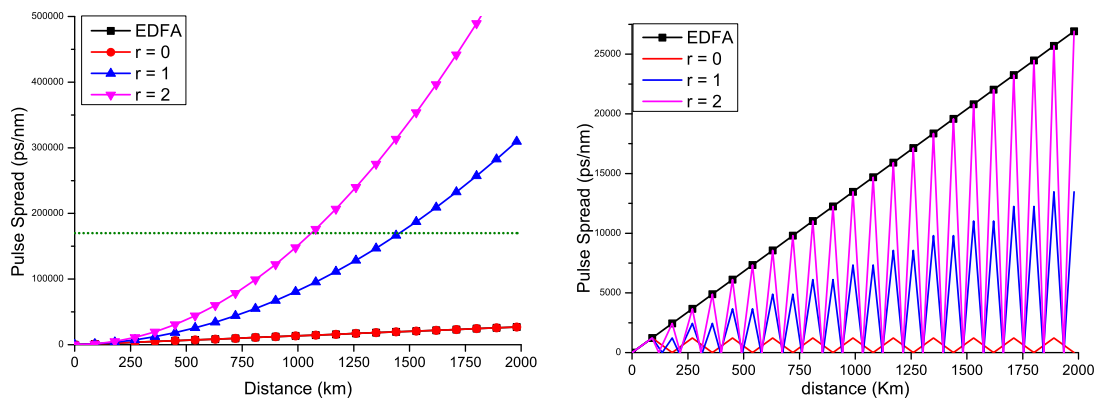


Figure 4.15: Comparison of dispersion maps induced by uncompensated 2000 km optical EDFA-based and single-pump OPA-based systems using equally-spaced by 90 km amplification along the link for non-phase-conjugated systems (left) and phase-conjugated systems(right). Dashed green line represents the limit in chromatic dispersion compensation provided by current coherent receivers

EDFA-based case, the transmission length attainable for a given pulse spread can be expressed as

$$L_{OPA} = \frac{\Delta T_{max}}{D\Delta\lambda_0 (1 + r^{\frac{N-1}{2}})} = \frac{L_{EDFA}}{(1 + r^{\frac{N-1}{2}})} \quad (4.46)$$

As the broadening factor increases, the spectral width of the signal grows faster after each interaction thus inducing an increasing spread rate after each span. This behaviour leads to a growth of the pulse spread as an arithmetic progression with the distance that can limit the performance of the system even if the OSNR at the receiver is within the working limits. The dispersion maps for different values of the broadening factor are shown on the left of Fig 4.15. The dotted line of this picture represents the approximate working limit of the electronic chromatic dispersion compensation (~ 10000 km).

For the case of a phase-conjugated OPA, and in the ideal case where no spectral broadening is taking place, pulse spreads and compressions alternate in consecutive spans leading to perfect chromatic dispersion compensation at the end of an even number of spans (this behaviour is shown in the red line on the right of Fig. 4.15). However, in the presence of spectral broadening each pulse expansion/compression is performed at a faster rate than in the previous span, achieving perfect compensation at a position before the end of the even-numbered spans is reached and inducing an overcompensation (compare the zero-cross points in the same picture for different values of r , each zero-cross represents a perfect compensation). The overcompensation value increases after each parametric interaction. Mathematically, this can be expressed as a chromatic dispersion coefficient D that exhibits an alternating sign and an increasing $\Delta\lambda$, leading to the expression

$$\Delta t_{out} = \sum_{i=1}^N (-1)^{i-1} DL\Delta\lambda_0 (1 + r^{(i-1)}) = \begin{cases} DL\Delta\lambda_0 (1 + r^{\frac{N-1}{2}}) & N \text{ odd} \\ | - DL\Delta\lambda_0 r^{\frac{N}{2}} | & N \text{ even} \end{cases} \quad (4.47)$$

where the absolute of the negative value shows that chromatic dispersion is overcompensated at the end of even-numbered spans due to the increased compression rate induced by the spectral broadening. Under these conditions, the transmission length attainable is limited by the value exhibited at the end of odd-numbered spans. This value is

$$L_{OPA^*} = \frac{N \cdot \Delta T_{max}}{D\Delta\lambda_0 (1 + r^{\frac{N-1}{2}})} = \frac{N}{(1 + r^{\frac{N-1}{2}})} L_{EDFA} \quad (4.48)$$

Fig. 4.15 shows that for very small values of the broadening factor the chromatic dispersion is completely compensated at the end of the even-numbered spans but, as the

broadening factor increases, the overcompensation grows leading, in the extreme case of $r = 2$, to the same spreads at the output of the span as in the EDFA case. An interesting case is that of $r = 1$, in which the overcompensation leads to a effective decrease in the pulse spread with respect to the EDFA case at the output of all spans.

The analysis in this section shows that the use of non-conjugated OPA in communication systems can compromise the performance if dithered waves are used as the pump waves. In order to recover the initial performance, a more powerful digital signal processing (DSP) should be employed, leading to more power hungry and expensive solutions. On the other hand, the use of phase-conjugated OPAs has the potential to decrease the complexity of such a DSP by decreasing the amount of computation required for chromatic dispersion compensation.

4.4 Effects on Channel Capacity

So far, the accumulation of three different types of noise has been analysed, showing that an accurate characterisation of the BER of phase modulated signals requires two magnitudes: COSNR and POSNR. Such a system exhibits features different from those of a chain of EDFAs because the additional types of noise degrade the performance of the system in different ways, thereby reducing the capacity of the transmission channel defined by it. This section presents this degradation in channel capacity.

The lower bound of the capacity of an optical fibre, defined as the minimum capacity achievable in the presence of noise or nonlinear effects, was theoretically modelled by *Mitra and Stark* [43, 154]. This model assumes that an input signal with power P is transmitted along a channel, yielding a signal degraded by additive noise power $\langle n^*n \rangle$ and phase noise with variance $\langle \phi^2 \rangle$.

According to this model, in the most general case, the lower bound of the capacity C_{LB} of such a channel can be expressed as [154]

$$C_{LB} = W \log_2 \left(1 + \frac{P e^{-\langle \phi^2 \rangle}}{\langle n^*n \rangle + P (1 - e^{-\langle \phi^2 \rangle})} \right) \quad (4.49)$$

where W represents the bandwidth of the signal.

This generic model accounts for additive and phase noise and can be extended to include multiplicative noise. As was explained in section 4.2.2, multiplicative noise can be considered as additive noise with a power dependent variance, therefore it can be included within the term $\langle n^*n \rangle$. The variance of the phase noise on the other hand, is directly related to the POSNR through equation (4.5). In this way the generic capacity shown in equation (4.49) can be rewritten as

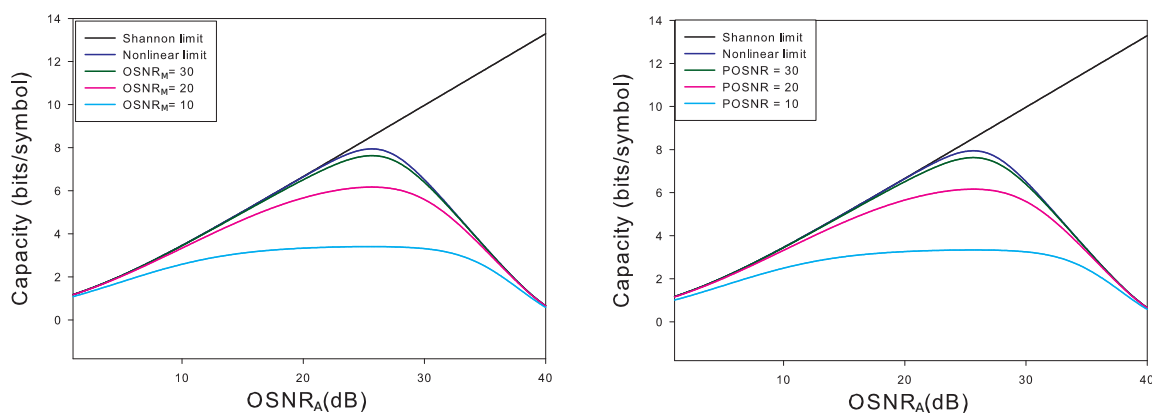


Figure 4.16: Degradation of channel capacity as multiplicative amplitude noise increases (left) and phase noise increases (right)

$$C_{LB} = W \log_2 \left(\frac{1 + COSNR}{1 + COSNR(1 - P \cdot \exp(1/POSNR))} \right) \quad (4.50)$$

where the equations (4.5) and (4.6) have been used. If several uncorrelated phase noise sources are considered, then this expression can be expressed as

$$C_{LB} = W \log_2 \left(\frac{1 + COSNR}{1 + COSNR(1 - P \cdot \exp(\sum 1/POSNR_i))} \right) \quad (4.51)$$

This general expression can be applied to the case of a system that generates phase noise via XPM and OPA interactions. The variance of the phase noise induced by XPM is shown in equation (3.24), although it is also expressed as $(P_0/P)^2$ where P_0 is called the nonlinear threshold of XPM [43]. On its part the variance of the phase noise generated by an OPA is shown in equation (3.16). In this manner an extended model of lower bound of the capacity can be obtained, leading to

$$C_{LB} = W \log_2 \left(\frac{1 + \frac{AOSNR \cdot MOSNR}{AOSNR + MOSNR}}{1 + \frac{AOSNR \cdot MOSNR}{AOSNR + MOSNR} \left(1 - P \cdot \exp \left(- (P/P_0)^2 - 1/POSNR_{OPA} \right) \right)} \right) \quad (4.52)$$

The effects of these two additional types of noise on channel capacity are shown in Fig. 4.16. The graph on the left shows the decrease in channel capacity as the MOSNR decreases while AOSNR and phase noise remain unchanged. The graph on the right shows the corresponding results for a decrease in POSNR induced by an OPA while AOSNR and MOSNR remain unchanged. The trends are similar in the two graphs, but not identical, due to the linear dependence of their noise variances with the signal power.

The expressions obtained in this section show that the decrease in channel capacity induced by multiplicative and phase noise is directly comparable to each other if the definitions of MOSNR and POSNR are used. In addition, these expressions show that, in the presence of OPAs, the limiting factor in the capacity of optical fibres is still the fibre nonlinearity (represented in this case by curve labelled as Nonlinear limit in Fig. 4.16).

4.5 Analysis of Photodetection

The formalism described up to this point allows for a characterisation of optical signals degraded by additive, multiplicative and phase noise. It has been shown that this degradation can be uniquely described by three quantities: the AOSNR, the MOSNR and the POSNR. This section analyses the degradation that these magnitudes undergo during the photodetection process. The aim of this section is to compare the impact of different detection schemes on a modulated signal. The analysis is restricted to BPSK signals, as they are the basis of the photodetection schemes of higher-order modulation formats. Electrical noise sources are assumed to be negligible with respect to beat noise. This limited scope in the study of photodetection prevents from modelling the impact of multiplicative noise during photodetection. Then, in this section only additive and phase noise are considered. Extensions including multilevel modulation formats and multiplicative noise are left as future extensions.

4.5.1 Effects of Phase Noise on Photodetection

Photodiodes detect the intensity rather than the amplitude of an optical field. Therefore differential and coherent detection techniques have been developed to use with phase encoded signals.

Differential detection techniques employ the phase difference between consecutive symbols to detect their value [182]. This detection scheme transforms phase transitions into intensity ones that are directly detectable by the photodiodes. In this context, if a phase-modulated signal is corrupted by phase noise, the quality of the phase-to-intensity transformation deteriorates and so does the performance after photodetection.

Coherent detection, on the other hand, uses an external narrow linewidth laser source to set a phase reference [183]. The inherent phase fluctuation that this laser exhibits is estimated by means of algorithms that perform carrier frequency and phase recovery. However, the performance of these algorithms is degraded in the presence of signal phase noise [184].

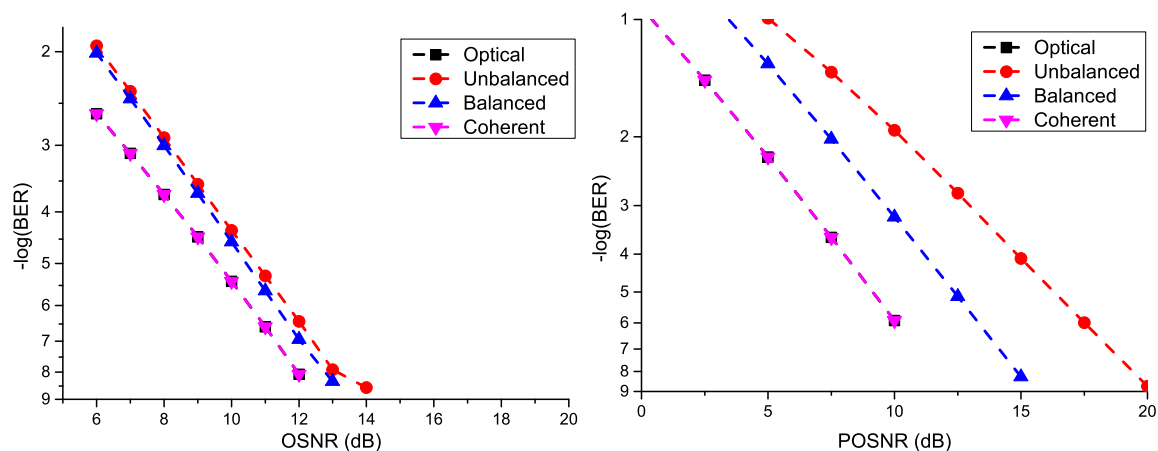


Figure 4.17: Comparison between the degradation in BER induced by each detection scheme with respect to BER of the signal before the photodetection (labelled as optical) for additive noise (left) and phase noise (right)

The effects of residual chromatic dispersion on both differential and coherent detection schemes need to be considered before any comparison between the two schemes can be made. As was already mentioned in Section 3.2.1, chromatic dispersion induces a phase-to-amplitude noise conversion that prevents from an accurate modelling of the degradation induced solely by phase noise to be devised. In the same manner, the linewidth of the local oscillator of a coherent receiver together with electronic chromatic dispersion compensation has been shown to lead to increased phase noise [126, 127, 185]. In order to avert this undesirable effects, the analysis presented in this section makes the following assumptions: (1) signals are fully compensated in terms of chromatic dispersion just before the photodetector, (2) the coherent receiver includes no electronic chromatic dispersion compensation and (3) the linewidth of its local oscillator is negligible.

4.5.2 Efficiency of Phase Noise Detection

The effects of additive and phase noise on optical signals were described in Section 4.2.2. In this section, the effect of photodetection on the noise performance of an optical signal is analysed. This task presents two main problems: first, the calculation of the BERs based on the integration of the PDFs of the signals after photodetection is not accurate enough to provide reliable results³, and second, the difficulty in the modelling of the performance of intradyne coherent receivers prevents from an accurate analytical treatment of these receivers. In sight of these circumstances, the analysis of the photodetection efficiency is performed by simulations rather than analytically.

³This analysis has been included in Appendix C

Monte-Carlo simulations of rectangular pulse shaped BPSK signals with no filtering (either optical or electric) were performed assuming ideal noiseless photodiodes in the presence of additive noise. The variance of noise was modified and the BER was computed for each of the detection schemes considered. The results of these simulations are shown on the left of Fig. 4.17, where the difference in the OSNR degradation induced by the two detection schemes are shown to be under 1 dB. These results match the theoretical predictions previously published [94, 161] and show that an ideal coherent receiver can photodetect BPSK optical signals without any additional penalty.

However, the results obtained from the same set of simulations when the signal is solely degraded by a zero-mean Gaussian white phase noise are very different. Differential schemes are far more sensitive to phase noise because they use the phase information coming from the (corrupted) signal used as the phase reference. This behaviour is shown on the right of Fig. 4.17 where the performance of the detection schemes is displayed as a function of the POSNR. The trend of the BER curves is very similar to that of the optical noise (black line) but each photodetection scheme exhibits a different degradation generated during the detection process. Balanced differential detection is more resilient to phase perturbation than unbalanced one because of the increased distance between symbols in the constellation after photodetection (see appendix C for clarification). On the other hand, ideal coherent detection, using a perfect estimation of the carrier phase, is shown to provide no additional degradation.

Fig. 4.17 right clearly shows that the photodetection of signals degraded by phase noise induces a degradation of the POSNR that is dependent on the detection scheme. In the following, this degradation is referred to as phase detection penalty (PDP). Unlike the ideal case, where ideal coherent receivers exhibit a negligible PDP, in reality the performance of a practical system is expected to perform in the range between an ideal coherent receiver and a balanced differential one. The main reason for this is that the necessary carrier phase estimations are based on past noisy samples; then a perfect phase estimation would represent the best case (the ideal coherent receiver) whereas the use of only one sample to estimate the phase would represent the worst case (the balanced differential receiver). The implementation of these algorithms is one of the most important factors in the determination of the final system performance. A comparison of the efficiency of these algorithms is out of the scope of these work, therefore only an analysis for the most common carrier phase recovery algorithm of BPSK signals is presented in this section [183].

This algorithm uses the phase of N previous symbols, stripped of the phase modulation, to estimate the phase of the carrier [183]. The erasure of the phase modulation is performed by elevating it to the M power, where M is the number of symbols of the constellation ($M = 2$ in the case of BPSK). This algorithm is sensitive to the phase noise and its performance depends on the number of symbols employed during the estimation. Several studies have been performed relating the number of symbols used

during estimation and the BER degradation [127, 184] but, to the best of my knowledge, none of them have accounted for the BER degradation of optical signals simultaneously degraded by additive and phase noise.

The OSNR and POSNR induced by coherent receivers was simulated for two different cases: (1) a zero-mean Gaussian white phase noise that represents the phase noise generated by XPM and (2) a one-dimensional random phase walk that represents the phase noise induced by the laser linewidth. Fig 4.18 shows the OSNR and the POSNR penalty induced by the estimation of the carrier phase depending for these two phase perturbations based on the number of symbols used for the estimation.

The graphs in the left column of Fig. 4.18 show the results for a XPM-type phase noise. This type of perturbation is shown not to induce any PDP if the number of symbols used for the estimation of the phase of the carrier is greater than 10. On the other hand, the graphs in the right column of Fig. 4.18 show the results for a linewidth-type phase perturbation. This perturbation is shown to induce a PDP if an excessive number of symbols (more than 100) is used for the carrier phase estimation. This PDP degrades the

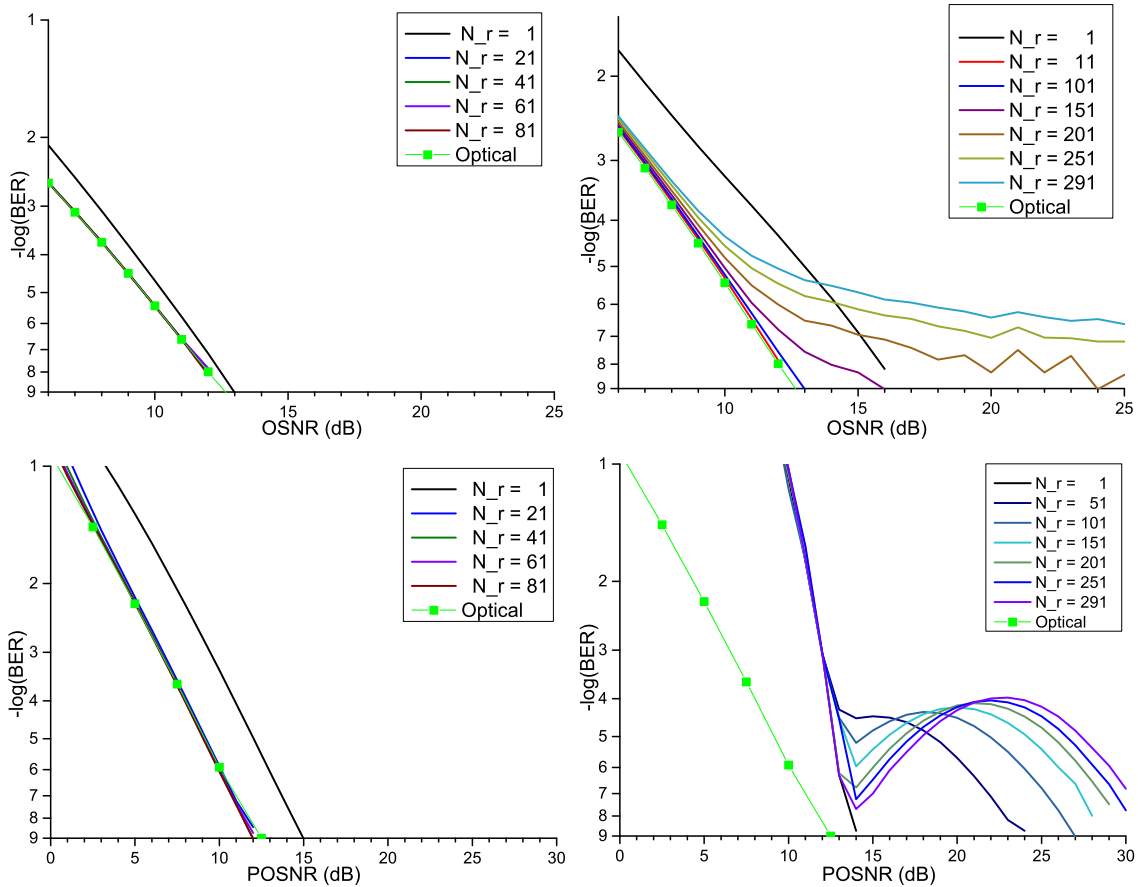


Figure 4.18: BER induced by coherent detection compared to the BER of the signal before photodetection (labelled as optical) in a signal degraded by ASE and XPM (left column) and ASE and laser linewidth (right column) for different number of symbols used for carrier phase recovery (N_r)

POSNR of the optical signal inducing an error floor on the BER of signals only degraded by additive noise (as was already shown in Ref. [184]). On the contrary, if the signal is only degraded by phase noise, the PDP increases with the number of symbols used.

It is to be noted that coherent receivers may use several additional signal recovery algorithms. eg. for carrier frequency recovery, PMD compensation and polarisation tracking [186]. A large variety of carrier frequency recovery algorithms have already been developed [187, 188], inducing different BER degradations in the presence of phase noise. Thus, the performance of coherent receivers is determined by the combined effects of these algorithms. A detailed analysis would entail a comparison between all the possible combinations of these types of algorithms, which is out of the scope of this work. In this way, this analysis is considered only as a future extension of the discussion contained in this section.

4.6 Discussion and Conclusions

Throughout this chapter an extension of the standard noise model of optical communications has been presented. This extended model theoretically addresses several physical phenomena exhibited in optical communication systems not analytically accounted for, making the estimation of their impact possible. However, the long length of this chapter calls for a summary of the results.

The first part of this chapter proposed a single-stage model for the most general amplifier currently available. The analysis of such an amplifier showed that the usual approach of computing multiplicative and phase noise as additional OSNR penalties is not accurate. In particular, multiplicative noise can only be modelled as an OSNR penalty for the case of PSK modulation formats. Applying this approach to high order modulation formats leads to an underestimation of the BER. On its part, phase noise requires the use of a different PDF to account for its impact and its modelling as an OSNR penalty also leads to an underestimation of the BER.

This analysis also showed that the main effect of phase noise in the presence of additive noise is the generation of an error floor, the extent of which is modulation dependent. Conversely, the main effect of multiplicative noise is the increase of the required COSNR in order to achieve the same level of BER as in the case of additive noise alone.

The next part of the chapter dealt with the accumulation of these types of noise in a chain of amplifiers. The analysis showed that, conversely to what could be expected, the accumulation of multiplicative and additive noise follows similar trends and is independent of the position of the amplifiers within the chain. This is due to the characteristic of optical fibres that attenuates both signal and ASE noise simultaneously. In addition, a model that accounts for the accumulation of XPM and PLT has been

proposed, showing that the impact of these noise sources is also independent of the position in the chain of amplifiers. The mathematical framework developed during this analysis allows for a description of a whole optical system using only two magnitudes, the COSNR, that accounts for the additive and multiplicative noise in conjunction, and the POSNR that accounts for the phase noise.

The analysis of the accumulation of phase noise in a dispersive environment addressed a limitation in systems where a chain of non-phase-conjugated OPAs is used within an optical system. In this case, the spectral broadening experienced by the signals due to optical parametric interactions together with the chromatic dispersion of the fibre induce an spreading in the pulse pulse that can require an increased complexity to be built in coherent receivers in order to compensate for it.

Once the accumulation of noise was modelled, the channel capacity of a channel degraded by these three types of noise analysed. It was shown that this capacity decreased due to the two new additional types of noise, but they do not impose tight bounds as in the case of the capacity limitations induced by XPM.

The last part of this chapter proposed an approximate model to account for the degradation induced by photodetection schemes. This analysis showed that photodetection does not induce a significant degradation in the AOSNR of BPSK signals but induces a degradation of the POSNR dependent on the modulation scheme. It was also shown that the PDP induced by coherent receivers heavily depends on the implementation of the algorithms of phase recovery.

In summary, this chapter has theoretically proposed a framework that models the phenomena susceptible to be present in optical communication systems. However, these conclusions must be experimentally confirmed. The corroboration of some of these conclusions is the subject of the following chapter.

Verification of Phase Noise Model

The strongest argument proves nothing so long as the conclusions are not verified by experience

Roger Bacon

The previous chapter developed a comprehensible extension to the noise model currently in use for the characterisation of optical communication systems. This model showed that the current approach of assuming phase noise as an OSNR penalty [162, 189] is not accurate and a novel model for phase noise was proposed. In this chapter, an experimental verification of the degradation induced by phase noise that this model addresses is presented, showing a good agreement with the theory presented previously.

One of the most important conclusions drawn from the previous chapter is the prediction of a degradation of the phase-encoded information, the very value of which is dependent on the detection scheme. This effect, referred to as phase detection penalty (PDP), is experimentally confirmed by comparing the BER obtained with unbalanced differential detection and coherent detection schemes under similar degradations of the optical signal.

Finally, this chapter presents the characterisation of a source of phase noise not modelled yet in optical systems: the pump dithering transfer (PDT). This noise source was mentioned in Chapter 3 but, due to its non-Gaussian character, it was excluded from the modelling performed in Chapter 4. The effects that this noise source induces on a modulated signal are shown to be comparable to that of pump linewidth transfer (PLT) if a proper definition of the POSNR induced by PDT is used.

5.1 Experimental Setup

The characterization of the effect of phase noise in parametric amplifiers was performed using the experimental setup shown in Fig. 5.1. This setup implements a single-pump FOPA based on four-wave mixing (FWM) in a highly nonlinear fibre (HNLF). The setup

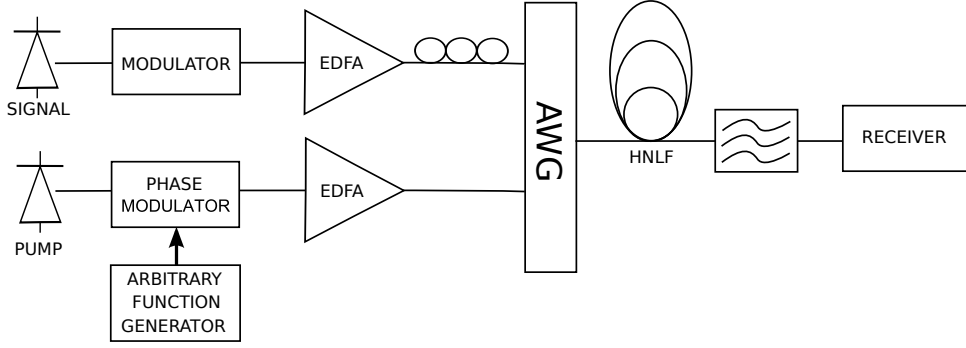


Figure 5.1: Experimental setup comprising erbium doped fibre amplifiers (EDFA), a highly nonlinear fibre (HNLF) and an arrayed waveguide grating (AWG)

comprises two lasers of 25 kHz linewidth, two EDFAs, an arrayed waveguide grating (AWG) used for multiplexing and ASE noise removal, a HNLF, a bandpass filter and an optical receiver. The signal laser was modulated with either a BPSK or a QPSK format at different repetition rates and amplified to obtain a power level of 6 dBm at the input of the HNLF. On its part, the pump laser was modulated using a phase modulator with $V_{\pi} = 5.5V$, which was driven by electrical signals generated using an arbitrary function generator (AFG). The pump was then amplified to obtain 21.5 dBm at the input of the HNLF. The HNLF was a 302m-long germanium-silicate strained dispersion-shifted fibre with a nonlinear coefficient of $11.6 (W \cdot km)^{-1}$, an averaged zero dispersion wavelength after straining of 1555 nm and a dispersion slope of $0.018 ps/(nm^2 \cdot km)$, providing a stimulated Brillouin scattering (SBS) threshold of 27 dBm.

The polarisation of the signal was adjusted using a polarisation controller (PC) to maximize the nonlinear interaction and the generated idler was filtered by a flat top filter and demodulated using different demodulators. The characterization of the phase noise during parametric interaction was performed by adding a phase distortion to the pump wave using waveforms generated by the AFG. The phase distortions that these waveforms induced in the pump wave were transferred to the amplified signals via the nonlinear interaction degrading their quality. In this chapter, two different phase perturbations are considered: PLT and PDT.

The implementation of the PLT was performed by implementing a laser linewidth emulation similar to the one described in Ref [190]. This emulation is implemented by a phase distortion in the form of a one dimensional random walk the variance of which between two consecutive samples is related to the linewidth $\Delta\nu$ of the emulated laser as in equation (3.12). After the parametric interaction, this distortion is transferred to the amplified signal, leading to an increased linewidth the value of which is shown in equation (3.16).

In Ref. [190] the implementation of the linewidth emulation was performed based on a I-Q modulator to avoid the chirp induced if the maximum displacement exceeds 2π . In this

experiment, the algorithm was slightly modified to avoid a maximum phase excursion larger than 2π and a phase modulator was used. The code of this implementation is included in Appendix A. Based on this modified algorithm, several random sequences were generated, emulating different linewidths up to a value of 87 MHz, the maximum that could be implemented with the model of AFG used.

Once the linewidth of the pump wave was chosen, the value of the POSNR after the parametric interaction could be obtained according to the following expression

$$POSNR^{linew} = \frac{1}{\langle \Delta\theta^2 \rangle} = \frac{1}{\pi (4\Delta\nu_p) T} \quad (5.1)$$

where $\Delta\nu_p$ represents the linewidth of the pump wave, T the symbol time. The linewidth of the input signal has been neglected. In this manner, by selecting random sequences with different emulated linewidth as the drive signal of the phase modulator, different POSNRs could be induced on the amplified signal.

Unlike PLT, PDT can be implemented in a simpler way. Since PDT is a deterministic perturbation, the generation of sequences emulating random walks is not required in this case, and the use of sine functions with different carrier frequencies suffices to obtain the desired set of POSNRs. A peak-to-peak amplitude similar to the V_π value of the phase modulator was configured and the value of the frequency f was selected to induce phase perturbations of different POSNR. Using this configuration, a phase change of π in a time of $1/2f$ was ensured, providing a constant phase drift between consecutive symbols of $\Delta\theta = 2\pi fT$, where T represents the symbol time. After the parametric interaction, this phase drift is transferred to the amplified signal according to equation (3.19).

In this case the relation between the dithering frequency and the POSNR is not so straightforward as with PLT and requires an additional explanation. PDT is a deterministic perturbation, the main effect of which on the constellation of amplified signals is not an increase in the variance of the phase noise of each symbol, as in the case of PLT, but the introduction of a phase offset $\Delta\theta$ between consecutive symbols. This distortion is shown in Fig. 5.2, where the inset at the top represents the constellation without pump dithering and the inset at the bottom represents the distorted constellation. This figure shows that even though PDT is a deterministic perturbation, the degradation induced on the probability of error is still stochastic due to the PDF of the additive noise.

This type of perturbation was already approximated by *Gordon* and *Mollenauer* for the case of NPN in Ref. [101]. This publication provides an approximate expression for the variance of a phase noise equivalent to the considered distortion. By repeating the same procedure for this particular situation, the following approximate expression for the POSNR induced by a dithering with frequency f is obtained

$$POSNR^{dither} \approx \frac{1}{3} \frac{AOSNR}{\Delta\theta} = \frac{1}{3} \frac{AOSNR}{2\pi fT} \quad (5.2)$$

where f represents the dithering frequency and T the symbol time. This expression clearly shows that the impact of pump dithering is related to the value of the AOSNR of the signal. In this sense, the dithering distorts the constellation but the probability of error is ultimately determined by the AOSNR of the signal.

After a parametric interaction, the dithering of the amplified signal increases according to equation (3.19), this effect leads to the following expression for the POSNR for a two-pump FOPA,

$$POSNR_{OPA}^{dither} \approx \frac{1}{3} \frac{AOSNR}{2\pi (f_{p1} + f_{p2}) T} \quad (5.3)$$

where f_{p1} and f_{p2} represent the dithering frequency of each pump wave. This can be easily reduced to the case of a single-pump FOPA by assuming $f_{p1} = f_{p2}$.

Thus, both the increase in the linewidth or dithering of parametrically amplified signals is bound to a decrease in their POSNR that, in turn, degrades their BER. In the following sections this degradation is experimentally characterised.

5.2 Preliminary Characterisations

So far, the POSNR induced by two phase noise sources after a parametric interaction has been proposed. The BER induced by PLT was already modelled in the previous chapter, however the BER induced by PDT is determined by the AOSNR and has not been modelled yet either theoretically or by simulation. In order to provide a basis for comparison between the degradation induced by each of these noise sources, Monte-Carlo simulations were performed assuming unbalanced and balanced differential detection schemes. Fig. 5.3 shows a comparison of the BER degradation induced by XPM, PDT and PLT with respect to the BER of the optical signal before the detection. In these simulations XPM was modelled as a zero-mean Gaussian phase noise, PLT as

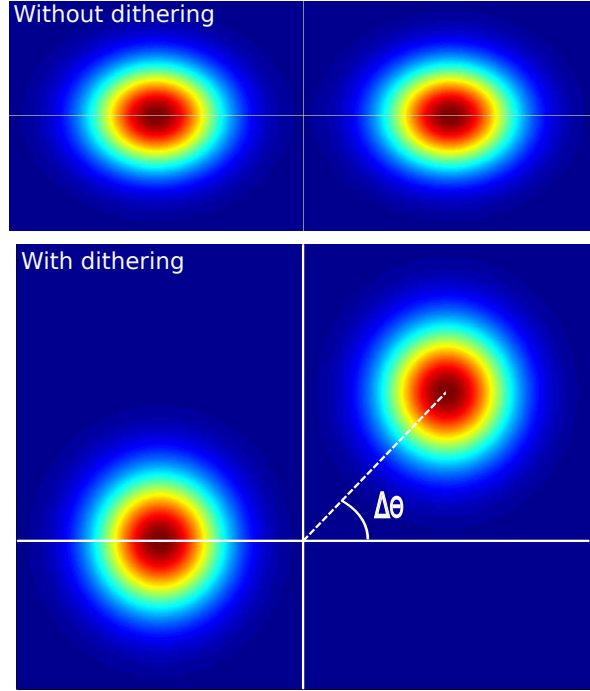


Figure 5.2: Constellation distortion induced by pump dithering

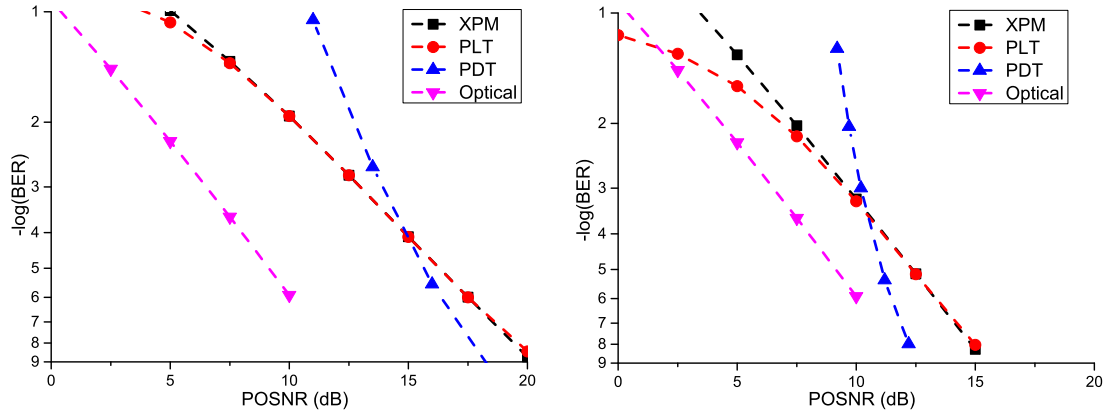


Figure 5.3: Comparison of the impact of XPM, PLT and PDT using unbalanced differential detection (left) and balanced differential detection (right)

a one-dimensional random walk and PDT as a deterministic phase perturbation of a signal with 25 dB of AOSNR. The theoretical model developed in the previous chapter accounts for a phase perturbation like that of XPM. PLT is shown to induce a similar perturbation although in environments of low POSNR the performance differs. On its part, PDT, due to its non-Gaussian nature, exhibits a higher slope than the two previous ones.

However, a comparison in terms of frequencies is more natural and direct. If similar values of POSNR are compared, then the resiliency of the signals to PDT and PLT can be easily estimated. Equations (5.1) and (5.3) can be used for this purpose. This procedure yields the following approximate relation

$$\Delta\nu \equiv \frac{3f}{AOSNR} \quad (5.4)$$

where $\Delta\nu$ represents the linewidth of the PLT and f represents the pump dithering. This expression shows that in an environment with high AOSNR, the value of the dithering frequency required to induce a degradation similar to that of PLT is several orders of magnitude higher than the pump linewidth. Thus, signals are more resilient to PDT than to PLT.

The experimental measurements designed to confirm the findings of these simulations need to be carefully considered to avoid an interference coming from spurious or undesired effects. High speed optical receivers are complex devices comprising several subsystems, the performance of which can be degraded in the presence of phase noise, thus leading to distortions in the measurements. In particular, several designs of clock recovery units have been shown to be sensitive to phase noise [191, 192]. The measurements taken with and without a clock recovery unit showed that, for the case of differential detection, a negligible difference in performance was obtained.

A characterisation in similar terms of coherent receivers was not possible. Practical implementations of coherent receivers use several algorithms for polarization tracking[193, 194], carrier frequency recovery[187, 188], clock recovery[191, 192] and carrier phase recovery[183], that prevent from a characterisation of the clock recovery unit in isolation. Furthermore, an analytical treatment of the cross-effects of all these algorithms is not possible, thereby restricting the analysis of the results to a mere computation of the PDP induced by this type of receivers.

As a consequence of the sensitivity to phase noise that the mentioned algorithms exhibit, the measurements will show that the performance of coherent receivers is far from the negligible PDP that is predicted for an ideal coherent receivers.

5.3 Phase Noise in Differential Detection Schemes

The measurements of the dependence of the BER on the frequency of the pump dithering were performed using the experimental setup shown in Fig. 5.1. A modulated signal was launched into the HNLF and wavelength converted using a phase-distorted pump wave. Then, the performance of the generated idler was assessed while its OSNR was kept at a constant level of 25 dB. The pump wave was modulated with sine functions of different frequencies to reduce the POSNR of the generated idler and measure the degraded BER that was induced.

These measurements are displayed in Fig. 5.4 left and clearly show the increase of the BER with the frequency of the pump dithering. If these measurements are displayed in function of the POSNR (using equation 5.3), as Fig. 5.4 right shows, then the slope of the measurements accurately follows the trend predicted by the simulations although an

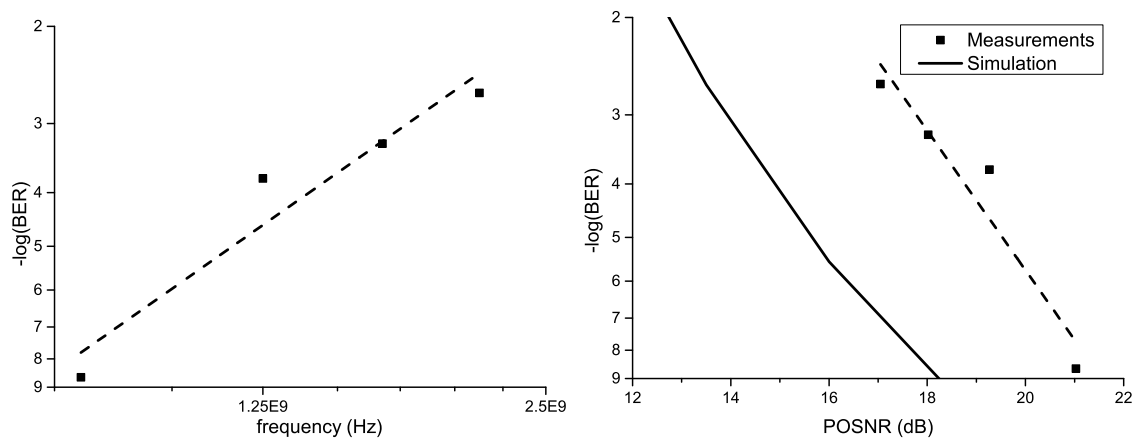


Figure 5.4: Characterization of BER vs.frequency generated by pump dithering transfer (PDT) in BPSK signals detected by an unbalanced differential receiver (left). Same results and comparison with simulation if equation 5.2 is used to compute the POSNR(right)

offset of 3 dB is exhibited. The cause of this difference requires further analysis and has not been addressed yet at the time of writing this document.

After the characterisation of the performance of the differential receiver in the presence of phase noise only was performed, a characterisation in environments where signals are simultaneously degraded by PDT and ASE noise was performed.

The effect of phase noise together with ASE noise after unbalanced differential detection was measured by allowing a variation of the AOSNR at the input of the differential receiver. In this case, several BER curves were taken for different dithering frequencies and received powers. The results of these measurements are shown in Fig 5.5. These measurements show no measurable error floor in the absence of pump dithering and an error floor that grows with the frequency of the pump dithering. The legend provides the dithering frequencies, configured at the AFG, necessary to induce the corresponding error floors in a NRZ 40 Gbps BPSK signal. This behaviour was already predicted theoretically in section 4.2.2 (see Fig. 4.9).

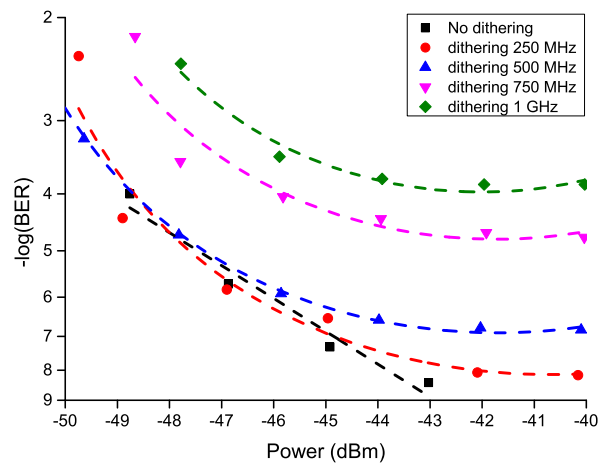


Figure 5.5: BER curves for different values of pump dithering for unbalanced differential detection for a 40 Gbps BPSK signal (right).

5.4 Phase Noise in Coherent Detection Schemes

Once the characterization of the differential receiver was performed, similar measurements were taken using a coherent receiver. The exact details of the algorithms that the commercial receiver internally implements were unknown, thereby the coherent receiver was considered as a black box. Unlike the differential receiver, a comparison between the effects of PLT with respect to PDT could be performed now.

As before, the sensitivity in the presence of phase noise only was measured whilst the OSNR was kept constant and either the frequency of the dithering or the emulated linewidth was changed. As it has already been mentioned, both frequencies are not directly comparable, as Fig. 5.6 left clearly shows. In this manner, the only fair comparison between the impact of the two types of perturbation on modulated signals is achieved in terms of their POSNR. This comparison is shown in Fig. 5.6 right, where the results of a NRZ 40 Gbps BPSK signal degraded by PLT and PDT and detected by a coherent receiver are presented. A comparison between Fig. 5.6 left and Fig. 5.4

left clearly indicate that coherent receivers are affected more severely from phase noise than differential receivers. The exact value depends on the particular algorithms that the coherent receiver internally implements, therefore each particular combination of algorithms must be characterised to obtain the phase detection penalty bound to it.

The flexibility in the reconfiguration of the commercial coherent receivers allowed for a characterisation of different bit rates and modulation formats. Equations 5.1 and 5.2 show that the symbol rate of the signal (represented in these expressions as $1/T$) is an important parameter in the assessment of the impact of phase noise. Thus, the BER depends not only on the frequency of the phase distortion but also on the symbol rate of the modulated signal. This dependence entails that a signal with a higher repetition rate would require a higher dithering or linewidth frequency to induce the same degradation as a lower repetition rate signal would. However, the performance in terms of POSNR remains unchanged with respect to the repetition rate, thereby inducing similar BERs.

A comparison of the BER induced on BPSK signals at different repetition rates in terms of the POSNR was studied. BER curves of 10 and 20 Gbps BPSK signals distorted by PLT and PDT were taken and the comparison of the performance in terms of the POSNR of the signals was assessed. This comparison is shown in Fig. 5.7 left, verifying that the performance in terms of POSNR is only dependent on the products $\Delta\nu \cdot T$ and $\Delta f \cdot T$. This allows to use the POSNR to estimate de BER of the signals independently of their bit rates.

Finally, a comparison between the influence of phase noise in BPSK and QPSK signals was performed using PDT as the noise source. The results of this comparison are displayed in Fig. 5.7 right, showing similar trends but an additional penalty of 3 dB with respect to the POSNR for the case of the higher density constellation. This result matches

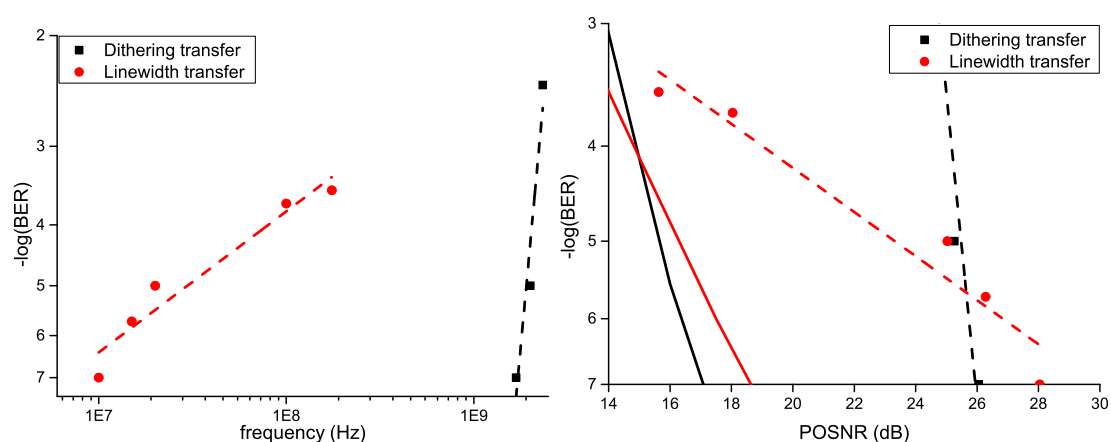


Figure 5.6: Characterization of BER vs. frequency generated by PDT and PLT in BPSK signals detected by a coherent receiver (left). Same results if equations 5.3 and 5.1 are used to compute the POSNR (right). Solid lines represent the BER of the signal after differential detection, showing the larger degradation induced by the coherent receiver

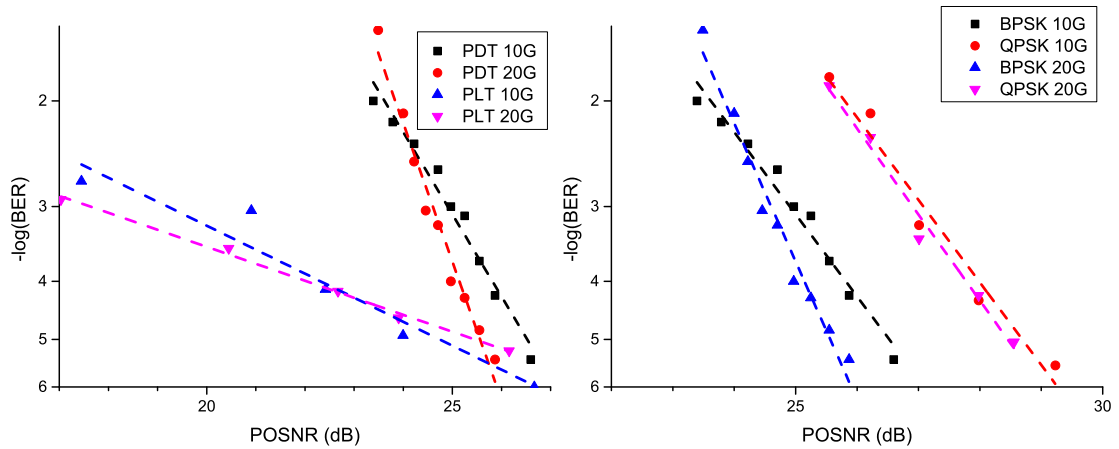


Figure 5.7: Characterization of BER vs. POSNR generated by pump dithering transfer (PDT) and pump linewidth transfer (PLT) in BPSK signals at different repetition rates (left). Comparison of BER vs. POSNR generated by PDT in BPSK and QPSK signals at different repetition rates (right)

the predictions of the theoretical model and of the simulations of a higher sensitivity to phase noise of high order constellation densities shown in Section 4.2.1.3 (see Fig. 4.5).

5.5 Conclusions

This chapter has presented an experimental verification of the effects that PLT and PDT induce on phase modulated signals. This verification has confirmed that a representation of the BER in terms of POSNR provides a framework for a proper comparison of the influence of different phase noise sources under the theoretical formalism presented in Chapter 4.

In addition, this chapter has presented a procedure for the characterisation of the PDP induced during photodetection, showing that even though coherent receivers have the potential to recover optical signals without any POSNR degradation, the use of phase and frequency recovery algorithms as well as polarisation tracking, PMD and chromatic compensation algorithms prevents from such a performance to be obtained and results in a larger POSNR degradation than that of differential receivers.

Finally, this chapter has shown that the previously presented formalism for the characterisation of phase noise is independent of both the symbol rate and the modulation format, showing the suitability of this approach in the modelling of optical communication systems.

Wavelength Conversion Experiments

To attain complete truth is not given to mortals, but to advance towards it by successive steps is not impossible

Bertrand Russel

The last two chapters have been devoted to a theoretical analysis of the impact of parametric processes on communication systems. This analysis has shown that, in addition to the ASE noise generated during parametric amplification, phase noise must be taken into account. The noise model presented in Chapter 4 describes the requirements that the components of OPAs must meet for a successful operation in real communication systems in terms of noise.

The present chapter explains how these requirements can be implemented and demonstrates the feasibility of operation of OPAs in optical communication networks with the required levels of reliability. This task is performed by implementing one of the most useful subsystem devices in optical communication systems: an all-optical wavelength converter (AOWC) [7].

The importance of the implementation of AOWCs lies in the avoidance of optical-to-electronic-to-optical conversion in reconfigurable optical add-drop multiplexers (ROADMs) and in the need to ensure a more efficient use of the spectrum in fibre networks [195, 196]. However, despite its importance, most work reported in the literature to date has focused on optimizing certain features of WCs [197–201] at the expense of others, rather than taking a holistic approach and ensuring that all features required of a practical network device are considered and incorporated.

During the last few years several optical fibre wavelength conversion schemes have been proposed based on a variety of physical processes. Some of these schemes achieve large conversion gains based on single-pump FOPA [198, 199] at the expense of narrow bandwidths of operation and polarisation sensitivity. Such implementations are quite simple and are based on the availability of low dispersion highly nonlinear fibres (HNLFs). However, this approach requires the use of a polarisation tracker and therefore is restricted to single channel wavelength conversion.

A different approach proposed the use of a dual-pump FOPA to achieve polarisation insensitivity by means of orthogonally-polarised pump waves. This technique can be implemented either with a polarisation diversity configuration, in which two single pump interactions in orthogonal polarisations are performed simultaneously, or with a configuration in which both pumps (also orthogonally polarised) interact and provide polarisation insensitive wavelength conversion. The implementation of the former technique in optical fibres requires polarisation maintaining fibres that induce undesirable differential group delay (DGD) of the converted signals between the two modes propagating in orthogonal polarisations, therefore it will not be considered in the rest of this work.

Orthogonally-polarised dual-pump FOPA in low-birefringence fibres, where the pump waves are placed at very close wavelengths have already been demonstrated for the implementation of polarisation insensitive AOWC [200, 201]. This approach still provides a high conversion gain and low BER degradation although the wavelength allocation of the converted signals does not allow compatibility with the standard ITU grid and makes the filtering of the pump waves difficult.

An alternative approach opted for a dual-pump FOPA with pump waves which were widely spaced in wavelength [197]. This setup provided a broad operational bandwidth, free of high-order mixing components at the expense of low gains. The low conversion gain exhibited by this scheme requires pump powers typically above the Brillouin threshold of the nonlinear fibre used, and therefore necessitates techniques to be employed to overcome this.

Thus, the development of an AOWC capable of operation in real systems requires to consider more aspects than the mere degradation induced by it. Developing a scheme capable of black-box operation in a real communication network involves establishing a trade-off between all the aforementioned features: broad bandwidth, high gain, insensitivity to both polarization and modulation format and ease of filtering. For a WC to be deployed in real systems, it is important that it satisfies all these requirements simultaneously. Furthermore, all-optical wavelength conversion schemes should be able to support multichannel operation in order to be economically viable and to improve their practicality.

In this chapter, two AOWC schemes based on four-wave mixing (FWM) in a highly nonlinear fibre (HNLF), pumped by two orthogonally polarized, widely frequency-spaced beams are presented. A basic AOWC implementing a one-direction WC is firstly presented and subsequently its extension implementing a two-direction WC is described and demonstrated. In addition, the long term stability of the WC, the major impairment for their implementation in real networks, is achieved through the development of a feedback system, which corrected for slow drifts of the relative states of polarization of

the two pumps and ensured that they remained orthogonally polarized over extended (effectively unlimited) periods of time.

The rest of this chapter is devoted to the back-to-back characterisation of the two schemes proposed, whereas the performance test of these WCs working in the most important types of optical transmission networks (point-to-point, switched and spatial division multiplexed) is presented in Chapter 8.

6.1 Basic Wavelength Converter Scheme

The task of developing a conversion scheme that meets all the requirements mentioned whilst being compatible with standard ITU frequency grids rules out some of the previously mentioned schemes. In this manner, single-pump FOPAs were discarded due to their polarisation sensitivity. Among the dual-pump FOPAs, the approach based on closely frequency-spaced pump waves was also discarded due to problems of compatibility with the standard frequency grid. In this manner, the scheme with the potential to meet all the requirements simultaneously is the one based on a dual-pump FOPA with widely-space pump waves. However, in order to achieve a good performance and exhibit all the aforementioned features simultaneously, several modifications were performed.

Fig. 6.1 shows the schematic of the WC. It incorporates two arrayed waveguide gratings (AWGs) to combine the incoming data signals to be converted with two orthogonally polarized pump beams (with linewidths of about 100 kHz each) at the input of the HNLF, and an output filter to allow simultaneous re-transmission of only the generated idlers. The scheme presents the following key characteristics:

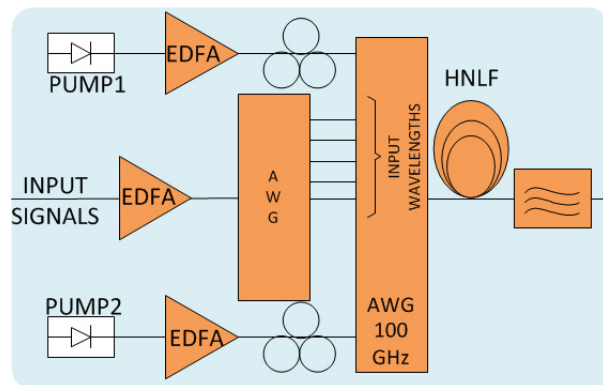


Figure 6.1: Wavelength converter set-up

- polarization- insensitive operation with respect to the input signals, ensured by the two orthogonally aligned pumps.
- easy filtering of the converted signals, allowed by the wavelength allocation of the two pumps, which ensures that any polarization-sensitive mixing components are separated with high extinction from the polarization-insensitive idlers.

- high and flat conversion gain across the whole conversion band, guaranteed by the use of a dual-pump FWM process in conjunction with a state-of-the-art HNLF.
- grid-aligned, black-box operation, allowed by the combination of an erbium-doped fibre amplifier (EDFA) at the WC input, followed by an AWG.
- multi-channel operation as the system is resilient to high-order (HO) mixing components.

Furthermore, the undesired HO mixing components that are not at the converted signal wavelengths can be easily filtered out at the output of the system, so that new signals can be added within the WC output bandwidth (at different wavelengths as compared to the converted ones) without extra penalty. Indeed, the WC output can be fed to a wavelength-selective switch (WSS) for filtering and combined with other channels, as will be described in the following sections and in chapter 8, which is the standard procedure used in ROADMs architectures.

At the WC input, the various signals were amplified up to a total power of 12 dBm and filtered by the AWGs in order to remove amplified spontaneous emission (ASE). The initial removal of ASE within the bandwidth of the converted signals is critical, since without this the conversion power penalty is increased by 5-6 dB. The channelized filtering characteristics of the AWG allow a single amplifier to be used even for operation with multiple channels. The second AWG also facilitates filtering of the ASE of the pumps, which were amplified so

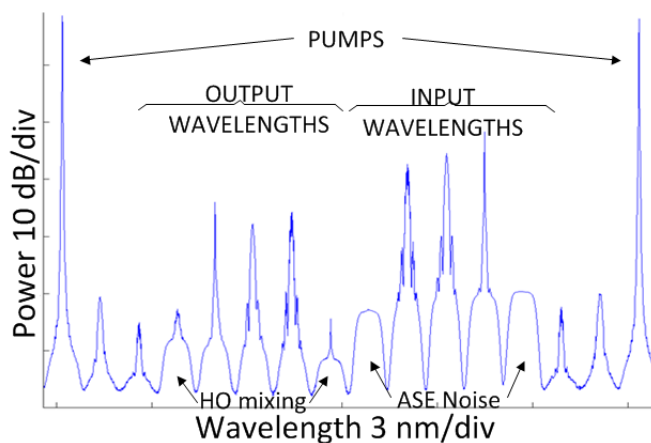


Figure 6.2: An example of a multi-channel non-linear interaction, as observed at the output of the HNLF

that the power of each of them was 21.5 dBm at the HNLF input. It is to be noted that while the use of the first AWG is not needed for single channel operation, it is essential for multi-channel operation. Therefore, it has been included in the various measurements presented in this chapter, to emphasize the flexibility of the scheme.

The 302m-long HNLF used was a germanium-silicate dispersion-shifted strained fibre with a nonlinear coefficient of $11.6 \text{ (W}\cdot\text{km)}^{-1}$, a dispersion slope of $0.018 \text{ ps}/(\text{nm}^2\cdot\text{km})$ and an average zero-dispersion wavelength (after straining) of 1555 nm. The strain gradient was applied along the HNLF to broaden the Brillouin gain bandwidth and reduce its peak gain, thereby increasing its stimulated Brillouin scattering (SBS) threshold to 27 dBm [202]. Finally, the (flat-top) coarse output filter was tuned to cover the entire output bandwidth.

Significant performance degradation due to FWM-induced pump depletion in the HNLF was avoided by keeping the EDFA used for the amplification of the input signals in automatic power control (APC) mode. In this mode, the overall output power of the EDFA remained constant, so that a pump-to-signal(s) ratio of at least 15 dB was maintained at the input of the HNLF.

An example of a typical nonlinear interaction for a mixed signal scenario (one OOK, one BPSK and one QPSK signal) is shown in Fig. 6.2, where the optical spectrum at the output of the HNLF is plotted. Due to the equal spacing between the input signals some of the higher order (HO) mixing components were generated at the same frequencies as the output signals. Nevertheless, if all the input channels have similar input powers, the level of cross-talk from these components can be kept below 20 dB, causing negligible signal degradation in multi-channel operation.

The bandwidth of the WC was ultimately determined by the bandwidth of the AWGs. This band of wavelengths where the converted signals could be allocated, was about half the spacing between the two pumps and could easily be tuned by reconfiguring the connections of the AWG input ports for the pump beams. For this characterization, the two pumps were set at 1562.23 nm (191.90 THz) and 1550.12 nm (193.30 THz), and the input channels were tuned between 1559.79 nm (192.2 THz) and 1556.55 nm (192.60 THz). A 1-nm guard band was used around the pump wavelengths to facilitate filtering of the idlers.

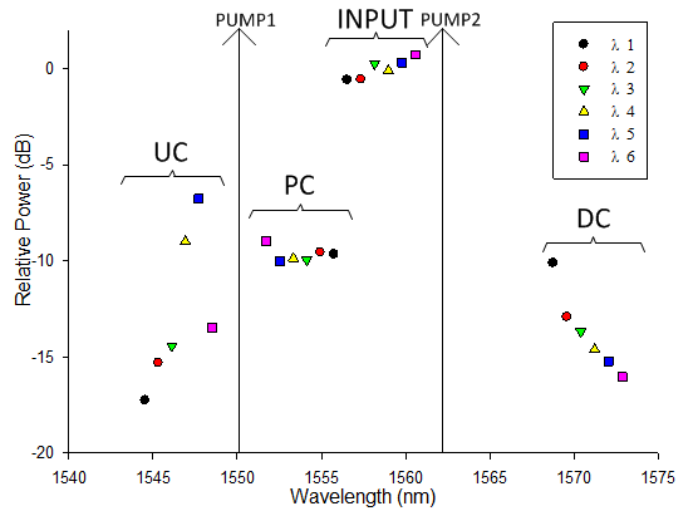


Figure 6.3: Characterization of the conversion efficiencies at the output of the HNLF for the three different types of idlers as a function of the wavelength of the signals

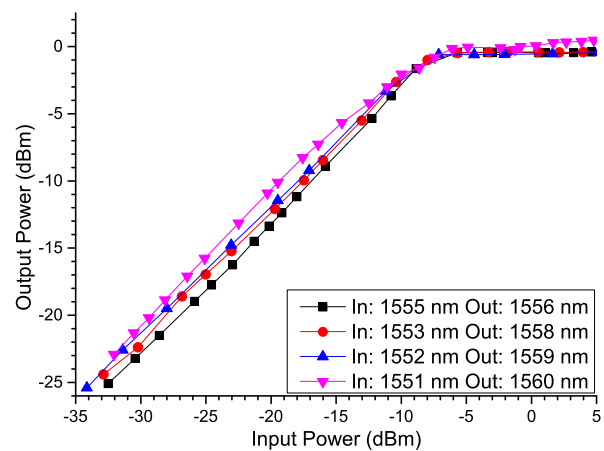


Figure 6.4: Wavelength converted signal output power as a function of the signal input power at the EDFA input for various input signal wavelengths. Only one signal is considered at a time

In general, a dual-pump parametric interaction can generate three distinct first-order FWM processes referred to as: phase conjugation (PC), Up-Conversion (UC) and Down-Conversion (DC) [62]. Figure 6.3 reports the characterization of these FWM interactions in the HNLF in terms of relative power of the wavelength converted signals as a function of the signal wavelength. The normalized signal power at the input of the HNLF is also shown for completeness. The figure shows a flat conversion gain (1 dB gain fluctuation) for the PC process. In contrast, the gain of the UC and DC processes depend strongly on the signal wavelength and exhibit a variation of more than 6 dB within the conversion band studied, due to the fact that phase matching plays a critical role in these interactions. On the other hand, the frequencies of the PC idlers are complex conjugated with respect to the input, whereas the UC and DC processes do not conjugate the input. Phase conjugation of the idlers does not constrain reception of any single-channel modulation format, although it does prevent transparent wavelength conversion of multicarrier modulation formats (since the subcarrier allocation is inverted during the parametric interaction), being chosen as output signals due to their constant conversion gain across the signal bandwidth rendering them suitable for multi-channel operation.

The wavelength converted output power of the whole black-box WC system (which includes the EDFA, two AWGs, the HNLF and the output filter) was subsequently characterised for the PC idlers as a function of the input signal power. This measurement was repeated for several input signal wavelengths (Fig. 6.4, note that for this experiment the wavelength allocation differed from Fig. 6.3). Since the EDFA operated in APC mode and as long as the operation was performed in the small signal regime, the signal power at the input of the HNLF changed in step with the power at the input of the WC system. Then two different regimes

could be identified in the operation of the WC, which in turn were mainly dependent on the EDFA operation: (i) a linear output power regime (constant gain regime), corresponding to input signal powers for which the EDFA operated in a linear fashion and (ii) a constant output power regime, corresponding to input signal powers for which the EDFA operated in gain saturation. In the first operating regime, the power of the wavelength converted signals varied as a function of the input signal wavelength by 2 dB, mainly due to the non-uniform gain of the EDFA across these wavelengths. The

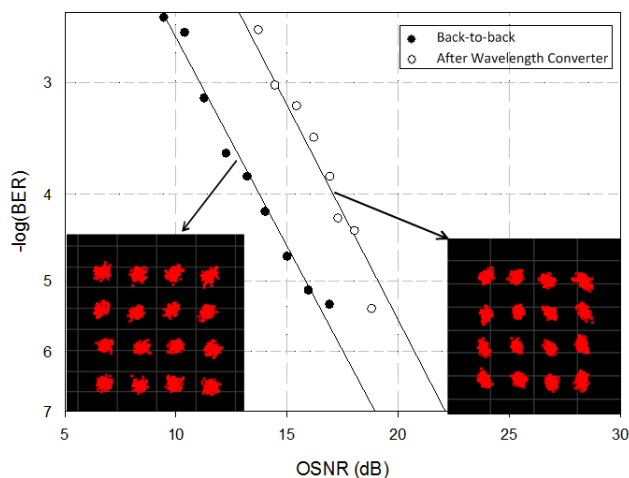


Figure 6.5: BER curves and constellation diagrams for the original (full circles) and wavelength converted (empty circles) 10 Gbd 16-QAM signal

small power variations (less than 0.5 dB) observed in the second operating regime, were due to non-uniformities in the insertion loss of the various ports of the AWGs, which were later shown to have a negligible effect on the system performance. It is worth emphasizing again that the pump-to-signal ratio was at least 15dB for all the various input signal powers, so that significant performance degradation due to FWM-induced pump depletion in the HNLF was avoided. In all the subsequent experiments the input power of the various signals was configured so that the WC operated in the constant output power regime and yielded a conversion gain of +1 dB.

As shown in Fig. 6.1, the polarisation alignment of the two pump waves was performed manually by adjusting their corresponding polarisation controllers (PCs), monitoring and minimising their mutual nonlinear interaction using an optical spectrum analyser. The polarization sensitivity achieved by this method was characterized with a slowly varying polarization scrambler (polarization modulation frequency of about 1kHz) connected at the input of the WC and the response to a continuous wave (CW) signal was monitored on a digital scope. Measurements were carried out over hundreds of seconds and showed a peak-to-peak PDL of 0.64 dB.

Finally, the conversion penalty of the WC for different signal modulation formats (OOK, BPSK, QPSK and 16-QAM), repetition rates (10 to 40 Gbd), polarisation multiplexing schemes and various wavelengths was measured. The WC showed similar performance in the cases of OOK, BPSK and QPSK with a power penalty at the receiver below 2.0 dB (at a bit error ratio (BER) of 10^{-5}) and a power penalty of 2.5 dB for the case of 16-QAM modulation formats. An example of the BER curves as a function of the optical signal-to-noise-ratio (OSNR) obtained for the original (back-to-back) and wavelength converted 10 Gbd 16-QAM signal at 1557.36 nm is displayed in Fig. 6.5, together with the corresponding constellation diagrams.

6.1.1 Performance Limiting Factors

Once the initial scheme proved to meet all the aforementioned requirements simultaneously and showed potential for practical applications, an analysis of the sources of degradation induced by the WC was performed with the aim of finding the best operating point possible. The WC was used in network experiments (Chapter 8) and this task was performed to understand how an optimised performance could be achieved. This analysis was based on the minimisation of the BER degradation while keeping the rest of the features of the WC (polarisation sensitivity, conversion gain, etc) as close to the original performance as possible.

As was mentioned in Chapter 3, the most important source of amplitude noise in OPAs is the ASE pump noise generated during the amplification of the pump wave(s) and the main sources of phase noise after a parametric interaction are mainly four: pump

linewidth transfer (PLT), pump dithering transfer (PDT), cross-phase modulation (XPM) and nonlinear phase noise (NPN). In this particular case, the use of any pump dithering technique was avoided through the use of an HNLF with a high SBS threshold.

In this manner, the most straightforward performance benefit could originate from a replacement of the 100 GHz AWG for a 50 GHz one, provided that the attenuation of the two AWGs is similar. This replacement would allow the transfer of a smaller amount of out-of-band noise by reducing the total ASE noise of the pumps at the input of the HNLF. This modification would reduce the OSNR penalty induced by additive noise but not by phase noise.

The effects of phase noise are manifested by the additional BER degradation induced during the conversion of the 16-QAM signals. This additional penalty is modulation-dependent, and is not present in either BPSK or QPSK signal. Chapters 4 and 5 showed that the type of noise that induces this degradation is phase noise. Thus an analysis of the phase noise generated by this wavelength conversion scheme could allow an insight on possible routes for the optimisation of the system.

Regarding the PLT, after the dual-pump parametric interaction, the linewidth of the amplified signal at the output increases by a value of about 200 kHz (see equation (3.16)), that corresponds to the sum of the linewidths of the pump waves. For the measured case of 10 Gbd signals this output linewidth induces a POSNR of 42 dB (see equation (4.5)). Taking into account the conclusions of the previous chapters, that show that the POSNR should be higher than 25 dB in order not to observe a BER degradation on a 16-QAM signal (see section 4.2.1.3), this result ensures that there was no measurable degradation coming from PLT regardless of the detection scheme used.

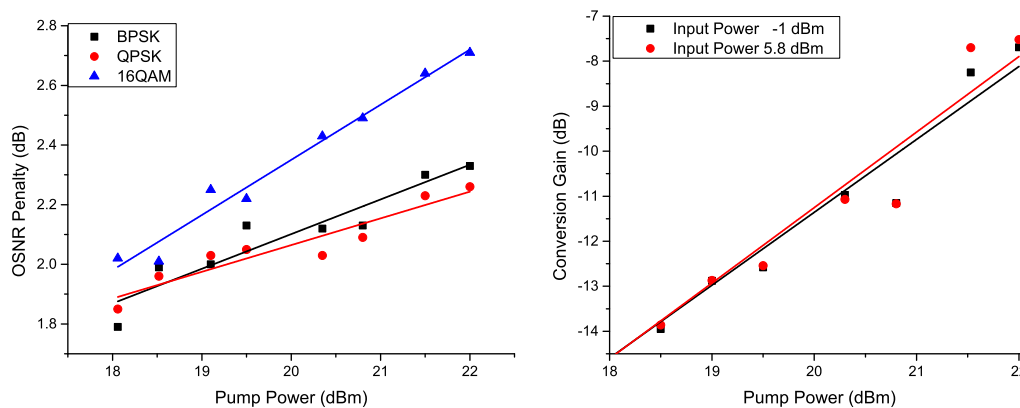


Figure 6.6: OSNR penalty as a function of the power per pump wave (left) and conversion gain as a function of the power per pump wave (right)

Thus, the additional degradation exhibited for 16-QAM conversions arises from XPM and NPN that are complex to model analytically in the case of parametric amplification. However, since XPM and NPN are dependent both on the signal power and the

pump power, their impact can be experimentally characterised by measuring the BER degradation induced at different pump powers.

In this sense, BER curves were taken at the input and the output of the WC for different pump powers and the OSNR penalty induced by the WC was measured for each pair of curves at a BER of 10^{-6} . This degradation was due to two noise sources: ASE noise generated by the pump amplification, that remained approximately constant in the range of pump powers studied, and XPM/NPN that was shown to vary with pump power. Fig. 6.6(left) shows the OSNR penalty as a function of the power per pump wave for BPSK, QPSK and 16-QAM modulation formats. The different slope in the degradation that the 16-QAM signal exhibits is attributed to the amplitude noise-to-phase noise conversion induced by the nonlinearity of the HNLF (NPN) and it is shown to increase linearly with pump power.

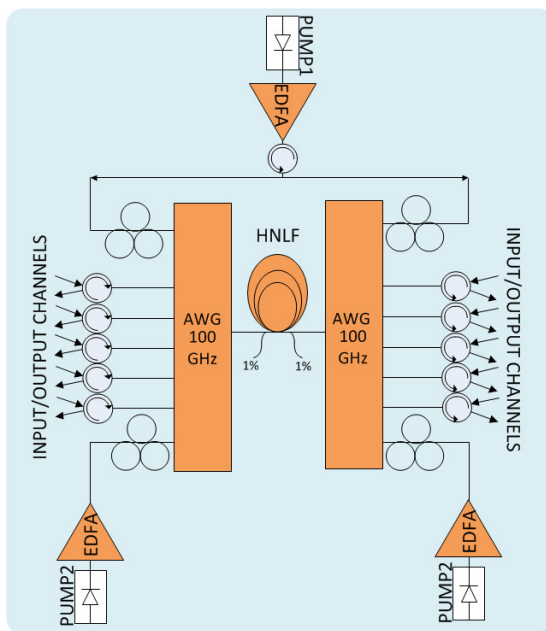
Parametric processes are extremely complicated to optimize with respect to XPM and NPN, because any modification in the pump power also impacts on the gain of the device. In this particular case, the scheme was much more sensitive to gain variations than to the NPN/XPM variations induced by the different pump powers. Fig. 6.6 shows that the gain undergoes a variation of 6 dB if pump powers are decreased by 4 dB whereas the OSNR penalty only decreases by 0.6 dB at a BER of 10^{-6} . However, this gain decrease must be compensated for using amplification that in turn will degrade the OSNR of the signal by more than 0.6 dB.

In this manner, the optimisation of the influence of the phase noise reduces to a trade-off between the reduction of the OSNR penalty induced by NPN/XPM and the increased OSNR penalty induced by the increased gain required in subsequent stages of amplification to compensate for the gain reduction in the WC. The systems experiments showed that the operation range with minimum degradation for this wavelength conversion scheme was achieved when the pump powers were in the range 20.5 – 21.5 dBm.

6.2 Bidirectional Wavelength Converter

The scheme previously implemented was modified by developing a more cost-effective solution based on the bidirectional use of parametric wavelength conversion in a HNLF. This configuration achieves an economy of components by allowing the use of the HNLF in both directions and the sharing of pump sources while offering the functionality of two independent wavelength converters. The choice of the frequency of the pump waves was independent for each direction, allowing the use of two shared pumps, one shared pump and two independent pump sources or four independent pump sources, thus facilitating considerable flexibility in the configuration of the system.

Fig. 6.7 shows the schematic of a bi-directional WC with three pump waves [8]. This scheme, relying on the previous design, exhibited a performance very similar to the one-directional design although some physical features that were unimportant in the one-direction WC should now be accounted for. As before, this scheme also multiplexes the waves into the HNLF using two 100-GHz grid AWGs that, in this case, allowed at the same time the rejection of the out-of-band ASE noise generated during pump and signal amplifications and eased the filtering of the converted signals. The discrimination



between input and output signals was achieved by placing circulators in front of the ports of the AWG, which provided an isolation of 45 dB, albeit at the expense of a small decrease in the conversion gain. The operating bandwidth of the converter, as well as the number of channels that it can support, are eventually determined by the characteristics of the AWGs. In principle, the AWGs could be replaced with wavelength selective switches (WSSs), in order to support full flexibility with respect to the input and output wavelength allocation.

An example of the nonlinear interaction observed in the bi-directional wavelength converter is shown in the left of Fig. 6.8. The figure shows only small differences between the gain achieved in the two directions, that come from unavoidable unequal phase matching conditions related to the different pump wave allocation in each direction and from small differences in the pump power for each direction. In this particular example,

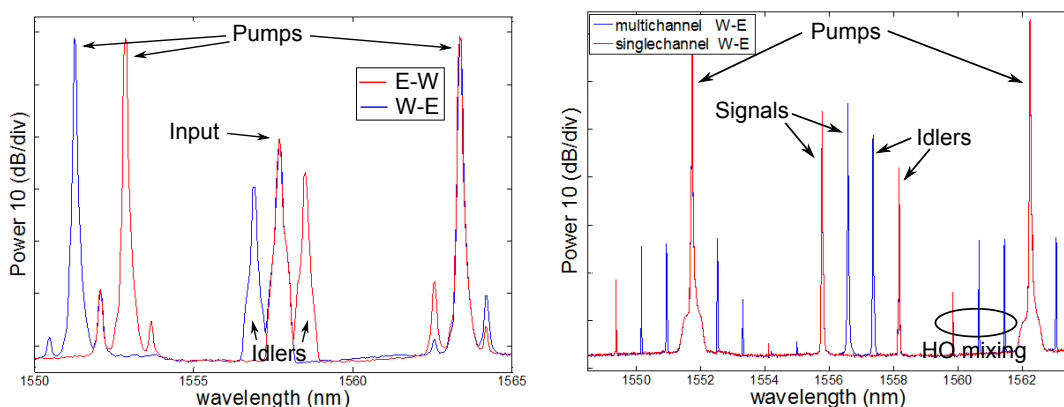


Figure 6.8: Comparison of nonlinear interaction for both directions (left) and comparison between single- and multi-channel in one-direction operation (right)

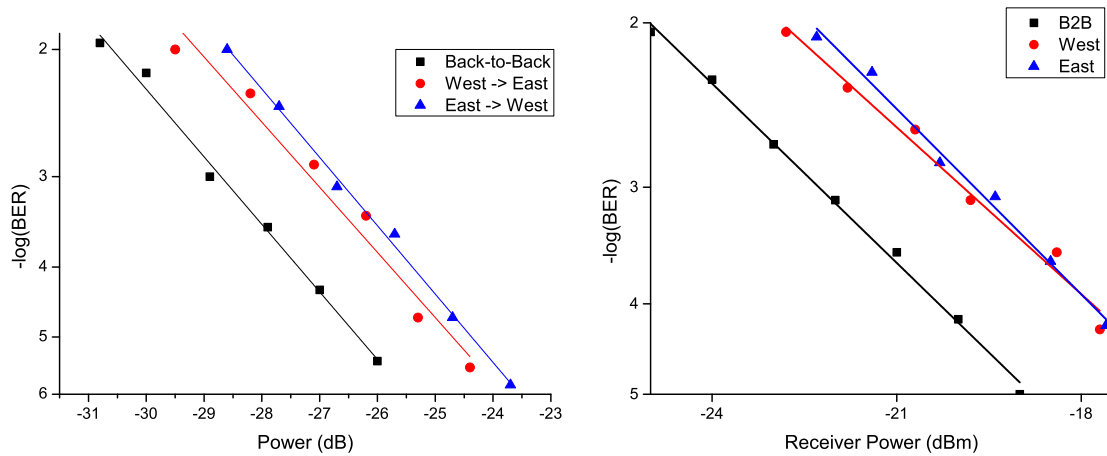


Figure 6.9: BER degradation induced by the bidirectional WC on a 10 Gbd BPSK (left) and on a 10 Gbd 16-QAM (right)

the generated idlers lay at different frequencies and an OSNR in excess of 30 dB was achieved for the three signals.

The main source of additional degradation in a bi-directional WC comes from Rayleigh back-scattering (RBS), which compromises the OSNR of the shared pump. The measured level of RBS in our implementation was 30 dB below the original signals and its only effective limitation was the restriction in the use of the pump wavelengths for signal allocation in the opposite direction.

Multichannel operation was tested showing that the factor limiting the performance in this case comes from high-order FWM mixing products, which were 20 dB below the level of the converted signals. This is shown in the right of Fig. 6.8, where the spectra of the nonlinear interactions in both single- and multi-channel operation are displayed. These spectra show that, if high order mixing is avoided by choosing a suitable allocation for the pump waves, the performance of the bidirectional WC exhibits no additional degradation in multi-channel operation with respect to the single-channel case.

The BER degradation induced by this bidirectional WC was also assessed for different modulation formats at 10 Gbd. Fig. 6.9 shows the degradation induced by this WC on BPSK (left) and 16-QAM (right) modulation formats. The OSNR penalty induced by it showed to be similar to the one-direction scheme with minor differences for each direction. The BER degradation induced by this scheme for different modulation formats, bit rates and polarisation multiplexing schemes is presented in Chapter 8, where network experiments based on this WC are discussed.

6.3 Automatic Pump Polarisation Alignment

As mentioned earlier, during the aforementioned tests the polarization adjustment of the two pumps was performed and maintained manually using the polarization controllers depicted in Fig. 6.1 and 6.7. This alignment was susceptible to vary with time due to the slow and random polarization drifts induced by temperature changes and mechanical vibrations [56, 203, 204], making it an impractical solution for real communication networks. This motivated the analysis and development of an automatic pump-alignment stabilization mechanism that is reported in this section.

In order to overcome the polarization sensitivity of FWM-based schemes, several approaches have been reported in the literature. For example, the large polarization dependent gain (PDG) of single-pump FWM schemes in low-birefringence HNLFs can be compensated for through the use of polarization tracking devices to dynamically align the polarization of the input signals to that of the pump. However, in multi-channel operation, even if a polarization tracker was to be used for each channel (with significant implications for the overall system cost) the dependence of birefringence with respect to the wavelength might lead to different conversion gains for each input signal, thereby reducing its potential functionality.

On the other hand, if a high-birefringence HNLF was to be used in a single-pump FWM approach to allow polarization insensitive operation of the parametric process, the differential group delay (DGD) effects induced on the converted signal(s) would restrict its practical implementation in high-speed systems [205].

In a dual-pump FWM scheme, such as the one considered in this work, where orthogonally-polarized pumps are employed to ensure operation that is insensitive to the signal polarization, the difficulty lies in maintaining the pump orthogonality at the input over time and along the length of the HNLF [197, 203]. Thus, the outcome of the wavelength conversion is determined by averaging all the possible relative alignments of the pumps during the propagation in the HNLF, assuming that the polarization of each pump can follow a three-dimensional random walk over the Poincaré sphere [56]. Note that this evolution can vary in time due to drifts in environmental factors, such as temperature, strain and acoustic perturbations.

In order to overcome this limitation, the implementation of Fig.6.1 was modified to include a feedback circuit that monitored just the performance of the nonlinear interaction between the two pumps in the HNLF without interfering with either of the original or the converted signals. The feedback circuit then dynamically readjusted the polarization of one of the pumps to maintain the desired performance over time.

Since a low-birefringence HNLF was considered (with a PMD of $0.58 \text{ ps}\cdot\text{km}^{-0.5}$), each pump did not have to be aligned to a preferred fibre polarization axis and only the relative polarization alignment between the two pumps had to be controlled and adjusted.

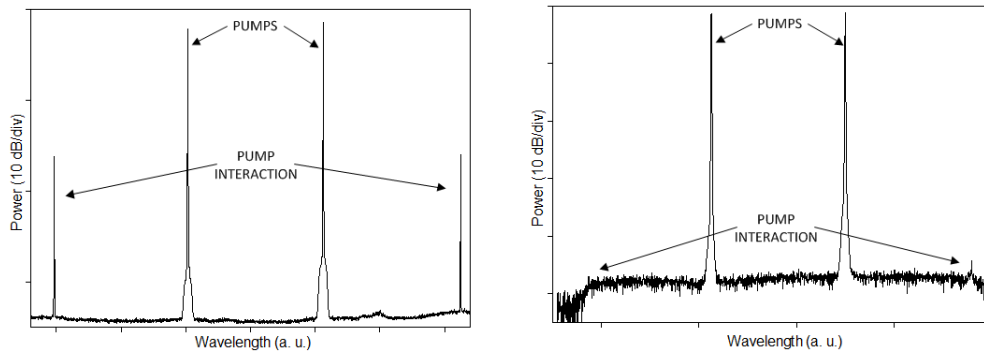


Figure 6.10: Degenerate nonlinear pump interaction for a random (left) and optimum (right) alignment of the pumps

The average power of the degenerate idlers generated by the nonlinear interaction in the HNLF between the two pumps was monitored at the output of the fibre. Then the feedback circuit targeted minimization of the sum of the average powers of the two idlers, which would imply that the length over which the two pump waves were cross-polarized inside the HNLF was maximized. Examples of this nonlinear interaction, when no signals were launched in the HNLF, are displayed in Fig. 6.10 for two different (relative) states of polarization of the two pumps.

The required modifications on the WC scheme are shown in Fig. 6.11 (which should be compared to Fig. 6.1). The modified system comprised a polarization tracker, a dual-frequency optical filter, a slow photodiode and a transimpedance amplifier. 1% of the power at the HNLF output was tapped off and filtered by a dual-frequency square-like filter of 0.1-nm bandwidth for each peak, allowing only the two idlers generated from the pump-to-pump interaction to go through. It is worth mentioning that it was observed that filtering and minimizing the power of only one of the idlers would not lead to the desired alignment between the two pumps. The filtered signal was then detected using the photodiode and the corresponding electrical signal was subsequently amplified by a transimpedance amplifier and used as a feedback signal into the polarization tracker.

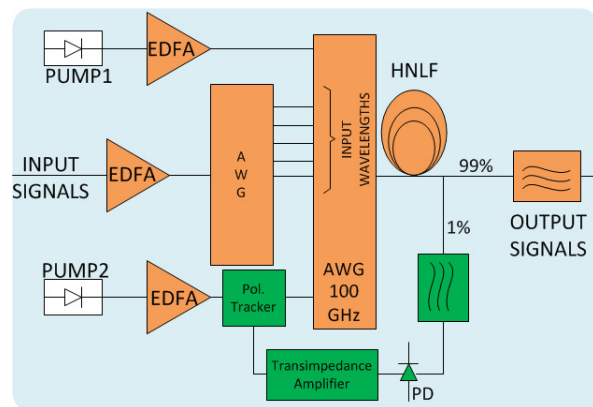


Figure 6.11: Modifications performed in the wavelength converter scheme to provide polarization stability. PD: photodiode

Unfortunately, the commercial polarization tracker that was available at the time of our experiments restricted the maximum optical power allowed at its input to only 20 dBm,

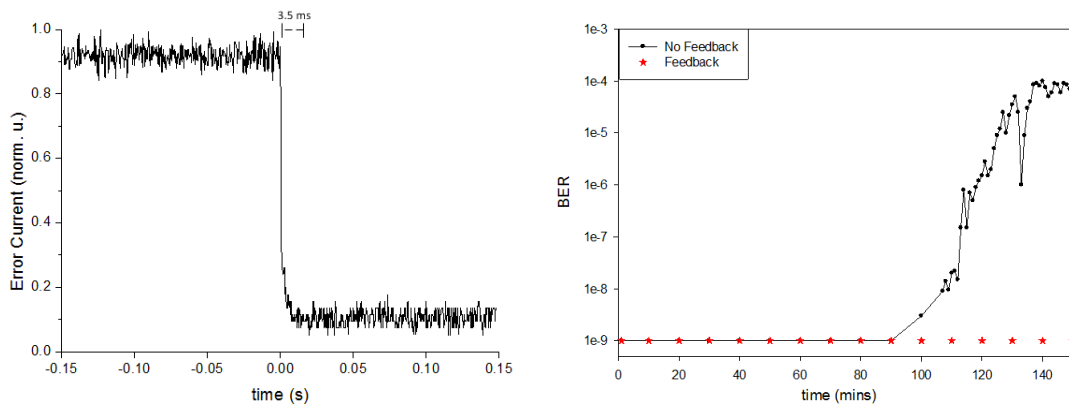


Figure 6.12: Experimental characterization of the pump alignment system: response time after switching on the automatic feedback (left) and BER curves in function of time in absence (right - black solid line) and presence (right - red dashed line) of the automatic feedback system

thereby preventing to launch the same pump power to the HNLFF as before (now only 16.5 dBm per pump was used at the input of the fibre, as opposed to 21.5 dBm in the experiments reported in previous sections). Therefore, the conversion gain obtained at the output of the system was compromised in this instance by 8 dB. (Inverting the order between the EDFA and the polarization tracker in the path of Pump2 in the setup of Fig. 6.11 would not solve the problem due to the residual PDG of the amplifier used. Indeed, in that configuration the polarization tracker would tend to align the pump polarization to the polarization axis that yielded minimum gain in the EDFA rather than to the polarization that would be orthogonal to the second pump). This restriction prevented from the implementation of this functionality during the experiments that will be presented in Chapter 8.

The best polarization tracker settings were found to be a fixed step size of 1° on the Poincaré sphere and an averaging over 15 samples to effectively reduce the noise bandwidth. The bandwidth of the polarization tracker (without averaging) was 500 kHz, so that any possible polarization drift could be easily followed with inexpensive discrete elements.

The performance of the feedback circuit was assessed in terms of (a) the response time required to lock to the desired polarization alignment and (b) the stability in maintaining the correct pump polarization alignment when operating the WC. The left of Fig. 6.12 shows the switch-on time of the feedback circuit. The pumps were initially co-polarized (representing the worst-case scenario) corresponding to a maximum PD current. The figure shows a response time of 3.5 milliseconds, indicating the time required by the system to find the desired alignment between the pumps. This time scale is much faster than any polarization drift induced by temperature changes and mechanical vibrations to any of the system components.

Fig. 6.12(right) shows the performance of the WC in terms of BER as a function of time (over a period of 150 minutes) when the automatic polarization alignment circuit was either used (red dashed curve) or not (black solid curve). For this characterization a 10 Gb/s NRZ OOK signal was used at the input of the WC. Note that when the automatic feedback circuit was not in use, the polarizations of the two pumps in the WC were initially optimized manually using the polarization controllers shown in Fig. 6.1. In contrast, the system was allowed to find the optimum operating point automatically in the case when the feedback system was in place. As can be seen, in the absence of the automatic alignment system the performance of the converted signal slowly and randomly degraded. Conversely, error-free operation ($\text{BER} < 10^{-9}$) was continuously maintained throughout the time that the feedback system was operational.

6.4 Conclusions

In this chapter, and based on the features of parametric processes explained in Chapter 2, two wavelength conversion schemes have been proposed and characterised. The good performance achieved in all the relevant features for optical communication systems allows their use in commercial networks with the required degree of reliability.

The noise model proposed in Chapters 3 and 4 allowed for an experimental analysis of the contributions of each noise source to the total BER degradation induced by both schemes. This study made possible an optimisation of the performance of these devices for their operation in real systems.

In addition, the robustness, the turn-key operation and the black-box configuration exhibited by these WCs allows their use both in current and future networks, where the growing degree of complexity requires an abstraction from the underlying physical processes and makes possible the use of the functional approaches commonly applied in system design.

Spatial Division Multiplexing Experiments

Success consists of going from failure to failure without loss of enthusiasm
Winston Churchill

The previous chapter presented and characterised two implementations of wavelength converters capable of operating in wavelength division multiplexed (WDM) systems. Currently, while WDM networking still represents the widely adopted standard in high capacity optical communications, current trends address a network evolution towards a new generation of transmission systems, the spatial division multiplexed (SDM) systems. An element of work in this project has related to the implementation of novel concepts for SDM systems, as well as some of the network operations that can benefit such systems.

SDM systems exhibit different features than WDM alone, that are necessary to understand in order to implement SDM components or adapt WDM ones to SDM networks. Thus this chapter is devoted to an analysis of the different proposed implementations of SDM networking and the characterisation of one of them, the multi-element fibre (MEF) technology. Thus the work presented in this chapter serves as a base for the wavelength conversion experiments that are presented in Chapter 8.

7.1 Aim of Spatial Division Multiplexing

As was already mentioned in the introductory chapter, the present annual growth rate of Internet traffic, close to 30%, and the saturation of the capacity optical fibres in the near future may lead to a turning point in the trend of a ever decreasing cost-per-bit due to the large numbers of fibres and wavelength division multiplexing (WDM) systems required in order to accommodate it.

Spurred by this realisation, SDM has been proposed as a way of improving both the cost and power efficiency of current optical networks by grouping parallel WDM systems into SDM systems with more *favourable economics*. This term is a blurred concept that

encompasses different points of view and that is necessary to clarify if the aim is one of adopting the most efficient way forward.

From the point of view of pure research, favourable economics mainly involves the decrease in the cost and power consumption. A large number of publications have discussed the benefits of its adoption [39, 206–208]. This perspective, even though it is very important, is not the only criterion to judge the suitability of an implementation of SDM as a solution.

From the perspective of the Internet Service Providers (ISPs), whose transmission systems usually require lifetimes between 10 and 25 years [209], it is necessary to provide compatibility with the already deployed fibres in order to exploit those existing resources as efficiently as possible. The high cost of a nationwide deployment indicates a difficulty in the adoption of metro or long-haul solutions that are not compatible with standard single mode fibres (SSMFs).

From the perspective of the operation and maintenance, a solution as simple and similar to WDM as possible is desirable. The cost of training the network operators and the long restoration times associated to complex solutions would lead to higher penalties due to breaching of the service level agreements (SLAs) signed with the customers.

The concept of cost saving coming from component sharing is very attractive but its impact in network operation, and therefore in maintenance costs, could be prohibitive in terms of compliance with SLAs. When a component shared among of all the spatial channels (i.e. the power supply) fails, then all the channels will be affected but, somewhat surprisingly, a failure of a component dedicated to a single spatial channel (i.e. the laser of one channel) can also affect all of the spatial channels even if their own dedicated components are not damaged. This is because of the integrated nature of some components that enforces the replacement of the whole module in which they are installed. In this sense, the dedicated components should allow *hot replacement*. This term refers to the capability of replacing parts of subcomponents within a module without the necessity of turning it off.

From the perspective of technical implementation, an SDM network must provide similar performance as N WDM systems in parallel. Such performance entails an exponential increase in the reliability of SDM components as the number of parallel systems increases. Standard processes for the characterisation and improvement of component and system reliability [210] clearly show the relation between an increasing complexity and a decreasing reliability, which highlights the extreme importance of the simplicity of a solution for its practical implementation to be considered. This is particularly important in submarine links where only one traffic cut is permitted due to component failures in every 25 years [211].

From the point of view of system performance, the main difference between WDM and SDM networks is the presence of crosstalk between spatial channels. If the aim of SDM is that of providing the same functionality as WDM, crosstalk must be kept under control or compensated for when the crosstalk levels are above 25 dB [212]. In practice, spatial crosstalk predominantly comes from two different sources: the inherent coupling between spatial modes and the coupling at the fibre and device interconnections – especially at splice points. Both sources of crosstalk are related to the optical part of the transmission link and must be addressed.

The importance of the crosstalk induced by splices depends on the reach of the system. In this manner, the crosstalk can be neglected in intra-data centre systems where the reach is approximately ~ 1 km. In these systems, the number of splices that the signal goes through is very small (usually < 5), thereby their effects are negligible. However, crosstalk must be unavoidably taken into account in metro and long-haul systems, where the reach is in the order of hundreds or thousands of kilometres and the distance between splices ranges between 1 km and 4 km. The compensation of crosstalk largely increases the complexity of the solution compromising its potential reliability and increasing its costs. Therefore keeping crosstalk under control is a key consideration for an efficient SDM implementation.

All these points, although of different relative importance, must be considered during the implementation of SDM networks. Accounting for all of them simultaneously makes this implementation very challenging. A decision on whether an SDM will ultimately be adopted or not will eventually depend on how successfully this system addresses these considerations.

7.2 Implementations of SDM

As of today there exist three main implementations of SDM, based on multi-core fibres (MCFs), multi-mode fibres (MMFs) and multi-element fibres (MEFs). These three fibre geometries are shown in Fig. 7.1, and exhibit very different layouts. The physical properties of these fibres are responsible for the advantages and drawbacks of each implementation, thus a quick review of the features of each type of fibres is of interest.

7.2.1 Multi-core Fibres

MCFs [36, 213, 214] allow transmission in parallel through a fibre with several cores. Therefore an increase in the number of parallel channels is achieved by increasing the number of cores. Mechanical constraints in the fibre fabrication limit the maximum outer diameter (OD) of MCFs to around $225\mu\text{m}$ [215]. Above that limit, the robustness

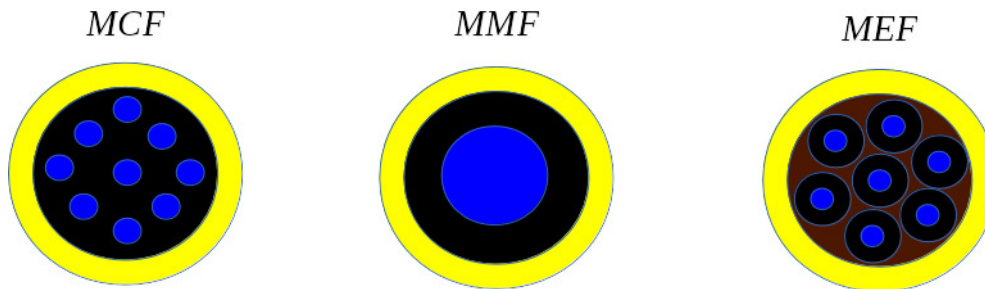


Figure 7.1: Fibre geometries of the current implementation of SDM

of the fibre decreases, making it unsuitable for deployment. This feature limits, in turn, the maximum effective core number to 13 [215]. At such large core numbers the distance between cores is such that the crosstalk seriously limits system performance. In addition, the access to individual cores requires either special bundles [213] or laser-written couplers [216] and the splices give rise to additional crosstalk between the cores. However, the development of spatially multiplexed lasers and photodetectors [217] can avoid the use of these multiplexers and simultaneously decrease the tens of thousands of connectors that data-centres require for operation [218].

MCF amplification has been demonstrated both in core-[219] and cladding-pumped [220] configurations. Core-pumped MCF amplifiers exhibit gains in the range 24-27 dB with noise figures (NF) ranging between 3-6 dB in the C-band, whereas the reported gain of cladding-pumped MCF amplifiers is in the range 15-20 dB with a NF ranging 4-8 dB in the L-band.

So far, MCFs have shown the record transmission capacity, overcoming the barrier of Petabit/s transmission [221], over distances of around 50 km. This demonstration required the use of a low-crosstalk MCF to decrease the coupling between the spatial channels and can be considered as being very close to the capacity limit that this fibre geometry can provide.

7.2.2 Multi-mode Fibres

MMFs [222] allow transmission in parallel through different propagation modes. The inherent mode coupling must be compensated for in order to avoid crosstalk. In intra-data centre or short reach systems, mode coupling does not impose any limit to the system capacity because it can be compensated for electronically through multiple-input multiple-output (MIMO) processing. However, the transmission in long haul optical communication systems will work in the strong coupling regime [223], thereby pushing the complexity of the digital signal processing (DSP) circuit and increasing the number of required input/output ports to levels that can make the whole system implementation unviable. The use of MIMO reduces both cost- and power-efficiency, and practical

implementations will become further complicated by the adoption of Flexgrid spectrum allocation [224] and the subsequent increase in the number of wavelengths per system. Moreover, since MIMO requires access to all the spatial channels to successfully decouple the information channels, it constrains the flexibility of the network by restricting switching in the spatial dimensions [39].

Conversely to MCFs, where the maximum number of effective spatial elements is limited by the outer diameter (OD) of the fibre, MMFs do not suffer from such restrictions. However the attenuation of the modes grows exponentially with the order of the mode [225], and since all supported modes must be used for MIMO to work properly, the effective range of MMF systems is that of the most lossy mode, leading to the need for more frequent electrical regeneration as the number of modes grows. Moreover, the complexity of MIMO processing also increases rapidly with the number of modes. In addition, the requirement of phase plates [226] or a photonic lantern [227] for coupling to/from the individual fibre modes poses an additional practical implication.

MMF amplification has already been demonstrated [228] for a three-mode amplifier. The main difference of these amplifiers with respect to their MCF counterparts is the addition of mode dependent loss and gain (MDL) that cannot be fully compensated for with MIMO processing and imposes a constraint to the capacity limits of MDM systems [223].

MMF-based transmission demonstrations [222] have not reached the levels of single mode ones [229] but it is expected to comfortably exceed this capacity in the near future. These demonstrations reached 73.7 Tb/s transmission over three fibre modes and offline MIMO processing. Different MMF-based demonstrations have shown transmission over five fibre modes [230] and a further increase in the number of modes is expected. However, the development of MIMO processing for these implementations is lagging behind due to the complexity and difficulty of its implementation. In this situation, it is conceivable that the capacity limits that this fibre geometry can provide are constrained by the electrical signal processing.

7.2.3 Multi-element Fibres

An MEF consists of a bundle of single-mode fibre-elements drawn together in a common polymer coating, each element comprising an independent core and cladding. The use of the polymer coating makes the reduction in the size of the fibre elements with respect to SSMF possible, offering the prospect of reducing the

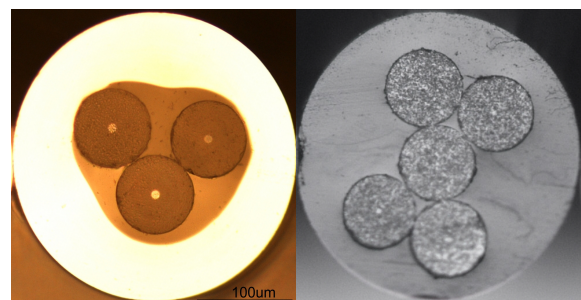


Figure 7.2: Different types of MEF implementations: passive MEF (left) and erbium doped MEF (right)

micro-bending losses relative to individual fibres of the same size. At the same time, the in-situ bundling process of MEF fabrication eliminates the need for a two-stage fabrication process that is required for ex-situ bundling of SSMF, and has the advantage of being more compact than an equivalent ex-situ fibre bundle (albeit not as compact as an MCF).

The distance between the fibre-elements of MEFs must be accurately controlled during the manufacturing process in order to obtain the required level of robustness necessary for deployment in optical transmission systems and without introducing any additional losses. The optimum spacing for a transmission fibre is achieved when the elements are very close, but not in physical contact. An example of this case is shown on the left inset of Fig. 7.2 [231, 232]. The attenuation and dispersion characteristics of MEFs have been observed to be similar to those of a SSMF drawn from the same starting preform [232]. MEFs exhibit crosstalk levels under 100 dB between the various elements and full compatibility with standard WDM components [3, 233].

The fibre geometry provides easy access to the individual elements simply by removing the common coating. In this manner, each element can be spliced individually with standard splicers to provide crosstalk-free connections. In addition, the connection to standard WDM components can be performed by splicing standard single mode fibre pigtails at each end of the elements, avoiding the need for the development of custom fan-in/fan-out devices.

MEFs can overcome the $225\mu\text{m}$ OD limitation exhibited by MCFs. However, the maximum OD that this geometry allows with any measurable loss of robustness is currently unknown. In the same manner, MEF has the potential to reduce the microbending losses induced by the use of elements of very small diameters. Similarly, the minimum diameter achievable free of microbending is also unknown. Therefore, currently it is not possible to estimate the maximum number of elements that can be implemented through MEF technology. So far, the most dense MEF manufactured consisted of a seven $80\mu\text{m}$ elements for a total OD of 300mm with a robustness similar to that of a SSMF.

MEF technology lends itself directly to the implementation of SDM amplifiers. If the fibre-elements are made to touch one another, a cladding-pumped multi-element erbium doped fibre amplifier (ME-EDFA) can be manufactured [234]. This design is similar to the GT-Wave concept used in high power fibre lasers [38]. By making the central fibre-element without a core, a pump source can be coupled into the ME-EDFA and the pump light diffuses into the erbium-doped fibre-elements (see right inset of Fig. 7.2). Since the geometry of the elements is similar to the transmission MEF, ME-EDFAs show no measurable crosstalk between elements [231]. Since a single multimode pump diode is shared among all of the elements, this pumping scheme exhibits a cost efficiency that together with the absence of any crosstalk between elements, makes MEF amplifiers a cost effective SDM technology.

MEFs were pioneered at the University of Southampton, and the first amplified transmission experiments using this technology were demonstrated within this project. The following section reports this work, and highlights how MEF transmission and amplification technology lends itself to a soft upgrade of SSMF systems.

7.3 Transmission Experiments

Impressive demonstrations have been presented in the last few years demonstrating the high transmission capacities that are enabled by the use of SDM based on either multi-core [213] or multi-mode [222] technologies. However, so far upgrade experiments have been restricted to basic demonstrations with point-to-point transmission links [235].

The most widespread conviction is that the deployment of SDM systems will start by migrating congested WDM spans to SDM ones [235, 236]. Nonetheless, this approach is hard to be adopted due to both the lack of benefits and the risks that it entails. Such upgrades have historically been chiefly performed in systems going from single-wavelength systems, like SONET or SDH, to multi-wavelength systems, like CWDM or DWDM. Under such circumstances, the upgrade has been beneficial because it enables a more efficient use of the optical spectrum. On the contrary, an upgrade from WDM to SDM, since it requires the deployment of a new transmission fibre, does not represent a more efficient use of existing resources and the upgrade becomes simply a swap. In this manner the WDM-to-SDM upgrade would involve all the risks and costs of a swap but would not provide the benefits of an upgrade.

A more realistic type of upgrade scenario is that of a hybrid deployment comprising both SSMFs and SDM fibres. This scenario, that demonstrates the capabilities and benefits to be had from SDM networking, was demonstrated in the context of the Photonic Hyperhighway Project [3]. The experimental setup of this demonstration is shown in Fig. 7.3. The transmitter consisted of 29 channels in the range between 1535 and 1562 nm, modulated using a $2^{31}-1$ 10Gbit/s NRZ OOK pseudorandom bit sequence. The transmission lines comprised (a) a cascade of two 3-element MEFs of respective lengths of 3.07 km and 9.5 km with an attenuation of 0.5 dB/km and (b) a WDM 400 km installed dark fibre link (part of UK's AURORA network). The MEFs were cascaded using SSMF

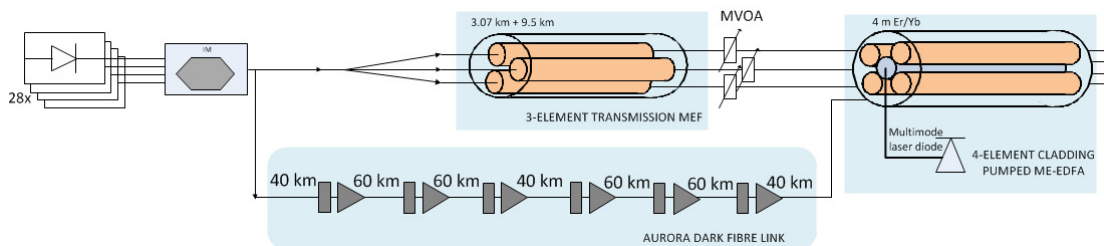


Figure 7.3: Fibre geometries of the current implementation of SDM

connectors that were spliced to each element of the MEF using standard splicers. A 4-element ME-EDFA was used at the output of the transmission line, such that the three elements of the MEF were connected to three of the input ports of the ME-EDFA, the fourth port of which was connected to the dark fibre link.

Between the output of the MEF and the input of the ME-EDFA, three manual variable optical attenuators (MVOA) were installed to fully compensate for the gain of the ME-EDFA. It is to be noted that the power of the spatial channels in the system was adjusted individually, allowing the compensation for either small differences between the elements of the MEF generated during the fabrication process or reconfigurations due to inhomogeneous degradation over time.

The 4-m long ME-EDFA actually comprised 5 individual elements, as shown in the right of Fig. 7.2. The central element was used to propagate the pump while the cores of the remaining four were co-doped with erbium and ytterbium and acted as the active fibres [234]. The measured gain and noise figure for the four elements of the amplifier are shown in Fig. 7.4. The differences in the values between

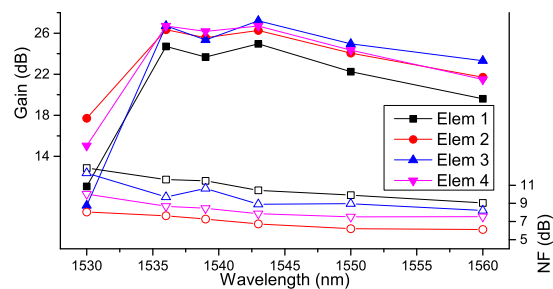


Figure 7.4: Gain and noise figure of the ME-EDFA

the elements are due to slight differences in the concentrations of erbium that were discovered after the manufacturing of the amplifier fibre. The minimum NF exhibited by this amplifier was 4.7 dB with a gain in the range 25-30 dB per fibre element in the C band. Nevertheless, the ME-EDFA exhibited a high absorption at 1530 nm due to the phosphosilicate host used. This feature, together with the cladding-pumping scheme, provides flatter and less noisy gain in wavelengths near the L band.

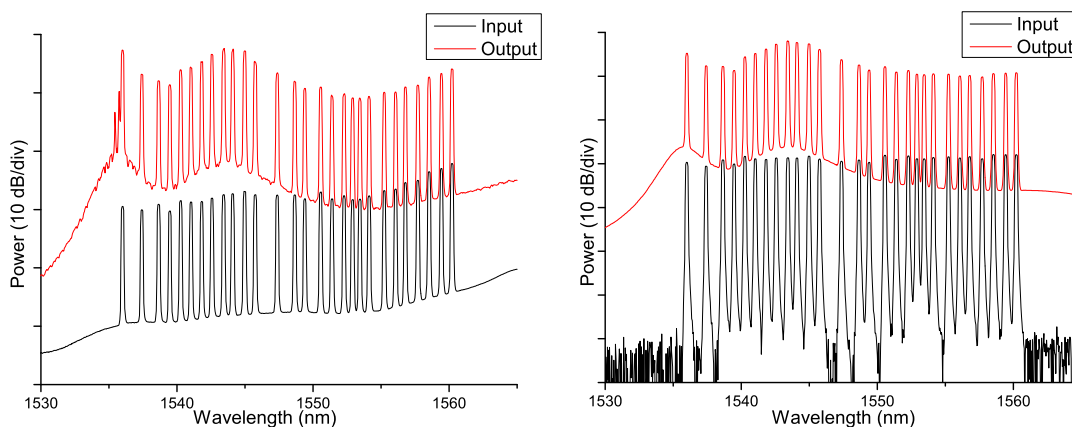


Figure 7.5: Spectrum of signals transmitted through the dark fibre link (left) and through the MEF (right) before and after being amplified by the ME-EDFA

Optical spectra characterising the operation of the ME-EDFA during the experiment are presented in Fig 7.5. This figure shows traces taken at the input and output of the ME-EDFA for the cases of transmission through the dark fibre link (7.5 left) and the MEF (7.5 right). Even without the use of a gain flattening filter, that could reduce the gain ripple to values under 1 dB, the difference in performance among the different channels was not a limiting factor after a single amplification stage.

The BER of all channels was assessed at the output of the amplifier while the full system was turned on and error-free transmission ($BER < 10^{-9}$) was verified for both the MEF and the dark fibre paths, exhibiting a BER degradation of ~ 2 dB. An example of this degradation is shown in Fig 7.6, where the BER of the channel at 1556 nm is displayed for the two signal paths considered.

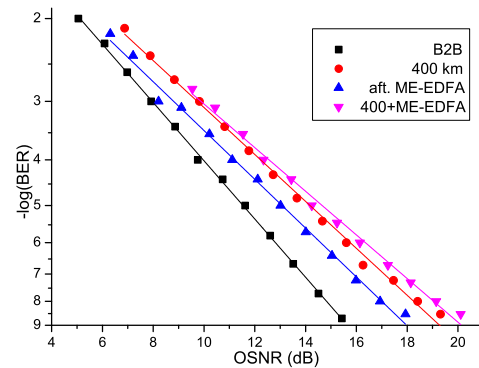


Figure 7.6: BER degradation induced by the ME-EDFA

In order to assess the performance of a chain of ME-EDFAs, a chain using the three MEF sections was tested. The 5 dB gain ripple of the ME-EDFA between the wavelengths at 1535 nm and that of 1560 nm accumulated, leading to unsuccessful transmission for the wavelengths near 1560nm. These wavelengths underwent lower gains and, after three stages of amplification, they could not be recovered error-free. This ripple could be compensated for with gain flattening filters that could be spliced at the output of the Erbium/Ytterbium doped fibres so that it does not impose a fundamental limit to the performance of this kind of amplifiers.

The crosstalk of the MEFs was measured by launching a total power of 20dBm at the input of each element of the MEF and measuring the power at the output of the rest of the elements. No power was detected at the output using both a power meter with a sensitivity of -70 dBm and a OSA with a sensitivity of -90 dBm. The presence of amplified spontaneous emission (ASE), prevented from carrying out the same test on the ME-EDFA. Instead, using the set-up of Fig. 7.3, the signals were characterised at each output port of the ME-EDFA while the remaining fibre elements of the amplifier were or were not carrying any data: By adjusting the OSNR of the signals traversing one element of the ME-EDFA, so that the BER at the output was 10^{-8} , the deviation from this BER value was measured while successively turning on the signals in the remaining fibre elements. There was no measurable degradation in the BER of any of the assessed channels independently of the number of elements of the ME-EDFA in use and their input powers.

These experiments, although showing attenuation values in the range of 0.5 dB/km and noise figures in the order of 5 dB, demonstrated a SDM implementation capable of operation in real environments and fully compatible with existing systems, allowing realistic upgrades to be performed.

7.4 Conclusions

This chapter has discussed the properties of the three most important implementations of SDM systems as candidates for the substitution of current WDM systems and for the evolution of in-plant fibre cabling.

From the point of view of in-plant fibre cabling, the use of the loosely coupled geometry of MCFs allows a cheap implementation and a simultaneous reduction of the increasing number of connectors. These features give MCFs very high probabilities of becoming the next standard in this field. Nevertheless, the presence of splicing-induced crosstalk is likely to inhibit its utilisation in outer-plant systems.

MEFs, exhibiting extremely low levels of crosstalk and direct compatibility with SSMF components and systems, has every chance of become the next generation of transmission systems provided that low loss fibres can be implemented and the noise figure and ripple of the ME-EDFA can be decreased to acceptable levels.

On its part, the incompatibility of MMFs with existing optical switching devices and the tight requirements that MIMO imposes both on network flexibility and performance, detract from a commercial implementation without a radical change in the conception of optical networks as they working nowadays. Such a paradigm shift presents several uncertainties and risks that some companies may not be willing to take.

Once the features of SDM networks have been discussed, components adapted to the peculiarities of these systems can be developed. In this sense, the operation and benefits of the wavelength conversion schemes proposed in Chapter 6 are demonstrated in the following chapter.

Network Experiments

Human intelligence is stultified when man sets fixed bounds to his curiosity
Norbert Wiener

Chapter 6 presented the back-to-back characterisation of two designs of wavelength converters (WCs), showing that they exhibit the features required for their successful implementation in wavelength division multiplexing (WDM) communication networks. In this chapter, system demonstrations of those experiments are presented, showing both the feasibility of operation and the new functionalities that WCs can deliver to current optical communication systems.

The system experiments that will be described in this chapter have considered two different environments: (a) a 1200-km point-to-point transmission experiment over installed fibre [2] and (b) an heterogeneous optical switched network [9]. In the first scenario the WC, configured as a black-box device, was placed at the mid-point of the fibre link (this was formed in a part of the UK's Aurora dark fibre network [237]) and its performance in transmission was measured. In the second scenario the WC was placed as a component in a reconfigurable optical add drop multiplexer (ROADM) and its functionality was used on demand in order to facilitate the optical switching capabilities provided by the ROADM. This second experiment was carried out in collaboration with the High Performance Network group at the University of Bristol within the context of the Photonics Hyperhighway project.

In addition, Chapter 7 provided an overview of the different features that space division multiplexed (SDM) systems exhibit with respect to WDM systems. These features require several changes if the aim is that of an efficient use of the new resources made available by this technology. The application of WC techniques to SDM networks is presented in the latter part of this chapter as a cost-efficient method for resolution of the new type of channel contention introduced by the addition of the spatial dimension to switched WDM networks. Once again, this experiment was carried out in collaboration with the High Performance Network group at the University of Bristol.

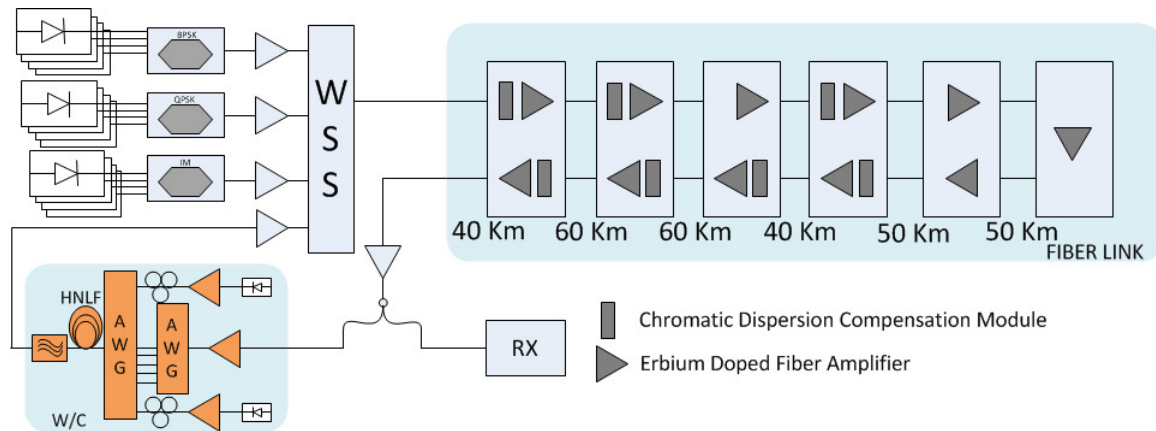


Figure 8.1: Experimental set-up of the transmission experiment. Rx: receiver. WSS: wavelength selective switch

8.1 Wavelength conversion in Point-to-Point Systems

After having characterized the WC as a stand-alone device, the system was introduced in the middle of an installed fibre link (the UK's Aurora dark fibre network) to assess its performance as a black box device (see Fig. 8.1). Six data channels were used in the transmission experiments, three of which were wavelength converted after transmission over 600 km, coupled with the original six channels and re-transmitted over the same distance. The fibre link comprised twelve spans, as shown in Fig. 8.1, with distances ranging between 40 and 60 km each. The chromatic dispersion in the link was not fully compensated in order to optimize the OSNR achieved at the receiver. Instead, a receiver with chromatic dispersion estimation and compensation (Agilent N43931A) was used to properly receive and characterize the signals after the first loop and after the WC. Note, however, that digital dispersion compensation was not required for the WC signals after the second passage through the loop, since the PC idlers conjugated the phase of the original signal at the mid-point of the system after the first circulation, therefore resulting in close to zero net dispersion after the second circulation in the same fibre link [238].

In order to test the performance and robustness of the setup, two distinct network scenarios were considered, involving the simultaneous conversion of three channels, which were dynamically reconfigured thanks to the flexibility provided by the WSS (Finisar Waveshaper 4000S). Different modulation format signals at different wavelengths and bit rates were considered in each case, aiming at highlighting different features of the WC.

Three different modulators were used at the transmission side to generate 10 Gbd OOK, BPSK and QPSK signals, modulated using a $2^{31}-1$ pseudo-random binary sequence (PRBS). OOK signals were modulated using a LiNbO_3 intensity modulator, BPSK signals using a LiNbO_3 phase modulator and QPSK signals using a delay line interferometer

(Kylia) after the BPSK modulator. (It is noted that the high optical signal-to-noise ratio requirements of 16-QAM modulation prevented from using the signals of Fig. 6.5 in any of the transmission experiments). The use of a partially dispersion-compensated transmission line ensured that the signals at the various wavelengths appeared decorrelated when reaching the WC. The signals were amplified and filtered using a WSS with a filter bandwidth of 50 GHz. The launched power per channel at the fibre link input was 2 dBm. Following wavelength conversion and after traversing the loop a second time, the converted signals were received, characterized in terms of constellation diagrams and BER and their performance was compared to that of the signals both after a first circulation around the loop and after passage through the WC.

8.1.1 Multi-Channel Operation: Scenario 1

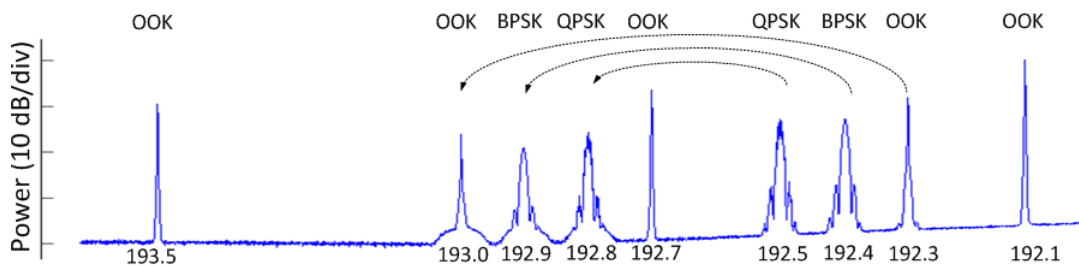


Figure 8.2: Spectral allocation of the various signals at the output of the transmission link for Scenario 1. Frequency references are given in THz

The first scenario that was considered highlights the modulation-independence and the multichannel operation of the scheme. In this scenario four non-return-to-zero (NRZ)-OOK signals at frequencies 192.1, 192.3, 192.7 and 193.5 THz, one NRZ-BPSK signal at 192.4 THz and one NRZ-QPSK signal at 192.5 THz were transmitted through the link. The rate of all signals was 10 Gbd. The signals at 192.3, 192.4 and 192.5 THz were chosen to be converted to 193.0, 192.9 and 192.8 THz, respectively, as shown in Fig. 8.2. One of the non-converted OOK signals was intentionally located in an unused part of the WC output bandwidth to prove negligible channel interference after further transmission.

The OSNRs required to achieve a BER of 10^{-3} for the signals that were wavelength converted are summarized in Fig. 8.3 for the back-to-back (B2B), after the first transmission (600 km), the wavelength conversion (600 km + WC) and the second loop transmission (600 km + WC + 600 km). This figure shows that the OSNR penalty due to wavelength conversion (the difference between circles and up-triangles in the left of Fig. 8.3) was very similar for the cases of BPSK and QPSK signals and was of the order of 2 dB.

It is to be noted that the coherent receiver used at the time of the measurements did not support OOK signals as a possible modulation format, so BER measurements could only be carried out at the end of the second loop, where digital dispersion compensation was

not required. For this case only, direct detection was used. Examples of eye diagrams and constellation diagrams observed at the input and at various transmission points are plotted in the right of Fig. 8.3 for OOK signals (top row), BPSK (middle row) and QPSK signals (bottom row).

8.1.2 Multi-Channel Operation: Scenario 2

The second scenario highlights both the wavelength selectivity and multichannel conversion of the scheme. In this scenario the same four NRZ-OOK signals as in the previous case, as well as two NRZ-QPSK signals at frequencies 192.5 THz (QPSK1) and 192.6 THz (QPSK2) were transmitted through the link. The symbol rate of all signals was again 10 Gbd. The signals at 192.3, 192.5 and 192.6 THz were chosen to be converted to 193.0, 192.8 and 192.7 THz, respectively as shown in Fig. 8.4.

As before, the OSNRs required to achieve a BER of 10^{-3} for the signals that were wavelength converted are summarized in the left of Fig. 8.5 for the back-to-back (B2B), after the first transmission (600 km), the wavelength conversion (600 km + WC) and the second loop transmission (600 km + WC + 600 km). As discussed previously, the OOK signals were not characterized at the intermediate stage, however their performance after the second passage through the loop was similar to that in Scenario 1.

It is to be noted that, in this scenario, the OSNR penalty undergone by QPSK2 was over 2.5 dB. This was a consequence of the lower power used for this signal as compared to the remaining signals at the input of the WC. This can also be appreciated in Fig. 8.5, showing a power difference of ~ 5 dB between the two signals, QPSK1 and QPSK2. As mentioned earlier, under these conditions the corresponding power ratio between QPSK2 and the generated HO mixing was lower than 20 dB, causing an increase in the

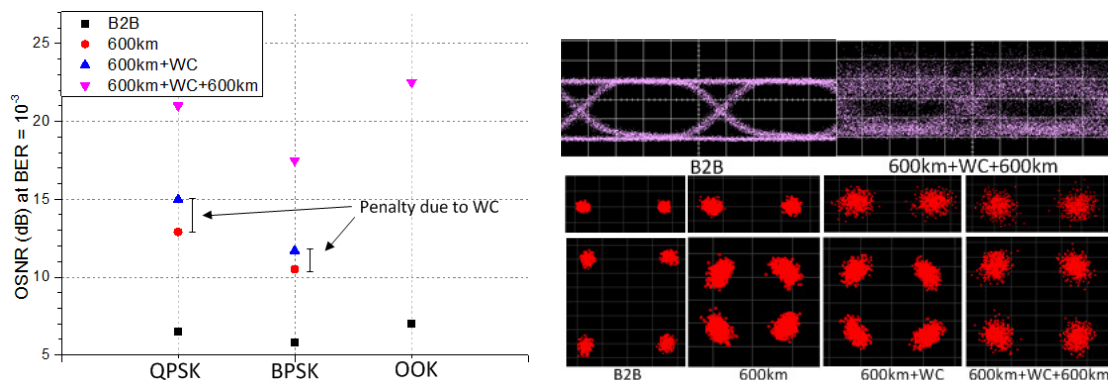


Figure 8.3: OSNR values for a BER of 10^{-3} at different transmission points for scenario 1 (left) and eye diagrams for the OOK signal (top row - time scale: 20 ps/div) and constellation diagrams for BPSK (middle row) and QPSK (bottom row) signals at different transmission points for scenario 1 (right)

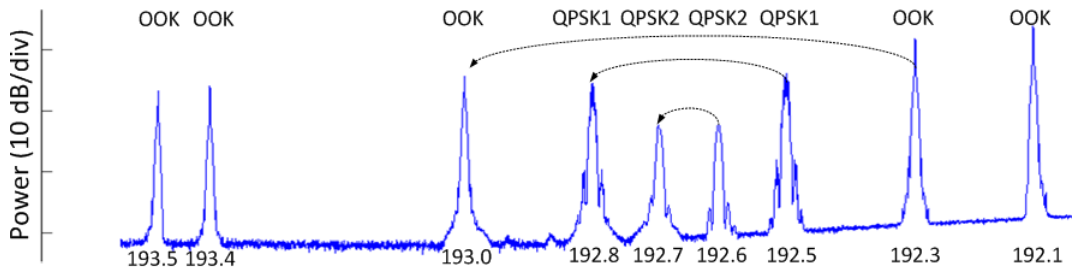


Figure 8.4: Spectral allocation of the various signals at the output of the transmission link for Scenario 2. Frequency references are given in THz

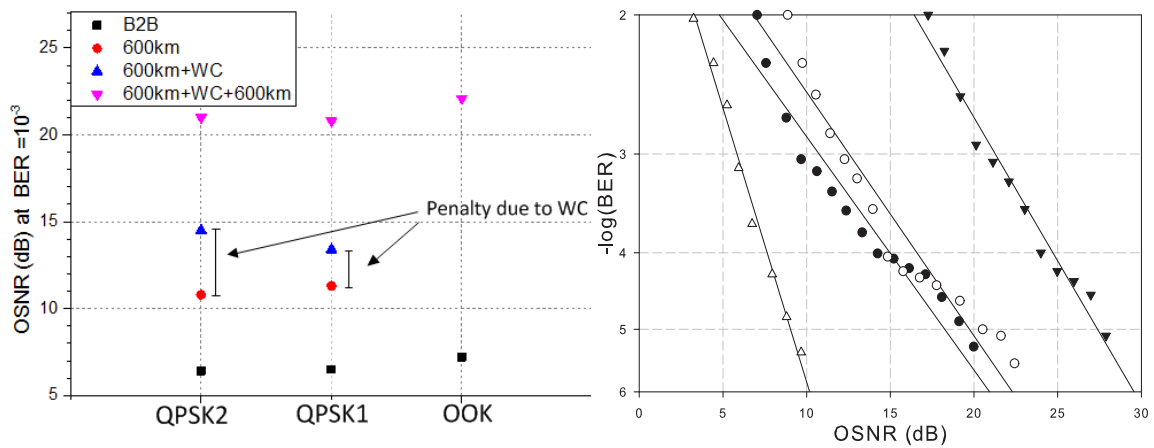


Figure 8.5: OSNR values for a BER of 10^{-3} at different transmission points for scenario 2 (left) and BER curves for QPSK1 back-to-back (B2B, open triangles), after the first transmission (600 km, solid circles), the wavelength conversion (600 km + WC, open circles) and the second loop transmission (600 km + WC + 600 km, solid triangles) (right)

power penalty for that particular channel. The BER curves for QPSK1 at different points along the transmission line are shown in Fig. 8.5.

8.2 Wavelength Conversion in Optical Switched Networks

Once the feasibility of implementing wavelength conversion in point-to-point transmission was demonstrated, the performance of this type of devices was investigated in optical switched networks, that exhibit larger variability and diversity in their operation. In these experiments, the WC was used as a component placed inside one of the ROADMs of a more complex network.

The diagram of the experimental setup is shown in Fig. 8.6 [9]. This scenario shows a switched network with five ROADMs capable of generating, receiving and routing wavelengths on demand. The input signals to the WC were dynamically routed from

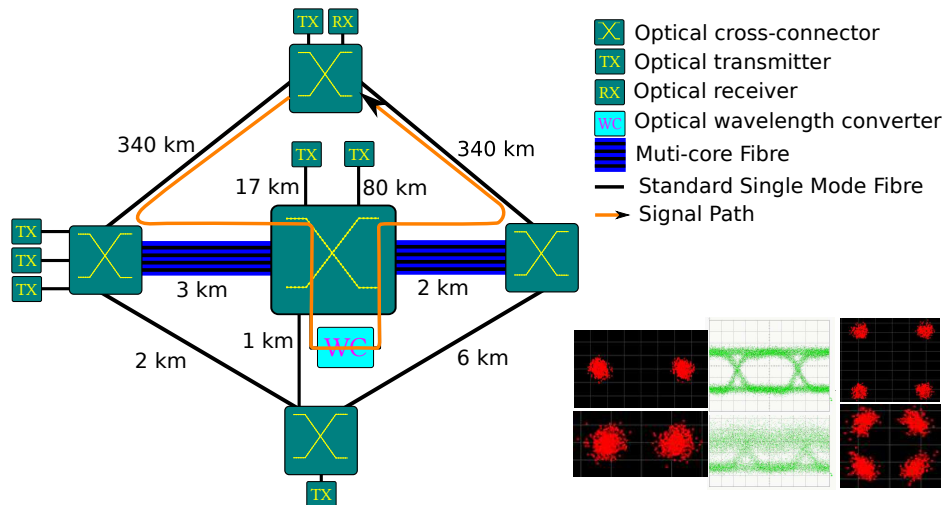


Figure 8.6: Scenario for characterisation of the WC in optical switched networks. Constellation and eye diagrams corresponding to the transmitted and received signals of the signal path

different sources, simultaneously wavelength converted and transmitted towards different destinations on demand. During these experiments the performance of the WC remained constant and exhibited similar behaviour as in the back-to-back or point-to-point experiments.

A detailed characterisation was performed for the route highlighted in orange in Fig. 8.6. This route represents fairly a typical metro network situation comprising two long amplified sections of 340km and passing through three ROADMS, where wavelength conversion is performed inside one of them. The two transmission sections of 340 km were formed in parts of the UK's Aurora dark fibre network [237] (the Essex to Southampton section of the network). The ROADMS were linked by means of 9-core multicore fibres of 2 km and 3 km length and their configuration was based on a MEMS and implemented an on-demand architecture [239]. This architecture proposes the use of a low-loss optical switch as the core of each ROADMS that allows for the routing of each optical signal through different subcomponents at each node depending on the function that needs to be implemented.

In this sense, in the first and third ROADMS in Fig. 8.6 were configured as pass-through nodes in which all the wavelengths coming from/to the dark fibre link were switched to/from one of the cores of the multicore fibre. On its part, the central ROADMS in Fig. 8.6 was configured in such a way that the optical signals were transmitted through three subcomponents. The optical signals were firstly demultiplexed using a wavelength selective switch (WSS), a part of them was used as the input to the WC and the rest were routed to a multiplexer together with the rest of the original signals. Even though multicore fibres were used to link the ROADMS, no contention problems derived from spatial switching were allowed during these tests.

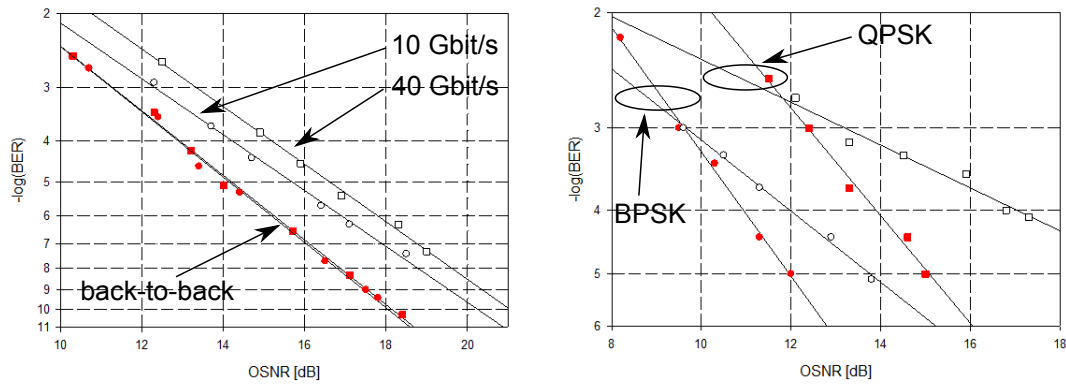


Figure 8.7: BER values measured for OOK signals (left) and PSK signals (right) in the optical switched scenario

The constellation and eye diagrams of the transmitted and received signals after the whole transmission path are displayed in the inset of Fig. 8.6 for different modulation formats. The corresponding BER curves measured at the transmitter and the receiver for OOK modulation at 10 and 40 Gbit/s are shown in Fig. 8.7 (left) whereas BER curves for BPSK and QPSK at 10 Gbit/s are shown in Fig. 8.7 (right). The penalty of the OOK signals was ~ 2 dB and ~ 3 dB for 10 and 40 Gbit/s respectively, exhibiting similar trends as the back-to-back signals for both cases. On its part the penalty exhibited by BPSK and QPSK signals was smaller ~ 1.5 dB although the presence of nonlinear effects induced a different slopes in the BER curves.

These experiments showed, for first time, the feasibility of implementation of all-optical wavelength conversion working as a black box in commercial networks with the required level of reliability (as demonstrated in Chapter 6), flexibility and compatibility with existing network topologies and architectures. In this sense, fibre-based wavelength conversion can be regarded as a mature technology to be considered for deployment in networks.

8.3 Wavelength Conversion in SDM Networks

The previous sections in this chapter showed the performance and the benefits of proposed implementations in current WDM networks in terms of a more efficient use of the optical spectrum. However, the question of optimum utilisation of the spectrum in future SDM networks will be a more complex and, at the same time, more important problem. SDM technologies have the potential to provide a dramatic increase in transmission capacity in a more cost- and power-efficient way than current WDM systems. At the network level, SDM introduces an additional degree of freedom in the form of the spatial dimension allowing a more efficient allocation of resources. However,

this additional level of flexibility introduces new challenges if the aim is that of an efficient management of resources.

In this context, and taking into account the experiments previously performed, the High Performance Network group at the University of Bristol requested the implementation of an evolution of the design of the WC to cope with the new contention problems that arise in SDM networks and that have been ignored in the previous experiments.

In particular, the introduction of SDM networking has resulted in an additional dimension that needs to be taken into account, leading to a more complex management of the new resources made available by it. In this manner, channel allocation in an efficient, flexible and dynamic manner presents new challenges when spatial channels allocated the same frequency need to be routed into a Flex-Grid WDM system based on standard single mode fibre (SSMF). This problem is particularly relevant at the edges of the network where the transmission medium changes from an SDM fibre to SSMF and must be addressed if the target is the development of flexible hybrid SDM/SSMF systems [10, 11].

Wavelength conversion can be used in SDM networks to implement conversion of a spatial superchannel to a spectral superchannel without electrical regeneration thus addressing a problem like the one shown in Fig. 8.8. This problem arises when several

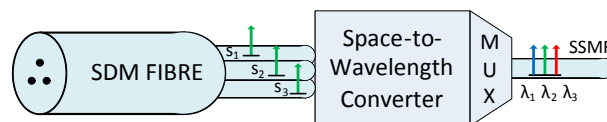


Figure 8.8: Contention problem arisen in hybrid SDM/SSMF systems

spatially-multiplexed channels with the same wavelength are to be routed to a single mode fibre. In this situation, all-optical wavelength conversion can be applied to them to address this contention problem. The implementation of such a space-to-wavelength converter can be based on a bidirectional optical wavelength converter, such as the one presented in Chapter 6 that exhibits an economy of components for these environments.

The performance of the space-to-wavelength converter was tested in a complex scenario (see Fig. 8.9) that emulates the interconnection between two data centres. Due to the

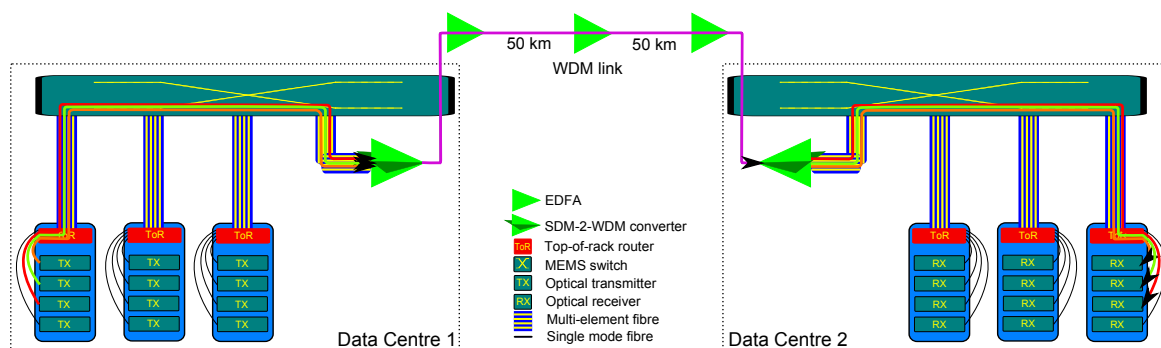


Figure 8.9: Scenario for characterisation of the WC in SDM networks

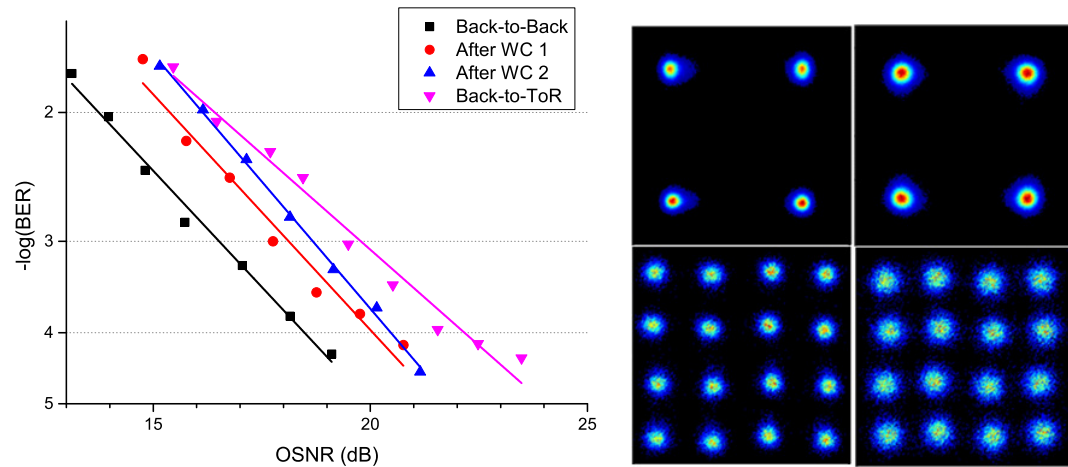


Figure 8.10: BER values measured for PDM-QPSK 40 Gbd signals (left) and constellation diagrams at transmission and reception for both modulation formats (right)

increasingly high density of fibres required for interconnection of equipment within data centres, the current trend suggests a progressive introduction of loosely coupled SDM fibres, such as multi-core or multi-element fibres, in order to increase the compactness of the structured cabling. However, the interconnection between data centres is performed through current WDM systems, leading to the aforementioned contention problems in hybrid environments when spatially multiplexed signals occupying the same frequency must be routed to the same single mode fibre.

The end-to-end experiment comprised the transmission of several channels at the same frequency between two data centres. These channels were transmitted through MEFs within the intra-data centre domain but contention resolution was required in order for them to be successfully transmitted through the WDM system that linked the two data centres. This contention resolution was performed by means of a space-to-wavelength converter and its wavelength-to-space counterpart. In this particular case, and due to the availability of a single space-to-wavelength converter, only two channels were transmitted, allowing the use of the wavelength converter as a space-to-wavelength converter in one direction and as a wavelength-to-space converter in the other.

The experiment was performed for two different modulation formats, polarisation multiplexed QPSK and polarisation multiplexed 16-QAM. In both cases the signals were modulated using a pseudo-random bit sequence (PRBS) of length $2^{31} - 1$ at a symbol rate of 40 Gbd. The pump powers used for each direction during this experiment were 20.40 and 21 dBm. These values showed to provide a good trade-off between the inherent OSNR penalty induced by the converter and the OSNR degradation induced by subsequent amplifications.

The total end-to-end OSNR degradation was 3.5 dB as shown in the left hand side of Fig. 8.10. This degradation includes both the space-to-wavelength conversion and the

amplification stages in the WDM link. In isolation, the converter exhibited a performance similar to the back-to-back operation in both directions, inducing an OSNR penalty of 1.9 dB. The constellation diagrams at the end of the transmission line for both modulation formats are shown in the right hand side of Fig. 8.10, showing the high quality of the recovered signal after the transmission.

In addition, the impact of the space-to-wavelength converter on the end-to-end latency of the full system was compared to that of an electrical wavelength converter. The latency of the optical solution was shown to be $70\mu s$, being limited by the speed of the analog-to-digital and digital-to-analog converters (DACs), whereas the latency of the electrical solution was in the order of hundreds of microseconds, due to the use of four additional DACs (two per conversion).

These experiments showed the potential benefits of the utilisation of space-to-wavelength converters as on-demand components in within reconfigurable network elements. The modulation independence of the WC prevents from the deployment of a pool of electric regenerators for each of the different modulation formats that coexists in commercial networks and that are currently used for contention resolution.

8.4 Conclusions

This chapter has presented a series of systems experiments that aimed at demonstrating the maturity of fibre-based all optical wavelength converters as devices that can provide reliable operation in commercial communication networks as well as the suitability of the particular subsystems that were described in Chapter 6.

The benefits of the wavelength converting systems developed in this thesis, originating from their modulation-, polarisation- and bit rate- independence have been demonstrated both in point-to-point and switched environments connected by installed fibre links, showing that they can provide a cost efficient alternative to a pool of electrical regenerators suitable for operation with different modulation formats and repetition rates.

Additionally, the potential benefits of the developed systems in future spatial division multiplexed systems have also been demonstrated, showing that they can be used to alleviate problems derived from the routing of signals coming from SDM fibres to standard single mode ones that will unavoidably arise in future data centre environments.

9.

Conclusions

It is only by the repeated study and perseverance joined to a natural taste, that a man can excel in the handling of anything

W. M. Thackeray

The dissertation of this work has been centred around two different tasks: the modelling of the noise and effects induced by parametric processes in optical communication systems and their application to commercial networking. The first task, mainly theoretical, has been described in Chapters 3, 4 and 5 whereas the latter one, eminently practical, has been described in Chapters 6, 7 and 8.

The key results presented in the aforementioned chapters are summarised in the following sections. Additionally, an outlook on future research directions worthwhile investigating are also provided for each topic.

9.1 Modelling

The modelling of parametric processes in optical communication systems started with an in-depth analysis of both the parametric interactions (Chapter 2) and the noise that these processes generate (Chapter 3). This analysis concluded with a classification of the noise sources generated in optical communication systems into three different categories: additive noise, multiplicative noise and phase noise. This classification allowed for a simplification in the calculations of the impact of these noise sources on modulated signals.

Unfortunately, this simplification was restricted to Gaussian noise sources, excluding the non-Gaussian ones from this analysis. A future extension to this kind of noise sources is desirable to account for their effects and improve the accuracy of the model. This task can be approached in two different manners: finding a Gaussian approximation of the non-Gaussian noise sources, which is usually the preferred way, and the consideration of

an additional noise source with non-Gaussian distribution, which can be mathematically very challenging.

Once the classification of noise sources was presented, a comprehensive description of the effect of these three noise types in communication systems was described (Chapter 4). This analysis showed that the effects induced by these noise types on modulated signals can be accurately characterized in terms of the BER induced, providing a new and powerful tool to design optical links. This tool is based on the description of the probability density functions of these noise types and how they degrade the BER either independently or in conjunction with each other. The model showed that, after a single amplification stage, phase noise cannot be modelled as an additional OSNR penalty, because this leads to an overestimation of the bit error rate and the use of a new probability density function is required for its computation.

The modelling of the accumulation of these noise sources was also analysed, yielding a model that computes the accumulation of amplitude noise independently of the accumulation of phase noise. Finally, the effects of photodetection were modelled, showing that in the presence of phase noise the BER of the signals can increase by a factor determined by the detection scheme used.

The validity of this model was partially validated through simulation (Chapter 4) and experimental measurements (Chapter 5). Monte-Carlo simulations were performed, showing the high accuracy of the model after a single amplification stage.

Laboratory measurements were taken confirming the predicted behaviour after a single parametric interaction and the influence of the photodetection scheme in the presence of phase noise. While it is true that these measurements do not fully validate of accuracy of the model, the trends and behaviours that the bit error rates exhibit in the presence of additive and phase noise match those predicted by the model.

As a future extension of this work, the accumulation of noise still needs to be validated in order to corroborate all the assumptions about the uncorrelated nature of the different noise types. This task can be accomplished either by using the same Monte-Carlo simulations after each stage of amplification or by taking laboratory measurements.

In addition to the modelled Gaussian distortions, a non-Gaussian distortion, the pump dithering transfer, was modelled (Chapter 5). As before, the measurements related to pump dithering transfer exhibited the trends predicted by the model. However, a mismatch of 3 dB between the theoretical model and the measurements must still be addressed.

This model can be used to estimate the performance of optical links that include parametric amplification as well as links simultaneously degraded by ASE noise and cross-phase modulation. In the first case, the impact of new effects, like the accumulation of the linewidth or the dithering of the pump waves, can be quantitatively estimated, whereas

in the latter one the degradation induced by cross-phase modulation can be accurately estimated.

9.2 Applications

The application of parametric processes to communication networks that was considered in this thesis was wavelength conversion (Chapter 6). Two different designs of wavelength converter were described, one in a one-directional operation and the other in a bidirectional operation, that was an extension of the uni-directional scheme. These devices meet all the necessary requirements to be installed in an optical communication system and the possible polarisation drifts of the pump waves were compensated for by developing an automatic pump alignment subsystem that allowed for turn-key operation.

The back-to-back performance of these devices provided transparent wavelength conversion of up to three input signals of a bandwidth narrower or equal to 100 GHz with a 2 dB OSNR degradation. The measured conversion gain was between -2 and 7 dB depending on the input power of the signal to be converted and the polarisation dependent gain exhibited was well below 1 dB.

These designs were tested with a variety of modulation schemes and bit rates as input signals. OOK, BPSK, QPSK and 16-QAM signals of bit rates ranging between 10 and 40 Gbps were successfully converted with these devices, exhibiting very similar performance in all the cases. In addition, polarisation multiplexed signals were also successfully converted with similar performance.

Once the laboratory characterisation was performed, the converters were tested in more challenging environments. The uni-directional wavelength converter was used in two field trials (Chapter 8) on point-to-point and optical switched networks, demonstrating the robustness of this implementation. On its part, the bi-directional wavelength converter was used in a spatial division multiplexing demonstration (Chapter 8).

During these experiments both designs exhibited the same performance as in operation without any transmission, and even allowed a dynamic reconfiguration of the input signals without affecting the performance of the communication channels in operation. These experiments demonstrated, for first time, the feasibility of operation of wavelength conversion in commercial networks and the benefits that this approach can provide in terms of efficient spectral use and cost efficiency.

These experiments also showed that SDM networks can greatly benefit from the use of wavelength conversion in terms of cost efficiency and latency, specially in the points of the network where WDM and SDM must coexist. The implementation of this functionality

would prevent the use of expensive electrical regeneration. One of the cases of particular interest is that of data centre interconnection, where the latency of the communications is of critical importance. The experiments showed that the use of optical wavelength conversion can reduce the latency in these environments.

Even though the performance exhibited by the wavelength converters allows them to operate in commercial networks, the future adoption of flexible grid in communication networks requires an improvement of the design of the wavelength converters to remove the restriction of a fixed channel allocation. In the same manner, it would be desirable to obtain higher gains and broader bandwidth of operation (allowing the simultaneous conversion of more channels). These tasks, presented as future extensions, may improve the cost efficiency of these devices and ease their adoption, therefore some possibilities for their implementation are discussed.

Flexible grid could be achieved by replacing the fixed grid filter for a wavelength selective switch. Higher gains could be achieved by increasing either the power of the pump waves or the nonlinear coefficient of the nonlinear fibre. In either case, the effect of self-phase modulation should be compensated for to avoid undesirable nonlinear effects. Finally broader bandwidth could be achieved by increasing the nonlinear coefficient of the fibre whereas its dispersion characteristics remain unchanged.

Additionally to the development of wavelength converters for SDM networks, this thesis reports the work performed in the characterisation of multi-element fibres (MEFs) as an alternative implementation of SDM. This novel type of fibres has the potential to implement SDM amplifiers with very highly efficient pump diffusion with no measurable levels of crosstalk. That is not the case for either multi-core or multi-mode amplifiers. Similarly, the potential of MEFs as transmission fibres has been demonstrated in systems experiments, showing that the flexibility of WDM networks can be achieved in their SDM counterpart.

Code of Phase Noise Simulations

The simulation of the phase noise in communication systems, in terms of probability density functions, has not been published in the literature. In this sense, the presentation of the code used during these simulations is of interest. The aim of this section is binding the theoretical definition of POSNR and its probability density function with the very values of the phase perturbation induced depending on the physical effect simulated.

In this manner, two chunks of code are presented, the first one showing the calculation of the BER induced by a mixture of additive and phase noise defined in terms of OSNR and POSNR and the second showing the implementation of the Gaussian random variables as function of OSNR and POSNR used during the Monte-Carlo simulations.

Analytical Computation of BERs

The following code presents an implementation of the calculations performed in Chapter 4 for the analytical calculation of the probability of error in the presence of both additive and phase noises. This code has been developed under GNU Octave but should also work in Matlab environments.

```
1 OSNR = 0:1:25;
2 osnr = 10.^(OSNR/10);
3 POSNR = 0:1:25;
4 psnr = 10.^(POSNR/10);
5
6 N = 4000; % 40000;
7
8 x = linspace(-5,5,N+1);           % +1 sample for 0 value
9 y = linspace(-0.999,0.999,N/5+1); % +1 sample for 0 value
10 % very important !!! sampling rate of x and y must be very similar
11 % otherwise the convolution operation provides an erroneous result.
12
13
14 theta0 = 0;                       % BPSK modulation format
15 %theta0 = pi/4;                   % QPSK modulation format
16 %theta0 = 3*pi/8;                % 8PSK modulation format
17
```

```

18 X = length(OSNR);
19 Y = length(POSNR);
20
21 BER = zeros(X,Y);
22 BER_orig = zeros(X,Y);
23 BER_pha = zeros(X,Y);
24
25 for i = 1:X % OSNR loop
26     for j = 1:Y % POSNR loop
27
28         sigma2 = 1/osnr(i);
29         sigma2_p = 1/psnr(j);
30
31         % Gaussian PDF
32         pdf_amp = 1/sqrt(2*pi*sigma2)*exp(-(x-cos(theta0)).^2/(2*sigma2));
33         [m,i_amp] = max(pdf_amp); % get the index of the mode
34
35         % Projectd phase noise PDF
36         pdf_pha = 1/sqrt(2*pi*sigma2_p).*exp(-(acos(y)-theta0).^2/(2*sigma2_p)).
37             ./sqrt(abs(1-sign(y).*y.^2));
38         pdf_pha = pdf_pha/trapz(y,pdf_pha); % normalisation
39
40         % convolution of PDFS
41         pdf_conv = conv(pdf_amp,pdf_pha,'full');
42         [m,i_conv] = max(pdf_conv); % get the index of the mode
43
44         % alignment of new mode to the previous index.
45         % Convolution does NOT shift the mode of the distribution!!
46         pdf_conv = pdf_conv((i_conv-i_amp):(i_conv+N-i_amp));
47         pdf_conv = pdf_conv/trapz(x,pdf_conv); % normalisation
48
49         % integration => probabilities of error
50
51         % full PDF
52         BER(i,j) = trapz(x(1:(N/2-1)),pdf_conv(1:(N/2-1)));
53         % only amplitude noise
54         BER_orig(i,j) = trapz(x(1:(N/2-1)),pdf_amp(1:(N/2-1)));
55         % only phase noise
56         BER_pha(i,j) = trapz(y(1:(N/10-1)),pdf_pha(1:(N/10-1)));
57     end % POSNR loop
58 end % OSNR loop
59
60 [XX,YY] = meshgrid(OSNR,POSNR);
61 mesh(XX,YY,log10(BER'));
62 xlabel('OSNR');
63 ylabel('POSNR');

```

Noise Generation in Monte-Carlo Simulations

The following chunk of code presents the implementation of the code that generates noise samples of additive, multiplicative and phase noise from the corresponding OSNRs defined in Chapter 4.

The code requires the GNU Scientific Library (<https://www.gnu.org/software/gsl/>) for complex number operations. This code was tested with the versions 1.15 and 1.16 of this library.

```
65  /*
66  * noise.c
67  *
68  */
69  #include <gsl/gsl_complex.h> // GNU scientific library
70  #define PI 3.141592654
71
72  /**
73   * generates a sample of a Gaussian r.v. with mean 0 and variance 1
74   * Taken from "Numerical Recipes in C"
75   */
76  double gaussrand(){
77     static double U, V;
78     static int phase = 0;
79     double Z;
80
81     if(phase == 0){
82         U = (rand()+ 1.) / (MAX RAND + 2.);
83         V = rand() / (MAX RAND + 1.);
84     }
85
86     if(phase == 0)
87         Z = sqrt(-2 * log(U)) * sin(2 * PI * V);
88     else
89         Z = sqrt(-2 * log(U)) * cos(2 * PI * V);
90
91     phase = 1 - phase;
92
93     return Z;
94 }
95
96 /**
97  * Generation of Additive noise
98  */
99 void awgnchannel(complex *signal, unsigned int len, double noisedB){
100    unsigned int i = 0;
101    double noiseNat = pow(10,0.05*noisedB);
102    // 0.05 => noise is defined in terms of electric field
103
104    if(noisedB == 0)
```

```

105     return;
106
107     for(i = 0; i < len; i++)
108         signal[i] = gsl_complex_add(signal[i],
109                                     gsl_complex_rect(noiseNat*gaussrand(),
110                                                         noiseNat*gaussrand()));
111     };
112 }
113
114 /**
115  * Generation of Multiplicative Amplitude noise
116  */
117 void mwgnchannel(complex *signal, unsigned int len, double noisedB){
118     unsigned int i = 0;
119     double noiseNat = pow(10,0.05*(noisedB));
120
121     if(noisedB == 0)
122         return;
123
124     for(i = 0; i < len; i++){
125         gsl_complex n = gsl_complex_rect(noiseNat*gaussrand(),
126                                         noiseNat*gaussrand());
127         n = gsl_complex_add_real(n,1);
128         signal[i] = gsl_complex_mul(signal[i], n);
129     }
130 }
131
132 /**
133  * Emulates nonlinear effects and phase noise with zero mean
134  */
135 void linebroadening(complex *signal, unsigned int len, double posnr){
136     unsigned int i;
137
138     /**
139      *  $\langle \phi^2 \rangle = 1.0/\text{posnr}$ ;
140      */
141     if(posnr == 0)
142         return;
143
144     double var_phi = 1.0/posnr;
145
146     for(i=0; i < len; i++){
147         signal[i] = gsl_complex_mul(signal[i],
148                                     gsl_complex_polar(1, sqrt(var_phi)*gaussrand()));
149     };
150 }
151 }
152
153 /**
154  * Emulates laser linewidth transfer.
155  */

```

```

156 void linebroadening_drift(complex *signal, unsigned int len, double posnr){
157     /**
158     *   Conversion between posnr and linewidth:
159     *
160     *   The phase variance between to symbols induced by laser linewidth is:
161     *
162     *    $\langle \phi^2 \rangle = \text{PI} * \text{linewidth} * T_{\text{symbol}}$ 
163     *
164     *   From:
165     *
166     *   "Theory of linewidth semiconductor lasers" C.H. Henry
167     *   IEEE JQE 18(2) 259--264 (1982)
168     *
169     *   Since  $\text{posnr} = 1 / \langle \phi^2 \rangle \Rightarrow \text{linewidth} = 1 / (\text{PI} * \text{posnr})$ 
170     *
171     *   *****
172     *
173     *   For the emulation of a linewidth, the variance of the Gaussian r.v.
174     *   is equal to  $\text{std} \langle \text{random Gauss} \rangle = \text{sqrt}(2 * \text{PI} * \text{linewidth} * T)$ 
175     *
176     *   From:
177     *
178     *   "Experimental demonstration of a flexible and stable semiconductor
179     *   laser linewidth emulator" Zuraidah Zan and Arthur James Lowery
180     *   Optics Express 18(13) 13880--13885 (2010)
181     */
182     unsigned int i;
183     double linewidth = 1.0/(PI*posnr); // assumed T = 1
184     double std = sqrt(2*PI*linewidth);
185
186     double last = 0;
187     for(i=0; i < len; i++){
188         // restricts to (-PI,PI) interval
189         const double LIM = PI;
190         double temp = std*gaussrand();
191         if (abs(temp + last) <= LIM ){
192             last += temp;
193         }
194         else if (abs(temp - last) <= LIM ){
195             last -= temp;
196         }
197         else {
198             // temp is bigger than 2*LIM => IMPLEMENTS 2*PI PERIODICITY
199             temp = temp - ((int)(temp/(2*LIM)))*2*LIM; // obtain the remainder
200             if(abs(last + temp) <= LIM)
201                 last += temp;
202             else
203                 last -= temp;
204         }
205         signal[i] = gsl_complex_mul(signal[i],gsl_complex_polar(1,last));
206     }

```

```

207 }
208
209 /**
210  * Emulates pump dithering transfer.
211  */
212 void linebroadening_dither(complex *signal, unsigned int len, double posnr){
213     /**
214      *
215      * Conversion between posnr and phase drift. The perturbation induced by
216      * a deterministic frequency drift after T seconds is:
217      *
218      *  $\Delta\langle\phi\rangle = 2\pi\text{frequency}\cdot T$ 
219      *
220      * This value is constant and represents the phase difference between
221      * samples (in the previous case it was a Gaussian r.v but now it is
222      * deterministic)
223      *
224      *  $\text{posnr} = 1/\Delta\langle\phi\rangle = 1/(2\pi\text{frequency}\cdot T)$ 
225      *
226      * No references. This is my own derivation
227      */
228     unsigned int i;
229     double std = sqrt(1.0/posnr); // deterministic perturbation
230     double last = 0;
231
232     for(i=0; i < len; i++){
233         const double LIM = PI;
234         double temp = std;
235         // same algorithm as with linewidth, but now the drift is deterministic
236         if (abs(temp + last) <= LIM ){
237             last += temp;
238         }
239         else if (abs(temp - last) <= LIM ){
240             last -= temp;
241         }
242         else {
243             // temp is bigger than 2*LIM => IMPLEMENTS 2*PI PERIODICITY
244             temp = temp - ((int)(temp/(2*LIM)))*2*LIM; // obtain the remainder
245             if(abs(last + temp) <= LIM)
246                 last += temp;
247             else
248                 last -= temp;
249         }
250
251         signal[i] = gsl_complex_mul(signal[i],gsl_complex_polar(1,last));
252     }
253 }

```

Gaussian approximation of phase noise

Chapter 4 showed that analytical values for the probability of error of signals degraded by phase noise can be obtained by integration of the PDF shown in equation (4.18). However, it is a common practice in communications to obtain Gaussian approximations of these PDFs. This approach entails the assumption that phase noise can be computed as an additional OSNR penalty.

In this appendix, an study of the accuracy of such approximation for the particular case of phase noise is presented. In this case, this task was performed by approximating the distribution shown in equation (4.18) by a Gaussian random variable with a proper variance. In doing so, the following approximated expressions for the BER of M-PSK modulation formats were obtained

$$\begin{aligned}
 P_{BPSK} &= \frac{1}{2} \operatorname{erfc} \left(\sqrt{\frac{AOSNR \cdot POSNR}{0.43 \cdot AOSNR + 1.85 \cdot POSNR}} \right) \\
 P_{QPSK} &= \frac{1}{2} \operatorname{erfc} \left(\sqrt{\frac{AOSNR \cdot POSNR}{3.22 \cdot AOSNR + 3.7 \cdot POSNR}} \right) \\
 P_{8PSK} &= \frac{1}{2} \operatorname{erfc} \left(\sqrt{\frac{AOSNR \cdot POSNR}{10 \cdot AOSNR + 11.1 \cdot POSNR}} \right)
 \end{aligned} \tag{B.1}$$

The estimation of the coefficients was performed by minimising the difference between the BER obtained with the exact calculation and the BER obtained with the previous expressions. The accuracy of these approximations was shown in Fig. 4.11 (compare the results with Fig. 4.9 in page 60). While an extremely good agreement is obtained for QPSK signals, the approximation leads to an underestimation of the probability of error the remaining cases. This decreased accuracy shows that phase noise cannot be modelled as an OSNR penalty.

PDFs after Photodetection

This appendix describes the distortion that phase noise induces on the PDF of the electrical signals after differential detection. For the sake of a clear explanation, firstly the effect of additive noise on the signals will be revisited and latterly extended by including the effect of phase noise on the schemes. In this sense, it is very useful to revisit the theory of direct detection event though it cannot directly detect phase modulated signal because this scheme is the basis of differential detection receivers.

Direct Detection

The simplest detection scheme used in optical communications is direct detection. This scheme is used to demodulate amplitude modulated signals because is insensitive to phase changes. Nevertheless, the statistics of electrical signals generated by this process are similar to that of differential receivers [161].

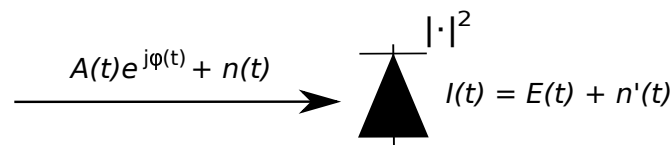


Figure C.1: Block diagram of a direct detection scheme

The diagram of a direct detection system is shown in Fig. C.1. The outcome of the detection process of an amplitude modulated signal (labelled as $A(t)$) is a signal stripped of any phase information ($\varphi(t)$). If the detection is performed on a signal degraded by an optical zero-mean Gaussian additive noise ($n(t)$), the outcome of the detection is accompanied by an additive noise with different statistical features ($n'(t)$). This electric noise is dependent on the signal energy ($E(t)$), on the optical noise power and on the number of states of polarization of the optical noise.

In this manner, for an OOK signal with energy levels 0 and E the Gaussian distribution of the optical noise is turned into a central χ^2 PDF for the case of energy level 0 and into a noncentral χ^2 PDF for the case of energy level E . The analytical expressions of these PDFs are

$$\begin{aligned}
 pdf_0(x, N_0, M) &= \frac{1}{N_0} \frac{\left(\frac{x}{N_0}\right)^{M-1} \exp\left(-\frac{x}{N_0}\right)}{(M-1)!} \\
 pdf_E(x, E, N_0, M) &= \frac{1}{N_0} \left(\frac{x}{E}\right)^{M-1/2} \exp\left(-\frac{x+E}{N_0}\right) I_{M-1}\left(2\frac{\sqrt{xE}}{N_0}\right)
 \end{aligned} \tag{C.1}$$

where E represents the pulse mean energy, N_0 the optical noise energy and $2M$ the number of degrees of freedom of the PDFs. M depends on the number of polarization states of the optical noise ($p = 1$ or 2), the symbol time (T) and the optical bandwidth (B). Its mathematical definition is: $M = pBT/2$ [161, 240].

Differential Detection

In order to detect optical BPSK signals, differential detection was introduced. In front of the photodetector a delay line interferometer (DLI) is placed that transforms phase shifts into amplitude ones [182]. A diagram of this detection scheme is shown in Fig. C.2.

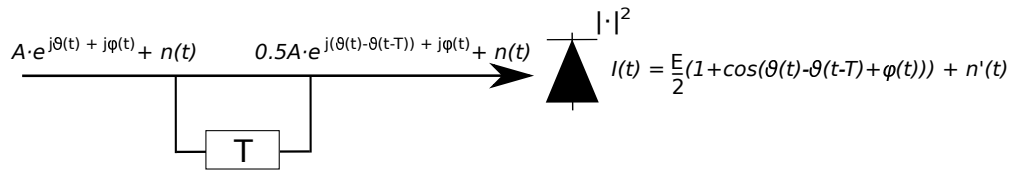


Figure C.2: Block diagram of a differential detection scheme

Depending on the phase difference between consecutive symbols ($\theta(t) - \theta(t - T)$ in Fig. C.2) the optical signal will undergo either constructive or destructive interference, producing a photocurrent whose values range between 0 and E . The installation of the DLI does not change the statistical properties of the electrical signals. In this manner, in the absence of phase noise, the PDFs of the symbols will be a central χ^2 for the 0 level (phase difference between consecutive symbols of π) and noncentral χ^2 for the E level (phase difference between consecutive symbols of 0).

However, in the presence of phase noise ($\varphi(t)$), this phase difference is not deterministic anymore, resulting in a neither fully-constructive nor fully-destructive interference. In this case, the photocurrent can be expressed as

$$I(t) = \frac{A}{2} (1 + \cos(\theta(t) - \theta(t - T)) \cos(\varphi(t)) + \sin(\theta(t) - \theta(t - T)) \sin(\varphi(t))) + n'(t) \tag{C.2}$$

In the case of a BPSK modulation format where the phase difference between consecutive symbol of 0 and π , the previous expression reduces to

$$I(t) = \frac{A}{2} (1 + \cos(\theta(t) - \theta(t - T))\cos(\varphi(t))) + n'(t) \quad (\text{C.3})$$

Thus, the effect of the phase noise after the DLI can be modelled as a perturbation that statistically changes the mean value of the optical signal power. The PDF of this perturbation results in an statistical average over all the possible χ^2 distributions that can be induced in the presence of phase noise. Mathematically this can be expressed as [241]

$$pdf_{diff}(x) = \int_{-\infty}^{\infty} pdf_E(E(\varphi), N_0, M) \cdot pdf_{\varphi}(\varphi, \varphi_0, \sigma_{\varphi}^2) d\varphi \quad (\text{C.4})$$

where pdf_E represents the χ^2 distribution shown in (C.1) with mean value $E(\varphi) = E_0/2(1 + \cos \varphi)$, pdf_{φ} is shown in equation (4.18).

The outcome of this averaging is displayed in Fig. C.3 for different values of AOSNR and POSNR. These figures show that changes in the ASE noise induce the modification of the spread of the distribution while the mean value is kept constant whereas changes in the phase noise create tails between both symbol means while the spread of the distribution remains unchanged.

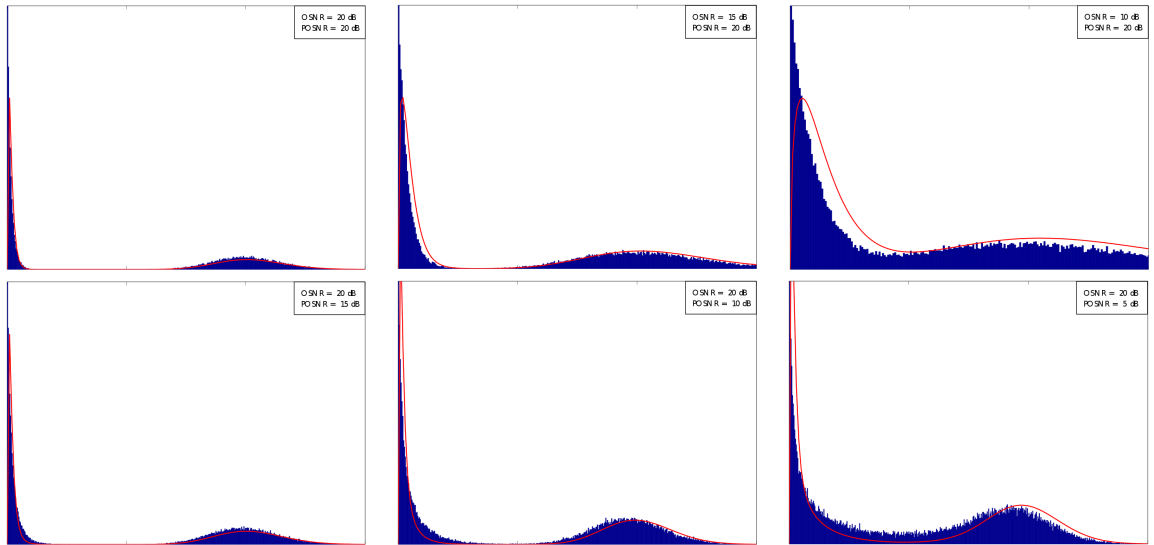


Figure C.3: Evolution of probability density functions for differential detection when OSNR decreases (top row) and when POSNR decreases (bottom row). Analytical curves shown in red and histograms from Monte-Carlo simulation shown in blue

Balanced Differential Detection

In order to increase the sensitivity of the previous scheme, balanced differential detection was developed. This configuration uses the second port of the DLI to increase the total signal power detected, but it does not result in an increase the performance in terms of BER with respect to the OSNR. The diagram of this detection scheme is shown in Fig. C.4.

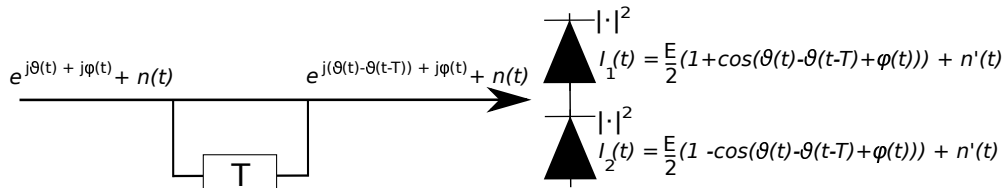


Figure C.4: Block diagram of a balanced differential detection scheme

The effect of the use of the second port of the DLI and the use of an additional photodetector doubles the distance between the symbols of the constellation (whose mean values are located now at $-E$ and E) whereas also doubles the received additive noise power. Therefore, the performance in terms of OSNR remains unchanged. However, the performance improves in terms of POSNR since it does not depend on the additive noise power. In this sense, this detection scheme is more insensitive to phase noise than the previous one.

In this case, the calculation of the PDF of the symbols can be performed on the basis of the PDF of the unbalanced case. As shown in Fig. C.4 the resulting photocurrents can be calculated from equation (C.3), leading to the following values

$$\begin{aligned} I_1(t) &= \frac{A}{2} (1 + \cos(\theta(t) - \theta(t-T))) \cos(\varphi(t)) + n'(t) \\ I_2(t) &= \frac{A}{2} (1 + \cos(\theta(t) - \theta(t-T) + \pi)) \cos(\varphi(t)) + n'(t) \end{aligned} \quad (\text{C.5})$$

where, as before, $\varphi(t)$ represents the phase noise. The PDFs of this photocurrents can be derived as before, leading to the following expressions:

$$\begin{aligned} pdf_1(x) &= \int_{-\infty}^{\infty} pdf_E(E_1(\varphi), N_0, M) \cdot pdf_{\varphi}(\varphi, 0) d\varphi \\ pdf_2(x) &= \int_{-\infty}^{\infty} pdf_E(E_2(\varphi), N_0, M) \cdot pdf_{\varphi}(\varphi, \pi) d\varphi \end{aligned} \quad (\text{C.6})$$

where E_1 and E_2 are the mean value energies for the detected symbols, being their values $E_1(\varphi) = E_0/2(1 + \cos \varphi)$ and $E_2(\varphi) = E_0/2(1 - \cos \varphi)$. Once these values are

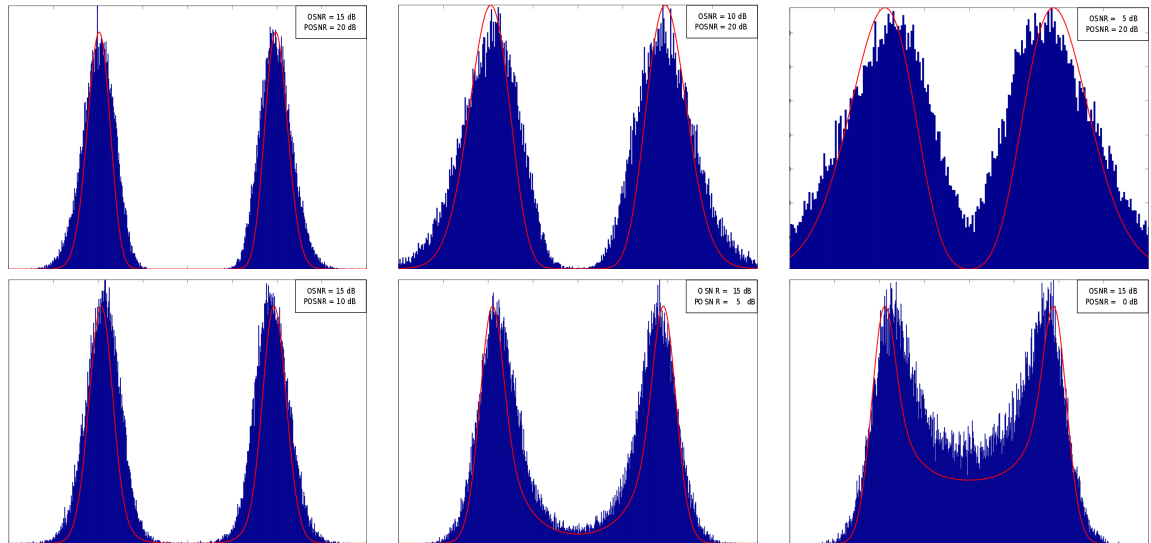


Figure C.5: Evolution of probability density functions for balanced differential detection when OSNR decreases (top row) and when POSNR decreases (bottom row). Analytical curves shown in red and histograms from Monte-Carlo simulation shown in blue

calculated, the PDF of the subtraction of currents can be obtained through the standard rules of statistics [168]

$$pdf_{bal}(x) = pdf_1(x) * pdf_2(-x) \quad (C.7)$$

where $*$ represents the convolution operation. This distribution is displayed in Fig. C.5 for different values of OSNR and POSNR. These figures show the same behaviour as before, creating growing tails between the symbols with the increase of the phase noise and spreading the distributions in case of increase of ASE noise.

List of Publications

Journal Papers:

- **V. J. F. Rancaño**, F. Parmigiani, P. Petropoulos, D. J. Richardson
"100-GHz grid-aligned multi-channel polarization insensitive black-box wavelength converter"
Journal of Lightwave Technology 32(17) 3027 (2014)
- **V. J. F. Rancaño**, S. Jain, T. May-Smith, S. Y. Yan, E. H. Salas, G. Zervas, D. Simeonidou, P. Petropoulos, and D. J. Richardson
"Demonstration of space-to-wavelength conversion in sdm networks,"
Photonics Technology Letters, to be published, 2015.
- S. Y. Yan, E. H. Salas, **V. J. F. Rancaño**, Y. Shu, G. Saridis, B. R. Rofoee, A. E. Peters, T. C. May-Smith, P. Petropoulos, D. J. Richardson, G. Zervas, and D. Simeonidou,
"Archon: a function programmable optical interconnect architecture for transparent intra and inter data center sdm/tdm/wdm networking,"
Journal of Lightwave Technology, to be published, 2015.
- S. Jain, **V. J. F. Rancaño**, T. C. May-Smith, P. Petropoulos, J. K. Sahu, D. J. Richardson
"Multi-element fiber for space-division multiplexing operations"
Optics Express 2014 Vol.22(4) pp.3787-3796
- N. Amaya, M. Irfan, G. Zervas, K. Baniyas, M. Garrich, I. Henning, D. Simeonidou, Y. R. Zhou, A. Lord, K. Smith, **V. Rancaño**, S. Liu, P. Petropoulos, D. J. Richardson
"Gridless optical networking field trial: flexible spectrum switching defragmentation and transport of 10G/40G/100G/555G over 620-km field fiber"
Optics Express 2011 Vol.19(26) pp.B277-B282

Invited Talks:

- **V. J. F. Rancaño**, S. Jain, T. C. May-Smith, J. K. Sahu, P. Petropoulos, D. J. Richardson
"Spatial Division Multiplexing using Multi-Element Fibers"
IEEE Summer Topicals Montreal 14-16 Jul 2014 TuE4.4
- **V. J. F. Rancaño**, S. Jain, T. C. May-Smith, J. K. Sahu, P. Petropoulos, D. J. Richardson
"Multi-Element Fibers in High Capacity Communication Systems"
Advanced Photonics Conference Barcelona 27-31 Jul 2014

Conference Papers:

- **V. J. F. Rancaño**, S. Jain, T. C. May-Smith, J. K. Sahu, P. Petropoulos, D. J. Richardson
"First demonstration of an amplified transmission line based on multi-element fibre technology"
ECOC 2013 London 22-26 Sep 2013 PD1.C.2 (Postdeadline)
- S. Y. Yan, E. H. Salas, **V. J. F. Rancaño**, Y. Shu, G. Saridis, B. R. Rofoee, A. E. Peters, S. Jain, T. May-Smith, P. Petropoulos, D. J. Richardson, G. Zervas, and D. Simeonidou
"First demonstration of all-optical programmable sdm/tdm intra-data centre and wdm inter-dcn communication,"
ECOC PD.1.2 (postdeadline) 2014.
- **V. J. F. Rancaño**, F. Parmigiani, P. Petropoulos, D. J. Richardson "100 GHz grid-aligned reconfigurable polarization insensitive black-box wavelength converter
Conference on Optical Fibre Communications OFC '13 Anaheim USA 19-21 March 2013 JTh2A.19
- **V. J. F. Rancaño**, F. Parmigiani, P. Petropoulos, D. J. Richardson
"Field trial experiment over 1200 km on a 100GHz grid-aligned multi-channel black-box wavelength converter"
Conference on Optical Fibre Communications OFC '13 Anaheim USA 17-21 March 2013 OTh1.C2
- J. K. Sahu, S. Jain, **V. Rancaño**, T. C. May-Smith, A. Webb, P. Petropoulos, D. J. Richardson
"Multi-element fiber for space-division multiplexing"
SPIE Photonics West San Francisco 1-6 Feb 2014 9009 (Invited)
- S. Jain, T. C. May-Smith, **V. J. F. Rancaño**, P. Petropoulos, D. J. Richardson, J. K. Sahu
"Multi-element fibre for space-division multiplexed transmission"
ECOC 2013 London 22-26 Sep 2013 Mo.4.A.2
- L. Jones, F. Parmigiani, **V. J. F. Rancaño**, M. A. Ettabib, P. Petropoulos, D. J. Richardson
"Transmission performance of phase-preserving amplitude regenerator based on optical injection locking"
OFC '13 Anaheim, USA 19-21 March 2013
- N. Amaya, M. Irfan, G. Zervas, K. Baniyas, M. Garrich, I. Henning, D. Simeonidou, Y. R. Zhou, A. Lord, K. Smith, **V. Rancaño**, S. Liu, P. Petropoulos, D. J. Richardson
"Gridless optical networking field trial: flexible spectrum switching, defragmentation and transport of 10G/40G/100G/555G over 620-km field fiber"
ECOC Geneva, Switzerland 18-22 Sep 2011 (Postdeadline)
- N. Gonzalez, G. Zervas, M. Irfan, R. Nejabati, D. Simeonidou, **V. Rancaño**, F. Parmigiani, P. Petropoulos, D. Richardson, J. Sakaguchi, W. Klaus, B. J. Puttman, T. Miyazawa, Y. Awaji, N. Wada, I. Henning
"On-demand spectrum and space defragmentation in an elastic SDM/FDM/TDM network with mixed multi-and single-core fiber links"
OFC '13 Anaheim 19-21 March 2013 OTh4B.3

Bibliography

- [1] V. J. F. Rancaño, F. Parmigiani, P. Petropoulos, and D. J. Richardson, "100GHz grid-aligned reconfigurable polarization insensitive black-box wavelength converter," in *OFC JTh2.A.19*, 2013.
- [2] —, "Field trial experiment over 1200 km on a 100GHz grid-aligned multi-channel black-box wavelength converter," in *OFC OTh1.C.2*, 2013.
- [3] V. J. F. Rancaño, S. Jain, T. C. May-Smith, J. K. Sahu, P. Petropoulos, and D. J. Richardson, "First demonstration of an amplified transmission line based on multi-element fibre technology," in *ECOC PD1.C.2*, 2013.
- [4] S. Jain, V. J. F. Rancaño, T. C. May-Smith, J. K. Sahu, P. Petropoulos, and D. J. Richardson, "Multi-element fiber for space-division multiplexing operations," *Optics Express*, vol. 22, no. 4, pp. 3787–3796, 2014.
- [5] V. J. F. Rancaño, S. Jain, T. C. May-Smith, J. K. Sahu, P. Petropoulos, and D. J. Richardson, "Spatial division multiplexing using multi-element fibers," in *IEEE Summer Topics (Invited)*, 2014.
- [6] —, "Multi-element fiber technology in high-capacity optical communication systems," in *Specialty Optical Fibers (Invited)*, 2014.
- [7] V. J. F. Rancaño, F. Parmigiani, P. Petropoulos, and D. J. Richardson, "100GHz grid-aligned multi-channel polarization insensitive black-box wavelength converter," *Journal of Lightwave Technology*, vol. 32, no. 17, p. 3027, 2014.
- [8] V. J. F. Rancaño, S. Jain, T. May-Smith, S. Y. Yan, E. H. Salas, G. Zervas, D. Simeonidou, P. Petropoulos, and D. J. Richardson, "Demonstration of space-to-wavelength conversion in SDM networks," *Photonics Technology Letters*, vol. to be published, 2015.
- [9] N. Amaya, M. Irfan, G. Zervas, R. Nejabati, D. Simeonidou, V. J. F. Rancaño, F. Parmigiani, P. Petropoulos, D. J. Richardson, J. Sakaguchi, W. Klaus, B. J. Puttnam, T. Miyazawa, Y. Awaji, N. Wada, and I. Henning, "On-demand spectrum and space defragmentation in an elastic SDM/FDM/TDM network with mixed multi- and single-core fiber links," in *OFC OTh4B.3*, 2013.

- [10] S. Y. Yan, E. H. Salas, V. J. F. Ranaño, Y. Shu, G. Saridis, B. R. Rofoee, A. E. Peters, S. Jain, T. May-Smith, P. Petropoulos, D. J. Richardson, G. Zervas, and D. Simeonidou, "First demonstration of all-optical programmable SDM/TDM intra-data centre and wdm inter-dcn communication," in *ECOC PD.1.2 (postdeadline)*, 2014.
- [11] S. Y. Yan, E. H. Salas, V. J. F. Ranaño, Y. Shu, G. Saridis, B. R. Rofoee, A. E. Peters, T. May-Smith, P. Petropoulos, D. J. Richardson, G. Zervas, and D. Simeonidou, "Archon: a function programmable optical interconnect architecture for transparent intra and inter data center SDM/TDM/WDM networking," *Journal of Lightwave Technology*, vol. to be published, 2015.
- [12] L. Jones, F. Parmigiani, V. J. F. Ranaño, M. A. Etabib, P. Petropoulos, and D. J. Richardson, "Transmission performance of phase-preserving amplitude regenerator based on optical injection locking," in *OFC OW4C.4*, 2013.
- [13] N. Amaya, M. Irfan, G. Zervas, K. Baniyas, M. Garrich, I. Henning, D. Simeonidou, Y. R. Zhou, A. Lord, K. Smith, V. J. F. Ranaño, S. Liu, P. Petropoulos, and D. J. Richardson, "Gridless optical networking field trial: flexible spectrum switching, defragmentation and transport of 10G/40G/100G/555G over 620-km field fiber," *Optics Express*, vol. 19, no. 26, B277–B282, 2011.
- [14] —, "Gridless optical networking field trial: flexible spectrum switching, defragmentation and transport of 10G/40G/100G/555G over 620-km field fiber," in *ECOC Th.13.K.1 (postdeadline)*, 2011.
- [15] K. G. Coffman and A. M. Odlyzko, in *Optical Fiber Telecommunications*. Academic Press, 2002, vol. IV-B, ch. 2.
- [16] P. M. Walker and S. L. Mathison, "Regulatory policy and future data transmission services," in *Compute Communication Networks*. Prentice Hall, 1973, pp. 295–370.
- [17] A. M. Noll, *Highway of Dreams: a critical appraisal of the Communications Superhighway*. Lawrence Erlbaum Associates, 1997.
- [18] ITU-T Recommendation G.732, 1988.
- [19] ITU-T Recommendation G.707, 1996.
- [20] L. Bergkamp, "The information highway and informed consent," *European Journal of Health*, vol. 3, pp. 1–7, 1996.
- [21] ITU-T Recommendation G.709, 2001.
- [22] K. Roberts, M. O'Sullivan, K.-T. Wu, H. Sun, A. Awadalla, D. J. Krause, and C. Laperle, "Performance of dual-polarization QPSK for optical transport systems," *Journal of Lightwave Technology*, vol. 27, no. 16, pp. 3546–3558, 2009.
- [23] *Implementation Agreement for Integrated Polarization Multiplexed Quadrature Modulated Transmitters*, Optical Internetworking Forum, 2010.

- [24] *Implementation Agreement for Integrated Dual Polarization Intradyne Coherent Receivers*, Optical Internetworking Forum, 2010.
- [25] ITU-T Recommendation G.694.1, 2012.
- [26] Huawei OSN 6800 Hardware Description V1R6.
- [27] K. G. Coffman and A. M. Odlyzko, "Internet growth: is there a Moore's Law for data traffic?," in *Handbook of Massive Data Sets*. 2002.
- [28] Cisco Virtual Network Index.
- [29] Minnesota Internet Traffic Studies. [Online]. Available: <http://www.dtc.umn.edu/mints/>.
- [30] *Metro network traffic growth: an architecture impact study*, Bell Labs, 2013.
- [31] *Global bandwidth research service*, Telegeography.
- [32] "Will traffic growth break the internet - and can optical communications help?," in *OFC. Rump Session*, 2014.
- [33] D. J. Richardson, J. M. Fini, and L. E. Nelson, "Space-division multiplexing in optical fibres," *Nature Photonics*, vol. 7, p. 354, 2013.
- [34] A. Chraplyvy, "The coming capacity crunch," in *ECOC. Plenary Paper*, 2009.
- [35] P. J. Winzer, R. Ryf, and S. Randel, "Spatial multiplexing using multiple-input multiple-output signal processing," in *Optical Fiber Telecommunications*. 2013, vol. VIB, ch. 10.
- [36] T. Hayashi, "Multi-core optical fibers," in *Optical Fiber Telecommunications*. 2013, vol. VIA, ch. 9.
- [37] D. W. Peckham, Y. Sun, A. McCurdy, and R. L. Jr., "Few-mode fiber technology for spatial multiplexing," in *Optical Fiber Telecommunications*. 2013, vol. VIA, ch. 8.
- [38] S. Alam, "Low cost multi-port reconfigurable erbium doped cladding pumped fibre amplifier," in *ECOC Paper 5.4.3*, 2000.
- [39] P. Winzer, "Spatial multiplexing: the next frontier in network capacity scaling," in *ECOC We.1.D.1*, 2013.
- [40] S. L. Jansen, D. van de Borne, B. Spinnler, S. Calabro, H. Suche, P. M. Krummrich, W. Sohler, G.-D. Khoe, and W. de Waart, "Optical phase conjugation for ultra long-haul phase-shift-keyed transmission," *Journal of Lighthwave Technology*, vol. 24, no. 1, pp. 54–64, 2006.
- [41] F. Parmigiani, R. Slavik, J. Kakande, C. Lundstrom, M. Sjodin, P. Andrekson, R. Weerasuriya, S. Sygletos, A. D. Ellis, L. Grüner-Nielsen, D. Jakobsen, S. Herstrom, R. Phelan, J. O'Gorman, A. Bogris, D. Syvridis, S. Dasgupta, P. Petropoulos, and D. J. Richardson, "All-optical phase regeneration of 40Gbit/s DPSK signals in a black-box phase sensitive amplifier," in *OFC PDP.C3*, 2010.

- [42] C. E. Shannon, "A mathematical theory of communication," *Bell System Technical Journal*, vol. 27, pp. 379–423, 1948.
- [43] P. P. Mitra and J. B. Stark, "Nonlinear limits to the information capacity of optical fibre communications," *Nature*, vol. 411, pp. 1027–1030, 2001.
- [44] P. N. Prasad and D. J. Williams, *Nonlinear Optical Effects in Molecules and Polymers*. Wiley and Sons, 1991.
- [45] R. W. Boyd, *Nonlinear Optics*, 3rd. Academic Press, 2008.
- [46] J. A. Armstrong, N. Bloembergen, J. Ducuing, and P. S. Pershan, "Interaction between light waves in a nonlinear dielectric," *Physical Review*, vol. 128, no. 2, pp. 606–622, 1962.
- [47] N. Bloembergen and P. S. Pershan, "Light waves at the boundary of nonlinear media," *Physical Review*, vol. 128, no. 2, pp. 606–622, 1962.
- [48] G. P. Agrawal, *Nonlinear Fiber Optics*, 4th. Academic Press, 2006.
- [49] R. H. Stolen, J. P. Gordon, W. J. Tomlinson, and H. A. Haus, *J. Opt. Soc. Am. B*, vol. 6, p. 1159, 1989.
- [50] C. Headley and G. P. Agrawal, Eds., *Raman Amplification in Fiber Optics Communication Systems*. Academic Press, 2005.
- [51] J. F. Nye, *Physical properties of crystals : their representation by tensors and matrices*. Oxford: Clarendon Press, 1957.
- [52] D. Marcuse, *Light Transmission Optics*, 2nd. Van Nostrand Reinhold, 1982.
- [53] A. W. Snyder and J. D. Love, *Optical Waveguide Theory*. Chapman and Hall, 1983.
- [54] D. Marcuse, *Theory of Dielectric Optical Waveguides*. Academic Press, 1991.
- [55] D. Marcuse, C. R. Menyuk, and P. K. A. Wai, "Application of the manakov-pmd equation to studies of signal propagation in optical fibers with randomly varying birefringence," *Journal of Lightwave Technology*, vol. 15, no. 9, pp. 1735–1746, 1997.
- [56] M. E. Marhic, *Fiber Optical Parametric Amplifiers, Oscillators and Related Devices*. Cambridge University Press, 2008.
- [57] C. J. McKinstrie, H. Kogelnik, G. G. Luther, and L. Schenato, "Stokes-space derivations of generalized schrodinger equations for wave propagation in various fibers," *Optics Express*, vol. 15, no. 17, pp. 10964–10983, 2007.
- [58] A. Mendez and T. F. Morse, Eds., *Specialty Optical Fibers Handbook*, 2nd. Academic Press, 2008.
- [59] F. Yaman, Q. Lin, G. P. Agrawal, and S. Radic, "Pump-noise transfer in dual-pump fiber-optic parametric amplifiers: walk-off effects," *Optics Letter*, vol. 30, no. 9, pp. 1048–1050, 2005.

- [60] C. J. Mckinstrie, M. Karlsson, and Z. Tong, "Field-quadrature and photon-number correlations produced by parametric processes," *Optics Express*, vol. 18, no. 19, pp. 19 792–19 823, 2010.
- [61] C. J. Mckinstrie, H. Kogelnik, R. M. Jopson, S. Radic, and A. V. Kanaev, "Four-wave mixing in fiber with random birefringence," *Optics Express*, vol. 12, no. 10, pp. 2033–2055, 2004.
- [62] C. J. Mckinstrie, S. Radic, and R. Chraplyvy, "Parametric amplifiers driven by two pumps," *J. of Selected Topics in Quantum Electronics*, vol. 8, no. 3, pp. 538–547, 2002.
- [63] C. J. Mckinstrie, S. Radic, and M. Raymer, "Quantum noise properties of parametric amplifiers driven by two pump waves," *Optics Express*, vol. 12, no. 21, pp. 5037–5066, 2004.
- [64] M. D. Levenson, R. M. Shelby, A. Aspect, M. Reid, and D. F. Walls, "Generation and detection of squeezed states of light by nondegenerate four-wave mixing in an optical fiber," *Physical Review A*, vol. 32, no. 3, pp. 1550–1562, 1985.
- [65] M. Meissner, C. Marquardt, J. Heersink, T. Gaber, A. Wietfeld, G. Leuchs, and U. Andersen, "All-fibre source of amplitude squeezed light pulses," *Journal of Optics B: Quantum and Semiclassical Optics*, vol. 6, pp. 652–657, 2004.
- [66] P. A. Andrekson, "Phase sensitive fiber optic parametric amplifiers," in *ECOC Paper Th.11.LeCervin.1*, 2011.
- [67] M. Vasiliev, "Distributed phase-sensitive amplification," *Optic Express*, vol. 13, no. 19, pp. 7563–7571, 2005.
- [68] P. A. Andrekson, C. Lundstrom, and Z. Tong, "Phase-sensitive fiber-optic parametric amplifiers and their applications," in *ECOC Paper We.6.E.1*, 2010.
- [69] R. Slavik, F. Parmigiani, J. Kakande, C. Lundstrom, M. Sjodin, P. Andrekson, R. Weerasuriya, S. Sygletos, A. D. Ellis, L. Grüner-Nielsen, D. Jakobsen, S. Herstrøm, R. Phelan, J. O’Gorman, A. Bogris, D. Syvridis, S. Dasgupta, P. Petropoulos, and D. J. Richardson, "All-optical phase and amplitude regenerator for next-generation telecommunications systems," *Nature Photonics*, vol. 4, pp. 690–695, 2010.
- [70] Z. Tong, C. Lundstrom, P. Andrekson, C. Mckinstrie, M. Karlsson, D. Blessing, E. Tipsuwannakul, B. Puttnam, H. Toda, and L. Gruner-Nielsen, "Towards the ultra-sensitive optical link enabled by low noise phase-sensitive amplifiers," *Nature Photonics*, vol. 5, no. 7, pp. 430–436, 2011.
- [71] C. Kittel and H. Kroemer, in *Thermal Physics*. W. H. Freeman and Company, 1998, ch. 4.
- [72] R. Kubo, "Statistical-mechanical theory of irreversible processes I," *J. of the Physical Society of Japan*, vol. 12, no. 6, pp. 570–586, 1957.
- [73] R. Kubo and M. Yokota, "Statistical-mechanical theory of irreversible processes II," *J. of the Physical Society of Japan*, vol. 12, no. 11, pp. 1203–1211, 1957.

- [74] L. Onsager, "Reciprocal relations in irreversible processes I," *Physical Review*, vol. 37, pp. 405–426, 1931.
- [75] —, "Reciprocal relations in irreversible processes II," *Physical Review*, vol. 38, pp. 2265–2279, 1931.
- [76] H. B. Callen and T. A. Welton, "Irreversibility and generalized noise," *Physical Review*, vol. 83, no. 1, pp. 34–40, 1951.
- [77] R. F. Greene and H. B. Callen, "On the formalism of the thermodynamic fluctuation theory," *Physical Review*, vol. 83, no. 6, pp. 1231–1235, 1951.
- [78] H. Risken, *The Fokker-Planck Equation*, 2nd. Springer-Verlag, 1989.
- [79] M. Lax, *Random Processes in Physics and Finance*. Oxford University Press, 2006.
- [80] C. W. Gardiner, *Handbook of Stochastic Methods: For Physics, Chemistry, and the Natural Sciences*, 2nd. Springer, 1986.
- [81] H. Heffner, "The fundamental noise limit of linear amplifiers," *Proceeding of IRE*, p1604, 1962.
- [82] C. M. Caves, "Quantum limits on noise in linear amplifiers," *Physical Review D*, vol. 26, no. 8, pp. 1817–1839, 1982.
- [83] P. C. Becker, N. A. Olsson, and J. R. Simpson, *Erbium Doped Fiber Amplifiers: Fundamentals and Technology*. Academic Press, 1989.
- [84] M. J. Digonnet, Ed., *Rare-Earth-Doped Fiber Lasers and Amplifiers*, 2nd ed. CRC, 2001.
- [85] A. Mendez and T. F. Morse, Eds., *Specialty Optical Fibers Handbook*. Academic Press, 2007.
- [86] E. Desurvire, *Erbium Doped Fiber Amplifiers: Principles and Applications*. Wiley and Sons, 1994.
- [87] S. Namiki, "Fiber raman amplifier," in *WDM Technologies Vol. II: Passive Optical Components*. 2003, ch. 10.
- [88] K. Rottwitt and A. Stentz, "Raman amplification in lightwave communication systems," in *Optical Fiber Telecommunications IV-A*. 2002, ch. 5.
- [89] P. L. Voss and P. Kumar, "Raman-noise-induced noise figure-limit for parametric amplifiers," *Optics Letters*, vol. 29, no. 5, pp. 445–447, 2004.
- [90] P. Kylemark, P. O. Hedekvist, H. Sunnerud, M. Karlsson, and P. A. Andrekson, "Noise characteristics of fiber optical parametric amplifiers," *Journal of Lightwave Technology*, vol. 22, no. 2, pp. 409–416, 2004.
- [91] A. Bogris, D. Syvridis, P. Kylemark, and P. A. Andrekson, "Noise characteristics of dual-pump fiber-optic parametric amplifiers," *Journal of Lightwave Technology*, vol. 23, no. 9, pp. 2788–2795, 2005.

- [92] E. W. Davis, V. L. Teofilo, B. Haisch, H. E. Puthoff, L. J. Nickisch, A. Rueda, and D. C. Cole, "Review of experimental concepts for studying the quantum vacuum field," in *Space Technology and Applications International Forum Proceedings*, 2006, pp. 1390–1401.
- [93] A. Durecu-Legrand, C. Simonneau, D. Bayart, A. Mussot, T. Sylvestre, E. Lantz, and H. Maillotte, "Impact of pump OSNR on noise figure for fiber-optical parametric amplifiers," *IEEE Photonics Technology Letters*, vol. 17, no. 6, pp. 1178–1180, 2005.
- [94] N. A. Olsson, "Lightwave systems with optical amplifiers," *Journal of Lightwave Technology*, vol. 7, no. 7, pp. 1071–1082, 1989.
- [95] M. E. Marhic, G. Kalogerakis, K. K.-Y. Wong, and L. G. Kazovsky, "Pump-to-signal transfer of low frequency intensity modulation in fiber optical parametric amplifiers," *Journal of Lightwave Technology*, vol. 23, no. 3, pp. 1049–1055, 2005.
- [96] L. Boivin, F. X. Kartner, and H. A. Haus, "Analytical solution to the quantum field theory of self-phase modulation with a finite response time," *Physical Review Letter*, vol. 73, no. 2, pp. 240–243, 1994.
- [97] D. J. Dougherty, F. X. Kartner, H. A. Haus, and E. P. Ippen, "Measurement of the raman gain spectrum of optical fibers," *Optics Letters*, vol. 20, no. 1, pp. 31–33, 1995.
- [98] A. Boskovic, S. V. Chernikov, J. R. Taylor, L. Gruner-Nielsen, and O. A. Levring, "Direct continuous wave measurement of n_2 in various types of telecommunication fiber at 1.55 μm ," *Physical Review Letter*, vol. 21, no. 24, pp. 1966–1968, 1996.
- [99] P. L. Voss and P. Kumar, "Raman scattering noise in phase-insensitive and phase-sensitive parametric processes in fibers," in *Frontiers in Optics Paper FThI2*, 2006.
- [100] E. Golovchenko, P. V. Mamyshev, A. N. Pilipetskii, and E. M. Dianov, "Mutual influence of the parametric effects and stimulated raman scattering in optical fibers," *IEEE Journal of Quantum Electronics*, vol. 26, pp. 1815–1820, 1990.
- [101] J. P. Gordon and L. F. Mollenauer, "Phase noise in photonic communications systems using linear amplifiers," *Optics Letters*, vol. 15, no. 23, pp. 1351–1353, 1990.
- [102] E. Jakeman and E. R. Pike, "Statistics of heterodyne detection of gaussian light," *Journal of Physics A*, vol. 2, no. 2, pp. 115–125, 1968.
- [103] G. Nicholson, "Probability of error of optical heterodyne DPSK system with quantum phase noise," *Electronics Letters*, vol. 20, no. 24, pp. 1005–1007, 1984.
- [104] Y. Yamamoto and H. A. Haus, "Commutation relations and laser linewidth," *Physical Review A*, vol. 41, no. 9, pp. 5164–5170, 1990.
- [105] C. H. Henry, "Phase noise in semiconductor lasers," *Journal of Lightwave Technology*, vol. 4, no. 3, pp. 298–311, 1986.

- [106] R. Hui and A. Mecozzi, "Phase noise of four-wave mixing in semiconductor lasers," *Applied Physics Letters*, vol. 60, no. 20, pp. 2454–2456, 1992.
- [107] A. P. Anthur, R. T. Watts, K. Shi, J. O'Carroll, D. Venkitesh, and L. P. Barry, "Dual correlated pumping scheme for phase noise preservation in all-optical wavelength conversion," *Optics Express*, vol. 21, no. 13, pp. 15 568–15 579, 2013.
- [108] C. Dziak, A. J. Moscho, Y. Li, M. Fanto, V. Kovanis, J. Malowicki, and L. F. Lester, "Measurement of the linewidth enhancement factor of a 1550nm injection-locked quantum dash laser," in *LEOS*, 2007, pp. 433–434.
- [109] T. Inoue, K. Tanizawa, and S. Namiki, "Guard-band-less and polarization-insensitive tunable wavelength converter for phase-modulated signals: demonstration and signal quality analyses," *Journal of Lightwave Technology*, vol. 32, no. 10, pp. 1981–1990, 2014.
- [110] A. Mecozzi, "Limits to long-haul coherent transmission set by the kerr nonlinearity and noise of the in-line amplifiers," *Journal of Lightwave Technology*, vol. 12, no. 11, pp. 1993–2000, 1994.
- [111] A. Demir, "Nonlinear phase noise in optical-fiber-communication systems," *Journal of Lightwave Technology*, vol. 25, no. 8, pp. 2002–2032, 2007.
- [112] S. Kumar, "Effect of dispersion on nonlinear phase noise in optical transmission systems," *Optics Letters*, vol. 30, no. 24, pp. 3278–3280, 2005.
- [113] J. Wang and K. Petermann, "Small signal analysis for dispersive optical fiber communication systems," *Journal of Lightwave Technology*, vol. 10, no. 1, pp. 96–100, 1992.
- [114] A. G. Green, P. P. Mitra, and L. G. L. Wegener, "Effect of chromatic dispersion on nonlinear phase noise," *Optics Letters*, vol. 28, no. 24, pp. 2455–2457, 2003.
- [115] S. Ryu, "Signal linewidth broadening due to nonlinear kerr effect in long-haul coherent systems using cascaded optical amplifiers," *Journal of Lightwave Technology*, vol. 10, no. 10, pp. 1450–1457, 1992.
- [116] C. Lorattanasane and K. Kikuchi, "Parametric instability of optical amplifier noise in long-distance optical transmission systems," *IEEE Journal of Quantum Electronics*, vol. 33, no. 7, pp. 1068–1074, 1997.
- [117] K. Kikuchi, "Enhancement of optical amplifier noise by nonlinear refractive index and group-velocity dispersion of optical fibers," *IEEE Photonics Technology Letters*, vol. 5, no. 2, pp. 221–223, 1993.
- [118] A. V. T. Cartaxo, B. Wedding, and W. Idler, "Influence of fiber nonlinearity on the phase noise to intensity noise conversion in fiber transmission: theoretical and experimental analysis," *Journal of Lightwave Technology*, vol. 16, no. 7, pp. 1187–1193, 1998.

- [119] ———, "Influence of fiber nonlinearity on fiber transfer function: theoretical and experimental analysis," *Journal of Lightwave Technology*, vol. 17, no. 10, pp. 1806–1813, 1999.
- [120] R. Elschner and K. Petermann, "Impact of pump-induced nonlinear phase noise on parametric amplification and wavelength conversion of phase-modulated signals," in *ECOC Paper 3.3.4*, 2009.
- [121] M. Matsumoto, "Phase-noise generation in an amplitude limiter using saturation of a fiber-optic parametric amplifier," in *ECOC Paper P.1.08*, 2008.
- [122] A. Sizmann and G. Leuchs, "The optical kerr effect and quantum optics in fibers," in *Progress in Optics*. 1999, vol. 39, ch. 5.
- [123] K. Tajima, "Self-amplitude modulation in PSK coherent transmission systems," *Journal of Lightwave Technology*, vol. 4, no. 7, pp. 900–904, 1986.
- [124] A. R. Chraplyvy, R. W. Tkach, L. L. Buhl, and R. C. Alfiness, "Phase modulation to amplitude modulation conversion of cw laser light in optical fibers," *Electronic Letters*, vol. 22, no. 8, pp. 409–411, 1986.
- [125] S. Yamamoto, N. Edagawa, H. Taga, Y. Yoshida, and H. Wakabayashi, "Analysis of laser phase noise to intensity noise conversion by chromatic dispersion in intensity modulation and direct detection optical-fiber transmission," *Journal of Lightwave Technology*, vol. 8, no. 11, pp. 1716–1722, 1990.
- [126] C. Xie, "Local oscillator phase noise induced penalties in optical coherent detection systems using electronic chromatic dispersion compensation," in *OFC OMT4*, 2009.
- [127] I. Fatadin and S. Savory, "Impact of phase to amplitude noise conversion in coherent optical systems with digital dispersion compensation," *Optics Express*, vol. 18, no. 15, pp. 16 273–16 278, 2010.
- [128] P. Winzer and R.-J. Essiambre, "Advanced optical modulation formats," in *Optical Fiber Telecommunications V-B*. 2008, ch. 2.
- [129] P. V. Mamyshev and N. A. Mamysheva, "Pulse-overlapped dispersion-managed data transmission and intrachannel four-wave mixing," *Optics Letters*, vol. 24, no. 21, pp. 1454–1456, 1999.
- [130] A. Mecozzi, C. B. Clausen, and M. Shtaif, "Analysis of intrachannel nonlinear effects in highly dispersed optical pulse transmission," *IEEE Photonics Technology Letters*, vol. 12, no. 4, pp. 392–394, 2000.
- [131] ———, "System impact of intra-channel nonlinear effects in highly dispersed optical pulse transmission," *IEEE Photonics Technology Letters*, vol. 12, no. 4, pp. 392–394, 2000.
- [132] X. Wei and X. Liu, "Analysis of intrachannel four-wave mixing in differential phase-shift keying transmission with large dispersion," *Optics Letters*, vol. 28, no. 23, pp. 2300–2302, 2003.

- [133] F. Zhang, C. Bunge, and K. Petermann, "Analysis of nonlinear phase noise in a single-channel return-to-zero differential phase-shift keying transmission systems," *Optics Letters*, vol. 31, no. 8, pp. 1038–1040, 2006.
- [134] S. Kumar, "Intrachannel four-wave mixing in dispersion managed RZ systems," *Journal of Lightwave Technology*, vol. 13, no. 8, pp. 800–802, 2001.
- [135] M. Forzati, J. Martensson, A. Berntson, A. Djupsjobacka, and P. Johannisson, "Reduction of intrachannel four-wave mixing using the alternate-phase RZ modulation format," *IEEE Photonics Technology Letters*, vol. 14, no. 9, pp. 1285–1287, 2002.
- [136] A. P. T. Lau, S. Rabbani, and J. M. Kahn, "On the statistics of intrachannel four-wave mixing in phase-modulated optical communication systems," *Journal of Lightwave Technology*, vol. 26, no. 14, pp. 2128–2135, 2008.
- [137] I. B. Djordjevic, B. Vasic, M. Ivkovic, and I. Gabitov, "Achievable information rates for high-speed long-haul optical transmission," *Journal of Lightwave Technology*, vol. 23, no. 11, pp. 3755–3763, 2005.
- [138] R. J. Essiambre, B. Mikkelsen, and G. Raybon, "Intra-channel cross-phase modulation and four-wave mixing in high-speed TDM systems," *Electronics Letters*, vol. 35, no. 18, pp. 1576–1578, 1999.
- [139] A. Maruta and S. Tomioka, "Intra-channel cross-phase modulation induced phase shift in optical RZ pulse propagation in dispersion managed line," in *IEEE Photonics Society*, 2010.
- [140] M. Winter, "A statistical treatment of cross-polarization modulation in DWDM systems and its applications," PhD thesis, Technischen Universitat Berlin, 2010.
- [141] M. T. Core, "Cross polarization interference cancellation for fiber optic systems," *Journal of Lightwave Technology*, vol. 24, no. 1, pp. 305–312, 2006.
- [142] A. D. Shiner, M. Reimer, A. Borowiec, S. O. Gharan, J. Gaudette, P. Mehta, D. Charlton, K. Roberts, and M. O'Sullivan, "Demonstration of an 8D modulation format with reduced inter-channel nonlinearities in a polarization multiplexed coherent system," *arXiv:1406.1460*,
- [143] T.-K. Chiang, N. Kagi, T. K. fong, M. E. Marhic, and L. G. Kazovsky, "Cross phase modulation in dispersive fibers: theoretical and experimental investigation of the impact of modulation instability," *IEEE Photonics Technology Letters*, vol. 6, no. 6, pp. 733–735, 1994.
- [144] M. Shtaif and M. Eiselt, "Analysis of intensity interference caused by cross-phase modulation in dispersive optical fibers," *IEEE Photonics Technology Letters*, vol. 10, no. 7, pp. 979–981, 1998.
- [145] R. Hui, K. R. Demarest, and C. T. Allen, "Cross-phase modulation in multispan WDM optical fiber systems," *Journal of Lightwave Technology*, vol. 17, no. 16, pp. 1018–1026, 1999.

- [146] J. Leibrich, C. Wree, and W. Rosenkranz, "CF-RZ-DPSK for suppression of XPM on dispersion-managed long-haul optical WDM transmission on standard single-mode fiber," *IEEE Photonics Technology Letters*, vol. 14, no. 2, pp. 155–157, 2002.
- [147] B. Xu and M. Brandt-Pearce, "Comparison of FWM- and XPM-induced crosstalk using the volterra series transfer function method," *Journal of Lightwave Technology*, vol. 21, no. 1, pp. 40–53, 2003.
- [148] K.-P. Ho and H.-C. Wang, "Comparison of nonlinear phase noise and intrachannel four-wave mixing for RZ-DPSK signals in dispersive transmission systems," *IEEE Photonics Technology Letters*, vol. 17, no. 7, pp. 1426–1428, 2005.
- [149] G. Bosco, A. Carena, V. Curri, R. Gaudino, and P. Poggiolini, "Parametric gain in WDM systems," in *LEOS Paper WZ5*, 1999.
- [150] A. Carena, V. Curri, R. Gaudino, P. Poggiolini, and S. Benedetto, "New analytical results on fiber parametric gain and its effects on ASE noise," *IEEE Photonics Technology Letters*, vol. 9, no. 4, pp. 535–537, 1997.
- [151] H. Kim, "Cross-phase-modulation-induced nonlinear phase noise in WDM direct-detection DPSK systems," *Journal of Lightwave Technology*, vol. 21, no. 8, pp. 1770–1774, 2003.
- [152] K.-P. Ho, "Error probability of DPSK signals with cross phase modulation induced nonlinear phase noise," *IEEE Journal of Selected Topics in Quantum Electronics*, vol. 10, no. 2, pp. 421–427, 2004.
- [153] K.-P. Ho and H.-C. Wand, "Cross-phase-modulation-induced crosstalk for RZ-DPSK signals in dispersive transmission systems," *Journal of Lightwave Technology*, vol. 24, no. 1, pp. 396–402, 2006.
- [154] L. G. L. Wegener, M. L. Povinelli, A. G. Green, P. P. Mitra, J. B. Stark, and P. B. Littlewood, "The effect of propagation nonlinearities on the information capacity of WDM optical fiber systems: cross-phase modulation and four-wave mixing," *Physica D*, vol. 189, pp. 81–99, 2004.
- [155] R. Dar, M. Feder, A. Mecozzi, and M. Shtaif, "Properties of nonlinear noise in long, dispersion-uncompensated fiber links," *Optics Express*, vol. 21, no. 22, pp. 25 685–25 699, 2013.
- [156] —, "Accumulation of nonlinear interference noise in fiber-optic systems," *Arxiv:1310.6137v5*, 2014.
- [157] M. Shtaif, R. Dar, A. Mecozzi, and M. Feder, "Nonlinear interference noise in WDM systems and approaches for its cancellation," in *ECOC Paper We.1.3.1*, 2014.
- [158] D. Marcuse, *Light Transmission Optics*. Van Nostrand Reinhold, 1982.
- [159] J. Johnson, "Thermal agitation of electricity in conductors," *Physical Review*, vol. 32, p. 97, 1928.

- [160] C. H. Henry and R. F. Kazarinov, "Quantum noise in photonics," *Reviews of Modern Physics*, vol. 68, no. 3, pp. 801–853, 1996.
- [161] D. Marcuse, "Derivation of analytical expressions for the bit-error probability in lightwave systems with optical amplifiers," *Journal of Lightwave Technology*, vol. 8, no. 12, pp. 1816–1823, 1990.
- [162] P. Poggiolini, "The GN Model of non-linear propagation in uncompensated coherent optical systems," *Journal of Lightwave Technology*, vol. 30, no. 24, pp. 3857–3879, 2012.
- [163] A. Papoulis, *Probability, Random Variables and Stochastic Processes*, 4th. McGraw-Hill, 2002.
- [164] S. Moro, A. Peric, N. Alic, B. Stossel, and S. Radic, "Phase noise in fiber-optic parametric amplifiers and converters and its impact on sensing and communication systems," *Optics Express*, vol. 18, no. 20, pp. 21 449–21 460, 2010.
- [165] J. G. Proakis, *Digital Communications*. McGraw-Hill, 2001.
- [166] R. G. Gallager, *Principles of Digital Communication*. Cambridge University Press, 2008.
- [167] F. Aurenhammer, "Voronoi diagrams – a survey of a fundamental geometric data structure," *ACM Computing Survey*, vol. 23, no. 8, pp. 345–405, 1991.
- [168] V. K. Rohatgi, *An Introduction to Probability Theory and Mathematical Statistics*. Wiley, 1976.
- [169] J. G. Proakis, in *Digital Communications*. McGraw-hill, 2001, ch. 5, p. 235.
- [170] C. R. Giles and E. Desurvire, "Propagation of signal and noise in concatenated erbium-doped fiber optical amplifiers," *Journal of Lightwave Technology*, vol. 9, no. 2, pp. 147–154, 1991.
- [171] N. Bergano, in *Optical Fiber Telecommunications IV-B*. Academic Press, 2002, ch. 4.
- [172] Z. Tong, A. Bogris, C. Lundstrom, C. McKinstrie, M. Vasilyev, M. Karlsson, and P. A. Andrekson, "Noise figure measurements in phase-insensitive and phase-sensitive fiber parametric amplifier cascade," in *OFC OWT4*, 2010.
- [173] H. T. Friis, "Noise figures of radio receivers," *Procs. IRE*, vol. 32, no. 7, pp. 419–422, 1944.
- [174] H. A. Haus, "The noise figure of optical amplifiers," *IEEE Photon. Tech. Lett.*, vol. 10, no. 11, pp. 1602–1604, 1998.
- [175] X. Guo, G. K. P. Lei, X. Fu, H. K. Tsang, and C. Shu, "Amplitude regeneration of 80-Gb/s polarization multiplexed RZ-DPSK signals in a dual-orthogonal-pump fiber optical parametric amplifier," in *OFC OTu2D.1*, 2013.

- [176] Z. Lali-Dastjerdi, O. Ozolins, Y. An, V. Cristofori, F. D. Ros, N. Kang, H. Hu, H. C. H. Mulvad, K. Rottwitt, M. Galilli, and C. Peucheret, "Demonstration of cascaded in-line single-pump fiber optical parametric amplifiers in recirculating loop transmission," in *ECOC Mo2.C.5*, 2012.
- [177] P. Minzioni, F. Alberti, and A. Schiffrini, "Optimized link design for nonlinearity cancellation by optical phase conjugation," *IEEE Photon. Tech. Lett.*, vol. 16, no. 3, pp. 813–815, 2004.
- [178] S. L. Hansen, D. van de Borne, B. Spinnler, S. Calabro, H. Suche, P. M. Krummrich, W. Sohler, G.-D. Khoe, and H. der Waardt, "Optical phase conjugation for ultra long-haul phase-shift-keyed transmission," *Journal of Lightwave Technology*, vol. 24, no. 1, pp. 54–64, 2006.
- [179] C. Xie, "Dispersion management in WDM coherent PDM-QPSK systems," in *ECOC 9.4.3*, 2009.
- [180] —, "WDM coherent PDM-QPSK systems with and without inline optical dispersion compensation," *Optics Express*, vol. 17, no. 6, pp. 4815–4823, 2009.
- [181] G. P. Agrawal, in *Fiber-Optic Communication Systems*. Wiley and Sons, 2002, ch. 2, p. 38.
- [182] X. Liu, S. Chandrasekhar, and A. Leven, in *Optical Fiber Telecommunications V-B*. Academic Press, 2008, ch. 4.
- [183] K. Kikuchi, in *Optical Fiber Telecommunications V-B*. Academic Press, 2008, ch. 3.
- [184] —, "Characterization of semiconductor-laser phase noise and estimation of bit-error rate performance with low-speed offline digital coherent receivers," *Optics Express*, vol. 20, no. 5, pp. 5291–5302, 2012.
- [185] W. Shieh and K.-P. Ho, "Equalization-enhanced phase noise for coherent-detection systems using electronic digital signal processing," *Optics Express*, vol. 16, no. 20, pp. 15718–15727, 2008.
- [186] S. Savory, "Digital coherent optical receivers: algorithms and subsystems," *IEEE Journal of Selected Topics in Quantum Electronics*, vol. 16, no. 5, pp. 1164–1179, 2010.
- [187] I. Fatadin and S. Savory, "Compensation of frequency offset for 16-QAM optical coherent systems using QPSK partitioning," *IEEE Photon. Tech. Lett.*, vol. 23, no. 17, pp. 1246–1248, 2011.
- [188] A. Leven, N. Kaneda, U.-V. Koc, and Y.-K. Chen, "Frequency estimation in intradyne reception," *IEEE Photon. Tech. Lett.*, vol. 19, no. 6, pp. 366–368, 2007.
- [189] A. Carena, G. Bosco, V. Curri, Y. Jiang, P. Poggiolini, and F. Forghieri, "EGN model of non-linear fiber propagation," *Optics Express*, vol. 22, no. 13, pp. 16335–16362, 2014.

- [190] Z. Zan and A. J. Lowery, "Experimental demonstration of a flexible and stable semiconductor laser linewidth emulator," *Optics Express*, vol. 18, no. 13, pp. 13 880–13 885, 2010.
- [191] F. M. Gardner, "A BPSK/QPSK timing-error detector for sampled receivers," *IEEE Trans. Comms*, vol. 34, no. 5, pp. 423–429, 1986.
- [192] T. Tanimura, T. Hoshida, S. Oda, H. Nakashima, M. Yuki, Z. Tao, L. Liu, and C. Rasmussen, "Digital clock recovery algorithm for optical coherent receivers operating independent of laser frequency offset," in *ECOC paper Mo.3.D.2*, 2008.
- [193] G. Welch and G. Bishop, *An introduction to the kalman filter*, Tech. Rep. TR 95-041, 2006.
- [194] B. Szafraniec, T. Marshall, and B. Nebendahl, *Kalman filter based estimation and demodulation of complex signals*, Agilent Technologies White Paper.
- [195] B. Ramamurthy and B. Mukherjee, "Wavelength conversion in WDM networking," *IEEE Journal of Selected Areas in Communications*, vol. 16, pp. 1061–1073, 1998.
- [196] J. Strand and G. Li, "Importance of wavelength conversion in an optical network," *Optical Networks*, vol. 2, pp. 33–39, 2001.
- [197] K. K. Y. Wong, M. E. Marhic, K. Uesaka, and L. G. Kazovsky, "Polarization-independent two-pump fiber optical parametric amplifier," *IEEE Photonic Technology Letters*, vol. 14, pp. 911–912, 2002.
- [198] P. Devgan, T. Renyong, V. S. Grigoryan, and P. Kumar, "Highly efficient multi-channel wavelength conversion of DPSK signals," *Journal of Lightwave Technology*, vol. 24, pp. 3677–3682, 2006.
- [199] A. H. Gnauck, E. Myslivets, M. Dinu, B. Kuo, P. Winzer, R. Jopson, N. Alic, A. Konczykowska, F. Jorge, J.-Y. Dupuy, and S. Radic, "All-optical tunable wavelength shifting of a 128-Gbit/s 64-QAM signal," in *ECOC Paper Th2.F.2*, 2012.
- [200] X. Li, J. Yu, Z. Dong, and N. Chi, "Wavelength conversion of 544-Gbit/s dual-carrier PDM-16QAM signal based on the co-polarized dual-pump scheme," *Optics Express*, vol. 20, pp. 21 324–21 330, 2012.
- [201] J. Yu, M.-F. Huang, and N. Cvijetic, "In-band wavelength conversion of 16x114-Gbps polarization multiplexed RZ-8PSK signals with digital coherent detection," in *OFC Paper OThS7*, 2009.
- [202] L. Grüner-Nielsen, D. Jakobsen, S. Herstrøm, B. Pálsdóttir, S. Dasgupta, and D. J. Richardson, "Brillouin suppressed highly nonlinear fibers," in *ECOC Paper We.1.F.1*, 2012.
- [203] C. R. Menyuk and A. Galtarossa, *Polarization Mode Dispersion*. Springer, 2005.

- [204] C. D. Poole and R. E. Wagner, "Phenomenological approach to polarization dispersion in long single-mode fibers," *Electronics Letters*, vol. 22, pp. 1029–1030, 1986.
- [205] S. Takasaka, M. Takahashi, Y. Mimura, M. Tadakuma, R. Sugizaki, and T. Yagi, "Polarization insensitive arbitrary wavelength conversion in entire C-band using a PM-HNLF," in *ECOC Paper Th.9.C.2*, 2010.
- [206] P. Winzer, "Optical networking beyond WDM," *IEEE Photonics Journal*, vol. 4, no. 2, pp. 647–651, 2012.
- [207] S. Randel, R. Ryf, and P. Winzer, "Spatial multiplexing for long-haul transmission," in *Photonics Conference (IPC)*, 2012.
- [208] R. Ryf, "Optical communication over few-mode fibers," in *IEEE Summer Topics*, 2014.
- [209] Telcordia standards TR-NWT-000764 and TR-NWT-001121.
- [210] A. D. K. nad J. Crocker, T. Chitra, and H. Srauga, *Reliability and Six Sigma*. Springer, 2006.
- [211] N. S. Bergano, "Undersea amplified lightwave system desing," in *Optical Fiber Telecommunications*. 1998, vol. IIIA, ch. 10.
- [212] P. Winzer, A. H. Gnauck, A. Konczykowska, F. Jorge, and J.-Y. Dupuy, "Penalties from in-band crosstalk for advanced optical modulation formats," in *ECOC Paper Tu.5.B.7*, 2011.
- [213] B. Zhu, T. Taunay, M. Fishteyn, X. Liu, S. Chandrasekhar, M. F. Yan, J. M. Fini, E. M. Monberg, and F. V. Dimarcello, "112-Tb/s space-division multiplexed DWDM transmission with 14-b/s/Hz aggregate spectral efficiency over a 76.8-km seven-core fiber," *Optics Express*, vol. 19, no. 17, pp. 16 665–16 671, 2011.
- [214] Y. Awaji, K. Saitoh, and S. Matsuo, "Transmission systems using multicore fibers," in *Optical Fiber Telecommunications*. 2013, vol. VIB, ch. 13.
- [215] J. Sakaguchi, B. J. Puttnam, W. Klaus, J.-M. D. Mendinueta, Y. Awaji, N. Wada, A A. Kanno, and T. Kawanishi, "Large-capacity transmission over a 19-core fiber," in *OFC Paper OW1L3*, 2013.
- [216] R. R. Thomson, H. T. Bookey, N. D. Psaila, A. Fender, S. Campbell, W. N. MacPherson, J. S. Barton, D. T. Reid, and A. K. Kar, "Ultrafast-laser inscription of a three dimensional fan-out device for multicore fiber coupling applications," *Optics Express*, vol. 15, no. 18, pp. 16 691–16 697, 2007.
- [217] B. G. Lee, D. M. Kuchta, F. E. Doany, C. L. Schow, C. Baks, R. John, P. Pepeljugoski, T. F. Taunay, B. Zhu, M. F. Yan, G. E. Oulundsen, D. S. Vaidya, W. Luo, and N. Li, "Multimode transceiver for interfacing to multicoregraded-index fiber capable of carrying 120-Gb/s over 100m lengths," in *IEEE Photonics Summer Topicals*, 2010.

- [218] M. A. Taubenblatt, "Optical interconnects for high-performance computing," *Journal of Lightwave Technology*, vol. 30, no. 4, pp. 448–458, 2012.
- [219] K. S. Abedin, T. F. Taunay, M. Fishteyn, M. F. Yan, B. Zhu, J. M. Fini, E. M. Monberg, F. Dimarcello, and P. Wisk, "Amplification and noise properties of an erbium-doped multicore fiber amplifier," *Optics Express*, vol. 19, no. 17, pp. 16 715–16 721, 2011.
- [220] Y. Mimura, Y. Tsuchida, K. Maeda, R. Miyabe, K. Aiso, H. Matsuura, and R. Sugizaki, "Batch multicore amplification with cladding-pumped multicore EDF," in *ECOC Paper Tu.4.F.1*, 2012.
- [221] A. Sano, h. Takara, T. Kobayashi, and Y. Miyamoto, "Petabit/s transmission using multicore fibers," in *OFC Tu2J.1*, 2014.
- [222] V. Sleiffer, Y. Jung, V. Veljanovski, R. van Uden, M. Kuschnerov, Q. Kang, L. Grüner-Nielsen, Y. Sun, D. J. Richardson, S. Alam, F. Poletti, J. Sahu, A. Dhar, H. Chen, B. Inan, T. Koonen, B. Corbett, R. Winfield, A. Ellis, and H. D. Waardt, "73.7 Tb/s (96x3x256-gb/s) mode-division-multiplexed DP-16QAM transmission with inline MM-EDFA," in *ECOC Paper Th.3.C.4*, 2012.
- [223] K.-P. Ho and J. M. Kahn, "Statistics of group delays in multimode fiber with strong mode coupling," *Journal of Lightwave Technology*, vol. 29, no. 21, pp. 3119–3128, 2011.
- [224] ITU-T Recommendation G.694.1 www.itu.int/rec/T-REC-G.694.1/.
- [225] G. Yabre, "Comprehensive theory of dispersion in graded-index optical fibers," *Journal of Lightwave Technology*, vol. 18, no. 2, pp. 166–177, 2000.
- [226] W. Q. Thornburg, B. J. Corrado, and X. D. Zhu, "Selective launching of higher-order modes into an optical fiber with an optical phase shifter," *Optics Letters*, vol. 19, no. 7, pp. 454–456, 1994.
- [227] S. G. Leon-Saval, A. Argyros, and J. Bland-Hawthorn, "Photonic lanterns: a study of light propagation in multimode to single-mode converters," *Optics Express*, vol. 18, no. 8, pp. 8430–8439, 2010.
- [228] Y. Jung, Q. Kang, V. A. J. M. Sleiffer, B. Inan, M. Kuschnerov, V. Veljanovski, B. Corbett, R. Winfield, Z. Li, P. S. Teh, A. Dhar, J. Sahu, F. Poletti, S. Alam, and D. J. Richardson, "Three mode Er³⁺ ring-doped fiber amplifier for mode-division multiplexed transmission," *Optics Express*, vol. 21, no. 8, pp. 10 383–10 392, 2013.
- [229] A. Sano, T. Kobayashi, S. Yamanaka, A. Matsuura, H. Kawakami, Y. Miyamoto, K. Ishihara, and H. Masuda, "102.3-Tb/s (224x548 Gb/s) C- and extended L-band all-raman transmission over 240 km using PDM-64QAM single carrier FDM with digital pilot tone," in *OFC Paper PDP5C.3*, 2012.
- [230] C. Koebele, M. Salsi, L. Milord, R. Ryf, C. A. Bolle, P. Sillard, S. Bigo, and G. Charlet, "40km transmission of five mode division multiplexed data streams at 100 Gb/s with low MIMO DSP complexity," in *ECOC Paper Th.13.C.3*, 2011.

- [231] S. Jain, T. C. May-Smith, V. J. F. Rancaño, P. Petropoulos, D. J. Richardson, and J. K. Sahu, "Multi-element fibre for space-division multiplexed transmission," in *ECOC Paper Mo.4.A.2*, 2013.
- [232] S. Jain, V. J. F. Rancaño, T. C. May-Smith, J. K. Sahu, P. Petropoulos, and D. J. Richardson, "Multi-element fiber for space-division multiplexing operations," *Optics Express*, vol. 22, no. 4, pp. 3787–3796, 2014.
- [233] J. K. Sahu, S. Jain, V. J. F. Rancaño, T. C. May-Smith, A. Webb, P. Petropoulos, and D. J. Richardson, "Multi-element fiber for space-division multiplexing," in *Proc. SPIE 9009, Next-Generation Optical Communication: Components, Sub-Systems, and Systems III, 90090C*, 2013.
- [234] S. Jain, T. C. May-Smith, and J. K. Sahu, "Cladding-pumped Er/Yb-doped multi-element fiber amplifier," in *Workshop on Speciality Optical Fibers and their Applications Paper 5.4*, 2013.
- [235] V. A. J. M. Sleiffer, H. Chen, Y. Jung, P. Leoni, M. Kuschnerov, A. Simperler, H. Fabian, H. Schuh, F. Kub, D. J. Richardson, S. U. Alam, L. Grüner-Nielsen, Y. Sun, A. M. J. Koonen, and H. Waardt, "Field demonstration of mode-division multiplexing upgrade scenarios on commercial networks," *Optics Express*, vol. 21, no. 25, pp. 31 036–31 046, 2013.
- [236] D. J. Richardson, "Multi-mode and multi-core EDFAs for spatial-division multiplexing," in *OFC Paper OTu3G.1*, 2013.
- [237] G. Zarris, E. Hugues-Salas, N. Amaya, R. Weerasuriya, F. Parmigiani, D. Hillerkuss, P. Vorreau, M. Spyropoulou, S. Ibrahim, P. Petropoulos, and D. Simeonidou, "Field experiments with a grooming switch for OTDM meshed networking," *Journal of Lightwave Technology*, vol. 28, pp. 316–327, 2010.
- [238] S. Y. Set, R. Girardi, E. Riccardi, B. Olsson, M. Puleo, M. Ibsen, R. Laming, P. Andrekson, F. Cisternino, and H. Geiger, "40Gbit/s field transmission over standard fibre using midspan spectral inversion for dispersion compensation," *Electronics Letters*, vol. 35, pp. 581–582, 1999.
- [239] N. Amaya, G. Zervas, and D. Simeonidou, "Architecture on demand for transparent optical networks," in *ICTON 2011*, 2011.
- [240] P. A. Humblet and M. Azizoglu, "On the bit error rate of lightwave systems with optical amplifiers," *Journal of Lightwave Technology*, vol. 9, no. 11, pp. 1576–1582, 1991.
- [241] X. Zhang, Z. Qu, and G. Yang, "Probability density function of noise statistics for optically pre-amplified DPSK receivers with optical mach-zehnder interferometer demodulation," *Optics Communications*, vol. 258, pp. 177–182, 2006.